2010-04-14

Thermal Conductivity of Nanowires, Nanotubes and Polymer-Nanotube Composites

NIHAR R. PRADHAN
Worcester Polytechnic Institute

Repository Citation

PRADHAN, N. R. (2010). *Thermal Conductivity of Nanowires, Nanotubes and Polymer-Nanotube Composites*. Retrieved from https://digitalcommons.wpi.edu/etd-dissertations/112

WORCESTER POLYTECHNIC INSTITUTE

THERMAL CONDUCTIVITY OF NANOWIRES, NANOTUBES AND POLYMER-NANOTUBE COMPOSITES

by

Nihar R. Pradhan

A thesis submitted in partial fulfillment for the
degree of Doctor of Philosophy

in the
Worcester Polytechnic Institute
Department of Physics

April 2010

GRADUATE COMMITTEE APPROVAL

I, Nihar R. Pradhan, declare that this thesis titled, 'Thermal properties of Nanowires, Carbon nanotubes and Polymer-carbon nanotube Composites' and the work presented in it are my own.

This dissertation has been read by each member of the following graduate committee and found to be satisfactory.

Signed/Date: Germano Iannacchione 6 April '10

PROF. GERMANO S. IANNACCHIONE, (Supervisor) Department of Physics, WPI

Signed/Date: 4/6/2010

PROF. ALEX ZOZULYA, Department of Physics, WPI

Signed/Date: 4/10/2010

PROF. JIANYU LIANG, Department of Mechanical Engineering, WPI

DECLARATION

I, Nihar R. Pradhan, declare that this thesis titled, 'Thermal properties of Nanowires, Carbon nanotubes and Polymer-carbon nanotube composites' and the work presented in it are my own. I confirm that:

- This work was done wholly or mainly while in candidature for a research degree at this University.
- Where any part of this thesis has previously been submitted for a degree or any other qualification at this University or any other institution, this has been clearly stated.
- Where I have consulted the published work of others, this is always clearly attributed.
- Where I have quoted from the work of others, the source is always given. With the exception of such quotations, this thesis is entirely my own work.
- I have acknowledged all main sources of help.

Signed: NPradhan.

Date: 04|06|2010

WORCESTER POLYTECHNIC INSTITUTE

Abstract

Worcester Polytechnic Institute
Department of Physics

Doctor of Philosophy

by Nihar R. Pradhan

The primary goal of this dissertation is to present an experimental study of heat transport properties in Nanowires, Nanotubes, and Polymer-nanotube composites. In addition, thermal relaxation behavior of these nanocomposites were also investigated.

The dissertation consists of six chapters. Chapter 1 is an Introduction, in which the discovery, structure and physical properties of Nanowires and Nanotubes are outlined. In Chapter 2, overview of some of the well known synthesis technique of nanotubes and nanowires were described. The phonon transport in nanowires and nanotubes with their bulk counterpart is shortly discussed. The phonon scattering mechanism plays an important role in low-dimensional materials and is one of the main foci of this chapter.

Chapter 3 contains the Experimental details of high-resolution AC Calorimetry that was used to measure the specific heat and thermal conductivity of these nano composites. In this chapter, we briefly described the theoretical and the experimental construction, how we estimate the specific heat and thermal conductivity. In this method one end of the sample is heated by a known oscillating field and in the other end oscillation of temperature was measured. The relaxation thermal properties of PMMA+SWCNT composites studied by Modulated Differential Scanning Calorimetry was another experimental technique discussed in this chapter.

Chapter 4 presents specific heat and thermal conductivity measurements of Cobalt Nanowires (Co NWs). Measurements were done on anisotropic and randomly oriented composite samples. Anisotropic composite samples were made by growing the nanowires inside the highly ordered parallel cylindrical porous structures of an Anodic Aluminum Oxide (AAO) template. Randomly oriented samples were made by releasing the nanowires from the template by dissolving the AAO and drop cast on a silver sheet. The detail about the sample preparation of this directional measurement is one of the challenging problems discussed here. X-Ray Diffraction experiment and morphology study are also discussed with the thermal properties. Bulk cobalt powder was

also chosen to compare with nanowires. The result shows a high reduction of thermal conductivity of nanowire compared to the bulk counterparts.

Chapter 5 describes the study of thermal properties of anisotropic Multi-Wall Carbon Nanotubes (MWCNTs) and randomly oriented MWCNTs and Single-Wall Carbon Nanotubes (SWCNTs) from 300 to 400 K. Measurements on a randomly oriented sample were done by depositing a thin film of CNTs suspended in a solvent solution within a calorimetric cell and then allowing the solvent to evaporate. Anisotropic samples were made by growing the nanotubes inside the highly ordered, packed AAO nanochannels. The specific heat of anisotropic MWCNTs (C_p) and randomly oriented MWCNTs (C_p^m) and SWCNTs (C_p^s) shows strong deviations above room temperature from graphite powder. Specific heat of randomly oriented MWCNTs and SWCNTs shows similar behavior with the specific heat of bulk graphite powder (C_p^B). Thermal conductivity of randomly oriented MWCNTs (κ_R^m) and SWCNTs (κ_R^s) followed similar behavior of the thermal conductivity of graphite powder κ_B, exhibiting a maximum value near 364 K indicating the onset of boundary-phonon scattering. The thermal conductivity ($\kappa_{\|}$) of anisotropic MWCNTs increased smoothly with the increase in temperature over all the temperature ranges studied, which indicated the one dimensional nature of heat flow.

Chapter 6 contains dynamics of thermal properties, such as specific heat, enhancement of thermal conductivity, and glass transitions of Carbon nanotubes polymer nano composites. The inherently high thermal conductivity of many nano-materials has great potential for enhancing heat transfer applications. For example, the thermal conductivity of a single Single-Wall Carbon Nanotube (SWCNT) was found to be 6600 Wm^{-1}K^{-1}, twice that of diamond. When such high thermal conductivity materials were dispersed in a low thermal conducting polymer, the effective thermal conductivity of the composite can change dramatically. In this paper, an AC calorimetric technique is used to measure the specific heat (C_p) and effective thermal conductivity (κ_{eff}) of composites containing a dispersion of SWCNT in Polymethyl Metha Acralite (PMMA) from 300 to 400 K as a function of SWCNT volume fraction. The composites are prepared by dispersing SWCNTs with PMMA in chloroform solution thoroughly by ultra-sonication at elevated temperatures then removing the solvent by degassing. A large enhancement of effective thermal conductivity is observed as SWCNT content increases from 0.5 to 7.93 vol%, reaching 130% of pure PMMA at room temperature. These results are found to be in good agreement with the theoretical model proposed by Nelsen, Hamilton-Crosser, Geometric, and Xue. Additional experiments using a Modulated Differential Scanning Calorimetry (MDSC) technique as a function of scan rate were combined with the AC measurements to track the slowing dynamics of the glass transition for these nano-composites.

After studying the dynamics of polymer-carbon nanotube composites with temperature in chapter 6, we decided to study the dynamics of glass transition temperature of these composite materials not only as a function of temperature but also with frequency of temperature modulation by MDSC. So, chapter 7 contains the dynamics of thermal study as a function of temperature, frequency of temperature modulation, carbon nanotube concentration and scan rate of temperature.

Chapter 8 contains the filling of carbon nanotubes/nanopipes channel with liquid crystal, then studies the Imaging and dynamics of the confined liquid crystal phase transitions by MDSC method.

It is shown that carbon nanotubes as components of various nanocomposites have a significant effect on the mechanical, electrical, and thermal properties of these hybrid materials. The results of these chapters of thesis indicate the potential of utilizing CNT-based nanocomposites towards mechanical, electrical, and thermal applications in many different technological fields. This study also helps to understand the many basic physics in the molecular level of the phonon transport mechanism in nanostructures, and the dynamics of molecules of polymers in composite systems, in a confined nanochannel.

Chapter 9 and 10 contains the conclusion and appendix of this thesis.

Acknowledgements

There are a few people I would like to thank for this great success. Firstly, I would like to express my extreme gratefulness to my Supervisor, Prof. Germano S. Iannacchione for leading me into the exciting nanoscience field, for encouraging me to be creative and think deeper, and advising me to try different ideas. His softness and humor along with the excellent guidance in research not only made me learn many techniques and understanding in research but also, I enjoyed the work in the Laboratory. I am indebted to our collaborator, Prof. Jianyu Liang, from the Department of Mechanical Engineering, WPI. Her ideas, encouragement and help to do the best research cannot be eclipsed. I would like to thank Prof. Liangs group for fabricating the high quality nanostructures which I studied. I really enjoyed the collaboration and sitting in group meetings.

I would also like to thank Mr. Roger W. Steele, technical operation manager. He was one of the people who was very keen to help when I needed any technical help with experiments during my research work.

I would like to express my thanks to our department secretaries, Jackie Malone and Margaret Caisse for their kind help throughout my research career in WPI and all other members from the WPI Physics Department. I would like to give my special thanks to the Physics department for supporting my Teaching Assistantship throughout the stay in WPI. Without this, it may not be possible for me to achieve this highest degree.

I am thankful to my friends and colleagues for sharing their valuable time with me around the WPI campus. I enjoyed staying near WPI.

Finally, I would like to express my deepest gratitude to my parents and my sisters for their love and support throughout my student life.

Contents

List of Figures

List of Tables

Abbreviations

CNT	Carbon Nano Tubes
SW	Single Wall
SWCNT	Single Wall Carbon Nano Tubes
MWCNT	Multi Wall Carbon Nano Tubes
STM	Scanning Tunneling Microscope
MIT	Massachusetts Institute Technology
PMMA	Poly Methyl Metha Acralite
PS	Poly Styrene
PP	Poly Propylene
PANI	Polyaniline
LBL	Layer By Layer Assembly
AC	Alternating Current
ACC	Alternating Current Calorimeter
TIM	Thermoal Interface Materials
TE	Thermo Electrics
SEM	Scanning Electron Microscope
XRD	X Ray Diffraction
DSC	Differential Scanning Calorimeter
MDSC	Modulated Differential Scanning Calorimeter
TMDSC	Temperature Modulated Differential Scanning Calorimeter
CVD	Chemical Vapor Deposition
LC	Liquid Crystal
CNPs	Carbon Nanopipes
MWCNPs	Multi Wall Carbon Nano Pipes
DOS	Density Of States

CoNWs	Cobalt Nano Wires
AAO	Anodic Aluminum Oxide
VLS	Vapor Liquid Solid
GE	General Electric
DMM	Digital Multi Meter
PRT	Platinum Resistance Thermometer
RTD	Resistive Temperature Device
PID	Propertional Integral Derivative
GPIB	General Purpose Interface Bus
TA	Thermal Analysis
RCS	Refrigerated Cooling System
EDS	Energy Dispersion Spectroscopy
NMR	Nuclear Magnetic Resonance

Physical Constants

Speed of Light	c	$=$	$2.997\ 924\ 58 \times 10^8\ \mathrm{ms^{-S}}$
Pi	π	$=$	3.14
Carbon 60	C_{60}		
Plank constant	h	$=$	$6.626068 \times 10^{-34}\ \mathrm{m^2\ kg\ s^{-1}}$
Boltzmann constant	k_B	$=$	$1.3806503 \times 10^{-23}\ \mathrm{m^2kg\ s^{-2}K^{-1}}$

Symbols

a	atomic spacing distance	m
P	power	Ws^{-1}
ω	angular frequency	rad s^{-1}
f	frequency	s^{-1}
κ	thermal conductivity	$\mathrm{W}m^{-1}K^{-1}$
C_p	specific heat	$\mathrm{J}g^{-1}K^{-1}$
C^*	heat capacity	$\mathrm{J}K^{-1}$
C_h	heat capacity of heater	$\mathrm{J}K^{-1}$
C_s	heat capacity of sample	$\mathrm{J}K^{-1}$
C_θ	heat capacity of thermister	$\mathrm{J}K^{-1}$
K	thermal conductance	$\mathrm{W}K^{-1}$
T	Temperature	K
T_{ac}	Oscillating temperature	K
C	chiral vector	$\mathrm{m}s^{-1}$
λ	wave length	m
v_g	group velocity	$\mathrm{m}s^{-1}$
ZT	thermoelectric figure of merit	
S	Seebeck coefficient	$\mathrm{V}K^{-1}$
ρ	electrical resistivity	Ωm
κ_p, κ_{ph}	thermal conductivity of phonon	$\mathrm{W}m^{-1}K^{-1}$
κ_e	thermal conductivity of electron	$\mathrm{W}m^{-1}K^{-1}$
l	mean free path	m
ν	phonon velocity	$\mathrm{m}s^{-1}$
τ	time constant	s

K	wave vector	m^{-1}
λ_{dom}	dominant wavelength of phonon	m
θ_D	Debye temperature	K
ω_D	Debye cut off frequency	m^{-1}
Q	heating voltage	V
τ_i	Internal relaxation time constant	s
τ_e	External relaxation time constant	s
Φ	phase shift	rad
ϕ	reduced phase shift	rad
A	Area	m^2
R	resistance	Ω
λ_p^B	Bulk phonon mean free path	m
$c_p^{\|}$	specific heat in parallel direction	J$g^{-1}K^{-1}$
c_p^R	specific heat in random oriented sample	J$g^{-1}K^{-1}$
c_p^B	specific heat of bulk sample	J$g^{-1}K^{-1}$
c_p^M	specific heat of MWCNT	J$g^{-1}K^{-1}$
c_p^S	specific heat of SWCNT	J$g^{-1}K^{-1}$
c_p^*	complex specific heat capacity	J$g^{-1}K^{-1}$
$c_p^{'}$	real specific heat capacity	J$g^{-1}K^{-1}$
$c_p^{''}$	imaginary specific heat capacity	J$g^{-1}K^{-1}$
$\kappa_{\|}$	thermal conductivity along the axis	W$m^{-1}K^{-1}$
κ_R	thermal conductivity in random sample	W$m^{-1}K^{-1}$
ϕ_m	mass fraction	
ϕ_v	volume fraction	
ρ_p	density of polymer	g$cm-3$
ρ_f	density of fill	g$cm-3$
T_g	glass transition temperature	K
T_{NI}	isotropic to nematic transition temperature	K

Dedicated to my
Lovely Parents...

Chapter 1

INTRODUCTION

1.1 Introduction of Carbon Nanotubes

1.1.1 Discovery of Carbon nanotubes

Carbon is a special element in nature, whose chemical versatility makes it the central agent in most applications. Until recently it has been well known that the pure carbon exists in two forms: diamonds and graphite. In 1985, Harold Kroto, Robert Curl, and Richard E. Smally discovered a new form of carbon, the fullerenes, which are molecules of pure carbon atoms bonded together forming geometrically regular structures [1]. The best known is the C_{60}, which has precisely the same geometry as the soccer ball, total 60 carbon atoms. Due to the similarity of structure developed by American architect, Buckminster Fuller, this new molecule was named the buckminster fullerene, or buckyball.

The Carbon Nanotubes (CNTs) were first prepared by M. Endo in 1978, as part of his PhD studies at the University of Orleans in France. He was able to produce very small diameter filaments (about 7 nm) using a vapour-growth technique, but these fibers were not recognized as nanotubes and were not studied systematically. It was only after the discovery of fullerenes, C_{60} in 1985 by Kroto [1], that researchers started to explore carbon structures further. In 1991, when the Japanese electron microscopist Sumio Iijima observed CNTs [2], the field really started to advance. He was studying the material deposited on the cathode during an arc-evaporation synthesis of fullerenes when he observed CNTs. A short time later, Thomas Ebbesen and Pulickel Ajayan, from Iijima's lab, showed how nanotubes could be produced in bulk quantities by varying the arc-evaporation conditions [4]. But the standard arc-evaporation method had produced only multiwall nanotubes. After some research, it was found that the addition of metals such as cobalt to the graphite electrodes resulted in extremely fine single-wall nanotubes. The synthesis in 1993 of SWNTs was a major event in the development of CNTs [3, 5]. Although the discovery of CNTs was an accidental event, it opened the way to flourishing research into the properties of CNTs in labs all over the world, with many scientists demonstrating promising physical, chemical, structural, electronic, thermal and optical properties of CNTs.

1.1.2 Structure and General Properties

Carbon nanotubes are made up of one or more wrapped seamless concentric cylindrical carbon honeycomb lattice or graphene sheet. The theoretically smallest nanotubes have diameters equal to diameters of C_{60} ($d = 0.7$ nm). The most important structures are single wall (SW) and multi walled carbon nanotubes (MWCNTs). Multi walls are concentric circles of SWCNTs. The primary symmetry classification of CNT is divided into two parts , achiral and chiral. An achiral nanotube is defined by a nanotube whose mirror image has an indistinguishable structure to the original one. And, as a consequence, it is superimposable to it. There are only two cases of achiral nanotubes: armchair and zig-zag nanotubes. Single walled carbon nanotubes are completely described, except for their length, by a single vector $\vec{C}$ pointing from the first atom towards the second one and is defined by the relation:

$$\vec{C} = n\vec{a_1} + m\vec{a_2} \tag{1.1}$$

where n and m are integers. $\vec{a_1}$ and $\vec{a_2}$ are the unit cell vectors of the two-dimensional lattice formed by the graphene sheets. The direction of the nanotube axis is perpendicular to this chiral vector. The length of the chiral vector $\vec{C}$ [Fig. 1.1] is the circumference of the nanotube and is given by the corresponding relationship:

$$c = |\vec{C}| = a\sqrt{(n^2 + nm + m^2)} \tag{1.2}$$

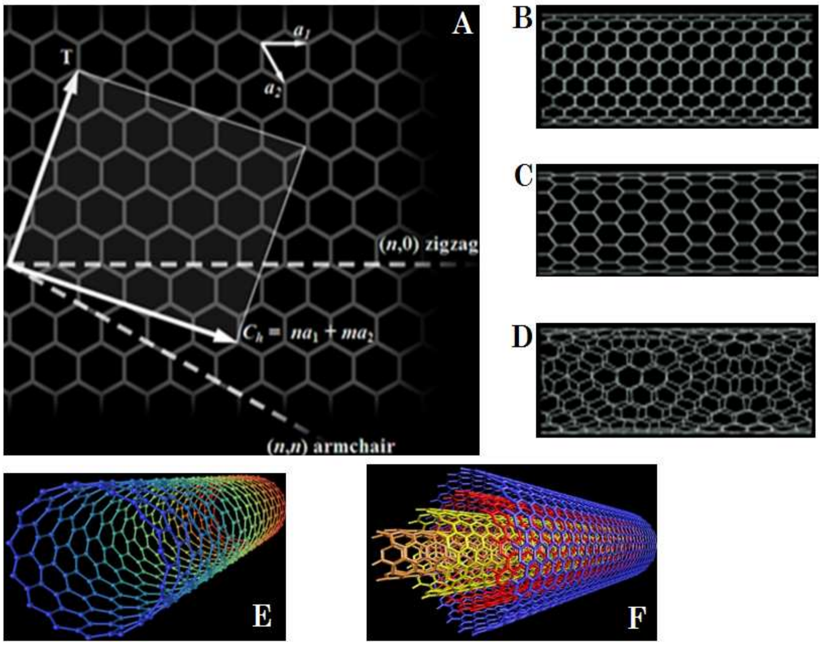

Figure 1.1: Chiral vector $\vec{C}$ and chiral angle θ with unit vectors shown in (A). (B) is armchair type $m = n$, (C) is zig-zag $m = 0, n \neq 0$, (D) is chiral type $m \neq n$, (E) shows single-wall and (F) Multi-wall carbon nanotubes. $\vec{a_1}$ and $\vec{a_2}$ are the unit cell vectors of the two-dimensional hexagonal graphene sheet. The circumference of nanotube is given by the length of chiral vector. The chiral angle θ is defined as the angle between chiral vector $\vec{C}$ and the zigzag axis [16].

where the value a is the length of the unit cell vector a_1 or a_2. This length a is related to the carbon-carbon bond length a_{cc} by the relation:

$$a = |\vec{a_1}| = |\vec{a_2}| = a_{cc}\sqrt{3} \tag{1.3}$$

Using the circumferential length c, the diameter of the carbon nanotube is thus given by the relation: $D = c/\pi$.

The angle between the chiral vector and zigzag nanotube axis is the chiral angle θ [Fig. 1.1]. With the integers n and m already introduced before, this angle can be defined by:

$$\theta = tan^{-1}\left(\frac{m\sqrt{3}}{m+2n}\right) \tag{1.4}$$

Nanotubes are only described by the pair of integers (n, m) which is related to the chiral vector. Three types of CNTs are revealed with these values: when $n = m$, the nanotube is called 'armchair' type ($\theta = 30^0$); when $m = 0$ and $m \neq 0$, the nanotube is called 'zig-zag' type ($\theta = 0^o$); when $m = n \neq 0$ and $m \neq n$, then it is called chiral type. The value of (n, m) determines the chirality of the nanotube and affects the optical, mechanical and electronic properties. Nanotubes with $|n - m| = 3q$ are metallic and those with $|n - m| = 3q \pm 1$ are semiconducting (where q is an integer).

The terminating cap of nanotube is formed from pentagons and hexagons. The smallest cap that fits on to the cylinder of the carbon tube, seems to be the well known C_{60} hemisphere. If we consider MWNTs, there are only a few possible sequences of (n, m) tubes to keep realistic intershell distance. For carbon materials, the intershell spacing "d" between two successive tubes is in the range from 0.344 nm to 0.36 nm [2, 6–9]. These values suggest a possible dependence of intershell distance on the tube size and some authors give an empirical relationship to fit TEM experimental data [14]:

$$d = 0.344 + 0.1\ exp\left(-\frac{c}{4\pi}\right) \tag{1.5}$$

where the term $c/2\pi$ is the radius of the tube. As a consequence of the tube diameter increase, the intershell distance decreases to 0.344 nm.

1.1.3 Physical Properties

Carbon nanotubes as a novel quasi one-dimensional material have stimulated great interest. From a theoretical point of view, SWCNT is ideal for study because of their relative simplicity. Although numerous theoretical calculations have been predicted, many novel physical and chemical properties are developed for carbon nanotubes. The nanometer size and random orientations of nanotube samples makes it extremely difficult to examine and certify these properties experimentally. However, taking advantage of the rapid progress of nano-fabrication and nano-manipulation, scientists are making fast progress on experimental studies and many valuable results have been obtained which agree well with theoretical predictions.

Since nanotubes are real ideal model systems for the investigations of low dimensional molecular conductors, measuring the electronic properties of individual nanotubes is always the focus of experimental studies. This is very challenging for two reasons. Both high quality nanotube samples and new techniques for making electrical contacts to individual tubes are necessary. Langer et al. reported the first measurement in MWCNT by using Scanning Tunneling Microscope (STM) lithography techniques [15]. They found that transport properties of MWCNT are consistent with the quantum transport behavior. Ebbesen systematically measured the conductance by four-probe measurement and observed both metallic and non-metallic behaviors [17]. Another versatile method of electrical contact was used by Frank et al. [18], where a single MWCNT attached to a STM tip was repeatedly immersed and pulled out of liquid metal like mercury. Surprisingly, a universal quantized conductance is measured at room temperature, providing evidence that transport in MWCNTs is ballistic over the distance of order of ≥ 1 μm.

Single wall nanotubes have well defined structures and relatively less defects. The success of synthesis of high-quality SWCNTs with uniform structures greatly stimulated experimental studies. The first results on individual SWNTs were obtained by Tans et al. [19], where they observed single electron transport with Columb blockade and resonant tunneling through single molecular orbitals. The STM was also used to measure the tunneling spectroscopy of nanotubes and found to be both metallic and semiconducting [20, 21]. Their data provided the first experimental verification of the bandstructure predictions. Their observed band structures quantitatively agree with the calculations.

1.1.4 Introduction to Thermal Transport in Low-dimensional Materials

Thermal transport in low dimensional systems has recently become a subject of consideration and much interest in the area of research. Due to the changing of length scale in electronics and optoelectronics devices from micro to nano scale length, there is much more interest to look at the properties of these materials for their outstanding applications.

The interest is drawn to new thermal transport science, that is operative at these small length scales and where quantum mechanical phenomena become significant and applied as different than the bulk counterpart. M. S. Dresselhaus and her groups from MIT have studied and made advancements in the field of thermal transport of low dimensional materials. At small length scales, the number of atoms or the number of electrons in the system become small, so that continuum mechanics and elastic continuum models have to be replaced by models that take into account the discrete nature of the electronic and vibrational states and their distribution in energy. In this realm, we can expect devices to be much smaller and faster, but to exhibit new unexpected phenomena of scientific interest and technological importance.

Two interesting limits of the thermal conductivity in nano-systems can be considered. In the high thermal conductivity limit, one might consider a single wall carbon nanotube, with cylindrical wall, one atom in thickness, 1 nm in diameter, and tens of microns in length. Advances in nanotechnology now are allowing measurements to be made for such a small object, which is expected to act like a heat pipe and to provide the highest thermal conductivity, exceeding that of any presently known material. In the opposite limit, effort is going into developing very low thermal conductivity nanostructures which might be used for thermoelectric devices, across which measurably large temperature gradients must be maintained and measured over submicron length scales. Thermoelectric properties are discussed briefly later.

Low-dimensional structures, such as quantum wells, superlattices, quantum wires, and quantum dots, offer new ways to manipulate the electron and phonon properties of a given material. In the regime where quantum effects are dominant, the energy spectra of electrons and phonons can be controlled through altering the size of the structures, leading to new ways to manipulate the properties of these materials, especially their thermal transport properties for selected applications. In this regime, each low-dimensional structure can be considered to give rise to a new material, even though the material may be made of the same atomic structure as its parent material. Each set of size parameters thus provides a new material that can be examined, both theoretically and experimentally, in terms of its thermal transport properties. Thus searching for materials with low-dimensional structures can be regarded as the equivalent of synthesizing many different materials from a small set of bulk materials and then measuring and optimizing their thermal transport properties for specific applications. Because the constituent parent materials of low-dimensional structures are typically simple materials with well-known properties, the low dimensional structures are amenable to a certain degree of analysis, prediction and optimization, while theoretical predictions for novel bulk materials are difficult. And each new material presents a different set of experimental and theoretical challenges, because it is often the case that neither their materials science nor their physical properties are adequately known.

There are several concepts behind using low-dimensional materials for thermoelectric performance. Thermoelectric performance depends upon three parameters S, σ and κ. The parameter which defined the thermoelectric materials is known as thermoelectric figure of merits and is defined as:

$$ZT = \frac{S^2 \sigma T}{\kappa} \tag{1.6}$$

where S is Seebeck coefficient ($= -\frac{\Delta V}{\Delta T}$) in Volt K^{-1}, σ is electrical conductivity in S m^{-1} and κ is thermal conductivity in W m^{-1} K^{-1}. Since these quantities in bulk materials are interrelated, its very difficult to vary/control each parameter independently without changing other parameters so that we can increase the value of ZT. This is because an increase in S usually results in a decrease in σ, and a decrease in σ produces a decrease in the electronic contributions to κ, following the WiedemannFranz Law [22] i,e.

At a given temperature, the thermal and electrical conductivities of metals are proportional, but raising the temperature increases the thermal conductivity while increases the electrical conductivity. This behavior is quantified in the Wiedemann-Franz Law:

$$\frac{\kappa}{\sigma} = LT \Rightarrow L = \frac{\kappa}{\sigma T} \tag{1.7}$$

where the constant of proportionality L is called Lorenz number. If the dimensionality of the material is decreased, the new variable of length scale becomes available for the control of materials properties. Then as the system size decreases and approaches nanometer length scales, it is possible to cause dramatic differences in the density of electronic states shown in Fig. 1.2, allowing new opportunities to vary S, σ, and κ quasi-independently when the length scale is small enough to give rise to quantum-confinement effects as the number of atoms in any direction. In addition, as the dimensionality is decreased from 3D crystalline solids to 2D (quantum wells) to 1D (quantum wires) and finally to 0D (quantum dots), new physical phenomena are also introduced and these phenomena may also create new opportunities to vary S, σ, and κ independently. These phenomena are discussed below. Furthermore, the introduction of many interfaces, which scatter phonons more effectively than electrons, or serve to filter out the low-energy electrons at the interfacial energy barriers, allows the development of nanostructured materials with enhanced ZT, suitable for thermoelectric applications.

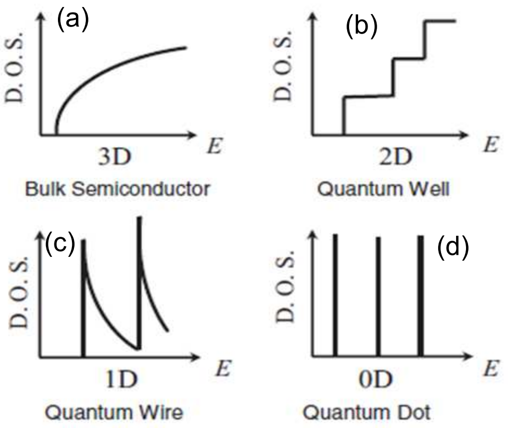

FIGURE 1.2: Electronic density of states for (a) bulk 3D crystalline semiconductor, (b) 2D quantum well, (c) 1D nanowire or nanotube, and (d) 0D quantum dot [23]. Materials systems with low dimensionality also exhibit physical phenomena, other than a high density of electronic states (DOS), that may be useful for enhancing thermoelectric performance.

For many years Bi is an attractive thermoelectric material because of the large anisotropy of constant energy surface of electrons, their high carrier mobility, high effective mass components that can be exploited for achieving a high electrical conductivity, and the heavy mass components that can be exploited to obtain a heavy DOS. Since Bi is a semi metal it has low Seeback coefficient S, because of the approximate cancellation of the electron and hole contributions to S [23, 24].

To achieve high thermo-electric figure of merits (ZT), we need to reduce the thermal conductivity without reducing electrical conductivity and its possible in nanostructure materials such as nanowires, described above. The first strategy to reduce thermal conductivity is to reduce the specific heat by altering the phonon dispersion relation, possibly through phonon confinement in super lattice and nanowires [25]. The second strategy is to reduce the lattice/phonon mean free path by scattering at boundaries, interface or phonon-phonon in nanowires, superlattices and nano-composites. This is because thermal conductivity is proportional to velocity of phonon (v), specific heat (C_p) and mean free path (λ).

$$\kappa = \frac{1}{3} C_p v \lambda \tag{1.8}$$

The first strategy is known as wave, coherent or quantum size effects [26, 27]. There is a key distinction between confinement by interfaces parallel to the transport direction (for example, nanowires and superlattices with in-plane transport) and confinement by interfaces perpendicular to the transport direction (superlattices with cross plane transport). For transport both parallel and perpendicular to the interfaces, the practical difficulty is maintaining phonon coherence. In a nanostructure the unit cell is much larger than in bulk, while after accounting for additional boundary scattering the mean free path is shorter than in bulk. With addition to this diffuse scattering reduce the interface scattering due to the randomizing the direction of scattered phonons.

The second strategy to reduce thermal conductivity is to reduce the mean free path by random scattering at boundaries and interfaces. This is known as particle or classical size effects, and coherent wave effects are ignored [28].

1.2 Thermal Properties of CNTs

The thermal wave propagation differs in carbon nanotubes from metal nanowires. Due to their unique crystalline structure, boundary scattering is nearly absent in CNTs. Thus CNTs show high thermal and electrical conductivity and this makes CNTs an ideal candidate for promising applications in nanoelectronics.

The potential applications and intriguing nanoscale thermal conduction physics has inspired several groups to measure CNTs thermophysical properties. Hone group [10] measured the temperature dependent thermoelectric power (TEP) of crystalline ropes of SWCNTs by simply applying a small temperature difference of maximum ± 0.2 K and measuring the voltage induced in the sample. They got moderately large holelike TEP at high temperature and the TEP approaches zero as $T \to 0$. Thermal conductivities of SWCNTs bundles and mats were measured by Hone group [11, 12]. The measured thermal conductance of millimeter size mat samples made of CNTs shows linear temperature dependence below 25 K and extrapolates to zero at zero temperature. The measurement results have advanced our understanding of thermal conduction in CNTs. However its very difficult to extract the thermal conductivity of single carbon nanotubes, due to the difficulty of measurement, tube-tube junction and tube-interface contact resistance. This is the primary reason theoretical values are always higher, an order of magnitude from the experimental values. Below room temperature Umklapp phonon-phonon scattering became very low or did even not occur [12, 13]. This indicates that the dominant scattering mechanism is phonon scattering by defects and boundaries of nanotubes wall. There are not too many but quite a lot of experimental and theoretical work has been done in low temperature thermal study, but there is no significant information available in high temperature thermal study of CNTs. Our work is based on above room temperature thermal properties of well aligned and random macroscopic composites of MW and SW carbon nanotubes. The phonon scattering mechanism depends upon the sample geometry, contact surface and interface roughness.

1.3 Thermal Properties of Polymer-Nanocomposites

A nanocomposite is defined as a material of more than one solid phase, where at least one dimension falls into the nanometer scale. The fabrication of nanocomposites opens up an attractive route to obtain novel, optimized, and miniaturized compounds that can meet a broad range of applications. In this context, the exceptional properties of nanoparticles have made them a focus of widespread research in nanocomposite technology. Since composites consist of several different components, superior physical and chemical characteristics of novel materials can be achieved. Therefore, the development of nanoparticle modified composites is presently one of the most explored areas in materials science and engineering [29].

Nowadays polymers play a very important role in numerous fields of everyday life due to their advantages over conventional materials (e.g. wood, clay, metals) such as lightness, resistance to corrosion, ease of processing, and low cost production. Besides, polymers are easy to handle and have many degrees of freedom for controlling their properties. Further improvement of their performance, including composite fabrication, still remains under intensive investigation. The altering and enhancement of the polymers properties can occur through doping with various nano-fillers such as metals, semiconductors, organic and inorganic particles and fibers, as well as carbon structures and ceramics [30–33]. Such additives are used in polymers for a variety of reasons, for example: improved processing, density control, optical effects, thermal conductivity, control of the thermal expansion, electrical properties that enable charge dissipation or electromagnetic interference shielding, magnetic properties, flame resistance, and improved mechanical properties, such as hardness, elasticity, and tear resistance [34–36].

Unique properties of carbon nanotubes (CNT) such as extremely high strength, lightweight, elasticity, high thermal and air stability, high electric and thermal conductivity, and high aspect ratio offer crucial advantages over other nano-fillers. The potential utility of carbon nanotubes in a variety of technologically important applications such as molecular wires and electronics, sensors, high strength materials, and field emission has been well established. Recently, much attention has been paid to the use of carbon nanotubes in conjugated polymer nanocomposite materials to harness their exceptional properties [18, 37]. CNT-based composites have attracted great interest due to an increasing technological demand for multifunctional materials with improved mechanical, electrical, thermal and optical performance, complex shapes, and patterns manufactured in an easy way at low costs. However, several fundamental processing challenges must be overcome to enable applicable composites with carbon nanotubes. The main problems with CNTs are connected to their production, purification, process ability, manipulation and solubility. Because of these difficulties, to date, the potential of using nanotubes as polymer composite has not been fully realized. There are only few nanotube-based commercial products on the market at present, which are in fact CNT/polymer composites with improved electrical conductivity [Hyperion Catalysis International]. This still requires intensive studies in order to compromise expectations with technological achievements in CNT composites. Since 1994, when Ajayan et al. [39] first introduced multiwall carbon nanotubes (MWCNTs) as filler materials in a polymer matrix, numerous projects have been focused on the fabrication, improvement, modeling, and characterization of such heterostructures [40–42].

The main objective of this study was to produce and investigate SWCNT-based nanocomposites as candidates for next generation of high-strength, light-weight, and conductive polymers. However, the effective utilization of CNTs in composite applications strongly depends on the ability to disperse them homogeneously throughout the matrix [18, 40, 41]. The surface of CNTs has to be modified in order to overcome their poor solubility. In this context, we used the well-known technique to disperse SWCNTs in solvents and polymers and then measured the specific heat and thermal conductivity with the different vol % of CNTs loading.

1.4 Review of CNT based Composites

These nanocomposite based polymers have been widely used for various products from automotive parts, electronics to commodities due to wealth of polymers suitable for each specific application. Nanotube based polymer composites, particularly CNT based, have a very rich application in the technological field due to their strength, stiffness and heat resistance. These properties depend upon the aspect ratios of fillers and the adhesive strength between filler and polymer matrix. The outstanding thermal and electrical conductivity of the carbon nanotubes make them promising filling material for the fabrication of new advanced composite systems for a broad range of technological applications. Efficient chemical functionalization of CNTs, homogeneous dispersions in solvents and supporting media, and good interconnectivity with matrix still remain very important issues that must be considered in order to achieve heterostructures with enhanced or even new properties. There are numerous methods and approaches for functionalization and further efficient dispersion of the carbon nanotubes in different media, as well as in literature. More details on the chemical modification of CNTs, the fabrication of various CNT-based composites, and their possible applications are presented below.

1.5 Properties of Polymer Nanocomposites

Polymers have been widely used for various products from automotive parts, electronic and commodities due to a wealth of polymers suitable for each specific application. Such polymers are usually reinforced with fillers such as glass, carbon fibers, carbon nanocomposites etc. to improve their properties (strength, stiffness, thermal conductivity, electrical conductivity etc.). The conventional micro filler polymer composites often result in phase separation and the degradation in polymer properties such as decrease ductile, poor moldability and surface smoothless of molded products. Therefore it is expected that the interface deficiency can be reduced and thermal properties can be improved by replacing these microfillers with extremely small nanofillers.

1.5.1 Mechanical Properties

The enhancement of mechanical properties of polymer nano composites can be attributed to the high rigidity and aspect ratio together with the favoring affinity between polymer and nanofillers. Some of the manufacturing companies have stepped forward to make novel nanocomposite products. The Toyota research laboratory first demonstrated the enhancement of nylon-nanocomposites. They observed and improved 40 % in tensile strength, 68 % in flexural strength, 68 % in tensile modulus and 120% in flexural modulus [68]. A dramatic enhancement was observed in exfoliated nanostructures such as thermoset amine-cured epoxy based MMT (mono-montmorillonite) nanocomposites and elastomeric epoxy [69, 70]. In contrast a relatively weak increase was reported for the intercalated nanocomposites such as those from clay and PMMA/PS (Polymethyl Metha-acralyte/Polystyrene) [67, 71]. The impact properties for nylon-6 nanocomposites was not affected too much as shown by whatever exfoliation process was used [73]. In the case of polypropylene (PP) nanocomposites [72], the slight enhancement in tensile strength is due to the lack of interfacial adhesion. The tensile strength decreased even more in PS intercalated nanocomposites due to the weak interaction at PS and clay interface [78].

1.5.2 Thermal Properties

The thermal properties can be characterized by different ways such as specific heat, thermal conductivity, thermal stability and so on. Thermal stability of polymer composites is generally estimated from the weight loss which comes from the formation of voltaic products. Recently there are many reports available on the improved thermal stability of nanocomposites [74–77].

The high thermal conductivity can be achieved by dispersing the nanoparticles in suitable methods. The high aspects ratio, high quality and well dispersed filler materials have much more enhancement in thermal conductivity.

1.5.3 Electrical Conductivity

Polymer nanocomposites exhibit unique electrical properties, which is mainly attributed to their ionic conductivity. The ionic conductivity of the polymer nanocomposites is strongly affected by the crystallinity of the materials.

Nanocomposites with conducting polymers have also been reported including polymers such as PANI [79–81], polypyrrole [82, 83] and polythiophene [82].

1.5.4 Automotive

Polymer nanocomposites offer higher performance with much less nanoparticles. This in turn results in significant affordable materials for automotive, aerospace, military, and sports equipment applications. The first commercial product of polymer nanocomposites is the timing-belt cover made from nylon 6 nanocomposites in Toyota Motors in the early 1990s [73]. Such timing-belt covers not only showed good thermal stability but also saved the weight up to 25 %. Besides that nylon 6 nanocomposites have also been used in engine covers, oil reservoir tanks and fuel hoses in the automotive industry. General Motors employed the thermoplastics Olefin nanocomposites for step-assist on Safari and Chevrolet in 2002. Such polymer nanocomposites can also be utilized as potential materials in various vehicles for external and internal parts such as mirror housings, door handles and under the hood parts.

1.6 Dispersion of Carbon Nanotubes

Due to the strong van der Waals attraction forces between carbon nanotubes, they tend to aggregate together inside the solution and form ropes, usually with highly entangled network structures. Thats why it is difficult to disperse CNT inside the polymers. But by careful procedure we can mix these two components without severe aggregation of nanotubes. The attractive forces also arise due to an entropic effect inside the polymer matrix [43]. Polymer chains in the region of the colloidal filler suffer an entropic penalty since roughly half of their configurations are precluded. Therefore, there is a depletion of the polymer in this region, resulting in an osmotic pressure forcing the filler particles to come together [18, 44–46].

The method of functionalizing nanotubes is a good choice. It requires chemical modifications of their surrounding surface supported by mechanical agitation methods such as ultrasonication and shear mixing [47–50]. Several functionalization methods are already reported. They are mainly based on the covalent (grafting-to and grafting-from) [51–53], and noncovalent (polymer wrapping) [51, 54–56], and non-covalent (polymer wrapping, π - π stacking interaction), adsorption of surfactants [58] coupling of surfactants and functionalities to CNTs described as follows:

(A) Covalent functionalization: Covalent methods refer to a treatment that involves bond breaking across the surface of the CNTs (e.g. by oxidation) which disrupts the delocalized π-electron systems and fracture of σ-bonds and hence leads to incorporation of other species across the CNTs surface. Introducing defects to the CNTs shell significantly alters the optical, mechanical and electrical properties of the nanotubes and leads to an inferior performance of the composites [57]. The advantage is that this kind of modification may improve the efficiency of the bonding between nanotubes and the host material (cross-linking). Therefore, the interfacial stress transfer between the matrix and CNTs may be enhanced leading to better mechanical performance.

(B) Non-covalent functionalization: This modification of the carbon nanotubes is of great advantage because no disruption of the sp^2 graphene structure occurs and the CNT properties are preserved. Its disadvantage concerns weak forces between wrapped/-coupled molecules that may lower the load transfer in the composite.

Various approaches for the fabrication of CNT-polymer composites were shown including different functionalization and dispersion methods of nanotubes [66]. The most important were:

1. Solution processing of composites: The most common method based on the mixing of the CNTs and a polymer in a suitable solvent before evaporating the solvent to form a composite film. The dispersion of components in a solvent, mixing, and evaporation are often supported by mechanical agitation (e.g. ultrasonication, magnetic stirring, shear mixing) [59, 60, 66].

2. Melt processing of bulk composites: This method concerns polymers that are insoluble in any solvent, like thermoplastic polymers [48, 61, 66]. It involves the melting of the polymers to form viscous liquids to which the CNTs can be added and mixed.

3. Melt processing of composite fibers: CNTs are added to the melts of the polymers. The formation of CNT/polymer fibers from their melts occurs through e.g. the melt-spinning process [62].

4. Composites based on thermosets: A thermoset polymer is one that does not melt when heated, such as epoxy resins. The composite is formed from a monomer (usually liquid) and CNTs, the mixture which is cured with crosslinking/catalyzing agents [63, 64].

5. Layer-by-layer assembly (LBL): CNTs and polyelectrolytes are used to form a highly homogeneous composite, with a good dispersion, good interpenetration, and a high concentration of CNTs. This method involves alternating adsorptions of a monolayer of components which are attracted to each other by electrostatic interactions resulting in a uniform growth of the films [65].

6. In-situ polymerization: The polymer macromolecules are directly grafted onto the walls of carbon nanotubes. This technique is often used for insoluble and thermally unstable polymers which cannot be melt processed. Polymerization occurs directly on the surface of CNTs [18, 41].

In general, all of these different techniques give various results in terms of the efficiency of the nanotubes dispersion, interfacial interaction between components, properties of the composites, and possible promising applications.

1.7 Thesis Overview

The major part of motivation for this thesis work is to understand and measure the thermal transport phenomena of nanotubes, nanowires and polymer nano-composites by using AC calorimetric techniques. In addition to this other physical properties of the materials are also discussed by other techniques. AC calorimetric techniques have been utilized to measure specific heat and thermal conductivity of these nano-composites. The main focus of this study is thermal characterization of novel nanostructures for TIM (Thermal interface materials) and TE (thermoelectric materials). There is not enough evidence about the thermal properties of nanostructures and this is one of the growing fields of research. So there is lot of experimental and theoretical evidence needed by the scientific community to apply these nanostructures in electronic, optoelectronic, sensors, and space applications. The other motivation for this thesis is to understand the thermal properties such as thermal conductivity and glass transition of carbon nanotubes dispersed polymer composites. The last part of thesis is the filling of liquid crystals inside carbon nanotubes/nanopipes and their alignment inside nanopipes. This work not only supports and helps us to understand the confinement effect of liquid crystal, but it also gives important information about the flow of liquid inside the nano-channel for potential applications to use nanopippets in drug delivery system inside the cell.

The different characterization fields of this work are: (a) specific and thermal conductivity of nanowires, carbon nanotubes and polymer nanotubes composite; (b) SEM, TEM, XRD, Optical characterization; (c) Electrical characterizations and (d) AC calorimetric techniques, (e) Modulated Differential Calorimetric (MDSC) study of glass transition of polymer nanocomposites, (f) imaging and studying dynamic properties of Liquid crystal confined inside carbon nanopipes. All these materials are presented in the following chapters.

After this introduction, Chapter 2 reviews the phonon transport in nanotubes and nanowires. Electron and phonons are the major heat careers in the materials. The role of phonon transport in bulk materials, nanowires and nanotubes are discussed. The effect of scattering of phonons plays an important role in the nanostructures thermal transport and these effects are analyzed with the quality of samples. It is very difficult to synthesize good quality or defectless nanowires or nanotubes. These defect occupied nanowires became aspects of reducing thermal conductivity of materials, suitable for thermoelectric application. The phonon scattering by defects produced in materials, dislocations and impurities are different in nanostructures.

Chapter 3 describes some of the methods of synthesis and thermal conductivity measurements of Nanowires and Nanotubes. The relevant methods of nanotubes and nanowires synthesis such as CVD, liquid-vapor deposition, and laser-ablation methods are shortly discussed. The AC calorimetric measurement and MDSC techniques are briefly discussed to measure specific heat and thermal conductivity of nano-composites.

Chapter 4 describes experimental methods to measure specific heat and thermal conductivity of Co NWs. Two different directional measurements of specific heat and thermal conductivity such as randomly oriented nanowires and anisotropic measurement are discussed. The phonon contribution in specific heat and thermal conductivity in nanowires is the main scientific evidence and the scattering mechanism holds during thermal wave propagation in these nanostructures are discussed. This chapter also describes the overview of some of the synthesis route for nanowires/nanotubes as desired configuration.

Chapter 5 contains results and discussion of specific heat and thermal conductivity of carbon allotropes, such as MW and SW carbon nanotubes, compared with micron size bulk graphite powders, The conductivity and temperature dependent resistivity are also measured and discussed in detail.

Chapter 6 contains measurement, results and discussions of specific heat and thermal conductivities of polymer SW carbon nanotubes composite. The enhancement of thermal conductivity is studied in PMMA polymers. Carbon nanotubes in different vol% are dispersed with PMMA in the most relevant and easy method, such that there is no agglomeration of nanotubes observed and then cast on to a silver sheet to make a thin film to study specific heat and thermal conductivities. The specific heat, thermal conductivity and behavior of glass transition were discussed with respect to different parameters such as temperature, scan rate of heating or cooling and nanotube concentrations.

Chapter 7 describes the dynamics of glass transition of PMMA+SWCNTs composites with temperature, frequency of applied temperature modulation, scan rate of temperature and different vol% of carbon nanotubes composites.

In chapter 8 we described how a small amount of LCs can be filled inside the MWCNPs. We studied the molecular behavior of these confined LCs by MDSC to know their orientations and dynamics inside the CNP channels with different applied frequency of temperature modulation.

Chapter 9 summarizes the thesis work and chapter 10 contains the appendix.

Bibliography

[1] H. W. Kroto, J. R. Heath, S. C. O'Brain, R. F. Curl, and R. E. Smalley, *Nature* **318**, 162 (1985).

[2] S. Ijima, *Nature* **354**, 56 (1991).

[3] S. Ijima and T. Ichihashi, *Nature* **363**, 603 (1993).

[4] T.W. Ebbesen and P.M. Ajayan, *Nature* **358**, 220 (1992).

[5] D. S. Bethune, C. H. Klang, M. S. de Vries, G. Gorman, R. Savoy, J. Vazquez, and R. Beyers, *Nature* **363**, 605 (1993).

[6] X. F. Zhang, X. B. Zhang, G. Van Tendeloo,S. Amelinckx, M. Op de Beeck, and J. Van Landuyt, *Journal of Crystal Growth* **130**, 368 (1993).

[7] Y. Saito, T. Y oshokawa, S. Bandow, M. Tomita, and T. Hayashi, *Phys. Rev. B* **48**, 1907,(1993).

[8] M. Bretz, B. Demczyk, and L. Zhang, *Journal of Crystal Growth* **141**, 304 (1994).

[9] X. Sun, C. Kiang, M. Endo, K. Takeuchi, T. Furuta, and M. Dresselhaus, *Phys. Rev. B* **54,** R12629 (1996).

[10] J. Hone, I. Ellwood, M. Muno, Ari Mizel, Marvin L. Cohen, A. Zettl, Andrew G. Rinzler, and R. E. Smalley, *Phys. Rev. Lett.* **80**, 1042 (1998).

[11] J. Hone, M. Whitney, C. Piskoti, and A. Zettl, *Phys. Rev. B.* **59**, R2514 (1999).

[12] J. Hone, M. C. Llaguno, N. M. Nemes, A. T. Johnson, J. E. Fischer, D. A. Walters, M. J. Casavant, J. Schmidt, and R. E. Smalley, *Appl. Phys. Lett.* **77**, 666 (2000).

[13] S. Berber, Y. K. Kwon, and D. Tomanek, *Phys. Rev. Lett.* **84**, 4613-4616 (2000).

[14] C. Kiang, M. Endo, P. Ajayan, G. Dresselhaus, and M. Dresselhaus, *Phys Rev Lett.* **81**, 1869,(1998).

[15] L. Langer, V. BaBayot, E. Grivei, J. P. Essi, J. P. Heramans, C. H. Olk, L. Stockman, C. Van Hasendonck, and Y. Bruynseraede, *Nature* **76**, 476 (1996).

[16] http://commons.wikimedia.org/wiki/File:$Types_of_\ Carbon_$Nanotubes.png .

[17] T. W. Ebbesen, H. J. Lezec, H. Hiura, J. W. Bennett, H. F. Ghaemi, and T. Thio, *Nature* **381**, 678 (1996).

[18] S. Frank, P. Poncharal, Z. L. Wang, and W. A. de Heer, *Science* **280**, 1744 (1998).

[19] S. J. Trans, M. H. Devoret, H. Dai, A. Theses, R. E. Smalley, L. J. Geerligs, and C. Dekker, *Nature* **386**, 474 (1997).

[20] J. W. G. Wildoer, L. C. Venema, A. G. Rinzler, R. E. Smalley, and C. Dekker, *Nature* **391**, 59 (1998).

[21] T. W. Odom, J. Huang, P. kim, and C. M. Lieber, *Nature* **391**, 62 (1998).

[22] A. Bejan and A. D. Allan, *Heat Transfer Handbook*, **NewYork,** Weily, 1338 (2003).

[23] M. Dresselhaus, G. Chen, M. Y. Tang, R. Yang, H. Lee, D. Wang, Z. Ren, J. P. Fleurial, and P. Gogna, *Advanced Materials* **19**, 1-12 (2007).

[24] M. Dresselhaus and J. P. Heremans, *Thermoelectrics Hand Book: Macro to Nano*, **Chapter 39**, (by Taylor and Francis Group, LLC 2006).

[25] C. Dames and G. Chen, *Thermoelectrics Hand Book: Macro to Nano*, **Chapter 42**, Taylor and Francis Group, LLC (2006).

[26] G. Chen, “Phonon transport in low-dimensional structures”, *Semicond. Semimetals* **71**, 203 (2001).

[27] B. Yang and G. Chen, “Phonon heat conduction in superlattice. In Chemistry, Physics, and Materials Science of Thermoelectric materials: Beyond Bismuth Telluride”, M.G. Kanatzidis, S.D. Mahanti and T.P. Hogan, Kluwer Academic/Plenum Publishers, New York (2003).

[28] G. Chen, “Nanoscale Energy Transport and Conversion”, *Oxford Univeristy Press*, **Oxford** (2004).

[29] P. M. Ajayan, P. V. Braun, and L. S. Schadler, "Nanocomposites science and technology", *Wiley VCH: Weinheim,*, **GR** (2003).

[30] S. Glushanin, V. Y. Topolov, and A. V. Krivoruchko, *Materials Chemistry and Physics* **97**(2-3), 357-364 (2006).

[31] P. Hine, V. Broome, and I. Ward, *Polymer* **46**(24), 10936-10944 (2005).

[32] N. Cioffi, L. Torsi, N. Ditaranto, G. Tantillo, L. Ghibelli, L. Sabbatini, T. Bleve-Zacheo, M. D'Alessio, P. G. Zambonin, and E. Traversa, *Chemistry of Materials* **17**(21), 5255-5262 (2005).

[33] A. Pelaiz-Barranco and P. Marin-Franch, *Journal of Applied Physics* **97**(3), 45 (2005).

[34] Z. M. Huang, Y. Z. Zhang, M. Kotaki, and S. Ramakrishna, *Composite Science and Technology* **63**(15), 2223-2253 (2003).

[35] J. Jordan, K. I. Jacob, R. Tannenbaum, M. A. Sharaf, and I. Jasiuk, *Materials Science and Engineering A-Structural Materials Properties Microstructure and Processing* **393**(1-2), 1-11 (2005).

[36] J. F. Gerard, "Fillers and filled polymers", Wiley-VCH: Weinheim (2001).

[37] L. N. An, W. X. Xu, S. Rajagopalan, C. M. Wang, H. Wang, Y. Fan, L. G. Zhang, D. P. Jiang, J. Kapat, L. Chow, B. H. Guo, J. Liang, and R. Vaidyanathan, *Advanced Materials* **16**(22), 2036-2040 (1004).

[38] "Carbon nanotubes science and applications"; CRC Press: Boca Raton, FL (2005).

[39] P. M. Ajayan, O. Stephan, C. Colliex, and D. Trauth, *Science* **265**, 1212-1214 (1994).

[40] P. J.F. Harris, "Carbon nanotubes and related structures new materials for the twenty-first century", Cambridge University Press: Cambridge (2001).

[41] M. J. O'Connell, "Carbon nanotubes properties and applications"; CRC Taylor and Francis: Boca Raton (2006).

[42] M. Moniruzzaman and K. I. Winey, *Macromolecules* **39**(16), 5194-5205 (2006).

[43] C. Bechinger, D. Rudhardt, P. Leiderer, R. Roth, and S. Dietrich, *Physical Review Letters* **83**(19), 3960-3963 (1999).

[44] A. Hirsch and O. Vostrowsky, *Functional Molecular Nanostructures* **245**, 193-237 (2005).

[45] S. Banerjee, M. G.C. Kahn, and S. S. Wong, *Chemistry-A European Journal* **9**(9), 1899-1908 (2003).

[46] K. Balasubramanian and M. Burghard, *Small* **1**(2), 180-192 (2005).

[47] H. L. Wu, C. C.M. Ma, Y. T. Yang, H. C. Kuan, C. C. Yang, and C. L. Chiang, *Journal of Polymer Science Part B-Polymer Physics* **44**(7), 1096-1105 (2006).

[48] M. L. Shofner, V. N. Khabashesku, and E. V. Barrera, *Chemistry of Materials* **18**(4), 906-913 (2006).

[49] P. Poncharal, C. Berger, Y. Yi, Z. L. Wang, and W. A. de Heer, *Journal of Physical Chemistry B* **106**(47), 12104-12118 (2002).

[50] W. Z. Tang, M. H. Santare, and S. G. Advani, *Carbon* **41**(14), 2779-2785 (2003).

[51] D. Baskaran, J. W. Mays, and M. S. Bratcher, *Polymer* **46**(14), 5050-5057 (2005).

[52] J. J. Ge, D. Zhang, Q. Li, H. Q. Hou, M. J Graham, L. M. Dai, F. W. Harris, and S. Z.D. Cheng, *Journal of the American Chemical Society* **127**(28), 59984-9985 (2005).

[53] Y. Liu, D. C. Wu, and W. D, *Angewandte Chemie-International Edition* **44**(30), 4782-4785 (2005).

[54] M. J. O'Connell, P. Boul, L. M. Ericson, C. Huffman, Y. H. Wang, E. Haroz, C. Kuper, J. Tour, K. D. Ausman, and R. E. Smalley, *Chemical Physics Letters* **342**(3-4), 265-271 (2001).

[55] A. Star, J. F. Stoddart, D. Steuerman, M. Diehl, A. Boukai, E. W. Wong, X. Yang, S. W. Chung, H. Choi, and J. R. Heath, *Angewandte Chemie-International Edition* **40**(9), 1721-1725 (2001).

[56] X. D. Lou, R. Daussin, S. Cuenot, A. S. Duwez, C. Pagnoulle, C. Detrembleur, C. Bailly, and R. Jerome, *Chemistry of Materials* **16**(21), 4005-4011 (2004).

[57] S. Ravindran, S. Chaudhary, B. Colburn, M. Ozkan, and C. S. Ozkan, *Nano Letters* **3**(4), 447-453 (2003).

[58] J. Chen, H. Y. Liu, W. A. Weimer, M. D. Halls, D. H. Waldeck, and G. C. Walker, *Journal of the American Chemical Society* **124**(31), 9034-9035 (2002).

[59] B. Safadi, R. Andrews, and E. A. Grulke, *Journal of Applied Polymer Science* **84**(14), 2660-2669 (2002).

[60] D. Qian, E. C. Dickey, R. Andrews, and T. Rantell, *Applied Physics Letters* **76**(20), 2868-2870 (2002).

[61] Q. H. Zhang, S. Rastogi, D. J. Chen, D. Lippits, and P. J. Lemstra, *Carbon* **44**(4), 778-785 (2006).

[62] T. D. Fornes, J. W. Baur, Y. Sabba, and E. L. Thomas, *Polymer* **47**(5), 1704-1714 (2006).

[63] A. Moisala, Q. Li, I. A. Kinloch, and A. H. Windle, *Composites Science and Technology* **66**(10), 1285-1288 (2006).

[64] J. A.Kim, D. G. Seong, T. J. Kang, and J. R. Youn, *Carbon* **44**(10), 1898-1905 (2006).

[65] A. A. Mamedov, N. A. Kotov, M. Prato, D. M. Guldi, J. Wicksted, and A. Hirsch, *Nature Materials* **1**(3), 190-194 (2002).

[66] J. N. Coleman, U. Khan, W. Blau, and Y. K. Gun'ko, *Carbon* **44**(9), 1624-1652 (2006).

[67] M. W. Noh and D. C. Lee, *Polymer Bull.* **42**, 619-626 (1999).

[68] Usuki, Kojima, A. Kawasumi, A. Okada, A. Fukusima, Y. Kurauchi, and O. Kamigaito, *Mater. Res.* **8**, 1185-1198 (1993).

[69] C. Zilg, R. Mulhaupt, and J. Finter, *J. Macromol. Chem. Phys.* **200**, 661-670 (1999).

[70] Z. Wang and T. Pinnavaia, *J. Chem. Mater.* **10**, 1820-1826 (1998).

[71] D. C. Lee and L. W. Jang, *J. Appl. Polym. Sci.* **61**, 1117-1122 (1996).

[72] N. Hasegawa, M. Kawasumi, M. Kato, A. Usuki, and A. Okada, *Journal of Applied Polymer Science* **67**(1), 87-92 (1998).

[73] A. Okada and A. Usuki, *Mater. Sci. Eng.* **C3**, 109-115 (1995).

[74] J. W. Gilman, *Appl. Clay Sci.* **15**, 31-49 (1999).

[75] J. Zhu, A. B. Morgan, F. J. Lamelas, and C. A. Wilkie, *Chem. Mater.* **13**, 3774-3780 (2001).

[76] M. Zanetti, G. Cammino, G. Thomann, and R. Mulhaupt *Polymer* **42**, 4501-4507 (2001).

[77] S. T. Lim, Y. H. Hyun, H. J. Choi, and M. S. Jhon, *Chem. Mater.* **14**, 1839-1844 (2002).

[78] A. Akelah and A. Moet, *J. Mater. Sci.* **31**, 3589-3596 (1996).

[79] V. Mehrota and E. P. Gianelis, *Solid State Communication* **77**, 155-158 (1991).

[80] Q. H. Zeng, D. Z. Wang, A. B. Yu, and G. Q. Lu, "Synthesis and Charaterization of Polyaniline-Montmorillonite Intercalation Nanocomposites". In Proceedings of Chemeca 2000: Oppertunities and challenges for the Resource and Processing Industries. Perth, Australia 9-12 July (2000).

[81] Q. H. Zeng, D. Z. Wang, A. B. Yu, and G. Q. Lu, *Nanotechnology* **13**, 549-553(2002).

[82] C. O. Oriakhi and M. M. Lerner, *Mater Res. Bull.* **30**, 723-729 (1995).

[83] V. Mehrotra and E. P. Giannelis, *Solid State Ionics* **51**, 115-122 (1992).

[84] C. Guthy, F. Gu, S. Brand, K. I. Winey, and J. E Fischer, *Transaction of the ASME* **129**, 1097-1099 (2007).

Chapter 2

PHONON TRANSPORT IN NANOWIRES AND NANOTUBES

2.1 Heat Transport in Nanotubes and Nanowires

2.1.1 Phonon Transport in Bulk Materials

In a solid, heat is transported by lattice/atomic vibrations called phonons and by charge carriers such as electrons and holes. This electronic contribution to thermal conductivity is the reason that materials that are good electrical conductors, such as metals, also have a high thermal conductivity. While the electronic component of the thermal conductivity may be significant for moderate to heavily doped semiconductors, the lattice contribution to heat transport typically dominates. Therefore, the focus of this work is on heat transport by the lattice.

The atoms in a solid crystal are held together in the form of a lattice by the chemical bonds between the atoms. These bonds are not rigid, but act like springs which connect the atoms, creating a spring-mass system. When an atom or plane of atoms is displaced, this displacement can travel as a wave through the crystal, transporting energy as it propagates. These waves can either be longitudinal where the displacement of the atom is in the same direction as the propagation of the wave, or they can be transverse where the atomic displacement is perpendicular to the direction of propagation. These lattice vibrations are quantized and are known as phonons.

By solving the equations of motion for these waves, one can determine the angular frequency (ω) of the waves as a function of their wavelength (λ) or their wavenumber (also called wavevector, k), where $k = 2\pi/\lambda$. The relationship between ω and k may then be plotted in the form of a dispersion relation. One important parameter that can be found from the dispersion relation is the group velocity (v_g), or speed of sound, of the phonons. The group velocity is defined as

$$v_g = \frac{d\omega}{dK} \tag{2.1}$$

which is simply the slope of the branch on the dispersion relation.

There are two distinct phonon branches in the dispersion relation. The lower branch is known as the acoustic branch since its group velocity is linear over a large range of wavenumbers, which is similar to sound waves. The upper branch is called the optical branch since this branch interacts with electromagnetic radiation and is responsible for the infrared properties of the crystal [26]. Since the group velocity in the acoustic branch is considerably larger than in the optical branch, the acoustic phonons contribute to the thermal conductivity to a much greater extent [27].

2.1.2 Phonon Transport in Nanotubes

The importance of phonons and their interactions in bulk materials is well known to those working in the fields of solid state physics, solid state electronic devices, optoelectronics, heat transport, quantum electronics and superconductivity. Phonons, i.e., quanta of lattice vibrations inside the materials medium, manifest themselves practically in all electrical, thermal and optical phenomena in semiconductors and other material systems. Phonon transport in nanostructures offers the opportunity to understand the basic science of phonon dynamics and transport, while allowing the ability to manipulate thermal properties. Reduction of the size of electronic devices below the acoustic phonon mean free path creates a new situation for phonon propagation and interaction. From one side, it complicates heat removal from the downsized devices. Optical phonons strongly influence optical properties of semiconductors while acoustic phonons are dominant heat carriers in insulators and technologically important semiconductors. Confinement of phonons in nanostructures and thin film can strongly affect the phonon group velocity, polarization, density of states and affect phonon interaction with electrons, defects and other phonons etc. The density of states in carbon nanotubes is very different than the bulk graphite in low energy states. The phonon density of states is calculated through band structure of isolated nanotubes, which is studied in Saito et al. [12–14] and Sanchez-Portal et al. [15] When a graphene sheet is rolled into a nanotube, the 2-D band structure folds into a large number of 1-D subbands. In a (10,10) tube, for instance, the six phonon bands (three acoustic and three optical) of the graphene sheet become 66 separate 1-D sub-bands. A direct result of this folding is that the nanotube density of states has a number of sharp peaks due to 1-D van Hove singularities, which are absent in graphene and graphite. Despite the presence of these singularities, the overall density of states is similar at high energies, so that the high temperature specific heat should be roughly equal as well. This is to be expected: the high-energy phonons are more reflective of carboncarbon bonding than the geometry of the graphene sheet. The phonon lifetime also changes and this arises from two sources. First, the phonon-phonon interactions can change because selection rules based on energy conservation and wave-vector relations depend on the dispersion relation. Second, boundary scattering can also affect thermal transport. Acoustic phonon dispersion is particularly strong in freestanding thin films or in nanostructures embedded into elastically dissimilar materials. Such modification may turn out to be desirable for some applications while detrimental for others. Thus, nanostructures offer a new way of controlling phonon transport via tuning its dispersion relation, i.e., phonon engineering [8]. It was reported [8] that cross-plane confinement of acoustic phonon modes leads to an in-plane decrease of the average phonon group velocity with a corresponding increase of the phonon scattering and reduction in the in-plane thermal conductivity. Before that, the acoustic phonon confinement was only considered in the context of its effect on the charge carrier mobility and electrical conductivity. Decreased averaged phonon group velocity in freestanding thin films or nanowires leads to the increased acoustic phonon relaxation on point defects (vacancies, impurities, isotopes, etc.), dislocations, as well as changes in three-phonon Umklapp processes. [29]. Thermal conductivity reduction, being bad news for the thermal management of downsized electronic devices, is good news for the thermoelectric devices, which require materials with high electrical conductivity and low thermal conductivity [9]. Thermal conductivity is the main parameter influenced by phonon propagation and this, in plane of thin films or along the length of nanowires, can decrease for two basic reasons. The first is the so-called classical size effect on thermal conductivity which is related to the increased phonon-rough boundary scattering [10]. This effect is pronounced when the feature size (size of the device) is on the order of phonon mean-free path [11].

2.2 Phonon Transport in Nanowires

Phonon transport is expected to be greatly impeded in thin (i.e., $d < \lambda$, where d is the diameter and λ is the phonon mean-free path) one-dimensional nanostructures as a result of increased boundary scattering and reduced phonon group velocities stemming from phonon confinement. Detailed models of phonon heat conduction in cylindrical [29] and rectangular [30] semiconducting nanowires that consider modified dispersion relations and all important scattering processes predict a large decrease ($> 90\%$) in the lattice thermal conductivity of wires tens of nanometers in diameter. Size-dependent thermal conductivity in nanostructures presents a major hurdle in the drive toward miniaturization in the semiconductor industry. Yet poor heat transport is advantageous for thermoelectric materials, which are characterized by a figure of merit ($ZT = S^2T/[\rho(\kappa_p + \kappa_e)]$, with S, T, ρ, κ_p, and κ_e the Seebeck coefficient, absolute temperature, electronic resistivity, lattice thermal conductivity, and electronic thermal conductivity, respectively. Typically, the conductivities improve as phonon transport worsens. A decade ago, the Dresselhaus group predicted that ZT can be increased above bulk values in thin nanowires by carefully tailoring their diameters, compositions, and carrier concentrations [31].

2.3 Phonon Scattering

When discussing heat transport in solids by phonons, an important factor is the degree to which these lattice waves are disrupted, or scattered. Phonons can be scattered by defects or dislocations in the crystal, crystal boundaries, impurities such as dopants or alloying species, or by interactions with other phonons. These scattering mechanisms can be grouped into two categories: elastic scattering between a phonon and an imperfection where the frequency of the incident phonon does not change, or inelastic scattering between interacting phonons where the frequency does change.

An important metric in the discussion of phonon scattering mechanisms is the phonon mean-free path λ, which is the average distance a phonon travels between collisions or scattering events. The mean free path is defined as

$$\lambda = \nu\tau \tag{2.2}$$

where ν is the phonon velocity and τ is the average time between scattering events (also called the mean free time). The mean-free path in material may be estimated using kinetic theory as [28].

2.3.1 Normal and Umklapp Scattering

Phonon scattering is highly frequency dependent and high frequency phonons are typically scattered more than low frequency phonons. For a harmonic oscillator, the spring constant is independent of the spring deformation. However, this is not the case for the bonds between atoms, as the spring constant can change if the bond is strained. So as one lattice wave propagates across a plane of atoms, the atoms will be displaced slightly from their equilibrium positions and the spring constant between those atoms will be modified. If another lattice wave is incident on these same atoms it will come across this different spring constant and it may scatter. This is the origin for Inelastic scattering.

There are two types of scattering observed due to the phonon-phonon interactions, (i) elastic scattering (Normal scattering) and (ii) Inelastic scattering (Umklapp scattering). The Fig. 2.1 illustrated the Normal and Umklapp scattering process, where Elastic scattering of phonons by crystal imperfections occur when the energy and frequency of phonons are conserved, and inelastic scattering between interacting phonons occur when the frequency changes.

Normal scattering process is the two phonons with wave vectors K_1 and K_2 that can combine to produce a third phonon with wave vector K_3 (Fig. 2.1 (A)) or one phonon K_1 can scatter to two phonon K_2 and K_3 , or one phonon can scatter into two phonons (Fig. 2.1 (B)). In these processes, phonon momentum, $\hbar$K , is conserved, thus normal processes do not produce any direct resistance to heat flow.

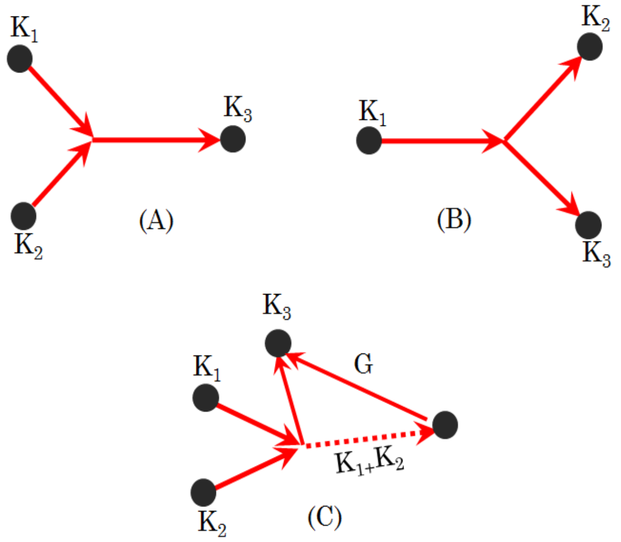

Figure 2.1: (A) and (B) are two processes known as A Normal process is when one phonon scatters into two phonons. (C) Umklapp process where two phonons combine to create a third. Due to the discrete nature of the atomic lattice there is a minimum phonon wavelength, which corresponds to a maximum allowable wavevector. If two phonons combine to create a third phonon which has a wavevector greater than this maximum, the direction of the phonon will be reversed or flipped over with a reciprocal lattice vector G, such that its wavevector is allowed.

The Umklapp process is very important to study in nanostructures. In this case K_1 and K_2 combine to form a third phonon $K_3 = K_1 + K_2$, but due to the discrete nature of atomic arrangement in crystal there is a minimum wavelength of phonon which can propagate through the crystal of $2a$, where a is atomic spacing. Since $k = 2\pi/\lambda$, hence upper limit of k is π/a. If the sum of K_1 and K_2 is greater than this maximum, the process can only be completed with the addition of what is known as the reciprocal lattice vector [32**?** , 33]. This reciprocal lattice vector flips the phonon over to a lower frequency and wave vector, and reverses the direction of the phonon as illustrated in Fig. 2.1 (C). Phonon momentum is not conserved during the umklap process, therefore producing a resistance to heat flow.

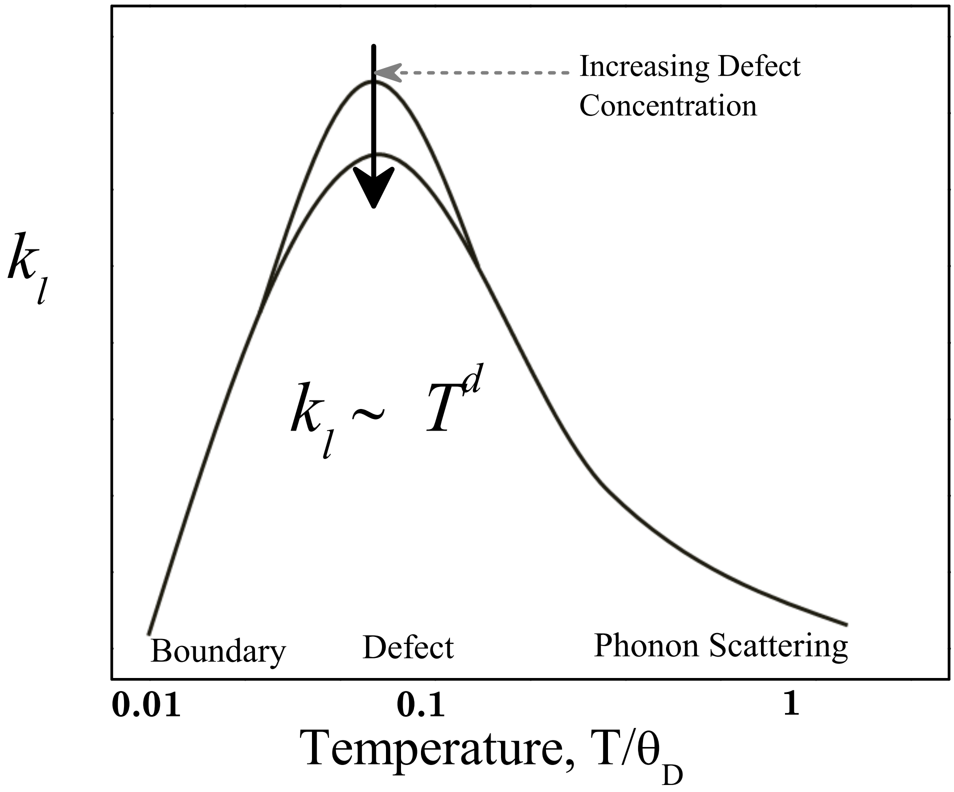

FIGURE 2.2: Temperature dependence of lattice thermal conductivity of solids. Boundary scattering dominates at lower temperatures, while impurity scattering becomes significant at intermediate temperatures. At high temperatures, inelastic scattering contributes considerably towards the overall thermal resistance.

2.3.2 Scattering by Defects, Dislocations and Impurities

When phonon propagates inside the material medium, in addition to the phonon-phonon interactions, phonon may scatter due to many parameters such as crystal imperfection, defects, dislocation, impurities etc.

Defects or dislocations in the atomic lattice have the effect of acting as a different mass and/or spring constant to the incident phonons. Impurity atoms will have a different mass and spring constant from the host atoms, thus disrupting phonon transport in a similar manner as described above. These impurity atoms can be in the form of dopant atoms or they can be species introduced to form an alloy. Alloying is a particularly effective way to reduce thermal conductivity. A good example could be, at room temperature, silicon [34] has a thermal conductivity of approximately 140 W/m-K and germanium [35] has a thermal conductivity of roughly 60 W/m-K. However, Si_xGe_{1-x} alloys [36] have a room temperature thermal conductivity of approximately 510 W/m-K, for Ge concentrations of 10 to 90%. A typical plot of phonon thermal conductivity of a material vs. temperature is shown in Fig. 2.2.

2.3.3 Temperature dependence of Phonon Scattering

Described above all different scattering processes in nanostructures or bulk materials may dominate heat transport in a material depending on temperature. This is due to the fact that the dominant wavelength of the phonon, λ_{dom}, and the temperature are related by an analogous Wien's displacement for phonons: $\lambda_{dom} = \frac{h\nu}{3k_BT}$, where h is Planck's constant. At low temperatures, the dominant phonon wavelength is so large that the phonons are not scattered by the defects. Moreover, as the dominant wavelength is large, corresponding wavevectors are small. Since large wavevectors are required for Umklapp scattering, this mechanism becomes unimportant, and phonon-phonon scattering is frozen out. Therefore, boundary scattering is the dominating mechanism at low temperatures as shown in Fig. 2.2. The phonon component of thermal conductivity, κ_{ph}, is defined as $\kappa_{ph} = \frac{1}{3}c_{ph}\nu_{ph}l_{ph}$, where c_{ph} is the phonon heat capacity, ν_{ph} is the speed of sound in the material, and λ_{ph} is the mean free path of the phonons. At low temperatures, ν_{ph} and l_{ph} are constant, and $c_{ph} \propto T^3$. Therefore, κ_{ph} also varies as T^3.

As the temperature increases, defect scattering becomes more dominant. This is due to the fact that the dominant phonon wavelength decreases as the temperature increases, and gradually becomes comparable to the size of the defects. This causes phonons to be scattered at the defect sites. For further increases in the temperature, wavevectors become so large that Umklapp scattering starts to play an important role.

A typical plot of phonon thermal conductivity of a material vs. temperature is shown in Fig. 2.2. For temperatures much smaller than the Debye temperature, as other scattering mechanisms are frozen out, boundary scattering is the dominating mechanism for heat transport. Debye temperature, θ_D, is defined as $\theta_D = \frac{h\omega_D}{k_B}$, where ω_D is the Debye cutoff frequency. In the middle range, where κ_{ph} plateaus, impurity scattering is more important. At higher temperatures, Umklapp-scattering becomes dominant and we observe a decline in the thermal conductivity. It is to be noted that impurity scattering may dominate over much of the temperature range for alloys and doped semiconductors as they have a large number of defects and impurities.

2.4 Summary

The phonon transport in nanostructure is different than their bulk materials. When we go from bulk to nanostructure, the materials structure and lattice arrangement are not exactly the same as bulk structure. There are a large number of defects produced during the nanostructure formation which significantly changes the phonon transport as compared to their bulk counterpart. Due to the high defects level inside the nanowires, thermal conductivity was drastically reduced compared to their bulk materials.

Bibliography

[1] G. A. Ozin, *Adv. Mater.* **4**, 612-649 (1992).

[2] R. J. Tonucci, B. J. Justus, A. J. Campillo, and C. E. Ford, *Science* **258**, 783-785 (1992).

[3] J. Y. Ying, *Science* **18**, 56 -63 (1999).

[4] J. Ling, H. Chi, A. Yin, and J. M. Xu, *Journal of Appl. Phys.* **91**, 2544 (2002).

[5] R. S. Wagner and W. C. Ellis, *Appl. Phys. Lett.* **4**, 89-90 (1964).

[6] E. I.Givargizov, *J. Cryst. Growth* **31**, 20-30 (1975).

[7] Y. Wu and P. Yang, *Chem. Mater.* **12**, 605-7 (2000).

[8] A. A. Balandin, *J. Nanosci. Nanotech.* **5**(7), 1015-1022 (2005).

[9] A. A. Balandin, *Phys. Low-Dim. Structures.* **73**(5/6), 73 (2000).

[10] A. A. Balandin, *Int. J. Therm. Sci.* **39**, 47 (2000).

[11] J. M. Ziman, "Electrons and Phonons", University Press, Oxford (1979).

[12] J. Hone, *Dekker Encyclopedia of Nanoscience and Nanotechnology.*, **DOI: 10:108/E-ENN 120009128,**, 60, (2004).

[13] R. T. Saito, T. Takeya, H. Kimura, M. S. Dresselhaus, and G. Dresselhaus, *Phys. Rev. Lett.* **57**, 4145-5 (2008).

[14] R. T. Saito, G. Dresselhaus, and M. S. Dresselhaus, *London: Imperial College Press.* (1998).

[15] Sanchez-Portal, D.; E. Artacho, J. M. Solar, A. Rubio, and P. Ordejon, *Phys. Rev. B.* **19**, 12678-88 (1999).

[16] Y. J. Zhang, Q. Zhang, N. L. Wang, Y. J Yan, H. H. Zhou, and J. Zhu, *J. Cryst. Growth.* **226**, 185-91 (2001).

[17] J. Westwater, D. P. Gosain, S. Tomiya, S. Usui, and H. Ruda, *J. Vac. Sci. Technol. B* **15**, 554-57 (1997).

[18] Y. Wu and P. Yang, *J. Am. Chem. Soc.* **123**, 3165-66 (2001).

[19] M. S. Gudiksen and C. M. Lieber, *J. Am. Chem. Soc.* **122**, 8801-2 (2000).

[20] Y. Wu, H. Yan, M. Huang, B. Messer, J. H. Song, and P. Yang, *Chem. Eur. J.* **8**, 1260-68 (2002).

[21] X. Duan and C. M. Lieber, *Adv. Mater.* **12**, 298-302 (2000).

[22] C. C. Chen, C. C. Yeh, C. H. Chen, Yu MY, and Liu HL, *J. Am. Chem. Soc.* **123**, 2791-98 (2001).

[23] J. Zhang, X. S. Peng, X. F. Wang, Y. W. Wang, and L. D, Zhang, *Chem. Phys. Lett.* **345**, 372-76 (2001).

[24] M. He, P. Zhou, S. N. Mohammad, G. L. Harris, and J. B. Halpern, *J. Cryst. Growth* **231**, 357-65 (2001).

[25] W. S. Shi, Y. F Zheng, N. Wang, C. S. Lee, and S. T. Lee, *J. Vac. Sci. Technol. B* **19**, 1115-18 (2001).

[26] N. W. Ashcroft and D. N. Mermin, *Solid State Physics*, Saunders College Publishing, Fort Worth (1976).

[27] C. L. Tien, A. Majumdar, and F. M. Gerner, *Microscale Energy Transport*, Taylor and Francis, Bristol, (1998).

[28] C. Kittel, “Introduction to Solid State Physics”, John Willey and Sons, New York 1996.

[29] J. Zou and A. Balandin, *J. Appl. Phys.* **89**, 293238 (2001).

[30] X. Lu, J. H. Chu, and W. H. Shen, *J. Appl. Phys.* **93**, 121929 (2003).

[31] L. D. Hicks and M. S. Dresselhaus, *Phys. Rev. B* **47**, 12727 (1993).

[32] N. W. Ashcroft and D. N. Mermin, “Solid State Physics”, *Saunders College Publishing*, **FortWorth,** (1976).

[33] C. L. Tien, A. Majumdar, and F. M. Gerner, “Microscale Energy Transport”, Bristol, *Taylor and Francis*, **Bristol,** (1998).

[34] Y. S. Touloukian, *Thermophysical Properties of Matter* **2**, 326-338 (1970).

[35] Y. S. Touloukian, *Thermophysical Properties of Matter*, **2**, 108-111 (1970).

[36] J. P. Dismukes, L. Ekstrom, E. F. Steigmeier, I. Kudman, and D. S. Beers, *Journal of Applied Physics* **35**, 2899-2970 (1964).

Chapter 3

EXPERIMENTAL METHODS FOR THERMAL MEASUREMENT

3.1 Materials and Synthesis

3.1.1 Nanowires and Synthesis Technique

Nanowires are especially very attractive for nanoscience studies as well as for nanotechnology applications. Nanowires have many advantages over bulk counterparts. Nanowires, compared to other low dimensional systems, have two quantum confined directions, while still leaving one unconfined direction for electrical conduction. This allows nanowires to be used in applications where electrical conduction, rather than tunneling transport, is required. Because of their unique density of electronic states (DOS), nanowires in the limit of small diameters are expected to exhibit significantly different optical, electrical, thermal and magnetic properties from their bulk 3D crystalline counterparts. The increased surface area, enhanced diameter-dependent bandgap, exciton binding energy, and increased surface scattering for electrons and phonons are just some of the ways in which nanowires differ from their corresponding bulk materials. Yet the sizes of nanowires are typically large enough ($>$ 1 nm in the quantum confined direction) to have local crystal structures closely related to their parent materials, thereby allowing theoretical predictions about their properties to be made on the basis of an extensive literature relevant to their bulk properties. Not only do nanowires exhibit many properties that are similar to, and others that are distinctly different from, those of their bulk counterparts, nanowires have the advantage from an applications standpoint that some of the materials parameters that are critical for certain properties can be independently controlled in nanowires, but not in their bulk counterparts, such as, for example, their thermal conductivity. Also certain properties can be enhanced non-linearly in small diameter nanowires, by exploiting the singular aspects of the 1D electronic density of states. Furthermore, nanowires have been shown to provide a promising framework for applying the "bottom-up" approach (Feynman, 1959) for the design of nanostructures for nanoscience investigations and for potential nanotechnology applications. From all these aspects: (1) these new research and development opportunities nanowires/nanotubes driven by, (2) the smaller and smaller length scales now being used in the semiconductor, opto-electronics and magnetics industries, and (3) the dramatic development of the biotechnology industry where the action is also at the nanoscale, the nanowire/nanotubes research field has developed with exceptional speed in the last few years. Therefore a review of the current status of nanowire/nanotubes research is of significant broad interest at the present time. It is the aim of this study to focus on nanowire properties that differ from those of their parent crystalline bulk materials, with an eye toward possible applications that might emerge from the unique properties of nanowires/nanotubes and from future discoveries in this field.

Before discussing some specific strategies for growing one-dimensional nanostructures, it is interesting to know the difference between growth methods and growth mechanisms. Growth mechanisms are the general phenomenon whereby a one-dimensional morphology is obtained, and the growth methods are the experimentally employed chemical processes that incorporate the underlying mechanism to realize the synthesis of these nanostructures. A novel growth mechanism should satisfy three conditions: It must (a) explain how one-dimensional growth occurs, (b) provide a kinetic and thermodynamic rationale, and (c) be predictable and applicable to a wide variety of systems. Growth of many one-dimensional systems has been experimentally achieved without satisfactory elucidation of the underlying mechanism, as is the case for oxide nanoribbons. Nevertheless, understanding the growth mechanism is an important aspect of developing a synthetic method for generating one-dimensional nanostructures of desired material, size, and morphology. This knowledge imparts the ability to assess which of the experimental parameters controls the size, shape, and monodispersity of the nanowires, as well as the ease of tailoring the synthesis to form higher-ordered heterostructures. In general, one-dimensional nanostructures are synthesized by promoting the crystallization of solid-state structures along one direction. The actual mechanisms of coaxing this type of crystal growth include (a) growth of an intrinsically anisotropic crystallographic structure, and (b) the use of various templates with one-dimensional morphologies to direct the formation of one-dimensional nanostructures.

In this chapter we have discussed (1) some common synthesis techniques that have successfully afforded high quality nanowires of large variety of materials, and (2) Phonon transport and mechanism inside the nanowires and nanotubes. There was also a short overview of synthesis methods approached by many groups to grow well defined, high quality and desired shapes and sizes of nanostructures. The synthesis methods of nanowires/nanotubes used for our study was described briefly in the next two chapters and more detail can be found in the Huanan Duan thesis [24].

3.2 CVD Methods, Template-Assisted Synthesis

The template-assisted synthesis of nanowires and nanotubes is a conceptually simple and intuitive way to fabricate highly ordered anisotropic nanostructures [1–3, 12]. These templates contain very small cylindrical pores or voids within the host material, and the empty spaces are filled with the chosen material, which adopts the pore morphology, to form nanowires. This method provides well aligned, densely packed and desirable sizes of nanowires/nanotubes.

Template Synthesis

In template-assisted synthesis of nanostructures, the chemical stability and mechanical properties of the template, as well as the diameter, uniformity and density of the pores are important characteristics to consider. Templates frequently used for nanowire synthesis include anodic alumina (Al_2O_3), nano-channel glass, ion track-etched polymers and mica films.

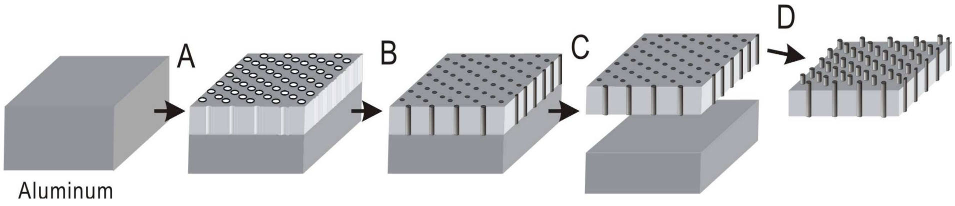

Figure 3.1: Synthesis method used for Co Nws.

Porous anodic alumina templates were produced by anodizing pure Al films in various acids [12]. Under careful chosen anodization conditions, the resulting oxide film possesed a regular hexagonal array of parallel and nearly cylindrical channels, as shown in Fig. 4.1

Co NWs were synthesized by electrodeposition assisted by a homemade anodic aluminum oxide (AAO) template. Fig. 4.1 provides a schematic of the synthesis steps. The AAO templates were obtained by a well-established two-step anodization process [4, 29]. The detail of anodization of nanowires was described in the experimental part of the next chapter and also can be found elsewhere [24].

3.3 Vapor-Liquid-Solid (VLS) Methods

This process was originally developed by Wagner and Ellis to produce micrometer-sized whiskers in the 1960s [5], later justified thermodynamically and kinetically [6], and recently reexamined by Lieber, Yang, and other researchers to generate nanowires and nanorods from a rich variety of inorganic materials [7–16]. Several years ago, people used in situ transmission electron microscopy (TEM) techniques to monitor the VLS growth mechanism in real time [17]. A typical VLS process starts with the dissolution of gaseous reactants into nanosized liquid droplets of a catalyst metal, followed by nucleation and

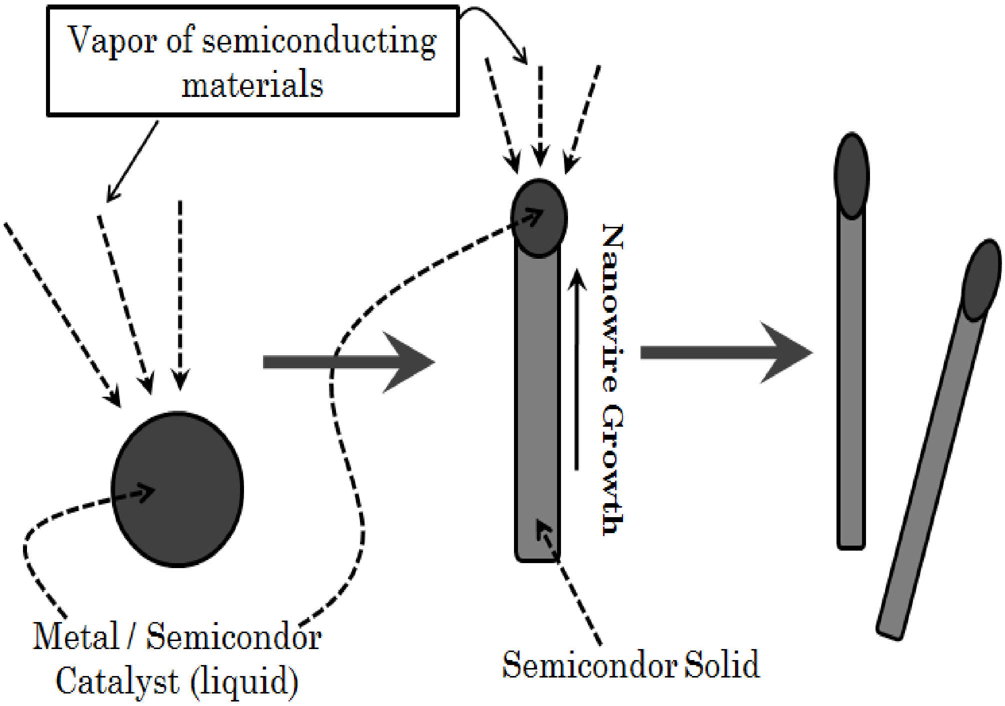

FIGURE 3.2: Schematic diagram illustrating the growth of semiconducting nanowires by the VLS mechanism [5].

growth of single-crystalline rods and then wires. The one-dimensional growth is induced and dictated by the liquid droplets, whose sizes remain essentially unchanged during the entire process of wire growth. Each liquid droplet serves as a virtual template to strictly limit the lateral growth of an individual wire. The major stages of the VLS process can be seen in Fig. 3.2, with the growth of a Ge nanowire observed by in situ TEM [17].

Carbon nanotubes have been fabricated by using the CVD method within the pores of anodic alumina templates to form highly ordered carbon nanotubes arrays. A small amount of Cobalt metal catalyst was electrochemically deposited on the bottom of the pores, then the template was placed in the furnace and heated at $\sim 700-800$ ^{o}C with flowing gas of N_2 and acetylene (C_2H_2) or ethylene (C_2H_4). The hydrocarbon molecules are polarized and form carbon nanotubes inside the pores of the AAO template with the help of metal catalysts. The detail about carbon nanotube synthesis is described in Chapter 5.

3.4 AC Calorimetry

The AC Calorimetry technique is ideal for the study of phase transition and thermal measurement for several important reasons. Measurements of heat capacity are made at near equilibrium conditions. This is crucial since much of the thermodynamic theory of phase transitions is based on equilibrium considerations. It also allows the use of averaging routines and total automation thus resolving remarkably small heat capacity changes. In most cases, only a small amount of material is required to achieve a high resolution. Finally, strict thermal isolation of the sample from the surroundings (as in an adiabatic technique) is not required. Its implementation is straightforward and adaptable to a variety of physical systems over a wide temperature range.

3.4.1 Theory

The AC Calorimetry technique was originally introduced by Sullivan and Seidel [1] in 1968. In this technique, sinusoidal heating by a voltage of frequency f_v is applied to the sample of interest inducing temperature oscillations of frequency $2f_v$. The heat capacity of the sample is inversely proportional to the magnitude of the temperature oscillations. The derivation given below is geometry independent, i.e., the locations of the applied heat and the sensing of the resulting temperature oscillations is unimportant provided certain requirements are met. A schematic representation of the thermal model is shown in Fig. 3.3

The fundamental principle of the AC calorimetry technique consists of applying periodically modulated, sinusoidal power, and measuring the resulting sinusoidal temperature response. As we will show later, the heat capacity of the sample is inversely proportional to the amplitude of the temperature oscillations. The derivation of the basic operating equations based on a simplified thermal model of the system is meeting certain requirements geometry independent.

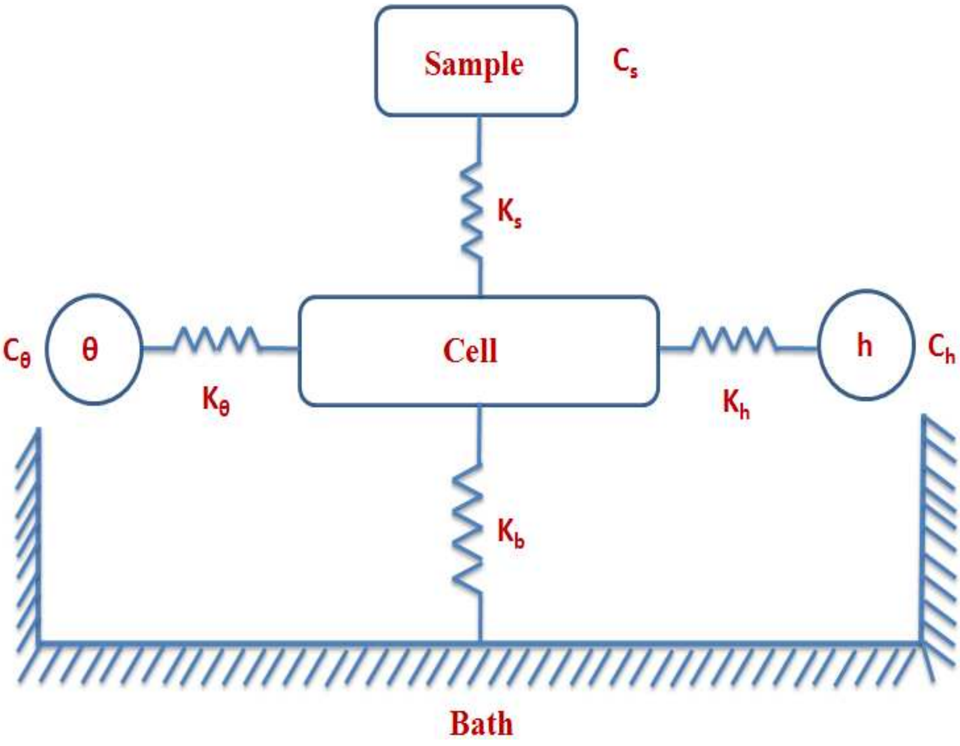

FIGURE 3.3: The physical system showing the respective thermal links to the sample, thermometer, heater, and bath. The cell is assumed to have a negligibly small internal time constant, i.e., low heat capacity and high thermal conductance, and can be treated as a "short". The addendum heat capacity consists of the cell, heater, thermometer, and adhesives.

It consists of a bath and heater, thermometer attached with a sample by a thermal conductance K_i $(i = \theta, s, h, b)$, and having heat capacities C_j $(j = \theta, s, h)$. The sample, of heat capacity C_s is linked by K_s to the cell. The entire assembly: sample, cell, heater, and thermometer, of total heat capacity C, is linked externally to a regulated thermal bath by a conductance, K_b. A heating voltage $Q = Q_0[cos(\omega_v t)]^2$, where $\omega_v = 2\pi f_v$ is the angular voltage frequency, is applied through the heater. This induces thermal oscillations of amplitude T_{ac} at an angular frequency, $\omega = 2\omega_v$.

From the solution of the thermal equations of a one-dimensional model for a planar sample with finite conductivity [2], the temperature as measured by the thermometer is given by

$$T_{ac} = T_b + \frac{Q_0}{2K_b} + \frac{Q_0}{2\omega C}\left[1 + \frac{1}{(\omega\tau_e)^2} + \omega^2(\tau_\theta^2 + \tau_h^2 + \tau_s^2)\right]^{-\frac{1}{2}} cos(\omega t - \alpha). \tag{3.1}$$

T_b is the bath temperature; the second term is identified as T_{dc}, the sample temperature resulting from the rms heating, while the last term is the induced temperature oscillations. The amplitude of the oscillations can be written in the simple form as

$$T_{ac} = \frac{Q_0}{2\omega C}\left[1 + \frac{1}{(\omega\tau_e)^2} + \omega^2\tau_i^2\right]^{-\frac{1}{2}}, \tag{3.2}$$

with the relaxation times defined by

$$\tau_e = \frac{C}{K_b}, \tau_\theta = \frac{C_\theta}{K_\theta}, \tau_h = \frac{C_h}{K_h}, \tau_s = \frac{C_s}{K_s}, \tag{3.3}$$

There are two important thermal relaxation time constants contained in Eq. (5.1), the external $\tau_e = R_eC$ and the internal $\tau_{ii}^2 = \tau_s^2 + \tau_c^2$ and $\tau_{ii} = (\tau_\theta + \tau_h + \tau_s)$. That is the sum of the squared thermal relaxation times for the sample (τ_s) and cell (τ_c). Here, R_s is the sample's thermal resistance and R_e is the external thermal resistance to the bath. There is also a phase shift Φ between the applied heat and resulting temperature oscillations but it is more convenient to define a reduced phase shift $\phi = \Phi + \pi/2$ for heating frequencies between $\frac{1}{\tau_e}$ and $\frac{1}{\tau_{ii}}$, $\Phi \approx -\frac{\pi}{2}$. The reduced phase shift, to the same accuracy as Eq. (5.1), is given by

$$\tan(\phi) = (\omega\tau_e)^{-1} - \omega\tau_i \tag{3.4}$$

where here $\tau_i = \tau_s + \tau_c$. Since τ_c is typically small compared to τ_s such that $\tau_i \cong \tau_{ii}$, Eq. (5.2) can be rewritten to give $\tau_s \equiv R_sC_s \cong \frac{1}{\omega^2\tau_e} - \frac{\tan\phi}{\omega}$. The measured reduced phase shift ϕ also contains a linear ω dependence due to the fixed digitization rate of the thermal oscillation as the heating frequency increases. The observed ϕ is then given by

$$\phi_{exp} = \arctan((\omega\tau_e)^{-1} - \omega\tau_i) + a\omega + \phi_0 \tag{3.5}$$

where a is determined by the digitization rate (in our case, $a \approx 1$) and ϕ_0 is the resulting phase shift due to the digitizing dead-time (delay), which for our apparatus is negligible.

The phase shift is related to both the heat capacity and the thermal conductive properties of the entire system. Using Eqs. 3.3 and Eqs. 3.5 and since the external time constant is typically temperature independent and can be measured separately, one can solve for K_s, the sample thermal conductance. If the thermal conductances and heat capacities of the thermometer and heater are small and nearly constant, i.e., $B = \tau_\theta + \tau_h \equiv$ constant, then K_s may be written as

$$K_s = C_s \left[\left(\frac{1}{\omega^2 \tau_e} - B \right) - \frac{1}{\omega \mathtt{tan} \phi} \right]^{-1}, \tag{3.6}$$

Equation 5.1 is an exact expression for the total heat capacity. However, by operating at a frequency such that the internal and external time constant do not dominate T_{ac}, an approximation can be made which greatly simplifies the relation between T_{ac} and C. This approximation may lead to a small error in the absolute heat capacity without loss of sensitivity to small changes. If the imposed oscillations are at a frequency "slower" than the sample internal equilibration time but "faster" than the external equilibration time (so that a negligible amount of heat is lost to the bath), then

$$\frac{1}{\tau_e} < \omega < \frac{1}{\tau_i}, \tag{3.7}$$

Now by solving equation 5.1

$$C \approx \frac{1}{\omega T_{ac}}, \tag{3.8}$$

The external time constant is controlled by tailoring the thermal link to the bath. It is usually made by thermally anchoring the heater and thermometer electrical leads to a temperature controlled reservoir. This thermal link, on the order of 10 to 100 seconds, is easily adjusted by selecting the appropriate material, length and cross-section for the leads.

Adjustment of the internal time constant is not as straightforward as it strongly depends on the thickness of the sample (the time constants of the thermometer and heater links are again neglected). If the sample thickness is less than the thermal diffusion length given by

$$l = \sqrt{\frac{2K_s A}{\omega C_s}}, \tag{3.9}$$

where K_s, is the sample thermal conductance, C_s, its heat capacity and A is the cross-sectional area of the sample, then, the right hand side of Eq. 3.7 is satisfied. Once satisfied, the location of the applied heat and the measurement of temperature becomes unimportant, i.e., the system is now geometry independent.

Experimentally, it is possible to verify if the requirements of Eq. 3.7 are satisfied by means of a frequency scan. Such a frequency profile is determined by maintaining the same voltage amplitude oscillations at constant temperature while sweeping the frequency and measuring the resulting temperature oscillations. A plot of ωT_{ac} vs ω, for a well designed cell, will typically show a "plateau" shown in frequency scan data of chapter 4. The plateau indicates the region where the heat capacity will be frequency independent and neither time constant plays a major role (see figure of frequency scan in chapter 4). The wider the plateau, the smaller the error associated with the use of Eq. 3.8.

Now going back to Eq. 5.1, the total heat capacity $C = C_s + C_c$ refers here to the combination of the sample and other cell components associated with the sample cell. Here, $C_c = C_H + C_{GE} + C_{AAO} + C_{Ag}$ accounts for the contributions to the cell heat capacity by the heater (H), General Electric #7031 varnish (GE), silver cell container (Ag), and the AAO template (for the parallel measurement). By subtracting the cell contributions, the heat capacity of the sample may be isolated $C_{Sample} = C - C_c$ and by dividing by the mass of the sample yields the desired specific heat. Note that the contribution of the carbon-flake thermistor (θ) is much smaller than all these elements and is typically ignored.

The *effective* thermal conductance, the inverse of the thermal resistance, of the sample can then be evaluated from the AC-calorimetric parameters as

$$K_s \cong \frac{\omega^2 \tau_e C_s}{1 - \omega \tau_e \tan \phi} \tag{3.10}$$

where K_s is in units of W K^{-1}. With the geometric dimensions of sample+cell configuration, the effective thermal conductivity κ_s in units of W m^{-1} K^{-1} can be calculated directly as $\kappa_s = K_s L/A$, where L is the thickness and A is the area of the sample.

3.4.2 Construction of AC Calorimeter

The Fig. 3.4 shows the construction of the AC Calorimeter. The cell which holds the sample is supported by the temperature controlled enclosed bath made by Cu. Sample

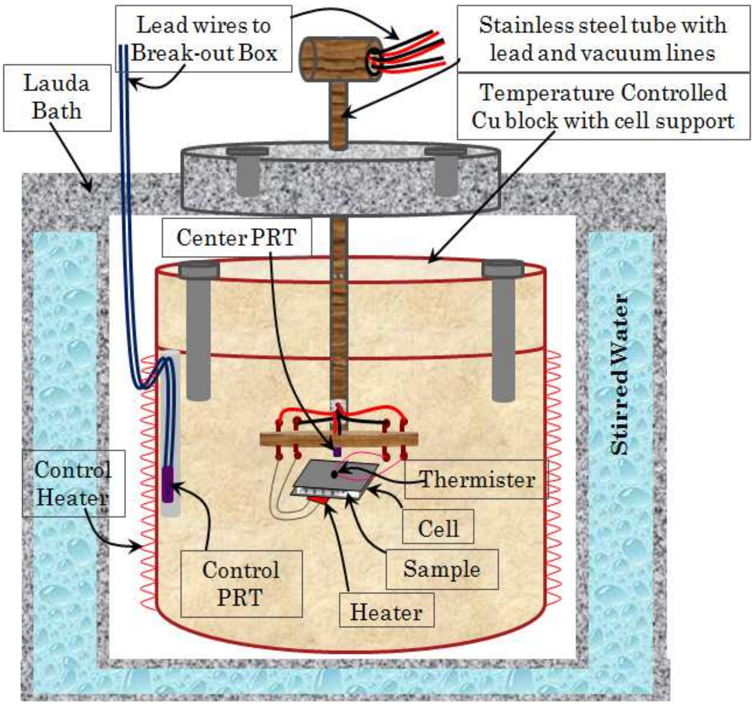

FIGURE 3.4: Design of AC Calorimeter for thermal measurement. Sample is flexibly hanged inside the Cu block which is temperature controlled via PID feedback loop.

and the cell can be hanged with the support called posts shown in Fig. 3.4. There are four posts connected on the plates at the end of the stainless steel pipe. The posts themselves are placed at a plate at the very end of the stainless steel tube. At the other end of the posts are soldered permanently the wires that connect the samples heater and thermistor to the break-out box, and from there to the Keithley DMM. There is also a center PRT (platinum thermometer PT-100, resistive temperature device (RTD), purchased from Lakeshore) thermometer which is very close to the sample to measure the sample temperature. There is also another control PRT inside the Cu block to know the temperature gradient between the samples environment and the bath. All the wires connected with the heater, thermister and thermometer are passed through a stainless steel tube to outside the break-out box. The temperature is controlled by the external heater attached with the cu block given as a control heater.

This sample supported bath is placed inside a modified Lauda bath model KS 20D, which provides a first temperature control stage with a stability of ±0.1 K. The temperature of the copper block is controlled from a Lakeshore temperature controller, model No 340. via Proportional-Integral-Derivative (PID) feedback loop [18]. The stable temperature inside the cavity where the sample is situated is $\approx 100\ \mu$K and in the cylindrical bath ±1 mK.

A Kapton insulated flexible heater from Omega Engineering with exact dimension with the Cu block are purchased and attached with glue on the outside of Cu block cylinder.

3.4.3 Electronic

Figure 3.5 shows the whole electronic diagram of instruments used for thermal characterization by AC Calorimeter. All the instruments are connected with the computer (Windows XP) via GPIB (General Purpose Interface Bus) interfaces of National Instrument software. The C++ program used to run the experiment was written by Alex Roshi and Germano Iannacchione. All the wires from the heater, thermister, and thermometers are connected with proper conductivity with the outside instrument.

The system makes full use of the Keithley DMM, Model 2002, with $8\frac{1}{2}$ digits of resolution, a 128 kB on board memory card, and a multiplex scanner card model 2001-SCAN [19]. The scanner card gives the possibility to completely automate the measurements. The card was configured to do 4-wire or 2-wire measurements. The resistance measurements of the center PRT and the thermistor are configured as 4-wire, while the voltage and resistance measurements, across the strain-gauge heater and the standard resistor, are configured as 2-wire measurements. The latter two measurements are needed in order to accurately determine the ac power applied at the cell.

Care was taken while measuring the PRT thermometer to minimize the self heating that comes as a consequence of current passing through the resistance from the measurement itself. This was seen to be very small and furthermore, would remain almost constant during the measurement. Thus it can safely be neglected as a correction to the temperature of the bath.

The electrical power dissipated in the strain-gauge heater is provided by an Hewlett Packard Function Generator, model HP 33120A [20]. The strain-gauge is connected in series with a high precision standard resistor R_{STD}. The purpose of this resistor is

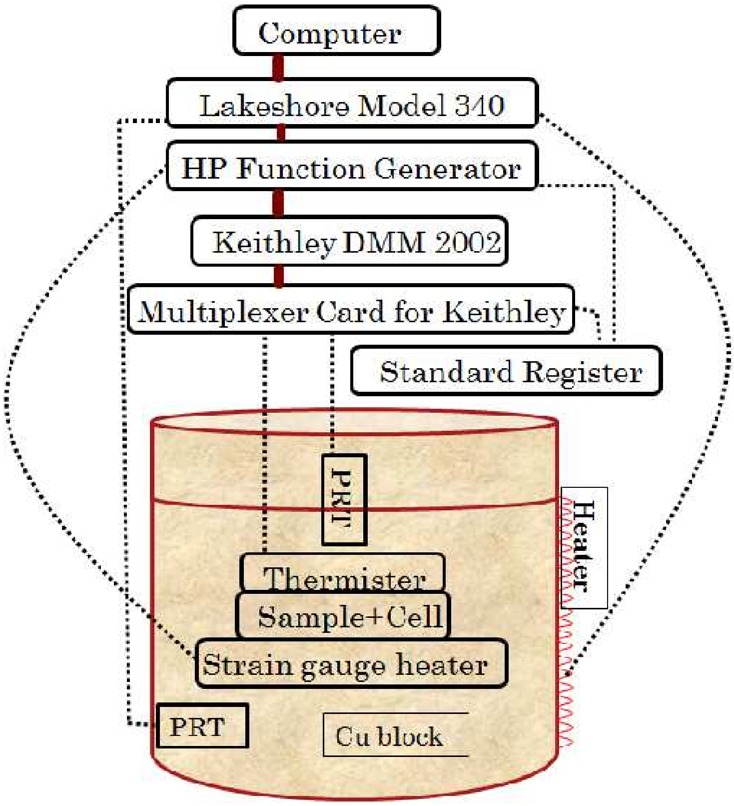

FIGURE 3.5: Electronic connection with the instrument used in Calore A. The instruments are controlled by C programming with the interface of GPIB and National Instrument software.

twofold. First it reduces the voltage across the strain gauge heater, and secondly, it is used to accurately measure the current through the heater, since $I_{HTR} = I_{STD}$ (by virtue of the series connection). As already mentioned, the bath temperature is controlled by the Lakeshore model 340 temperature controller. The cables for the heater and the control PRT pass through a hole at the top of the Lauda bath directly to the Lakeshore terminals.

3.5 Modulated Differential Scanning Calorimeter

The Differential Scanning Calorimeter (DSC) is a thermal analysis instrument that determines the temperature and heat flow associated with material transitions as a function of time and temperature. There are number of applications and DSC can be used to measure the following properties:

1. Glass transition
2. Melting temperature
3. Heat of fusion
4. Percent crystallinity
5. Crystallization kinetics and phase transitions
6. Oxidative stability
7. Curing kinetics

There are two kinds of DSC (i) Heat-Flux DSC and (ii) Power Compensated DSC

3.5.1 Heat-Flux DSC:

In a heat flux DSC, the sample material, enclosed in a pan and an empty reference pan are placed on a thermoelectric disk surrounded by a furnace. The furnace is heated at a linear heating rate and the heat is transferred to the sample and reference pan through thermoelectric disk. However owing to the heat capacity of the sample there exists a temperature difference between the sample and reference pans which is measured by area thermocouples and the consequent heat flow is determined by the thermal equivalent of Ohm's law,

$$q = \frac{\Delta T}{R} \tag{3.11}$$

where q = sample heat flow, ΔT = temperature difference between sample and reference and R = resistance of thermoelectric disk.

3.5.2 Power-Compensated DSC

In power compensated calorimeters, the sample and reference pan are in separate furnaces heated by separate heaters. Both the sample and reference are maintained at the same temperature and the difference in thermal power required to maintain them at the same temperature is measured and plotted as a function of temperature or time. We have the model Q200 DSC with the Tzero technology.

The simple relationship explained above for heat flux DSC considers that the differential heat flow is only due to the heat capacity associated with heating the sample. Hence the heat flow equation consists of only one term. It does not take into account the extraneous heat flow within the sensor or between the sensor and the sample pan. That is the heat flow due to cell imbalances between the sample and reference sides are not considered.

The Tzero cell or Tzero technology are specifically designed to account for those heat flows. The cell sensor consists of a constantan body with separate raised platforms to hold the sample and reference pans. The platforms are connected to the heating blocks or the base by thin walled tubes that create thermal resistances between the platforms and the base shown in Fig. 3.6. Thermocouples on the underside of each platform measure the temperature of the sample and the reference and a third thermocouple measures the temperature at the base. The heat flow expression for this cell arrangement is given by.

$$q = \frac{-\Delta T}{R_r} + \Delta T_0 \frac{R_r - R_s}{R_r R_s} + (C_r - C_s)\frac{dT_s}{dt} - C_r \frac{d\Delta T}{dt}. \tag{3.12}$$

Where T = measured sample temperature (T_s) minus measured reference temperature (T_f)
T_0 = measured base temperature of sensor minus measured sample temperature (T_0-T_s)
T_0 = temperature for control
R_r = reference sensor thermal resistance
R_s = sample sensor thermal resistance
C_r = reference sensor heat capacity
C_s = sample sensor heat capacity.

The first term in this expression is the equivalent of the conventional single-term DSC heat flow expression. The second and third terms account for the difference between the sample and reference resistances and capacitances respectively. The fourth term accounts for the difference in heating rate between the sample and reference. The equation can be further modified to account for pan heat flow effects.

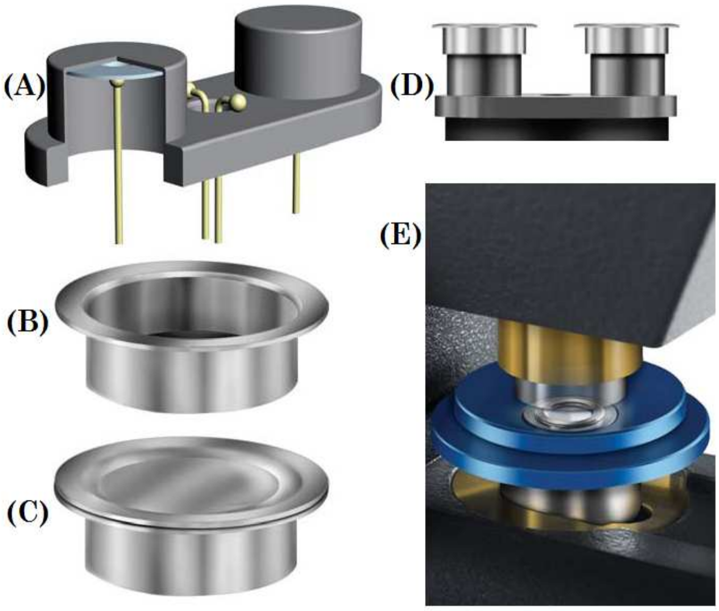

FIGURE 3.6: (A) DSC sample stage connected with the heater, (B) Hermetic pan and (C) Hermetic pan attached with lead, (D) Pans on the sample stage shown on (A), one is the sample pan and other is the reference pan nad (E) DSC Tzero press, which takes sample encapsulation to a new level of performance and convenience in crimp and hermetic sealing of a wide variety of materials [25]. This new universal press has a smooth operating mechanism and automated force adjustment.

3.5.3 Temperature Modulated Differential Scanning Calorimeter

Differential scanning calorimetry (DSC) involves heating and cooling a sample at a constant rate. This technique was established during the 1960s and remained unchanged for almost three decades. During the 1990s, a new technique, temperature modulated differential scanning calorimeter (TMDSC) was developed. The concept behind TMDSC has been around since 1910 [21, 22], although no concrete model existed at the time. Gobrecht et al. [23] first introduced a model for TMDSC and cited several technical limitations. In 1993, the concept was reintroduced by Reading, who had overcome the limitations observed by Gobrecht.

The basic principle behind TMDSC is quite simple. A constant heating rate, similar

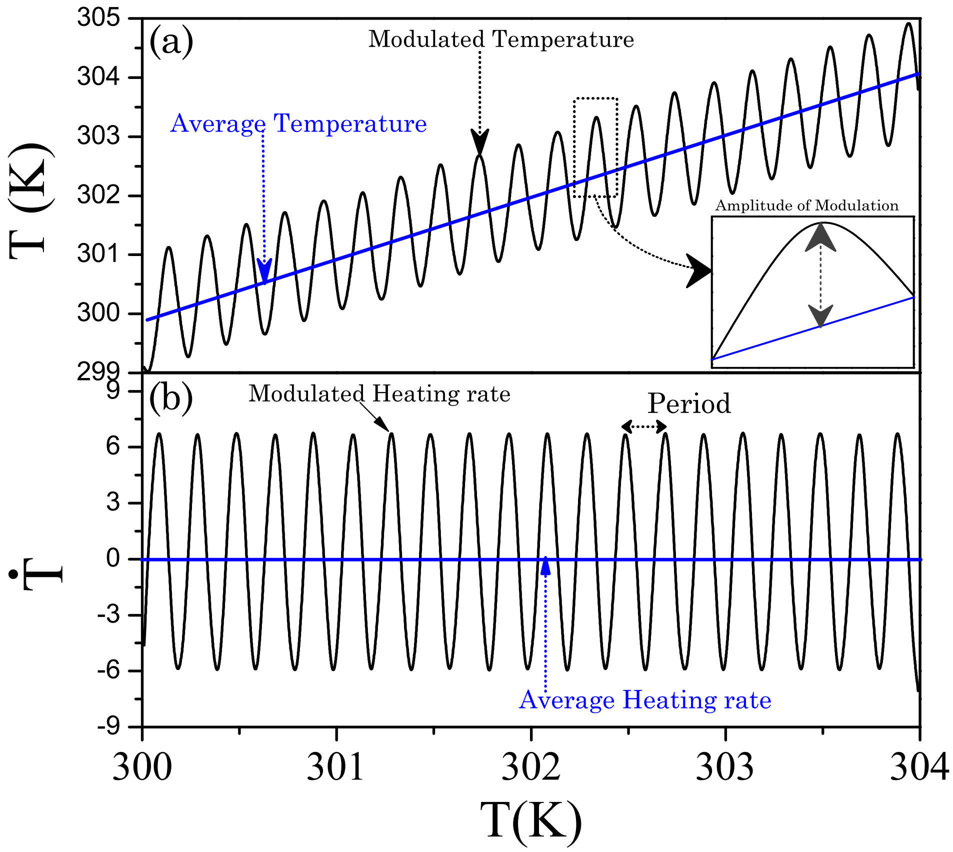

FIGURE 3.7: (a) Temperature evolution of MDSC signal contains (a) raw data of modulated temperature with amplitude showing in inset and (b) derivative of modulated temperature is equivalent to modulated heating rate with temperature scan.

to the one used in conventional DSC, is modulated by superimposing upon it a periodic temperature modulation of a certain amplitude and frequency. This results in a simultaneous introduction of two different time scales in the experiment: a long time scale corresponding to the underlying heating rate, and a shorter time scale (or cycle) corresponding to the period of the modulation [23]. Figure 3.7 illustrates an example of temperature evolution of the MDSC signals as a function of temperature scan. (a) MDSC raw data, modulated temperature and average temperature and (b) is the derivative of temperature modulation known as modulated heating/cooling rate and average signals.

3.5.4 Components of DSC Q200

The Q200 DSC consists of 3 basic units:

Furnace: This is the main assembly where the sample and reference are heated as per the set temperature program.

Cooling system: This unit enables to cool the sample and assist in achieving the desired temperature program.

Computer: This serves as an interface between the user and the instrument and enables automatic control of instrument as per the parameters set.

The furnace or DSC cell dissipates heat to the specimens via a constantan disc. The disc has two raised platforms on which the sample and reference pans are placed. The platforms are connected to the heating block (base) by thin walled tubes that create thermal resistances between the platforms and the base. A chromel disc and connecting wire are attached to the underside of each platform, and the resulting chromel- constantan thermocouples are used to determine the differential temperatures of interest. Alumel wires attached to the chromel discs provide the chromel-alumel junctions for independently measuring the sample and reference temperature. A separate thermocouple embedded in the heating block measures the temperature of the base and serves as a temperature controller for the programmed heating cycle. An inert gas is passed through the cell at a constant low rate of about 50 ml/min.

There are different types of cooling system that can be used in conjunction with DSC. The choice of cooling system depends on the temperature range that you wish to use for your experiments. Details of the types of cooling systems and their usage conditions can be found in the online TA Instrument website or DSC manual.

We have a refrigerated cooling system (RCS) in our lab with DSC Q200, which is used to cool DSC experiments. It consists of a two-stage, cascade, vapor compression refrigeration system and can be used for experiments requiring cooling within an operating range of $-90\ ^{o}$C to 550 ^{o}C. The maximum rate of cooling depends on the temperature range of the bexperiment. The flange temperature used to be $\approx -90\ ^{o}$C.

Using the instrument:

In order to perform DSC experiments you have to follow this general outline. In some cases, not all of these steps are required. The majority of these steps are performed using the instrument control software. The instructions needed to perform these actions can be found in detail in the online help in the instrument control program; therefore they will be discussed briefly here

1. Calibrating the instrument
2. Selecting the pan type and material
3. Preparing the sample
4. Creating or choosing the test procedure and entering sample and instrument information through the TA instrument control software
5. Setting the purge gas flow rate
6. Loading the sample and closing the cell lid (Automated opening and closing in DSC Q200)
7. Starting the experiment

To obtain accurate results, the following procedures can be carefully applied.

Sample Preparation:

Doing this before setting up the instrument is a good idea so you can run the experiment as soon as the instrument is ready; in fact, make up all your samples so they are ready to run before you waste machine time by trying to weigh and run the DSC at the same time.

Selecting pan type:

Samples to be used in differential scanning calorimetry are small pieces that are enclosed in special aluminum pans for experiments up to 600^0C. Pans made of gold, copper, platinum or graphite are used for high temperature runs (up to 725^0C) . Pans are crimped closed using TA's Blue DSC sample Press. Crimped pans improve the thermal contact between the sample, pan and disc, reduce thermal gradients in the sample, minimize spillage, and enable retention of the sample for further study. For most experiments on solid polymeric materials, non-hermetic pans (ones that don't seal airtight) are appropriate. Hermetic pans are normally used only for special applications like studies of volatile liquids including specific heat, studies of materials that sublime, studies of aqueous solutions above 100^0C, examinations of materials generating corrosive or condensable gases, and examinations of materials in self-generating atmospheres and also for liquid crystals. We used hermetically sealed pans for polymer-carbon nanotube composites and liquid crystal sample. Our sample press is normally set up for non-hermetic pans, but a few simple adjustments can be made for others.

Generally the appropriate mass range for samples in DSC is 1 mg to 10 mg. If you have a bulk piece of material, it is necessary to convert this to a form that can be used in the DSC. No matter what, you should never touch a sample, pan or lid with your bare hands, oils from your skin can give their own results in the DSC. Use gloves and goggles while preparing samples. It is important to accurately measure its mass because this is entered into the DSC so that it can give you data that is independent of sample size.

- Start by placing a pan and a lid (they look very similar but the lid is in fact slightly smaller) open-side-up on the microbalance and note down its mass.

- Weigh your sample separately and note its mass

- Then, using tweezers place your sample in the pan and place the lid on top.

- Place them in the sample press as shown in Fig. 3.6.

- Pull the lever down. If the press is set up correctly, it should press the lid down onto the pan and the side walls will wrap around the top

- Place the sample pan in the auto sampler tray and note the position number

- You need a reference pan. For T4P heat flow we have a reference pan in the R2 position in the auto sampler tray. Take it out with tweezers, weigh it and place it back in the tray. You need to do it only once. For subsequent runs you can use the same reading. If you don't find a reference pan you can make one by taking an empty pan and lid, weighing it and then crimping it as explained above.

- You need to enter the sample and reference pan weights in the test procedure. Hence note it in your notebook during sample preparation.

Purge gas:

Sample atmosphere during DSC experiments can be controlled by connecting purge gases to the system.

1. Turn on the nitrogen cylinder. Make sure that the pressure of your purge gas source is regulated between 100 and 140 kPa gauge (15 and 20 psi) before you turn on the cooler, otherwise the sample part will get frigid.
2. Set the flow rate to the recommended value of 50 mL per minute for your experiments on the Notes Page of the Experiment View. Click Apply to save the changes

Calibration:

The Instrument needs to be calibrated in equal environmental conditions and parameters of the experiment needed to run. There are two different calibration methods to do, one is for DSC calibration and the other one is for MDSC calibration for doing MDSC experiments. The Auto calibration wizard method works very well to do the calibration. We just need to follow the procedure as you start calibrating.

For running the heating/cooling of the sample for DSC measurement, the following steps can be edited in the procedure list.

Now say you want to heat the sample and cool it again over the same range. You would simply insert another ramp line after the isothermal, enter your ramp rate again and enter the end temperature. So the editor will look something like this

1. Equilibrate at temperature T_1
2. isothermal for 10 min
3. ramp at $2^0 C$/min to Temperature T_2
4. Equilibrate at temperature T_2
5. isothermal for 10 min
6. ramp at $2^0 C$/min to Temperature T_1

For MDSC run the procedure in editor to look something like this

1. Equilibrate at temperature T_1
2. isothermal for 10 min
3. Modulate at 60 sec/min
4. ramp at $2^0 C$/min to Temperature T_2

5. Equilibrate at temperature T_2
6. isothermal for 10 min
7. Modulate at 60 sec/min
8. ramp at 2^0C/min to Temperature T_1

Scan rates:

The whole concept of DSC is that the sample remains in thermal equilibrium, which is clearly not possible while changing temperature. The only way to achieve this is to have an infinitely slow heating rate. So the slower the heating rate the better the results. However the runs need to completed in practical time also. For standard DSC I have found that 10^0C/min seems to be a reasonable value which is also mostly used for polymeric materials. But we measure glass transition of polymers in a different scan rate dependent, so we went with 10^0C/min to 0.01^0C/min. If you want really good results for a single scan you can go down to 2^0C/min, or less. But then the run takes longer, so usually you want to find the medium that gives you run times that are reasonable but still give you good results. And this is dependent upon materials to materials. Scan rate is something you can play with when you first start running experiments.

3.6 Overview

In this experimental chapter, we focused on the different major experimental techniques used for thermal characterization. These techniques are also described with more detail in some of the other chapters. Different techniques shortly mention the fabrication procedure of Carbon nanotubes and nanowires people generally used. Some of the techniques give a large quantity of samples with different diameters and lengths, like in the laser ablation method. Some of the methods are very slow, expensive and not suitable to produce a large quantity of materials in a small time interval like in the CVD grown method, Electro Chemical Anodization technique etc. But the quality could be better. The experimental procedure in the AC Calorimeter and DSC or MDSC procedure is thoroughly described.

Bibliography

[1] P.F. Sullivan and G. Seide1, *Phys. Rev.* **173**, 679 (1968).

[2] H.S. Caarslaw and J.C. Jaeger, *Conduction of Heat in Solids*, **Oxford Press** (1959).

[3] L. D. Hicks and M. S. Dresselhaus, *Phys. Rev. B* **47**, 12727 (1993).

[4] J. Ling, H. Chi, A. Yin, and J. M. Xu*Journal of Appl. Phys.* **91**, 2544 (2002).

[5] R. S. Wagner and W. C. Ellis, *Appl. Phys. Lett.* **4**, 89-90 (1964).

[6] E. I.Givargizov, *J. Cryst. Growth* **31**, 20-30 (1975).

[7] Y. Wu and P. Yang, *Chem. Mater.* **12**, 605-7 (2000).

[8] Y. J. Zhang, Q. Zhang, N. L. Wang, Y. J Yan, H. H. Zhou, and J. Zhu, *J. Cryst. Growth.* **226**, 185-91 (2001).

[9] J. Westwater, D. P. Gosain, S. Tomiya, S. Usui, and H. Ruda, *J. Vac. Sci. Technol. B* **15**, 554-57 (1997).

[10] M. S. Gudiksen and C. M. Lieber, *J. Am. Chem. Soc.* **122**, 8801-2 (2000).

[11] Y. Wu, H. Yan, M. Huang, B. Messer, J. H. Song, and P. Yang, *Chem. Eur. J.* **8**, 1260-68 (2002).

[12] X. Duan and C. M. Lieber, *Adv. Mater.* **12**, 298-302 (2000).

[13] C. C. Chen, C. C. Yeh, C. H. Chen, Yu MY, and Liu HL, *J. Am. Chem. Soc.* **123**, 2791-98 (2001).

[14] J. Zhang, X. S. Peng, X. F. Wang, Y. W. Wang, and L. D, Zhang, *Chem. Phys. Lett.* **345**, 372-76 (2001).

[15] M. He, P. Zhou, S. N. Mohammad, G. L. Harris, and J. B. Halpern, *J. Cryst. Growth* **231**, 357-65 (2001).

[16] W. S. Shi, Y. F Zheng, N. Wang, C. S. Lee, and S. T. Lee, *J. Vac. Sci. Technol. B* **19**, 1115-18 (2001).

[17] Y. Wu and P. Yang, *J. Am. Chem. Soc.* **123**, 3165-66 (2001).

[18] Lakeshore Cryotronics, *http://www.lakeshore.com*

[19] Keithley Instruments, Inc., *http://www.keithley.com*

[20] Agilent Technologies, Inc., *http://www.agilent.com*

[21] O. M. Corbino, *Physikalische Zeitschrift* **11**, 413-417 (1910).

[22] O. M. Corbino, *Physikalische Zeitschrift* **12**, 292-295 (1911).

[23] H. Gobrecht, K Hamann, and G. Willers, *Journal of Physics E-Scientific Instruments* **4**(1), 21 (1971).

[24] Huanan Duan, *(PhD Thesis: Available in WPI library)*, **URN:etd-052809-122349** (2009).

[25] TA Instrument, New Castle, Delaware USA, *http://www.tainstruments.com*

Chapter 4

THERMAL CONDUCTIVITY OF COBALT NANOWIRES

4.1 Introduction of Co NWs

Rapid progress in the synthesis, characterization, and processing of materials on the nanometer scale has created promising applications for industry and science. Commensurate in the reduction of size is the reduction of dimensionality. One-dimensional (1-D) materials, such as nanowires and nanotubes, attract substantial interest due to the constraints that dimensionality places on physical properties, which is an area of great scientific research. Also, such systems are important for their potential in optoelectronics, sensing, energy conversion, as well as electronic and computing devices [1–7]. While most of the current research effort has been focused on electronic and optical properties, thermal transport properties are starting to attract great interest for basic science and intriguing technical applications [8].

When crystalline solids are confined to the nanometer scale, phonon transport can be significantly altered due to various effects such as increased boundary scattering, change in phonon dispersion, and quantization of phonon transport [5, 6]. Many materials with high thermal conductivity, such as diamond, graphite, natural graphite/epoxy, copper, carbon, as well as SiC and carbon nanotubes, have been investigated and demonstrated promising potential for electronic and optoelectronic devices. Many of these materials can be used in commercial and aerospace applications, including power systems, servers, notebook computers, aircraft, spacecraft and defense electronics [9]. Predicting the thermal conductivity of nanowires plays a crucial role in two important fields: (i) heat dissipation, which is essential for designing future microprocessors, where nanowires may be used as heat drains [6] and (ii) new thermoelectric materials, in which a small thermal conductivity combined with high electronic conductivity typically yields high thermo-power. Because of the unique properties of nanowires, better performance of thermoelectric refrigeration could be realized [8–10, 14]. Knowledge of nanowire thermal and thermoelectric properties is critical for the thermal management of nanowire devices and essential for the design of nanowire thermoelectric devices.

Several theoretical studies on the thermal conductivity (κ) of nanowires [5, 15–21] have shed light on the physics of their basic properties. It is generally understood that nanoscale porosity decreases the permittivity of amorphous dielectrics. But porosity also strongly decreases thermal conductivity [15, 22]. For nanowires with diameters smaller than the bulk phonon mean-free-path (λ_p^B), theory suggests that the thermal conductivity of nanowires will be reduced when compared to the bulk [5, 15, 17, 19–21]. However, there are no predictions regarding the influence of confinement on the behavior of the specific heat (c_p). Knowledge of both c_p and κ is important in determining the thermal relaxation time of materials. It is notable that there have been comparatively few experimental investigations at room temperature and above. The lack of experimental data is due to the difficulty in preparing single nanowire samples with the required specifications. Moreover, measurements made parallel or perpendicular to the long axis of a single nanowire or nanotube are difficult. The use of these materials are more likely in large macroscopic composites where their distribution can be controlled.

Cobalt is a magnetic material and Co nanowires (Co NWs) have distinctive magnetic properties, displaying promising use in applications such as recording media, nanosensors and nanodevices. There are a few experimental investigations of Co NWs magnetic properties [23, 25]. So far to our knowledge there is no experimental work done in measuring thermal conductivity of Co NWs.

This work employs an AC (modulation)-calorimetric technique to measure simultaneously the specific heat (c_p) and thermal conductivity (κ) as a function of temperature on composite samples containing Co NWs from 300 to 400 K. Anisotropic composites of Co NW consist of nanowires grown within the highly ordered, densely packed array of parallel nanochannels in anodized aluminum-oxide. Random composites are formed by drop-casting a thin film of randomly oriented Co NWs, removed from the anodized aluminum-oxide host, within a calorimetric cell. The specific heat measured with the heat flow parallel to the Co NW alignment ($c_p^{||}$) and in the random sample (c_p^R) deviates strongly in temperature dependence from that measured for bulk, amorphous, powder cobalt under identical experimental conditions. The thermal conductivity for random composites (κ_R) follows a bulk-like behavior though it is greatly reduced in magnitude, exhibiting a broad maximum near 365 K indicating the onset of boundary-phonon scattering. The thermal conductivity in the anisotropic sample ($\kappa_{||}$) is equally reduced in magnitude but increases smoothly with increasing temperature and appears to be dominated by phonon-phonon scattering. By utilizing both a thin film of randomly oriented Co NWs between thin silver sheets and a composite material containing highly ordered Co NWs array embedded in an aluminum oxide matrix (also sandwiched between thin silver sheets), measurements were made over randomly oriented Co NWs and parallel to the long-axis of Co NWs. For comparison a thin film of bulk cobalt in the form of an amorphous powder was also studied under identical experimental conditions.

Following this introduction, Sec. 4.2 describes the synthesis of the samples and the experimental technique. The results and discussions for the bulk cobalt and Co NWs samples are presented in Sec. 4.3. Section 5.4 draws conclusions and presents possible future directions.

4.2 Synthesis and Characterization of Cobalt Nanowires

Co NWs were synthesized by electrodeposition assisted by a homemade anodic aluminum oxide (AAO) template. Fig. 4.1 provides a schematic of the synthesis steps. The AAO templates were obtained by a well-established two-step anodization process [24, 27–29]. Briefly, the first anodic oxidation of aluminum (99.999% pure, Electronic Space Products International) was carried out in a 0.3 M oxalic acid solution at 40 V and 10 °C for 16 – 20 hr. The porous alumina layer formed during this first anodization step was completely dissolved by chromic acid at 70 °C. The treated sample was then subjected to a second anodization with the same conditions as the first. The thickness of the anodic film was adjusted by varying the time of the second anodization step. The resulted AAO templates can be further treated by acid etching to widen the nanopores.

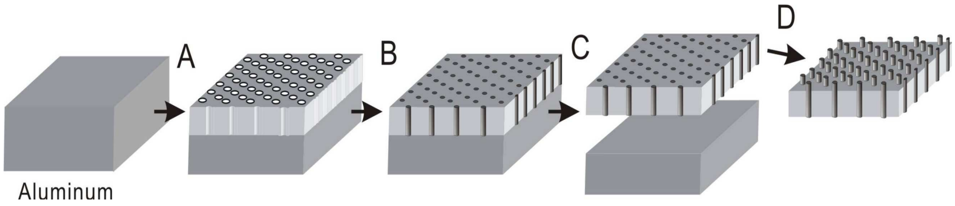

FIGURE 4.1: Synthesis process of Co NWs by electrodeposition. The anodized-aluminum-oxide (AAO) template is obtained by electro-chemical anodization of a pure aluminum sheet (A), the cobalt metal nanowires are electro-deposited inside the pores (B), the separation of Co NWs from Al substrate (C), and finally, the Co NW sample with exposed tips from AAO template (D) after wet etching.

Pore diameters were controlled to within 45 – 80 nm by varying the anodizing voltage and etching time.

Cobalt nanowires were then electrochemically deposited by AC electrolysis in this nanoporous template using 14 V at 100 Hz for 150 mins in an electrolyte solution consisting of 240 g L^{-1} of $CoSO_4{\cdot}7H_2O$, 40 g L^{-1} of HBO_3, and 1 g L^{-1} of ascorbic acid [24, 29]. After Co deposition, AAO can be partially or fully removed by etching with a 2 molar NaOH solution to either expose the tips of the Co NWs or to obtain Co NW powders.

The CO NWs were examined by x-ray diffraction (XRD) using a Rigaku CN2182D5 diffractometer and scanning electron microscopy (SEM) using a JEOL JSM-982 microscope equipped with energy-dispersion x-ray spectroscopy (EDS).

For comparison, bulk cobalt powder from Aldrich Inc. (-100 mesh, $99.9+\%$ pure) with particle size in the range of 2 to 10 μm was chosen. This bulk powder was used after degassing and drying in vacuum at ~ 100 °C.

4.2.1 AC Calorimetry

A modulated (AC) heating technique is used to measure the heat capacity of the Co NWs and bulk powder cobalt samples. In this technique, the sample and cell, loosely coupled to a constant thermal bath, are subjected to a small, oscillatory, heat input. The specific heat and the thermal conductivity can be determined by measuring the frequency dependence of the amplitude and phase of the resulting temperature oscillation. The heat input $P_0 e^{-\omega t}$ with $P_0 \approx 0.5$ mW is supplied to the sample+cell typically results in a modulated temperature having an amplitude $T_{ac} \approx 5$ mK. The experimental details of our application of AC-calorimetry can be found elsewhere [23–25].

The amplitude T_{ac} is inversely proportional to the heat capacity of the sample. The measured T_{ac} is related to the applied power, heating frequency, total heat capacity, and the various thermal relaxation times by

$$T_{ac} = \frac{P_0}{2\omega C} \left(1 + (\omega\tau_e)^{-2} + \omega^2 \tau_{ii}^2 + \frac{2R_s}{3R_e} \right)^{-1/2} \tag{4.1}$$

where P_0 is the power amplitude, ω is the angular frequency of the applied heating power, and $C = C_s + C_c$ is the total heat capacity of the sample+cell. Here, $C_c = C_H + C_{GE} + C_{AAO} + C_{Ag}$ accounts for the contributions to the cell heat capacity by the heater (H), General Electric #7031 varnish (GE), silver cell container (Ag), and the AAO template (for the parallel measurement). By subtracting the cell contributions, the heat capacity of the Co NWs may be isolated $C_{CoNW} = C - C_c$ and by dividing by the mass of Co NWs yields the desired specific heat. Note that the contribution of the carbon-flake thermistor (θ) is much smaller than all these elements and is typically ignored.

There are two important thermal relaxation time constants contained in Eq. (5.1), the external $\tau_e = R_e C$ and the internal $\tau_{ii}^2 = \tau_s^2 + \tau_c^2$ that is the sum of the squared thermal relaxation times for the sample (τ_s) and cell (τ_c). Here, R_s is the sample's thermal resistance and R_e is the external thermal resistance to the bath. There is also a phase shift Φ between the applied heat and resulting temperature oscillations but it is more convenient to define a reduced phase shift $\phi = \Phi + \pi/2$ since for heating frequencies between $1/\tau_e$ and $1/\tau_{ii}$, $\Phi \approx -\pi/2$. The reduced phase shift, to the same accuracy as

Eq. (5.1), is given by

$$\tan(\phi) = (\omega\tau_e)^{-1} - \omega\tau_i \tag{4.2}$$

where here $\tau_i = \tau_s + \tau_c$. Since τ_c is typically small compared to τ_s such that $\tau_i \cong \tau_{ii}$, Eq. (5.2) can be rewritten to give $\tau_s \equiv R_s C_s \cong 1/(\omega^2\tau_e) - (\tan\phi)/\omega$. The measured reduced phase shift ϕ also contains a linear ω dependence due to the fixed digitization rate of the thermal oscillation as the heating frequency increases. The observed ϕ is then given by

$$\phi_{exp} = \arctan((\omega\tau_e)^{-1} - \omega\tau_i) + a\omega + \phi_0 \tag{4.3}$$

where a is determined by the digitization rate (in our case, $a \approx 1$) and ϕ_0 is the resulting phase shift due to the digitizing dead-time (delay), which for our apparatus is negligible. Figure 4.2 shows a typical frequency scan of an AAO only sample at 340 K and illustrates the two relaxation time constants. The solid lines are fits using Eqs. (5.1) and (4.3) and indicate the quality of this thermal model. Several such scans were performed at various temperatures to ensure the applicability of thermal analysis. The temperature dependent data shown below were done at a fixed frequency of $\omega = 0.1885$ s^{-1}, which is above but close to $1/\tau_e$. In Fig. 4.2 at frequencies near twice $1/\tau_i$, a pronounced dip in the temperature amplitude occurs at 3.13 s^{-1} as well at multiples of this frequency. These features are likely due to the formation of standing waves within the cell and occur when the thermal diffusion length are multiple fractions of the physical thickness of the cell.

The *effective* thermal conductance, the inverse of the thermal resistance, of the sample can then be evaluated from the AC-calorimetric parameters as

$$K_s \cong \frac{\omega^2\tau_e C_s}{1 - \omega\tau_e \tan\phi} \tag{4.4}$$

where K_s is in units of W K^{-1}. With the geometric dimensions of sample+cell configuration, the effective thermal conductivity κ_s in units of W m^{-1} K^{-1} can be calculated directly as $\kappa_s = K_s L/A$, where L is the thickness and A is the area of the CoNWs.

4.2.2 Sample Configurations

The cell and Co NWs samples were prepared in two different ways for measurements with the heat flow parallel to the long-axis (anisotropic, denoted with superscript $\|$)

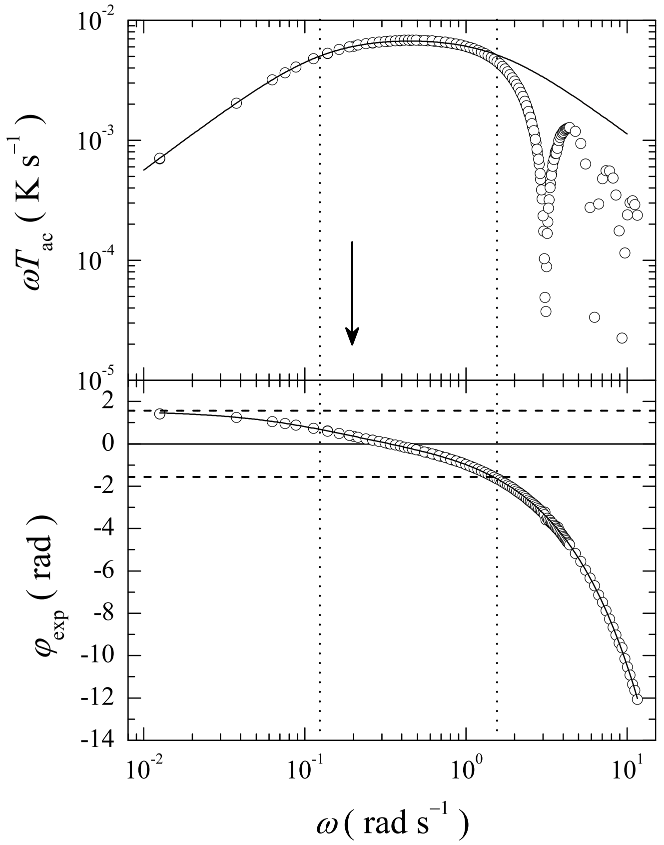

FIGURE 4.2: Typical frequency scan of an AAO sample at 340 K representative of all scans performed for all samples. Top: traditional view of the amplitude frequency dependence using a log-log plot of ωT_{ac} versus ω. Bottom: semi-log plot of the observed ϕ versus ω where the horizontal dashed lines indicate $\pm\pi/2$. The solid lines are fits to these data using Eqs. (5.1) and (4.3), respectively, yielding consistent time constants. The resulting internal and external time constants are denoted in the plots as the vertical dotted lines. Note that the operating frequency for temperature scans is indicated by the arrow. See text for details.

and through a randomly oriented (denoted with superscript R) film of nanowires. The sample+cell configuration for the anisotropic measurement is shown in Fig. 4.3(a) and Fig. 4.4. The general sample+cell configuration consists of a sandwich arrangement of heater, thin silver sheet (0.1 mm thick and 5 mm square), sample, thin silver sheet, and thermistor, all held together by thin applications of GE varnish.

For the anisotropic configuration, the Co NWs embedded in an AAO template were first separated from the Al substrate by wet etching in a 0.1% $HgCl_2$ solution, and the barrier layer was removed by wet etching in 0.5% H_3PO_4 for 30 mins. To ensure a good thermal contact between the Co NWs and the silver sheets, the AAO template was etched by 0.1 M NaOH solution to expose about 2 μm Co NWs on both ends. The typical thickness of Co NWs-AAO sample is about 20 μm. It was carefully sandwiched between the two

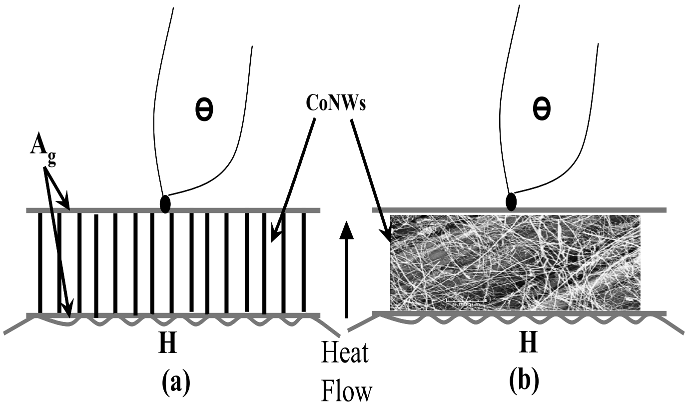

Figure 4.3: Sample + Cell configuration for thermal study. (a) Anisotropic Co NWs configuration. (b) Randomly oriented Co NWs configuration. Labels are H - heater, θ - thermistor, Ag - silver sheet.

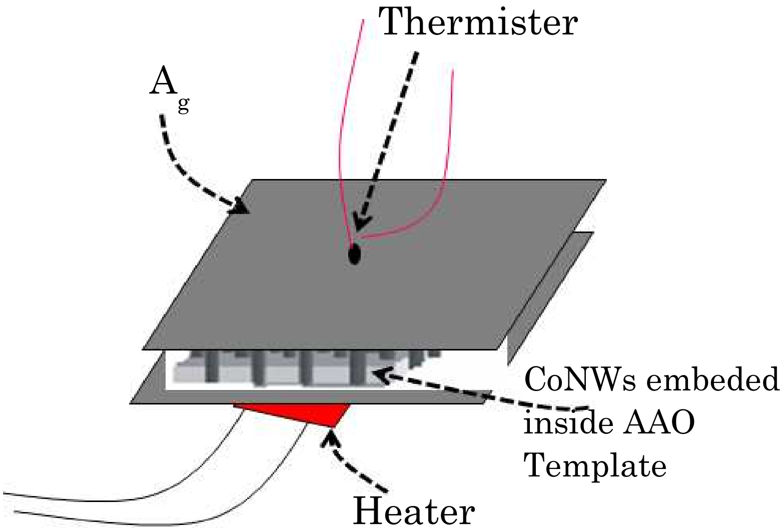

Figure 4.4: 3D cartoon of Sample + Cell configuration for thermal study, where nanowires were embedded inside the AAO template and sandwiched between two silver sheet.

silver sheets and secured by a thin layer of GE varnish. A 120 Ω strain-gauge heater is attached to one side of the stack and a 1 MΩ carbon-flake thermistor to the other side by GE varnish.

Measurements with the heat flow through a randomly oriented film of nanowires were conducted in a similar arrangement, as shown in Fig. 4.3(b). Co NWs were released from the AAO template by completely dissolving the AAO in 0.1 M NaOH. The powder formed of Co NWs were then dispersed in ethanol and drop cast onto one of the cell's silver sheets. This deposition resulted in a film of random oriented Co NWs approximately 0.1 mm thick. The remaining components of the cell were attached again by a thin application of GE varnish. In this randomly oriented sample Co NWs, the heat flow was averaged over all orientations of the nanowires.

For comparison, bulk powder measurements were done under nearly identical experimental conditions. The many point contacts between particles of pure powder Co mimic the random arrangement of the thin film configuration of Co NWs. All sample+cell arrangements had essentially identical areas, contact resistances between sample and cell, and similar thicknesses. In the random oriented and bulk powder sample+cells, the silver sheets might not be perfectly parallel to each other in the sandwich arrangement, but did not touch each other.

Estimation of specific heat and effective thermal conductivity of the cobalt bulk and nanowire samples is straight-forward. Each component of the above described sample+cell arrangement was measured separately to determine the contribution of the thin silver sheets, heater, thermistor, GE varnish, and an empty AAO template (identically prepared but without the embedded Co NWs) as measured by the calorimeter under identical experimental conditions. The specific heat (c_p) of the cobalt is then calculated by subtracting these contributions from the total heat capacity and dividing by the cobalt mass. For the anisotropic sample, the mass of the Co NWs embedded in the AAO template was estimated by weight of released Co NWs per unit area. When calculating the effective thermal conductance, we assumed that the entire sample was covered by the cobalt for the bulk powder and random Co NW samples, and Co NWs are parallel to each other for anisotropic samples in AAO nanochannels.

For these measurements, contact resistance plays an important role. All samples and the components of the sample+cell, were measured under identical configurations (thickness, area, mass, and external thermal link). All have the sample, Co powder or NWs, attached to the silver cell with GE varnish as the thermal contact. Thus, the contact resistance contribution should be essentially the same for all measurements. This crucial similarity as well as the choice of bulk Co powder for comparison, allows the behavior of Co NW in the macroscopic samples to be isolated.

4.3 Results and Discussion

4.3.1 Morphology and microstructure study of Co NWs

Fig. 4.5 shows SEM images of Co NWs embedded in the AAO templates. In Fig. 4.5(a), an oblique view of the sample before etching by NaOH solution shows the highly ordered hexagonal pattern of the nanopores. The pore diameter and interpore separation are about 80 and 40 nm, respectively. Fig. 4.5(b) is an SEM image of the Co NWs with the tips exposed by about 2 μm and Fig. 4.5(c) is a high-magnification image of the cobalt nanowires.

With careful control of the etching process, etching in NaOH solution for 10 minutes is sufficient to expose all of the NWs tips. The majority of the Co NWs stood straight upward without severe agglomeration. If etching for prolonged time, the exposed Co NWs tended to bend and bundle together, forming islands.

A microstructure study of the as-prepared Co NWs was performed by x-ray diffraction (XRD) and shown in Fig. 4.6. The results demonstrate that the Co NWs consists of a mixture of *fcc* and *hcp* structures. This is consistent with a nuclear magnetic resonance (NMR) study by Strijkers. et al. [26] on Co NWS synthesized by direct current method. The XRD peaks near 41.685° and 47.57° correspond to the $(10\bar{1}0)$ and $(10\bar{1}1)$ planes of the *hcp* structure. The peak near 51.522° is attributed to the (200) plane of the *fcc* structure. The peak near 44° could be a combination of the diffraction from the (0002) plane of the *hcp* structure and the (111) plane of the *fcc* structure; that near 75° could be a combination of the diffraction from the (1120) plane of the *hcp* structure and the (220) plane of the *fcc* structure. It is also shown that the fabricated Co nanowires have a preferential orientation of direction (0002). The preferred orientation of the nanowires

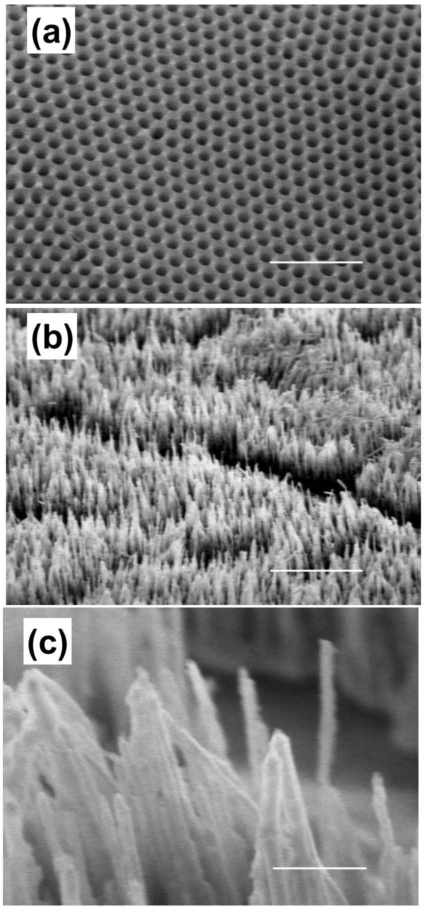

FIGURE 4.5: SEM images of (a) the as-prepared Co NWs sample before etching, (b) "forest" of Co NWs after partially etching of the AAO membrane, and (c) Co NWs with higher magnification. The scale bar is 500 nm (a), 5 μm (b), and 500 nm (c).

is attributed to the growth of the nanowires within the pores of the alumina film. No diffraction peaks from cobalt oxide or from the alumina are seen in Fig. 4.6.

4.3.2 Specific heat of Co NWs

The Specific heats of bulk powder cobalt as well as anisotropic Co NWs and randomly oriented CoNWs mat configuration are shown in Fig. 4.7. The specific heats of all samples were determined as a function of temperature from 300 to 400 K. The cobalt bulk powder sample measurement yields a $c_p^B = 0.49$ J g^{-1} K^{-1} at 300 K increasing smoothly to 0.61 J g^{-1} K^{-1} at 400 K. This result is about 13 % higher in magnitude at 325 K but similar in temperature dependence with the literature [30, 31] and indicates the absolute uncertainty in magnitude. However, as is typical for an ac-calorimetric technique, the relative uncertainty (i.e. temperature dependence) is much higher (better than 0.5 %).

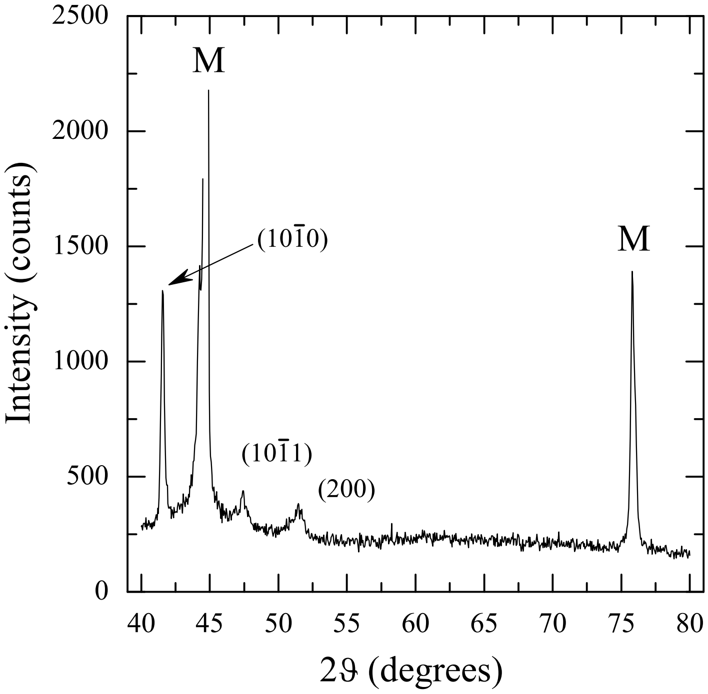

FIGURE 4.6: XRD pattern of Co NWs showing different planes.

The magnitude of the specific heat for the two CoNW samples are $c_p^{||} = 0.53$ J g^{-1} K^{-1} and $c_p^R = 0.50$ J g^{-1} K^{-1} at 300 K. For the anisotropic Co NW configuration, $c_p^{||}$ increases linearly from room temperature to ~ 320 K in a fashion similar to bulk sample. Above 320 K, $c_p^{||}$ increases much more rapidly with temperature than the bulk. In the case of randomly oriented mat sample, c_p^R increases more rapidly than that of either the anisotropic or the bulk sample from 318 to 387 K, above which it begins to decrease.

In principle, since the specific heat is a scalar quantity related to the thermal fluctuations of internal energy, one would expect that c_p should be independent of heat-flow geometry for a given structure of the cobalt. The differences observed here are likely due to the composite nature of the sample+cell configuration. The similarity, at least just above room temperature, between $c_p^{||}$ and c_p^B is understandable as in this heat-flow configuration, the length of the Co NWs is comparable to the size of the bulk powder sample. The deviation beginning at ~ 320 K may be a consequence of the 1-D nature of the nanowires since one might expect "bunching" of the phonons (phonon-phonon scattering) to dominate at some elevated temperature. For the random Co NW film sample, there is likely a very large number of contacts, on the nanometer scale, between individual Co NWs. Thus, the c_p^R measured is almost certainly an effective value for

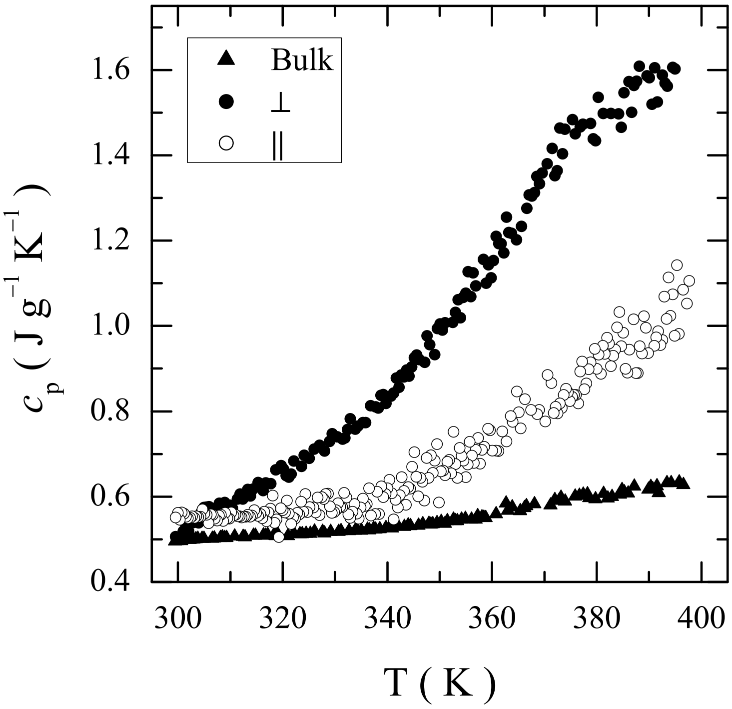

FIGURE 4.7: Specific heat of bulk powder cobalt (solid triangles) and randomly oriented Co NWs samples (dots) and anisotropic Co NWs samples (open circles) from 300 to 400 K.

the sample+cell composite. However, the observed strong temperature dependence and maximum at ∼ 370 K for c_p^R is an intriguing indication of engineering materials with specific thermal properties.

4.3.3 Thermal Conductivity of Co NWs

Fig. 4.8(a) shows the effective thermal conductivity of bulk powder cobalt at 300 K to be $\kappa_B \approx 67$ W m^{-1} K^{-1} with a strong temperature dependence reaching a maximum at ∼ 360 K. The literature value for pure cobalt at 300 K is 90 W m^{-1} K^{-1} and displays only a weak temperature dependence [32]. The extracted thermal conductivity κ_B is lower by 20 % which is most likely due to incomplete filling of the cell. The maximum observed is also likely due to the powder nature of micron sized amorphous particles sandwiched

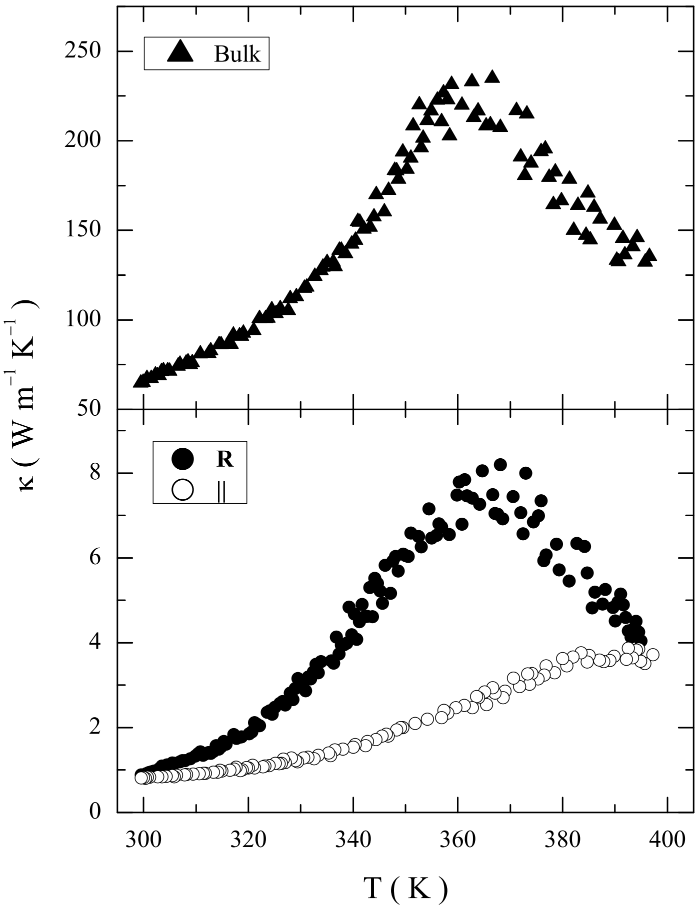

FIGURE 4.8: Top panel - Effective thermal conductivity of bulk Co as a function of temperature from 300 to 400 K. Bottom panel - Effective thermal conductivity of anisotropic Co NWs (open circles) and randomly oriented powder CoNWs (dots) as a function of temperature from 300 to 400 K.

in the cell where boundary-phonon scattering begins to dominate at $\sim$ 360 K. Again, as with the specific heat, the uncertainty in these measurements are typical for the absolute value but retains the high relative precision. The choice of samples and the carefully matched sample+cell configuration allow for direct comparison between these bulk measurements with those for the Co NW samples.

The derived thermal conductivity of the Co NWs for the two heat-flow configurations are shown in Fig. 4.8(b). Both $\kappa_{\|}$ and κ_R have values 83 times less than the bulk at 300 K. However, for increasing temperatures, $\kappa_{\|}(T)$ behaves quite differently from the observed bulk trend, increasing in a smooth manner up to $\sim$ 380 K at which a small "kink" is seen to a nearly constant value of $\kappa_{\|} \approx 4$ W m^{-1} K^{-1}. Although the uncertainty in absolute values is higher for the measured κ compared to c_p, the marked reduction of magnitude of κ in both configurations with respect to the bulk is consistent with the 1-D nature of the materials, in which phonon boundary scattering dominates the phonon - phonon scattering. Very similar results are reported in bismuth telluride nanowires by Zhou et al. [33]. However, for $\kappa_{\|}$, the kink to a constant value at $\sim$ 380 K may be an indication of a cross-over from phonon-phonon to defect-phonon scattering within the NWs. For the random Co NW sample, κ_R exhibits a similar temperature dependence as the bulk, although of greatly reduced magnitude. As with κ_B, the observed maximum for κ_R seen at $\sim$ 360 K is again likely due to the composite nature of the sample+cell arrangement and the onset of boundary-phonon scattering. The junctions between the nanowires dominant the heat transfer for κ_R just as the contacts between bulk powder particles were for κ_B. The slight difference in temperature for the observed maximum is consistent with the bulk powder particles being of much larger size (microns) compared to the diameter of the nanowires.

To better compare the temperature dependence of the effective thermal conductivity, normalized values (to that observed at 300 K, i.e. κ/κ_{300K}) are shown in Fig. 4.9 for the bulk powder and the Co NWs in the two heat-flow configurations. The fractional change of κ is much larger in the randomly oriented Co NWs samples and, as mentioned previously, is likely due to the enormous number of wire-wire junctions. The fractional change of the anisotropic configuration matches closely up to 360 K with the bulk cobalt powder. Above 360 K the bulk begins to decrease. Although study on Co NW with different diameters is still on-going in our lab, it has been recently found that the thermal conductivity of silicon nanowires increases with increasing diameter [34], consistent with a cross-over to bulk-like behavior seen in our investigation between the random film of Co NW and bulk-powder Co.

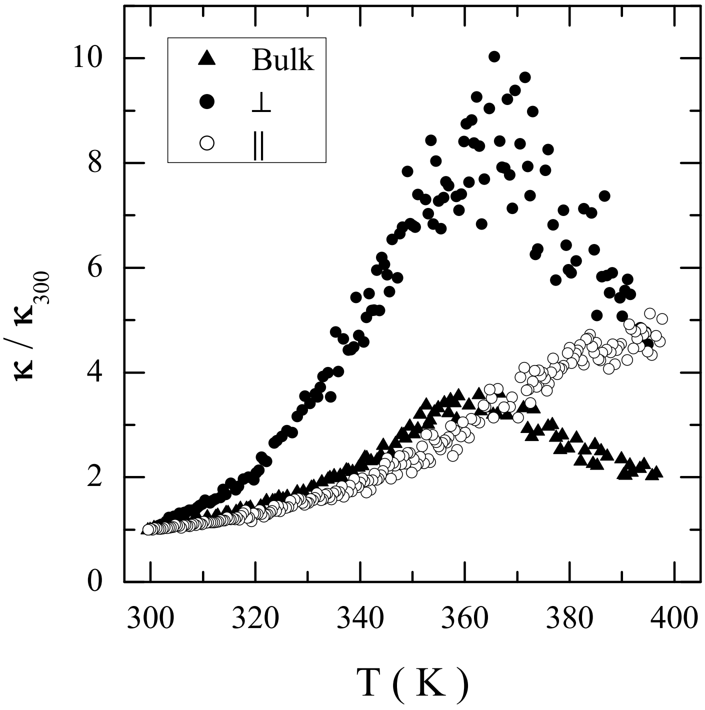

FIGURE 4.9: Normalized effective thermal conductivity of bulk cobalt (solid triangles), anisotropic (open circles), and randomly oriented Co NWs sample (dots) as a function of temperature from 300 to 400 K.

4.3.4 Phonon Mean-Free-Path

Although the results obtained here are for macroscopic composite samples, some insight can be obtained by considering the contribution of phonons with respect to the heat-flow configurations. The lattice specific heat provides important information of the modified phonon spectrum in low-dimensional system such as nanotubes and nanowires [35, 36]. The temperature dependent phonon mean-free-path (λ_p), obtained from thermal conductivity measurements, is the result of scattering of phonons from domain boundaries, by defects, and/or phonon-phonon scattering [37]. Therefore, it is interesting to estimate λ_p in nanowires and compare the relative magnitudes among the samples studied.

The phonon mean-free-path may be calculated from the experimentally measured thermal conductivity and specific heat using

$$\lambda_p = \frac{3\kappa}{v_p c_p \rho}, \tag{4.5}$$

where ρ is the mass density of the cobalt sample and v_p is the velocity of phonons in cobalt (here taken as that for pure cobalt 4700 m s^{-1} and a constant). The values estimated for anisotropic Co NW is $\lambda_p^{\|} \approx 485$ nm and in the random configuration is $\lambda_p^R \approx 203$ nm at 300 K. For the bulk powder cobalt sample, $\lambda_p^B \approx 40$ μm at 300 K. Since the cobalt nanowires are 20 μm long, 80 nm in diameter, and that bulk particles are 2 - 10 μm in size, one would expect that boundary scattering would dominate for the randomly oriented Co NWs samples ($\lambda_p^R > 80$ nm) and bulk powder ($\lambda_p^B > 10$ μm) beginning at the lowest temperatures. Conversely, one would not expect boundary-phonon scattering to play a significant role for the anisotropic configuration since $\lambda_p^{\|} \ll 20$ μm, instead one can consider phonon-phonon or defect-phonon scattering mechanisms. The maximums observed in κ for the bulk and randomly oriented Co NW configuration could be the result of the onset of additional scattering mechanisms.

It is interesting to note that the maximums in κ and c_p seen for the randomly oriented mat sample of Co NWs do not occur at the same temperatures, being ~ 365 K and ~ 382 K, respectively. Also, the maximum in κ observed in the bulk are not reflected by a similar feature in c_p just as the plateau in κ seen for the anisotropic Co NW configuration has no companion feature in its c_p. These observations indicate that the fluctuations in internal energy reflected in c_p are independent to the scattering mechanisms responsible for the κ results in these macroscopic composite sample+cell arrangements.

The assumption of using the pure cobalt phonon velocity as a constant in temperature and the same for all samples is a weak one. From the definition of the thermal diffusivity, $\alpha = \kappa/c_p\rho$, one can estimate the temperature dependence of the product of the phonon mean-free-path and the phonon velocity as

$$\alpha\rho = \lambda_p v_p \rho/3 = \frac{\kappa}{c_p} \tag{4.6}$$

where α is the thermal diffusivity. Here, we assume that the mass density ρ is taken as constant and so, from Eq. (4.6) gives $\lambda_p v_p \propto \kappa/c_p$. Fig. 4.10 shows the result for the

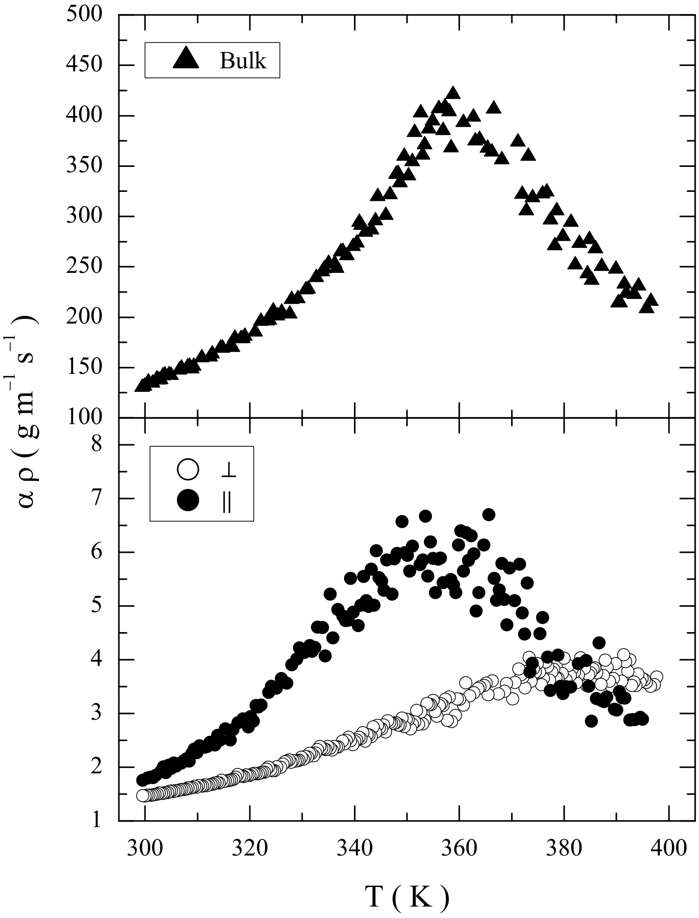

FIGURE 4.10: Plot of the product of mass density (ρ) and thermal diffusivity (α) over the temperature range 300 to 400 K. Top panel - Bulk cobalt. Bottom panel - anisotropic (open circles) and randomly oriented Co NWs sample (dots). Note that $\alpha\rho \propto \lambda_p \nu_p$, see text for details.

bulk powder and the Co NW configurations studied as a function of temperature. A broad maximum centered at $\sim$ 350 K is seen for the Co NW(random mat) sample and a much sharper "peak" is seen at a slightly higher temperature of 360 K for the bulk cobalt. For Co NW($\|$), only a plateau is revealed beginning at 380 K. These results suggest that the phonon mean-free-path and velocity are not trivially related and have complex temperature dependence for these macroscopic composite samples.

4.4 Summary

We report the experimental results of the specific heat and effective thermal conductivity of two types of arrangement of Co NWs, i.e. randomly oriented and anisotropic, and compare them with bulk cobalt powders. The particle nature of the bulk-powder and randomly orientated Co NWs leads to strong deviations of both κ and c_p from that of pure solid cobalt. The κ and C_p exhibit a much stronger temperature dependence and show peak-like maximums versus temperature. The results suggest the dominance of phonon-boundary scattering in the temperature range 300 to 400 K, whereas the thermal properties of the more uniform and confined anisotropic Co NWs samples demonstrate smooth temperature dependence, which suggests the dominance of phonon-phonon or phonon-defect scattering. These results suggest that the composite materials containing nanowires can be engineered for a wide range of applications.

Bibliography

[1] P. G. Collins, H. Bando and A. Zettl, *Nanotechnology*, **9** 153 (1998).

[2] Y. Cui and M. Lieber, *Science*, **291** 851 (2001).

[3] M. S. Dresselhaus, Y-M. Lin, S. B. Cronin, O. Rabin, M. R. Black, G. Dresselhaus and T. Koga, *Semicond. Semimet*, **71** 1 (2001).

[4] Y. Wu, R. Fan and P. Yang, *Int. J. Nanosci*, **1** 1 (2002).

[5] Ronggui Yang and Gang Chen and M. S. Dresselhaus *Phys. Rev. B*, **72**, 125418 (2005).

[6] N. Mingo and L. Yang and D. Li and A. Majumdar *Nanoletters*, **132,** 12, 1713 (2003).

[7] A. D. McConnel and K. E. Goodson *Ann. Rev. Heat Transfer*, **14,** 129 (2005).

[8] D. G. Cahill, W. K. Ford, K. E. Goodson, G. D. Mahan, A. Majumdar, H. J. Maris, R. Merlin and S. R. Phillpot, *J. Appl. Phys.*, **93,** 2, 793 (2002).

[9] J. Zou and A. Balandin, *Proc. Electrochem. Soc.*, **2001,** 19, 70 (2001).

[10] G. Mahan, B. Sales, J. Sharp, *Physics Today*, **50,** 42 (1997).

[11] S. Brands, B. Leven, and G. Dumpich, *J. Appl. Phys.*, **97**, 114311 (2006).

[12] U. Ebels, A. Radulescu, Y. Henry, L. Piraux, and K. Ounadjela, *Phys. Rev. Lett.*, **84**, 983 (2000).

[13] S. Mani, T. Saif, and J. H. Han, *IEEE Trans. Nanotechnol.*, **5**, 138 (2006).

[14] L. D. Hicks, M. S. Dresselhaus, *Phys. Rev. B*, **47,** 12727 (1993).

[15] D. Li, Y. Wu, P. Kim, L. Shi, P. Yang and A. Majumdar, *Appl. Phys. Lett.*, **14,** 2934 (2003).

[16] S. Barman and G. P. Srivastava, *Phys. Rev. B*, **73,** 205308, (2006).

[17] Y. Chena, D. Lib, J. Yangc, Y. Wuc, J. R. Lukesd, A. Majumdare, *Physica B*, **349,** 270 (2004).

[18] Y. Chen, D. Li, J. R. Lukes and A. Majumdar, *J. Heat Trans.*,**127,** 1129 (2005).

[19] S. Volz and G. Chen, *Appl. Phys. Lett.*, **75,** 2056 (1999).

[20] R Prasher, *Phys. Rev. B*, **74,** 165413 (2006).

[21] K-Q Chen, W-X Li, W. Duan, Z. Shuai, B-L Gu, *Phys. Rev. B*, **72,** 045422 (2005).

[22] T. M. Trit, *Science*, **283,** 804 (1999).

[23] J. Xu, X. Huang, G. Xie, Y. Fang and D. Liu, *Material Letters*, **59,** 981-4 (2005).

[24] J. Liang, H. Chik, A. Yin and J. M. Xu, *J. Appl. Physics*, **91,** 2544 (2002).

[25] L. Vila, J. M. George, G. Faini, A. Popa, U. Ibels, K. Ounadjea and L. Paux, *IEEE Trans. on Mag.*, **38,** 5, 185 (2002).

[26] G. J. Strijkers, J. H.J. Dalderop, M. A.A. Broeksteeg, H. J.M. Swagten and W. J.M. de Jonge, *J. Appl. Phys.*, **86,** 9, 5141-5145 (1999).

[27] Z. F. Zhou, Y. C. Zhou, Y. Pan and X. G. Wang, *Mat. Lett.*, **62,** 3419-3421 (2008).

[28] J. Liang, H. Chik and J. M. Xu, *IEEE J. Select. Top. Quant. Electron.*, **8,** 998 (2002).

[29] J. Li, C. Papadopoulos, J. M. Xu and M. Moskovits, *Appl. Phys. Lett.*, **75,** 367 (1999).

[30] R. RamjiRao and A. Ramanand, *Phys. Rev. B*, **19,** 4, 1972 (1979).

[31] W. Bendick and W. J. Pepperhoff, *J. Phys. F: Metal Phys.*, **11,** 11, 2185 (1979).

[32] Terry M Tritt, ,Thermal conductivity: Theory Properties and Application, *Kluwer Academyc/Plenum Publishers*, **4** (2004).

[33] J. Zhou, C. Jin, J. Seol, X. Li and L. Shi, *Appl. Phys. Lett.*, **87,** 133109 (2005).

[34] A. Hochbaum, R. Chen, R. D. Delgado, W. Liang, E. C. Garnett, M. Najarian, A. Majumdar and P. Yang, *Nature*,**451,** 163 (2008).

[35] C. Dames, B. Powdel, W. Z. Wang, J. Y. Huang, Z. F. Ren, Y. Sun, J. I. Oh and G. Chen, *Appl. Phys. Lett.*,**87,** 031901 (2005).

[36] J. Hone, B. Batlogg, Z. Benes, A. T. Johnson and J. E. Fischer, *Science*,**289,** 1730 (2000).

[37] J. Hone, M. Whitney, C. Piskoti and A. Zettl, *Phys. Rev. B*,**59,** 4, R2514 (1999).

Chapter 5

THERMAL CONDUCTIVITY OF SINGLE-WALL AND MULTI-WALL CARBON NANOTUBES COMPOSITES

5.1 Introduction of Carbon Nanotubes

Since their discovery in 1991 by Sumio Ijima [1], carbon nanotubes (CNTs) have been the focus of intense research and have many potential applications in electronic, optical, thermal management and energy conversion devices because of their unique properties. The electrical and mechanical properties of CNTs have been extensively investigated [2, 3], while the thermal properties of CNTs are of interest in basic science as nanotubes are model systems for low-dimensional materials. However, for large scale technical applications, the manipulation of single nanotubes becomes impractical. Several groups have measured the thermal properties of millimeter sized thin CNT films and packed carbon fibers [4–10]. Current efforts to exploit the attractive properties of carbon nanotubes have focused on macroscopic composites containing engineered or self-assembled arrays of CNTs. One route has been to order the CNTs through the interaction of an anisotropic liquid crystalline host [11] while another route has been to grow the CNT within the ordered porous structures of a host matrix [12].

Numerous studies, mostly theoretical, have been recently conducted to understand the thermal properties of CNTs and assess their potential for applications [13–18]. These theoretical investigations have indicated that single-wall CNTs (SWCNT) have the highest thermal conductivity along the long axis of the nanotube, predicted to be as high as 6600 W m^{-1} K^{-1} at room temperature [19]; three times that of diamond. The experimentally measured thermal conductivity of an individual multi-wall CNT (MWCNT) is reasonably consistent and was found to be 3000 W m^{-1} K^{-1} [20]. However, the thermal conductivity of a random film sample of SWCNT was reported to be only 35 W m^{-1} K^{-1} [7]. For SWCNT bundles, the reported value of thermal conductivity was 150 W m^{-1} K^{-1} by Shi et al. [21]. The thermal conductivity of aligned MWCNTs samples was reported to range between 12 to 17 W m^{-1} K^{-1} [10] and even as low as 3 W m^{-1} K^{-1} [22]. Other results found it somewhat higher near 27 W m^{-1} K^{-1} [4, 23, 24]. An attempt to understand this wide variation of the measured thermal conductivity (and to a lesser extent the specific heat) of MWCNTs evoked the existence of thermal boundary resistance as a possible mechanism for the dramatically lower thermal conductivity of MWCNT bundles and films compared to that of a single MWCNT [25]. However, the situation remains unresolved.

In this chapter, we report measurements of the specific heat and effective thermal conductivity by an AC-calorimetric technique on composites containing random and aligned dense packing of carbon nanotubes. For the random film of CNTs, the heat flow is predominately perpendicular to the long nanotube axis while in the composites of aligned CNTs in dense packed nano-channels of anodic aluminum oxide (AAO) the heat flow is primarily along the long axis. The bulk powder graphite was also studied as a reference having a similar packing of nano-particles within an identical sample+cell arrangement. The temperature scans ranged from 300 to 400 K for aligned MWCNTs in AAO, and randomly oriented films of MWCNTs, SWCNTs, and graphite powder. In general, the temperature dependence of the specific heat of randomly oriented films of MWCNTs and SWCNTs is similar with that of bulk graphite powder. In contrast, the specific heat of aligned MWCNTs in AAO has a weaker temperature dependence than bulk behavior above room temperature. The effective thermal conductivity of randomly oriented MWCNTs and SWCNTs is similar to that of powder graphite, exhibiting a maximum value near 364 K indicating the onset of boundary-phonon scattering. The effective thermal conductivity of the anisotropic MWCNTs increases smoothly with increasing temperature and is indicative of the one-dimensional nature of the heat flow.

Following this introduction, the experimental details including material synthesis, composite sample fabrication, and calorimetric details are shown in Sec. 7.2. The resulting data are presented and discussed in Sec. 5.3. Conclusions are drawn and future work outlined in Sec. 5.4.

5.2 Experimental

5.2.1 Synthesis of Carbon Nanotubes and Samples

Multi-wall carbon nanotubes were synthesized by a chemical vapor deposition (CVD) technique in an AAO template as shown in Fig. 5.1. The AAO template was obtained by a two-step anodization process; details of which have been previously published [12, 26, 27]. Briefly, the first-step anodization of aluminum (99.999 % pure, Electronic Space Products International) was carried out in a 0.3 Molar oxalic acid solution under 40 V at 10 ^{0}C for 16 – 20 hr. The porous alumina layer formed during this first anodization step was completely dissolved by chromic acid at 70 ^{0}C. The sample was then subjected to a second anodization step under the same conditions as the first. The thickness of the porous anodic film was adjusted by varying the time of the second anodization step. The resulted AAO templates can be further treated by acid etching to widen the nanopores. For the samples used in this work, the pore diameter was controlled to within $45-80$ nm by varying the anodizing voltage and etching time.

Cobalt particles, used as catalysts for the carbon nanotube growth, were electrochemically deposited at the bottom of the pores using AC electrolysis (14 V at 100 Hz) for 30 sec in an electrolyte consisting of $CoSO_47H_2O$ (240 g/L), HBO_3 (40 g/L), and ascorbic acid (1 g/L). The ordered array of nanotubes were grown by first reducing the catalyst by heating the cobalt-loaded templates in a tube furnace at 550 ^{0}C for 4 hr under a CO flow (60 cm^3 min^{-1}). The CO flow was then replaced by a mixture of 10 % acetylene in nitrogen at the same flow rate. In a typical synthesis, the acetylene flow was maintained for 1 hr at 600 ^{0}C. The as-prepared MWCNTs embedded in the AAO template were used as the aligned MWCNT sample. The MWCNTs can be released from the template by removing the aluminum oxide in a 0.1 Molar NaOH solution at

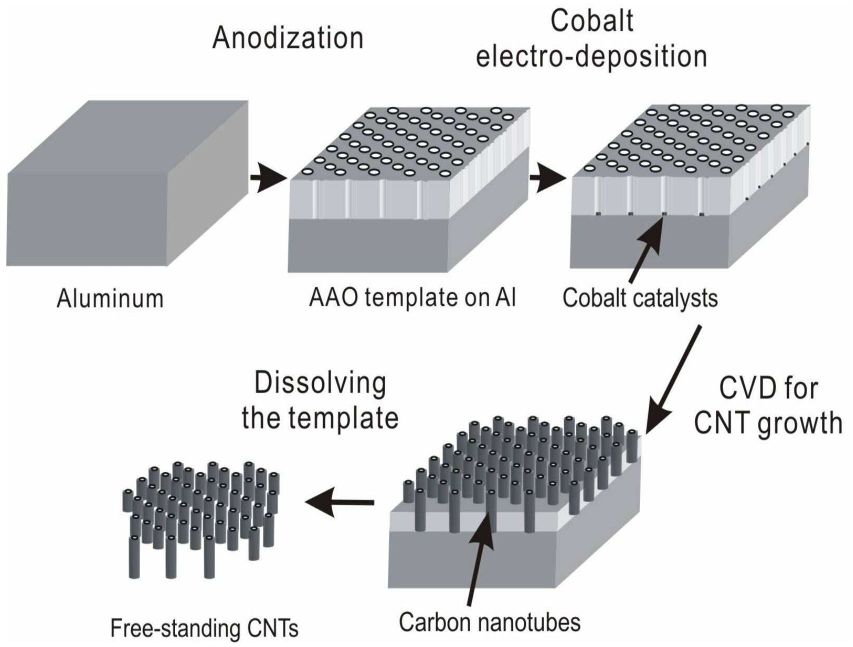

FIGURE 5.1: Diagram of the synthesis steps of CNTs by chemical vapor deposition. The anodized-aluminum-oxide (AAO) template is obtained by electro-chemical anodization of a pure aluminum sheet, the cobalt catalyst are electro-deposited inside the pores and the CNT is grown by CVD method. The CNTs are separated from Al substrate by dissolving AAO template with NaOH solution.

60 – 80 ^{0}C for 3 hr. The released MWCNTs were used to make a randomly oriented MWCNT film sample. From a 3 cm^2 MWCNT+AAO sample, 1.82 mg of MWCNTs were released corresponding to an embedded mass of MWCNT of 0.61 mg cm^{-2}. From the dimensional information of the MWCNT and assuming an AAO pore density of about 10^{10} cm^{-2}, a theoretical value of the MWCNT mass per area of MWCNT+AAO is 0.86 mg cm^{-2}, reasonably close to the measured value. The mass of the MWCNTs embedded inside the AAO template sample was thus estimated by using the measured mass of released CNTs per unit area of composite.

Single-wall carbon nanotubes (SWCNT) were obtained from Helix Material Solutions, Inc. [28] and used without further processing. The reference graphite powder was obtained from AGS and has the following composition; 95.2 % carbon, 4.7 % ash, and 0.1 % moisture and other volatiles. The graphite powder was used after degassing at 100 ^{0}C under vacuum for 2 hr. Morphology of the MWCNTs, SWCNTs and graphite particles were examined by a JEOL JSM-7000F scanning electron microscope (SEM) and a Philips CM12 transmission electron microscope (TEM) before the calorimetric measurements. Aspects of the sample morphology, particularly the diameters of the CNTs, were analyzed using the *Image J* processing software. The dimensions were measured 10 times from multiple TEM images for all samples and the average and standard deviations were reported.

For the calorimetric measurements, contact resistance plays an important role. All samples and the components of the sample+cell, were measured under identical experimental conditions (e.g. thickness, area, mass, and external thermal link), and were similarly configured in a sandwiched pattern between two silver or silver and aluminum oxide (for aligned MWCNTs) samples. Although the similarity of construction should result in similar contact resistance, due to local variation of surface roughness, sample-to-sample variations, and uncertainties in particle geometries, the contact resistance should be considered averaged over the ∼cm in-plane length-scale of the composite sample and thus lead to large uncertainties in the absolute magnitude of the derived thermal conductivity. However, the relative precision of the temperature dependence of the thermal conductivity should be comparable.

5.2.2 Sample+Cell Configurations

Details of the experimental sample+cell configuration have been reported elsewhere [12] and also shown in Fig. 5.2.

Briefly, the aligned MWCNT+AAO sample were in excellent thermal contact on one end by their anchoring to the Al base of the AAO and contact on the other end was made to a thin silver sheet by a thin layer of GE varnish (General Electric #7031 varnish). The typical thickness of MWCNT+AAO sample was about 20 μm. This aligned sample was arranged as a silver sheet/GE varnish/MWCNT+AAO/Al sandwich. One side of the ‘stack’ has attached a 120 Ω strain-gauge heater and the other a 1 MΩ carbon-flake thermister. For the randomly oriented thin film samples, the powder-form MWCNTs, separately obtained SWCNTs, and graphite powders were drop cast on a thin silver sheet then sandwiched by another identical silver sheet on top by a thin layer of GE varnish forming a nearly identical ‘stack’ (in dimension and total mass) as the aligned sample. All components of all sample+cells were carefully massed in order to perform background subtractions.

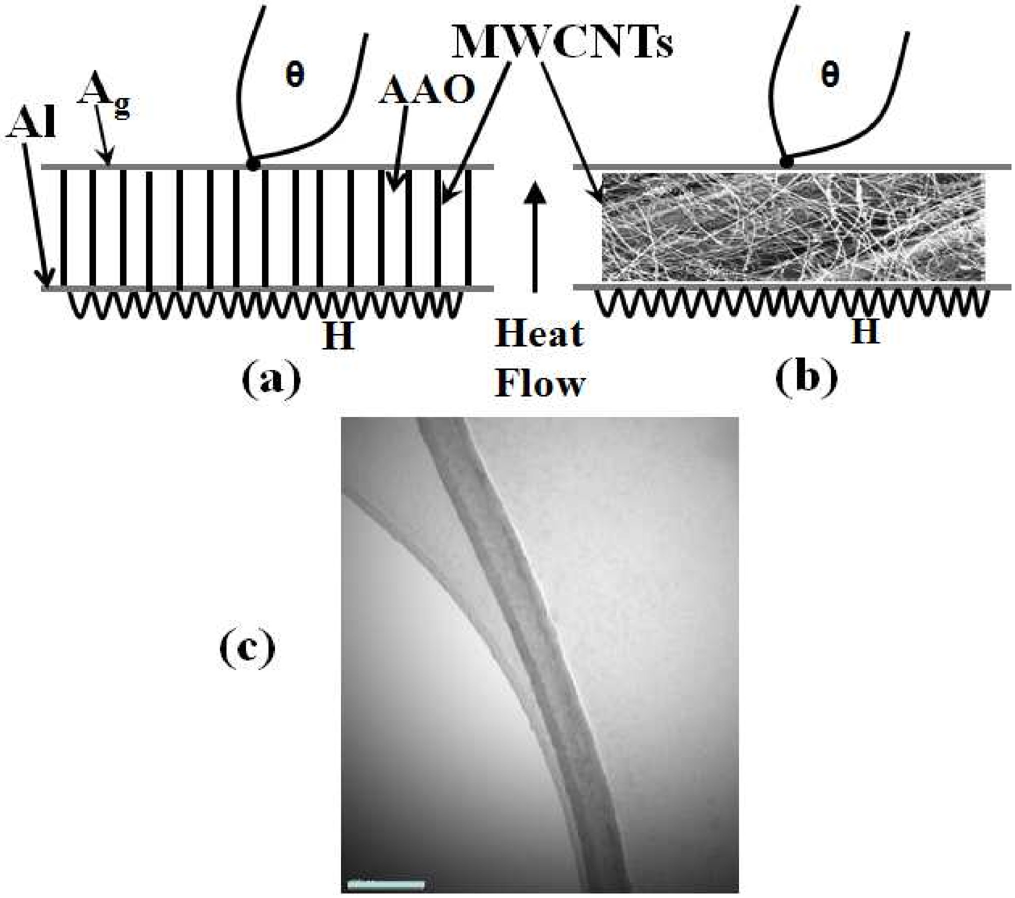

FIGURE 5.2: In (a) and (b), a cartoon depicting the sample cell configuration for the aligned MWCNT+AAO sample (a) and for the random film of MWCNT, SWCNT, or graphite powder samples (b). In (c) a typical TEM of a MWCNT is shown with the bar in the lower left of the micrograph representing 100 nm. Image analysis of such micrographs yield the geometric properties of the CNTs.

5.2.3 AC-Calorimetric Technique

An AC (modulated) heating technique is used for the measurements presented in this paper. A sinusoidal heat input $P_0 e^{-wt}$ with $P_0 \approx 0.5$ mW was supplied to one side and the resulting modulated temperature oscillation T_{ac} was measured at the opposite side of the sample+cell. The experimental technique details can also found elsewhere [12]. The amplitude T_{ac} can be expressed as:

$$T_{ac} = \frac{P_0}{2\omega C}\left(1 + (\omega\tau_e)^{-2} + \omega^2\tau_{ii}^2 + \frac{2R_s}{3R_e}\right)^{-1/2}, \tag{5.1}$$

where ω is the applied heating frequency, $C = C_s + C_c$ is the total heat capacity (C_s is the heat capacity of sample and C_c is the heat capacity of cell). Here, $C_c = C_H + C_{GE} + C_{AAO} + C_{Ag} + C_{Al}$ for the aligned MWCNT+AAO sample and $C_c = C_H + C_{GE} + C_{Ag}$ for randomly oriented MWCNT, SWCNT, and bulk powder graphite samples. By subtracting the cell contribution, the heat capacity of the carbon nanotubes may be isolated as $C_{CNT} = C_s = C - C_c$ and $C_p = C_s/m$, where m is the mass of the nanotubes or graphite powder. The contribution of the carbon-flake thermister is negligible, having a very weak temperature dependence, and so, is ignored.

There are two important thermal relaxation time constants in Eq. (5.1), $\tau_e = R_e C$ and $\tau_{ii}^2 = \tau_s^2 + \tau_c^2$, the external and internal respectively, where τ_s refers to sample relaxation and τ_c refers to cell relaxation time constants. Here, R_s is the sample internal thermal resistance and R_e is the external thermal resistance linking the sample+cell to the bath. The reduced phase shift (ϕ) between the input heat and resulting temperature oscillation as a function of heating frequency scan can directly measure τ_e and τ_i using:

$$\tan(\phi) = (\omega\tau_e)^{-1} - \omega\tau_i, \tag{5.2}$$

where $\tau_i = \tau_s + \tau_c$ and typically $\tau_c \ll \tau_s$, hence $\tau_i \simeq \tau_{ii}$. Eq. (5.2) can be rewritten to give $\tau_s \equiv R_s C_s \cong 1/(\omega^2\tau_e) - (\tan\phi)/\omega$. The effective thermal conductance, the inverse of the effective thermal resistance, of the sample can then be evaluated from the experimental parameters as:

$$K_s \cong \frac{\omega^2\tau_e C_s}{1 - \omega\tau_e \tan\phi} \tag{5.3}$$

where K_s is given in Watts per Kelvin. With the known geometric dimensions of the sample, the effective thermal conductivity κ_s can be estimated as $\kappa_s = \frac{K_s L}{A}$, with L the thickness and A the area of the sample.

In order to extract the effective thermal conductivity, certain geometric estimates were needed. The outer and inner diameter of MWCNT was taken as 54 and 22 nm, respectively. See Section 5.3A for details. By assuming the density of nanotubes to be 1.3 g cm^{-3} and the interlayer separation of graphene sheets as 0.34 nm [29], the estimated mass is found to be ~ 30 % higher than that determined by sample area and gives a conservative estimate of absolute uncertainty. To extract the thermal conductivity, the whole area of the AAO pores is assumed to be filled by MWCNTs to determine the effective thermal conductivity. By subtracting the inside hollow area of each nanotubes, the estimated value of thermal conductivity for anisotropic MWCNT could be two orders of magnitude larger. Thus, the absolute value of the conductivity is not well known but its temperature dependence should be well defined.

5.3 Results and Discussion

5.3.1 Morphology Study

Scanning electron microscope images were taken of the samples studied and are shown in Fig. 5.3. For the aligned MWCNT embedded in the AAO channels, the cross-section SEM in Fig. 5.3(a) shows that each channel contains a well-confined MWCNT suggesting a very high filing fraction (essentially 1), with all the channels and MWCNTs parallel to each other throughout the thickness of the MWCNT+AAO composite.

As confirmed by previous studies [27, 29], the outer diameter of the MWCNTs were determined by the 60 nm pore size of the AAO template. The analyzed tunneling electron micrographs, an example shown in Fig. 5.2c, indicate that the inner diameter of the synthesized MWCNT was 22 ± 8 nm and the outer diameter 54 ± 5 nm. As shown in Fig. 5.3(b), the liberated MWCNTs thin films are randomly oriented, laying flat with one on top of the another. In Fig. 5.3(c), the randomly oriented SWCNT thin films appear to be highly entangled. Here, SWCNTs are approximately 1.3 nm in diameter,

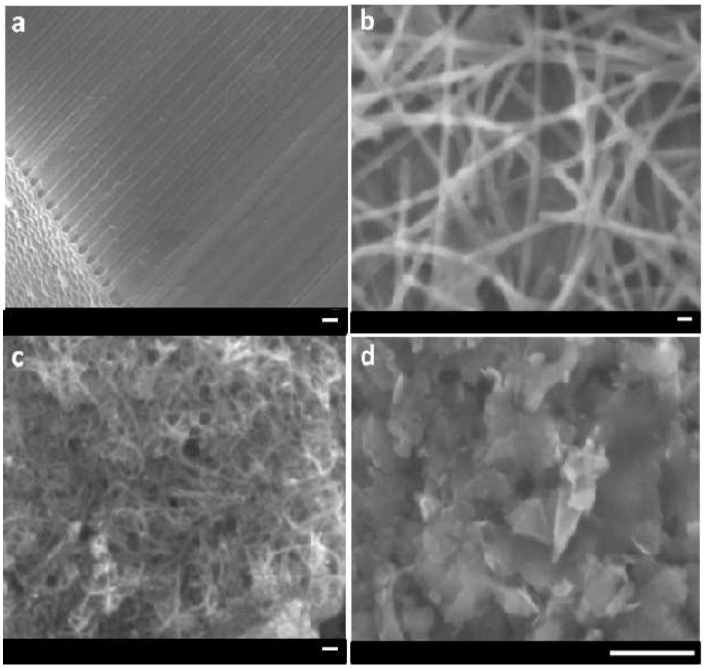

FIGURE 5.3: SEM micrographs of arrays of MWCNTs inside AAO template (a), released MWNTs from AAO template (b), SWCNTs (c), and graphite powder (d). MWCNTs are 20 μm long with 60 nm outside and 25 nm outer diameter. The scale bar in (a), (b) and (c) are 100 nm and in (d) is 1 μm.

$0.5-40$ μm long, and $\gtrsim 90$ % pure [28]. The reference sample of graphite powder shown in Fig. 5.3(d) has a large particle size of ~ 1 μm and a wide particle size distribution.

5.3.2 Specific heat of CNT composites

The anisotropic measurement of specific heat ($c_p^{||}$) and randomly oriented specific heat (c_p^M) for MWCNT, randomly oriented specific heat (c_p^S) for SWCNT, and that of bulk graphite powder (c_p^B) are shown in Fig. 5.4. The specific heat of all samples were determined as a function of temperature from 300 to 400 K on heating. The bulk graphite powder sample yields a $c_p^B = 0.73$ J g^{-1} K^{-1} at 300 K and a weak, nearly-linear, temperature dependence up to 360 K reaching 0.80 J g^{-1} K^{-1}. These values obtained from our experimental arrangements are 2.1% higher and 5.5% lower, respectively, from literature values [30] and indicate in absolute value uncertainty of about 5% (conservatively) and an uncertainty in slope of about 7%.

For the aligned MWCNT composite sample $c_p^{||} = 0.74$ J g^{-1} K^{-1} while for the randomly oriented thin film sample $c_p^M = 0.75$ J g^{-1} K^{-1} at 300 K, very similar to bulk graphite

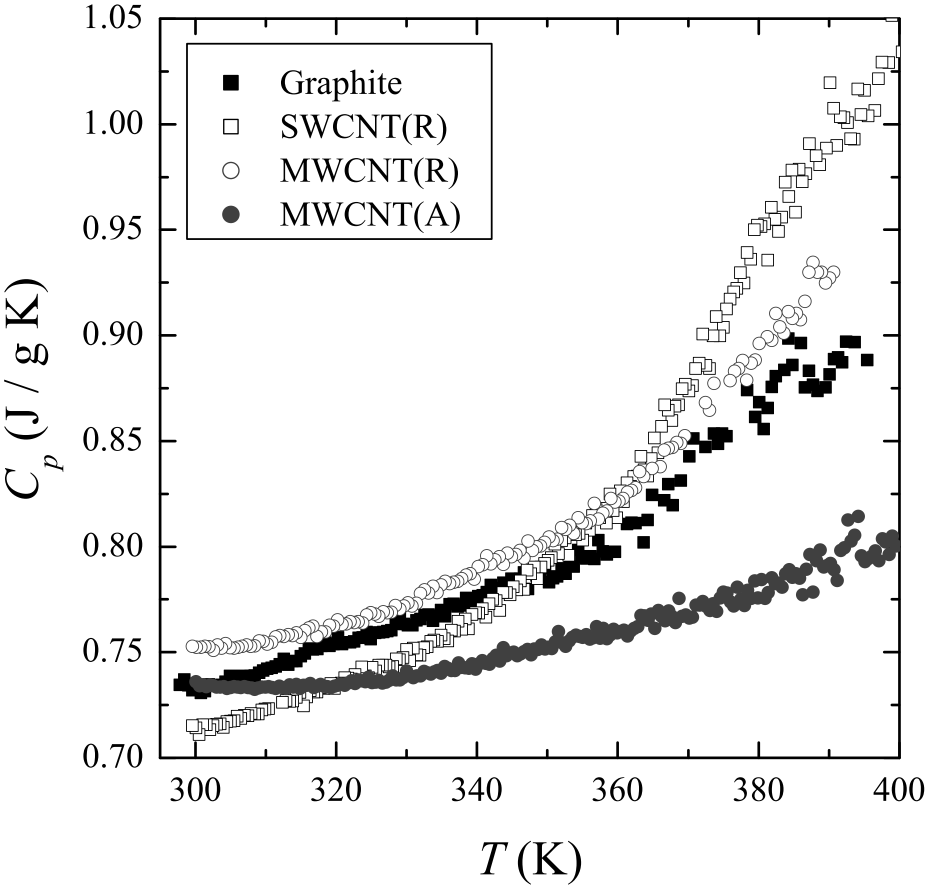

FIGURE 5.4: The measured specific heat of bulk graphite powder (solid squares), SWCNT (open squares) and MWCNT (open circles) random thin film samples (labeled R), and aligned MWCNTs measured parallel to the long axis (solid circles - labeled A) from 300 to 400 K.

with similar temperature dependence. For the randomly oriented SWCNT thin film sample, $c_p^S = 0.72$ J g^{-1} K^{-1} at 300 K and increases linearly up to 362 K similar to bulk graphite, but then exhibits a much stronger temperature dependence up to 385 K, reaching $c_p^S = 1.02$ J g^{-1} K^{-1}. There are few experimental or theoretical investigations of the specific heat or thermal conductivity reported in the literature at these high temperatures. One of the few, Yi et al [4], reported the specific heat of a single aligned MWCNT at 300 K to be ≈ 0.5 J g^{-1} K^{-1} while similar temperature dependence up to 400 K have been observed [31]. Several studies at lower temperatures have shown that nanowires and nanotubes can have very different phonon dispersion than in the bulk due to phonon confinement, wave-guiding effects, and increased elastic modulus, that effectively determine phonon velocity [32–35].

It is expected that the magnitude of the specific heat of graphite and carbon nanotube samples would be the same at high temperatures, as seen from low temperatures up to 200 K [36]. This is generally true for our results, to within 7% for the reference graphite powder and the random films of SWCNT and MWCNT samples. Variations among these samples of the magnitude of c_p is likely due to the composite nature of the sample arrangement. However, the temperature dependence of the aligned MWCNT in the AAO channels is much weaker than can be explained by experimental uncertainties.

5.3.3 Thermal Conductivity of CNTs

Fig. 5.5 shows the effective thermal conductivity of bulk graphite powder, randomly oriented thin films of SWCNTs and MWCNTs (labeled with an R extension), as well as aligned arrays of MWCNT in AAO (labeled with an A extension) from 300 to 400 K. The bulk graphite and MWCNT(R) samples are nearly identical up to about 360 K after which, near 365 K, a broad peak is observed (slightly sharper for the graphite). The SWCNT(R) sample has a higher magnitude and weaker temperature dependence as bulk graphite and MWCNT(R) but reaches the same magnitude at a broad peak or plateau near 365 K. These results are similar to a broad peak-like behavior in the thermal conductivity simulated by Osman [37] with the heat flow perpendicular to the nanotube long axis. These results are also consistent with measurements for bulk powder cobalt and random thin films of cobalt nanowires [12]. It is likely that the thermal conductivity of these structures over this temperature range is dominated by phonon-boundary scattering. Basically, the randomly oriented thin films of CNTs behave similar to the graphite powder due to the large number particle boundary contacts/junctions. The broad peak near 365 K can be understood as due to the phonon-phonon bunching at these boundaries, which can cause a dramatic reduction of the thermal conductivity. For SWCNT(R) thin films, the effective thermal conductivity is 0.8 W m^{-1} K^{-1} at 300 K and increases linearly up to 360 K, then its decreases slowly with further increasing temperature. This is consistent with that observed by Hone's group [5–8] on a similar sample arrangement finding κ = 0.7 W m^{-1} K^{-1} at 300 K. The uncertainty of the absolute magnitude depends strongly on the density of CNTs per unit area of film and the results presented here likely underestimate the true value. However, the larger magnitude of κ for the SWCNT(R) sample would be expected from the smaller diameter of the SWCNTs compared to the studied MWCNTs or the size of the graphite powder particles.

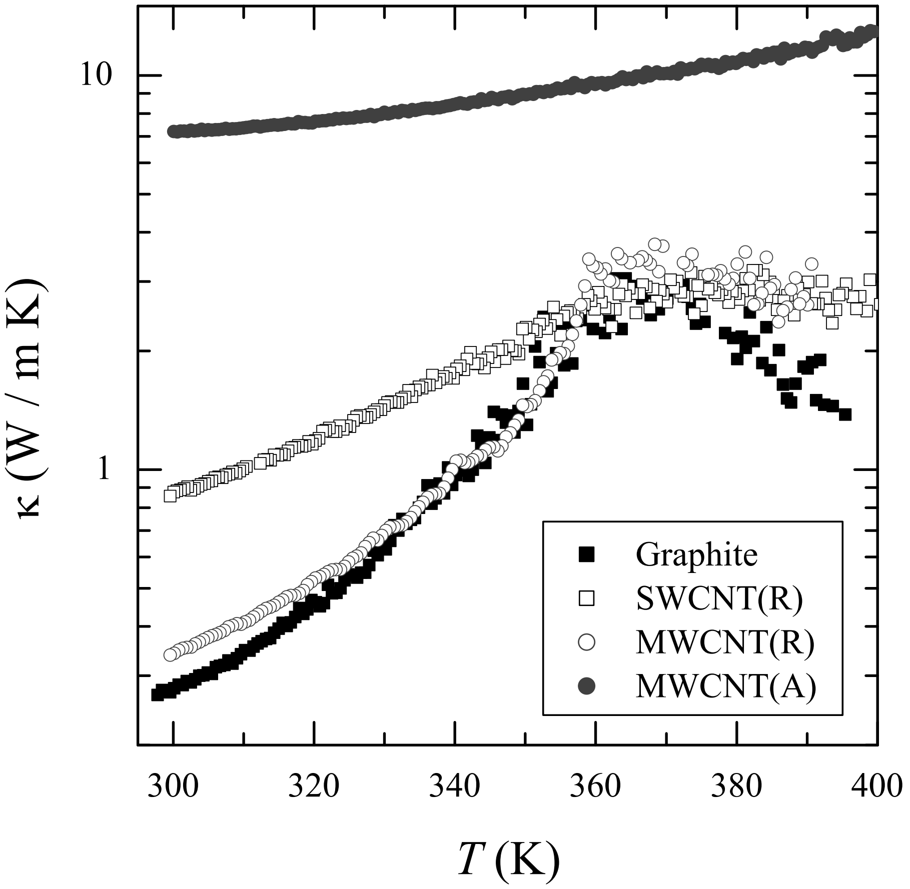

FIGURE 5.5: A semi-log plot of the derived effective thermal conductivity of bulk graphite powder (solid squares), random thin films of SWCNT (open squares) and MWCNT (open circles), as well as aligned MWCNT (solid circles) as function of temperature from 300 to 400 K.

The observed temperature dependence of the effective thermal conductivity of aligned MWCNT inside the AAO nanochannel, MWCNT(A) is quite different than the random thin film samples as seen in Fig. 5.5. The derived MWCNT(A) κ is about 23 times that of bulk graphite powder or MWCNT(R) thin films and 8 times that of SWCNT(R) thin film at 300 K. Unlike the random thin film samples, κ of MWCNT(A) increases smoothly from 300 to 400 K without any indications of a plateau or broad peak. Similar observations of a smoothly increasing thermal conductivity have been reported for CNTs aligned by a magnetic field [38] and supports the one-dimensional nature of the heat flow in our sample. From purely geometric considerations, the estimated value of thermal conductivity for a single MWCNT along the long axis at 300 K is approximately 700 W m^{-1} K^{-1}. While the uncertainty of the absolute magnitude of these measured effective κ are large, perhaps as large as an order of magnitude, it cannot explain the difference with that expected for a 'scaled-up' geometric estimate of κ along the long axis. Similarly for random thin film samples, an estimate assuming the whole sample area is filled completely by sample (a filling fraction of 1) yields a value at least two orders of magnitude or larger than that derived here. Thus, the composite nature of these macroscopic samples must be intrinsically different than simply scaling up the behavior of a single nanotube to these dimensions.

To better compare the temperature dependence of the effective thermal conductivity, normalized values (to that observed for each sample at 300 K, i.e. κ/κ_{300K}) of the bulk graphite powder, the random thin films of SWCNT(R) and MWCNT(R), as well as aligned MWCNT(A) in AAO a shown in Fig. 5.6. This construction illustrates the fractional change of the observed κ and indicates that the random thin film samples are all dominated by its granular nature while the aligned MWCNT sample, though higher in magnitude, has a much smaller fractional change up to 400 K.

The effective thermal conductivity is greatly affected by the interface contact resistance between surfaces and sample as well as among the sample particles (nanotubes or graphite powder) [39, 40]. The results presented in this work reveal that the heat transfer in aligned nanotubes is dominated by the nanotube-nanotube interfacial resistance, nanotube length, diameter, and spacing. Paradoxically, the nanotube thermal resistance decreases with increasing nanotube length [39, 41]. For aligned MWCNT+AAO, the heat flow is essentially one-dimensional across each single nanotube, but their coupling to the AAO matrix and the cell surfaces leads to increased thermal resistance. However, in the case of a randomly oriented thin film sample, the nanotube-nanotube resistance decreases due to the proliferation of contacts among nanotubes improving the heat exchange. In all samples, the interfacial resistance also depends upon the geometry of the contacting surfaces through surface roughness [42]. Anharmonic phonons can be created, destroyed or scattered from each other leading to a finite mean-free-path and so, limiting the thermal conductivity [43].

The heat transfer across interfaces can be represented by a single parameter known as the thermal interfacial resistance R [39] and is given by

$$R = A\Delta T/Q = t/(\kappa A); \qquad (5.4)$$

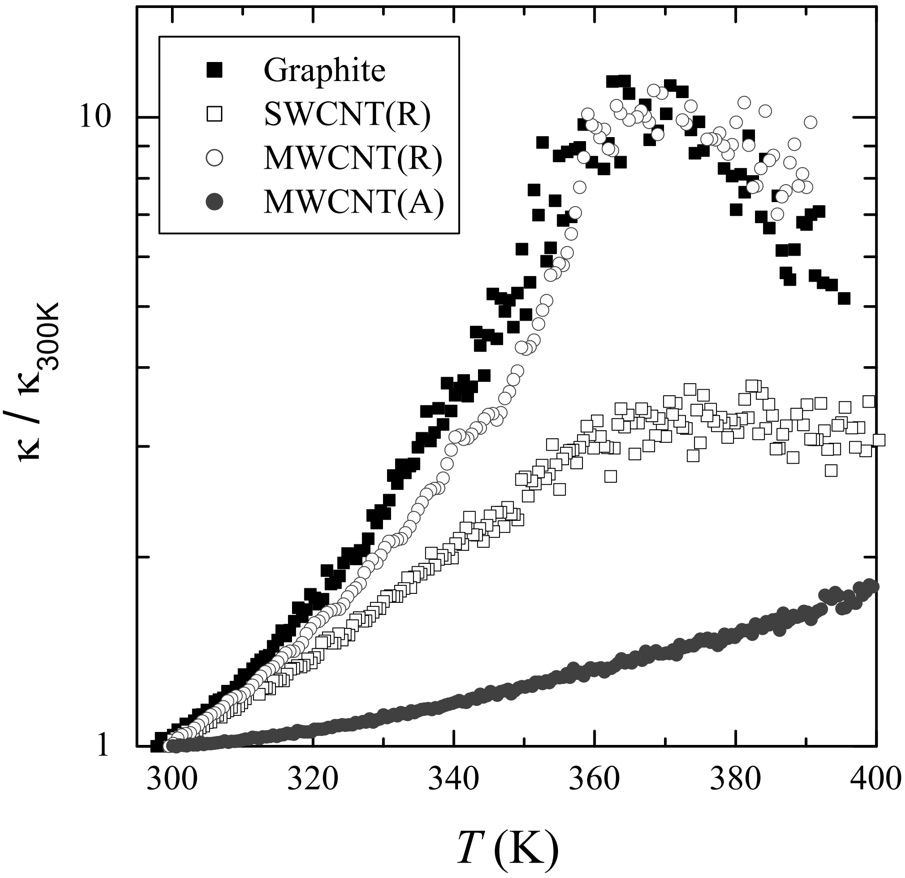

FIGURE 5.6: A semi-log plot of the effective thermal conductivity normalized to that determined for each sample at 300 K to reveal the fractional change as a function of temperature. Shown are the bulk graphite powder (solid squares), random thin films of SWCNT (open squares) and MWCNT (open circles), along with aligned MWCNT (solid circles) from 300 to 400 K.

where A is the area of the interface contact, ΔT is the steady-state temperature jump between two surfaces of contact, Q is the rate of heat flow across the interface, t is the thickness of sample, and κ is the thermal conductivity. Equation (5.4) applies to one-dimensional heat flow through the area A across the thickness t.

Since the heat flow in these measurements across the randomly oriented and aligned samples are the same, the thermal contact resistance between nanotubes or powders (in randomly oriented sample), nanotubes-matrix (in aligned sample), as well as between contact areas plays an important role and induces temperature gradients. Recently reported calculations describe the effect of thermal contact resistance on a random film sample of carbon nanotubes and obtained a very low thermal conductivity as compared to that along the long axis of a single nanotube [44]. The energy transfer between carbon nanotubes in van der Waals contact is limited by a large contact resistance [39] arising from weak inter-particle bonding. The contact resistance for larger diameter CNT is smaller than the smaller diameter CNT due to larger contact area, whereas the number of contacts per unit volume will be larger for smaller nanotubes due to large aspect ratio.

5.4 Summary

In this work, experimental results of the specific heat and effective thermal conductivity of a macroscopic composite containing randomly oriented single-wall and multi-wall carbon nanotubes, graphite powder, and aligned multi-wall carbon nanotube embedded in a porous aluminum matrix are reported from 300 to 400 K. The specific heat is generally consistent among all carbon samples with the graphite powder and random thin film of MWCNT being most similar. The random thin film of SWCNT has a stronger while the aligned MWCNT in AAO has a weaker temperature dependence than the bulk behavior measured here. Though small, these differences are due to the intrinsic properties of SWCNT for the former and the macroscopic arrangement in the composite for the latter sample. The effective thermal conductivity reveals the most striking effect of composite construction. In all the random thin film samples of SWCNT, MWCNT, and graphite powder, a broad peak like feature is seen in κ near 365 K, similar to that seen in similar cobalt-based composites [12]. The absolute value of effective thermal conductivity measured here of the single-wall and multi-wall CNTs are expected to be different because of their differences in length, diameter, and overall purity. Given that all three random thin film sample+cell configuration of SWCNT(R), MWCNT(R), and graphite powder are nearly identical, the phonon-boundary scattering mechanism is the most likely and the difference in absolute value is likely due to uncertainties in mass approximation and sample purity.

These results on how the thermal properties of carbon nanotube composites vary with construction can be combined with the recent work of Hone's group [7, 8] on the thermal conductivity for an unaligned SWCNT sample in the presence of a magnetic field finding ≈ 25 W m^{-1} K^{-1} at 300 K and increases with increasing temperature until saturating at ≈ 35 W m^{-1} K^{-1} near 400 K. Thus, detailed engineering of thermal properties is a strong possibility. Future work on more complex composite arrangements would further detail the possible variations and should hopefully inspire complimentary theoretical or computational work to better understand such systems.

Bibliography

[1] Ijima Sumio, *Nature.*, **354,** 8, No.56 (1991).

[2] C. H. Olk and J. P. Heremans, *J. Mater Res.*, **9,** 259 (1994).

[3] C. Dekker, *Physics Today.*, **52,** 22 (1999).

[4] W. Yi, L. Lu, Z. Dian-Lin, Z. W. Pan and S. S. Xie, *Phys. Rev. B.*, **59,** R9015 (1999).

[5] J. Hone, M. Whitney, C. Piskoti and A. Zettl, *Phys. Rev. B.*, **59,** R2514 (1999).

[6] J. Hone, M. Whitney, C. Piskoti and A. Zettl, *Synthetic Metals.*, **103,** 2495 (1999).

[7] J. Hone, B. Batlogg, Z. Benes, A. T. Johnson and J. E. Fischer,*Science*, **289**, 1730 (2000).

[8] J. Hone, M. C. Llaguno, N. M. Nemes, A. T. Johnson, J. E. Fisher, D. A. Walters, M. J. Casavant, J. Schmidt and R. E. Smalley, *Appl. Phys. Lett.*, **77,**, 666 (2000).

[9] J. Hone, M. C. Llaguno, M. J. Biercuk, A. T. Johnson, B. Batlogg, Z. Benes and J. E. Fisher, *Appl. Phys. A: Mater Sci. Process.*, **74,** 339 (2002).

[10] D. J. Yang, Q. Zhang, G. Chen, S. F. Yoon, J. Ahn, S. G. Wang, Q. Zhou, Q. Wang and J. Q. Li, *Phys. Rev. B.*, **66,** 165440,(2002).

[11] R. Basu and G. S. Iannacchione, *Appl. Phys. Lett.*, **93,** 183105 (2008).

[12] N. R. Pradhan, D. Huanan, J. Liang and G. S. Iannacchione, *Nanotechnology*, **19,** No.48, 485712 (2008).

[13] T. Tong, A. Majumdar, Y. Zhao, A. Akashi, L. Delzeit and M. Meyapan, *IEEE.*, **,** 1406-1411 (2006).

[14] K. Zhang, Y. Chai, M. M. F. Yuan, D. G. W. Xio and P. C. H. Chan, *Nanotechnology.*, **19,** 215706 (2008).

[15] Y. Xu, C. Leong, D. D. L. Chung, *Journal of Electronic Materials.*, **36,** No.9, 1181 (2007).

[16] Jong-Jin Park and M. Taya, *Journal of Electronic Packaging*, **128,** 46, May (2006).

[17] P. B. Amama, B. A. Cola, T. D. Sands, X. Xu and T. S. Fisher, *Nanotechnology.*, **18,** 385303 (2007).

[18] J. Xu and T. S. Fisher, *International Journal of Heat transfer.*, **49,** 1658 (2006).

[19] S. Berber, Y. K. Kwon, and D. Tomanek, 84 (2000)., *Phys. Rev. Lett.*, **84,** No.20, 4313-6 (2000).

[20] P. Kim, L. Shi, A. Majumdar, and P. L. McEuen, *Phys. Rev. Lett.*, **87,** 215502 (2001).

[21] L. Shi, D. Li, C. Yu, W. Jang, D. Kim, Z. Yao, P. Kim, and A. Majumdar, *J. Heat Transfer.*, **125,** 881 (2003).

[22] H.-L. Zhang, J.-F. Li, B.-P. Zhang, K.-F. Yao, W.-S. Liu, and H. Wang, *Phys. Rev. B*, **75,** 205407 (2007).

[23] S. Xie, W. Li, Z. Pan, B. Chang, and L. Sun, 61, 1153 (2000). *J. Phys. Chem. Solids.*, **61,** 1153 (2000).

[24] L. Lu, W. Yi, and D. L. Zhang, *Rev. Sci. Instrum.*, **72,** 2996 (2001).

[25] R. Prasher, *Phys. Rev. B*, **77,** 075424 (2008).

[26] J. Li, C. Papadopoulos, J. M. Xu and M. Moskovits, *Appl. Phys. Lett.*, **75,** 367 (1999).

[27] J. Liang, H. Chik, A. Yin, and J. M. Xu, *J. Appl. Phys.*, **91,** 2544 (2002).

[28] http://www.helixmaterial.com (2009).

[29] J. G. Lavin, S. Subramoney, R. S. Rou, S. Berber, and D. Tomanek, *Carbon*, **40,** 1123 (2002).

[30] T. Nihira and T. Iwata, *Phys. Rev. B*, **68,** 134305 (2003).

[31] H. Xie, *J Mater Sci.*, **42,** 3695 (2007).

[32] M. S. Dresselhaus, Y. -M. Lin, S. B. Cronin, O. Rabin, M. R. Black, G. Dresselhaus, and T. Koga, *Semicond. Semimetals*, **71,** 1 (2001).

[33] M. X. Gu, T. C. Yeung, C. M. Tan, and V. Nosik, *J. Appl. Phys.*, **100,** 094304 (2006).

[34] L. G. C. Rego and G. Kirczenow, *Phys. Rev. Lett.*, **81,** 232 (1998).

[35] G. Mahan, *Phys. Rev. B*, **65,** 235402 (2002).

[36] A. Mizel, L. X. Benedict, M. L. Cohen, S. G. Louie, A. Zettl, N. K. Budraa, and W. P. Beyermann, *Phys. Rev. B*, **60,** 3264 (1999).

[37] M. A. Osman and D. Srivastava, *Nanotechnology*, **12,** 21 (2001).

[38] J. E. Fischer, W. Zhou, J. Vavro, M. C. Liaguno, C. Guthey, R. Haggenmuller, M. J. Cassavant, D. E. Walters, and R. E. Smalley, *J. Appl. Phys.*, **93,** 2157 (2003).

[39] H. Zhong and J. R. Lukes, (2006). *Phys. Rev. B*, **74,** 125403 (2006).

[40] S. Shenogin, L. Xue, R. Oziski, P. Keblinski, and D. G. Cahill, *J. Appl. Phys.*, **95,** 8136-44 (2004).

[41] S. T. Huxtable, D. G. Cahill, S. Shenogin, L. Xue, R. Ozisiki, P. Barone, M. Usrey, M. S. Strano, G. Siddons, M. Shim, *Nat. Mater.*, **2,** 731 (2003).

[42] G. L. Pollack, *Rev. Mod. Phys.*, **41,** 48 (1969).

[43] F. Y. Meng, S. Ogata, D. S. Xu, Y. Shibutani, and S. Q. Shi, (2007). *Phys. Rev. B*, **75,** 205403 (2007).

[44] R. S. Prasher, X. J. Hu, Y. Chalopin, N. Mingo, K. Lofgreen, S. Volz, F. Cleri, and P. Keblinski, *Phys. Rev. Lett.*, **102,** 105902 (2009).

Chapter 6

THERMAL PROPERTIES AND GLASS TRANSITION IN PMMA+SWCNT COMPOSITES

6.1 Introduction of Polymer-Carbon Nanotubes Composite

Carbon nanotubes (CNTs) have outstanding electrical, mechanical, optical, and thermal properties with significant promise in a vast range of applications such as quantum wires [1], tips for scanning probe microscope [2], and molecular diodes [11]. Polymers play an important role in numerous fields due to their advantages in lightness, ease of processing, resistance to corrosion, and low cost production. To improve the performance of polymers, composites of polymers and a filler, namely micron-scale aggregate or fibers, have been extensively used and studied. The use of nano-scale fillers such as metals, semiconductors, organic and inorganic particles, and fibers, especially carbon structures [5–8], are of particular interest and the subject of intense investigation. The unique properties of carbon nanotubes offer crucial advantages over other nano-fillers.

The potential of using carbon nanotubes as filler in polymer composite has not been fully realized because of processing difficulties. Currently, there are only a few carbon nanotube-based, commercial products on the market with improved electrical conductivity [Hyperion Catalysis International]. Thermal management such as heat removal from ICs is a critical problem that limits potential miniaturization, speed and reliability [9] of micro electronics. For most modern microelectronic devices, cooling is restricted by the thermal conductivity of the polymeric packaging materials, since polymers typically have low thermal conductivity as compared to other materials. To enhance the thermal conductivity of polymers, fillers with higher thermal conductivity is required. The thermal conductivities of composites (polymer+fillers) is controlled by (i) filler concentration, (ii) filler conductivity, (iii) filler geometry, (iv) interface conductance between filler and polymer, and (v) homogeneity of the filler dispersion. The small particle sizes of nano-fillers are expected to disperse more homogeneously within a polymer host than larger micro/milli-fillers. However, there remains serious gaps in the fundamental understanding of the interaction between nano-fillers and polymers that lead to the properties of the composite materials.

Relaxation processes in amorphous materials are particularly important to understanding macroscopic properties. Calorimetry, such as DSC, has revealed enthalpic (energy) relaxations occurring near the glass transition T_g in polymers aged after a variety of heating treatments. It is well known that annealing or variation of heating and cooling rates leads to significant hysteresis in T_g because of structural relaxations [10, 11]. The introduction of nano-fillers are expected to strongly influence these short-range structural relaxations. However, the effective utilization of CNTs in polymer composite applications strongly depend upon the quality/uniformity of the nanotubes and the ability to disperse them homogeneously throughout the polymer host [12, 13]. Thus, the main objective of this work is to produce and investigate polymer+Single-wall CNT (SWCNT) nano-composites materials, which are candidates for next-generation of high-strength, light weight, and enhanced thermal conducting materials.

This report describes a simple yet effective method to controllably disperse SWCNTs in the polymer polymethyl-metha-acralyte (PMMA) and presents a detailed calorimetric study using modulation (ACC) and modulation-differential-scanning (MDSC) calorimetric techniques. The PMMA+SWCNT composites were prepared by dispersing SWCNTs and PMMA in a chloroform solution using sonication then slowly evaporating the chloroform leaving a homogeneous dispersion. The specific heat and effective thermal conductivity of the composites were determined by ACC from 300 to 400 K as a function of

SWCNT content. An enhancement of the effective thermal conductivity is observed as the mass fraction of SWCNTs (ϕ_m) increases from 0.014 to 0.083. These experimental results are in good agreement with a simple geometric model [17] at low SWCNT content but are better described by more sophisticated models [19–21] above $\phi_m \sim 0.034$. The glass transition dynamics of pure PMMA and PMMA+SWCNT samples were studied by MDSC as a function of temperature scan rate. The hysteresis between heating and cooling of the reversible specific heat decreases with decreasing scan rate for pure PMMA but is essentially unchanged in the composites, indicating the SWCNT may be quenching glassy structural dynamics. In all samples, the effective glass transition temperature, T_g increases with increasing scan rate (though less so for higher ϕ_m SWCNTs) but the MDSC determined T_g are consistently below the scattered values determined by the ACC method. This discrepancy is attributed to the effect of prolonged heat treatment of the composite for the ACC measurements.

Following this introduction, we describe the experimental procedures for the calorimetric methods and sample preparation and this again follows results and discussion with theoretical models for thermal conductivity in composite systems. A general conclusion in the end describes future directions.

6.2 Experimental

6.2.1 Modulation Calorimetry (ACC):

In the ACC technique, the sample and cell, loosely coupled to a constant thermal bath, are subjected to a small oscillatory heat input. The specific heat and the effective thermal conductivity can be determined by measuring the frequency dependence of the amplitude and phase of the resulting temperature oscillation. The heat input, $P_0e^{-\omega t}$ with $P_0 \approx 0.5$ mW, is supplied to the sample+cell and typically results in a modulated temperature having an amplitude $T_{ac} \approx 5$ mK. In the sample+cell "sandwich" or "stack" arrangement used in this study, the total measured heat capacity is written as $C = C_s + C_c$, where C_s is the heat capacity of the PMMA or PMMA+SWCNT composite sample and C_c is the heat capacity of cell. The cell heat capacity consists of $C_c = C_H + C_{Ag} + C_{GE}$, where C_H is the heater, C_{Ag} is the silver sheets, and C_{GE} is the GE varnish (used to attach all the components) contribution. The heat capacity of the PMMA or PMMA+SWCNT composite is $C_s = C - C_c$ and specific heat capacity determined as $C_p = C_s/m_s$, where m_s is the mass of the sample. The contribution of the carbon-flake thermister, used to measure the temperature, is small compared to all other components and is neglected. The ACC experimental procedure details can be found elsewhere [22–25] and the method to estimate the effective thermal conductivity can be found in Refs. [22, 26, 27]. The *effective* thermal conductance K_s in units of WK^{-1}, the inverse of the thermal resistance, of the sample is given by

$$K_s \cong \frac{\omega^2 \tau_e C_s}{1 - \omega \tau_e \tan \phi} \tag{6.1}$$

where $\tau_e = R_e C_s$ is the external thermal relaxation time constant, R_e the external thermal resistance, ω the oscillatory frequency, and $\phi = \Phi + \pi/2$ is determined from the phase shift Φ between the heat input and resulting temperature change. With the geometric dimensions of sample+cell configuration, the effective thermal conductivity κ_s in units of W m^{-1} K^{-1} can be calculated directly as $\kappa_s = K_s L/A$, where L is the thickness and A is the cross-sectional area of the sample.

High-resolution ACC was performed using a home-built calorimeter. The general sample+cell configuration consisted of a "sandwich" or "stack" arrangement of heater, thin silver sheet (0.1 mm thick, 5 mm square), PMMA/SWCNT/PMMA+SWCNT sample, thin silver sheet, and thermistor, all held together by thin applications of GE varnish. Here, the two silver sheets do not directly contact each other. The sample area closely matches the dimensions of the heater attached to one silver sheet. A 120 Ω strain-gauge heater is attached to one side of the "stack" and a 1 MΩ carbon-flake thermistor to the other side by GE varnish. The sample was kept inside a thermal bath maintained at a controlled fixed temperature. By supplying an oscillating voltage to the heater, small temperature oscillations are induced in the sample+cell detected by the thermister. Scanning temperature is accomplished by changing the bath temperature. The resolution of the sample+cell and bath temperatures are in μK range.

Modulated (temperature) differential scanning calorimetry (MTDSC/MDSC) allows for simultaneous measurements of the heat flow and heat capacity. This is a more refined version of the conventional DSC method. MDSC differs from conventional DSC in that the sample is subjected to a more complex heating program, incorporating a sinusoidal temperature modulation onto an underlying linear heating ramp. Whereas DSC is only capable of measuring the total heat flow, MDSC can simultaneously determine the non-reversible (kinetic component) and the reversible (heat capacity component) heat flows. In this MDSC technique, the reversible heat capacity signal was determined automatically by integrating the total heat flow rates over time. A detailed description of the MDSC method can be found elsewhere [28, 29].

The MDSC experiment was performed using a Model Q200 MDSC from TA Instruments, Inc. Samples were heated for 15 min at 127 ^{0}C in vacuum to remove any trapped chloroform, prior to mounting in the MDSC, and subjected to underlying heating and cooling rates of 10, 5, 1, 0.5, and 0.1 K/min and a temperature modulation amplitude of 0.6 K with a period of 60 s. Dry ultra pure Nitrogen gas was purged through the sample holder in a rate of 50 ml/min during the experiment.

6.2.2 Preparation of PMMA+SWCNT Composites:

The polymer PMMA ($M_n = 120,000$ g mol^{-1}, obtained from Aldrich) was first dissolved in a dilute chloroform solution. The required amount of SWCNTs (*Helix Materials Solutions, TX*, purity > 90 %, ash ≈ 5 %) was also dispersed into a dilute chloroform solution and sonicated for 12 hr to separate the bundles of nanotubes into individual particles. Scanning electron micrographs of the SWCNT material used in this work, presented in a previous report [26], found the diameter to be 1.3 nm and the length varying from 0.5 to 50 μm. Both the PMMA+chloroform dilute solution and the SWCNT dispersed in chloroform solution were then mixed together and again kept $\approx$ 6 hr in an ultrasonic bath. After the PMMA+SWCNT+chloroform dilute solution was finally mixed with a touch mixer (Fisher Touch-Mixer model 12-810) for 10 mins, no detectable precipitation was observed. Immediately after this final mixing, the solution was drop cast onto a thin silver sheet to form a thin film of PMMA+SWCNT and placed for 6 hrs under vacuum to remove the chloroform. The typical thickness of the sample film is between 150 to 200 μm. The sample was then sandwiched between two thin silver sheets with GE varnish (General Electric #7031 varnish) and again dried under vacuum to remove any solvents from the varnish.

A description of the ACC sample+cell preparation used here have been previously reported [22, 26, 27]. All five PMMA+SWCNT and pure PMMA samples were prepared using this same method/conditions and used for both ACC and MDSC measurement.

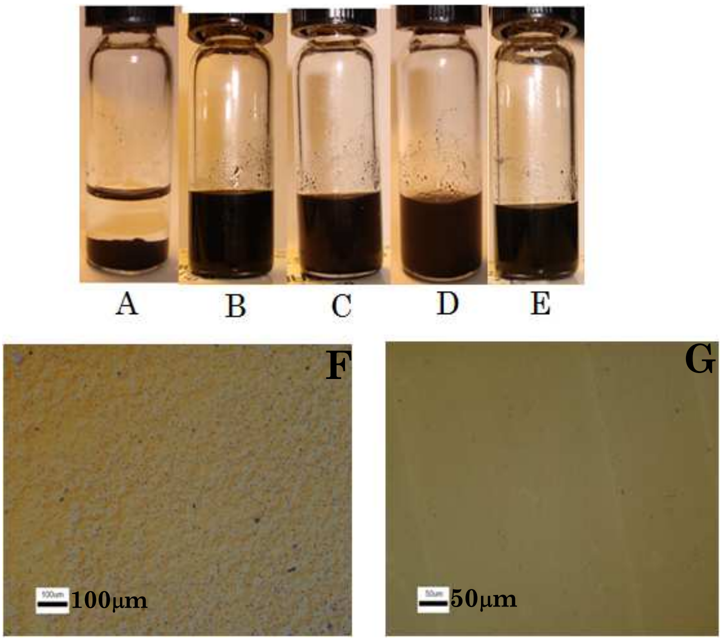

Figure 6.1: A: Mixture of PMMA and SWCNTs composites before dispersion, B: just after dispersion, C: after one day of dispersion, D: after two days dispersion and E: after 5 days of dispersion. F: is the optical micrograph images shows poor quality of dispersion, which was taken without sufficient time of sonication and mixing with touch mixture, G: shows the good quality of dispersion of SWCNTs inside PMMA with sufficient time of dispersion and then with touch mixture.

The mass fraction of SWCNT in the composite samples ϕ_m was calculated from the mass of the carbon nanotubes and PMMA while the volume fraction of SWCNT ϕ_v was derived by taking the density of the PMMA polymer as $\rho_p = 1.2$ g/cm^3 and assuming the density of carbon nanotubes as $\rho_f = 1.4$ g/cm^3:

$$\phi_m = \frac{M_f}{M_T} = \frac{M_f}{M_f + M_p} \tag{6.2}$$

$$\phi_v = \frac{V_f}{V_T} = \frac{\rho_p M_f}{\rho_f M_p + \rho_p M_f} \tag{6.3}$$

where M_f is the mass of filler (SWCNTs) and M_p is the mass of polymer (PMMA).

All samples have essentially the same thickness and cross-sectional areas. Thus, the thermal contact resistance of all samples are approximately same and should not play a role in comparing results as a function of SWCNT content. For the MDSC measurements, the samples were sealed inside a standard hermite pan. The mass of the sample pan and reference pan was very close to each other to minimize the uncertainty of measurement.

Table 6.1: Specific heat and thermal conductivity results at 300 K and 399 K for pure PMMA and PMMA+SWCNT samples determined by ACC. An effective scan rate of 0.04 K min^{-1} was used with C_p given in J g^{-1} K^{-1} and κ in W m^{-1} K^{-1}.

wt%	vol%	C_p^{300}	C_p^{399}	κ_{300}	κ_{399}
PMMA	0.00	1.61	2.31	0.172	0.245
1.40	1.27	1.68	2.35	0.192	0.267
1.98	1.79	1.68	2.37	0.202	0.285
4.46	3.90	1.69	2.45	0.275	0.398
6.00	5.20	1.69	2.46	0.330	0.481
9.33	7.93	1.70	2.47	0.395	0.555

The mass of the pan used was 50.4 ± 0.4 mg with the mass difference between sample and reference pans between 0.3 to 0.5 mg. After casting the required amount of sample, the remaining solution of PMMA+SWCNT+choloform was stored in a tightly capped bottle. No significant segregation occurred over several days indicating the quality of the dispersions.

6.3 Results and Discussion

6.3.1 Specific heat of PMMA+SWCNT composites

Figure 6.2 (top panel) presents ACC determined specific heat of pure PMMA and five PMMA+SWCNT samples ranging from $\phi_m = 0.014$ to 0.086 mass fraction of SWCNTs.

The specific heat of all samples exhibit a similar temperature dependence from ≈ 300 to 400 K with only a small change in its absolute value. Since ϕ_m is small, C_p is not expected to vary substantially and so these results more reflect the reproducibility of the absolute value of C_p measurements by the ACC technique. The experimental C_p value for pure PMMA is found to be 1.61 J g^{-1} K^{-1}, about 10 % above the literature value [14, 16] and within 18 % at 307 K of the value reported by Assael et.al [15]. Specific heat values of pure PMMA and PMMA+SWCNT composites at 300 K (glass state) and 399 K (liquid state) are given in Table 6.1. The C_p values of PMMA+SWCNT composites vary slightly from pure PMMA at room temperature and in a manner similar to that reported for composites of nanotubes dispersed in polystyrene [18]. The variation of C_p values between PMMA and PMMA+SWCNT composites is likely due to experimental uncertainty, especially in the mass measurements of the sample+cell components.

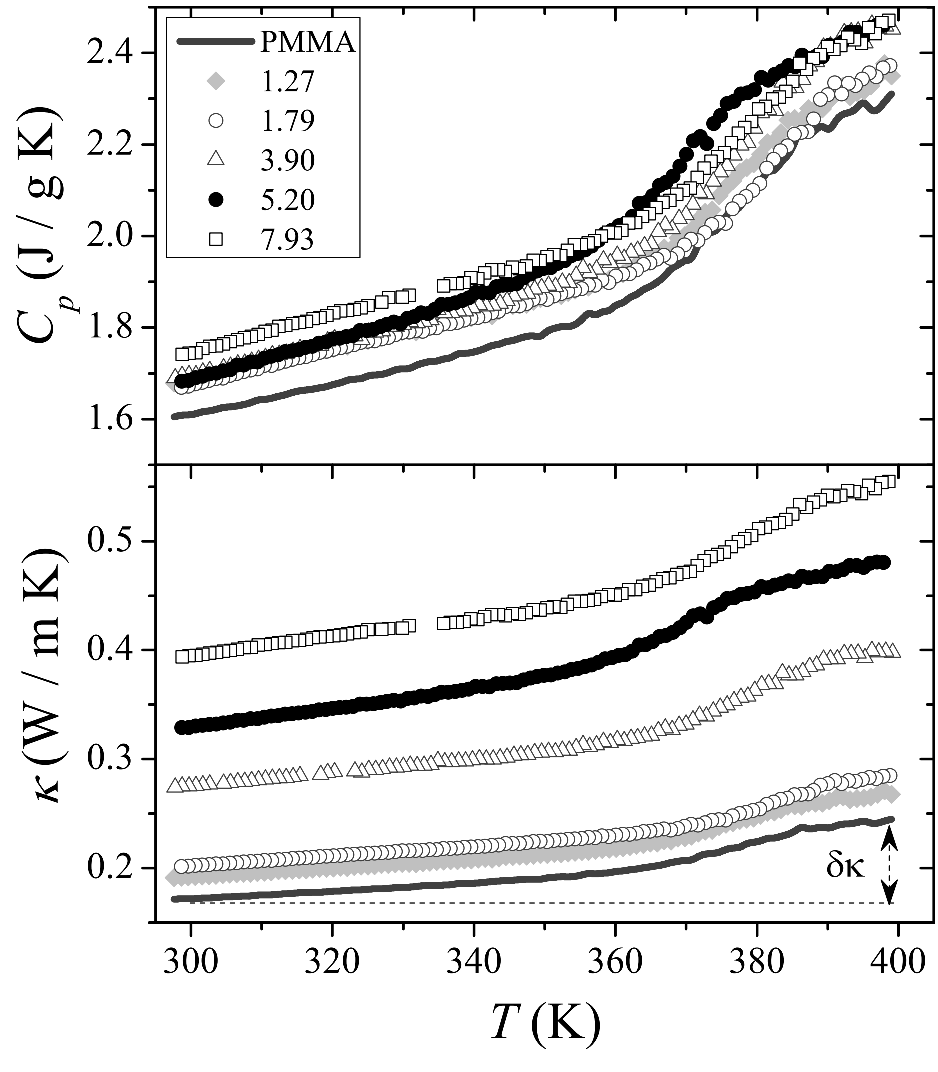

Figure 6.2: The effective specific heat (top panel) and thermal conductivity (bottom panel) of pure PMMA and five PMMA+SWCNTs composite samples from 300 to 400 K. See legend. In lower panel, the definition of the effective thermal conductivity increase between the glass and liquid state $\delta\kappa$ is presented.

TABLE 6.2: Glass transition temperatures T_g, the inflection point of the C_p step, in Kelvin and enthalpy hysteresis ΔH_{hyst}, difference in ΔH between heating and cooling, in J g^{-1} determined by ACC at 0.04 K min^{-1} and by MDSC extrapolated to zero-scan rate (T_g^0) for pure PMMA and PMMA+SWCNT samples.

wt%	vol%	T_g^0(MDSC)	T_g(AC)	ΔH_{hyst}(MDSC)	ΔH_{hyst}(AC)
PMMA	0.00	351.4	375.8	0.121	0.028
1.40	1.27	356.6	376.0	0.055	0.028
4.03	3.58	362.1	378.0	0.060	0.10
7.46	6.45	369.2	371.0	0.065	....

The effective glass transition temperature T_g measured by ACC, taken as the inflection point of the C_p rise, is scattered and tabulated in Table 7.1.

It should be noted that glassy relaxations are highly temperature scan rate and thermal history dependent. Here, the ACC measurements were done with an extensive heat treatment as compared to the MDSC experiments and is likely the cause for the fluctuating T_g observations by ACC. For the ACC experiments, all samples were kept for 4 hrs at 400 K to maintain thermal equilibrium before taking the first temperature scan. For the MDSC experiments, the samples were heated to ≈ 100 K for only 15 min in vacuum to remove any trapped solvent. The effect of heat treatment and the MDSC results are presented in Section III.D.

6.3.2 Thermal Conductivity of PMMA+SWCNT Composites

Figure 6.2 (lower panel) presents the effective thermal conductivity κ using ACC of pure PMMA and PMMA+SWCNT samples from $\phi_m = 0.014$ to 0.083. The effective thermal conductivity was derived from the heat capacity measurements and frequency scans performed at regular temperature intervals, the details of the experimental derivation of κ can be found elsewhere [22, 26, 27]. The effective κ for pure PMMA was found to be 0.172 W m^{-1} K^{-1} at 300 K and increases with temperature revealing a step-like feature near and about the glass transition. The absolute value of the derived κ is within 14 % at 307 K and 9 % at 352 K of the literature value for pure PMMA [15].

As shown in Fig. 6.2, κ monotonically increases with increasing SWCNT content for all PMMA+SWCNT samples, exhibiting similar temperature dependencies as pure PMMA. The percent increase of κ from pure PMMA is 60 % with increasing $\phi_m = 0.043$, nearly 90 % for $\phi_m = 0.057$, and 130 % for the $\phi_m = 0.083$ PMMA+SWCNT samples. This observed increase of κ with increasing SWCNT content is consistent with the dispersed CNTs forming an ever denser random network within the host polymer. At low ϕ_m, the SWCNTs are more-or-less individual strands surrounded by the polymer medium of high thermal resistance. As ϕ_m increases, contact among SWCNTs increases, via mainly through van der Waals interactions, eventually forming a percolated thermal path across the polymer host. Previous studies found an enhancement of thermal conductivity of about 250 % for $\phi_m = 0.11$ SWCNTs in PMMA [30, 31]. Though consistent, the somewhat smaller increase in κ observed here may be due to (a) the quality/homogeneity of the nanotubes, (b) the quality of the SWCNT dispersion in the polymer, (c) the short average length of the nanotubes, and/or (d) the smaller diameter of the nanotubes.

The effect of a homogeneous random dispersion can be crucial because once the nanotube concentration increases, the nanotubes tendency to bundle increases. Once bundles form, the thermal pathways through a network of SWCNT become 'jammed' resulting in a more modest increase in κ. The influence of the nanotube geometry, average length and diameter, on the thermal conductivity of the composite can also be large since these factors directly influence the packing fraction of SWCNT that in turn plays an important role in the enhancement of the thermal conductivity. Also, the diameter of the nanotube is important because, in general, the contact resistance decreases with increasing CNT diameter due to the larger contact area in addition to the increase in the number of contacts per unit volume [32]. The thermal boundary resistance between carbon nanotubes and polymer/liquid environment composites has been simulated and indicate large local temperature gradients as a function of distances from the nanotube long axis with constant radial heat flow [32, 33]. It was estimated that the temperature decreases 40 % just 20 ^0A away from the long axis of the nanotubes, in the polymer-liquid interface region. This particular simulation result suggests that large enhancement of κ in these composites would only be expected for samples with small mean-distance between CNTs, hence high ϕ_m.

Figure 6.3 (top panel) shows the percent increase of κ from pure PMMA, $\Delta\kappa = 100 \times (\kappa_{(f+p)} - \kappa_p)/\kappa_p$, at 300 K(glass state) and 399 K (liquid state). Figure 6.3 (bottom panel) shows the change in thermal conductivity between glass and liquid states, $\delta\kappa = \kappa_l - \kappa_g$, with the arrow indicating $\delta\kappa$ for pure PMMA. Both log-log plots in Fig. 6.3 indicate an increasing κ from pure polymer and between glass and liquid states with increasing SWCNT ϕ_m where $\delta\kappa$ reveals a broad step-like increase. It should be noted

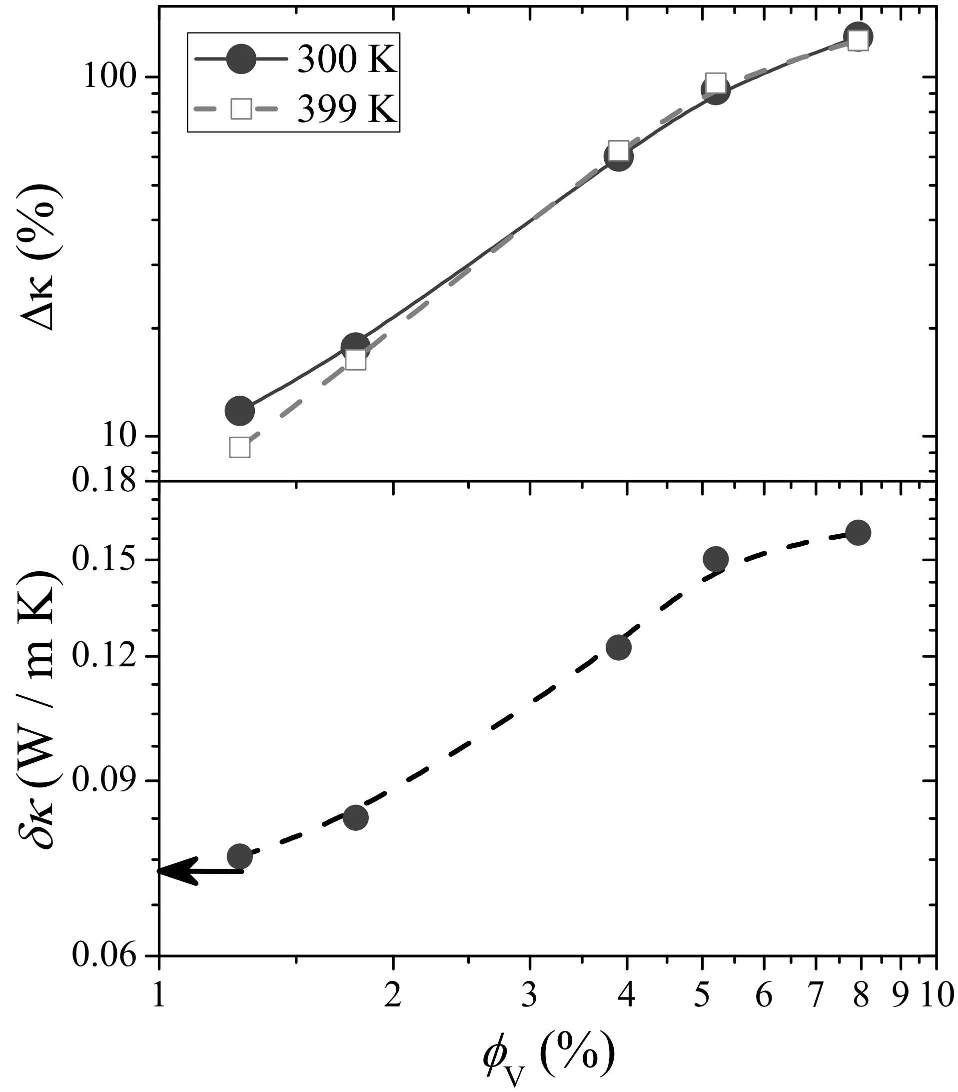

Figure 6.3: Log-log plot of the percent enhancement of the thermal conductivity, $\Delta\kappa$ from pure PMMA (top panel) and the change in thermal conductivity $\delta\kappa$ (bottom panel) of PMMA+SWCNT composites between the glass (300 K) and liquid states (399 K), as a function of SWCNT mass fraction ϕ_m. Arrow indicates the $\delta\kappa$ for pure PMMA.

that the thermal conductivity in the glass state is largely dependent on the vibrational modes and in the liquid state is dominated by translational motion of the molecules. This suggests that the phonon propagation is much stronger through nanotubes in the liquid state than in the glass state for these composites.

6.3.3 Composite Thermal Conductivity Models

There have been many theoretical models reported in the literature for polymer nanocomposites, nanofluids, and carbon nanotubes or nanofibers in oil systems. Among the most relevant models are Lewis/Nielsen [19], Hamilton/Crosser [20], Geometrical [17], and Xue [21] models. Each are described below and compared to the observed κ for the PMMA+SWCNT samples.

The Lewis/Nielsen model was initially proposed to estimate electrical and thermal conductivities for a two-component system [19]. Since the thermal conductivity of the filler (nanotubes) is much higher than that of the polymer, the shape and size of the filler becomes significant. The Lewis/Nielsen model considered the shape of the dispersed particle (their anisotropic character) and the particle packing. It has since been shown that the nanoparticle shape and dimensions play an important role [34, 35]. The Lewis/Nielsen model for the effective κ of a two-component system is given by

$$\frac{\kappa_c}{\kappa_p} = \frac{1 + AB\phi_v}{1 - B\psi\phi_v} \tag{6.4}$$

where $\psi = 1 + \left(\frac{1-\rho}{\rho^2}\right)\phi_v$, and κ_c, κ_p, and κ_f are the thermal conductivities of the $c$omposite (PMMA+SWCNTs), $p$olymer (PMMA), and $f$iller (SWCNTs), respectively. The parameter $A = K - 1$ depends primarily upon the shape of the dispersed particles and how they are oriented with respect to the direction of thermal or electric current, aspect ratio, and is related to the generalized Einstein coefficients K_E. The parameter $B = (\kappa_f/\kappa_p - 1)/(\kappa_f/\kappa_p + A)$ describes the relative conductivity of the two components. The parameter ψ is determined by the maximum packing fraction ρ. In the original Nielsen model [19], ρ for a randomly oriented rod-like filler is $\rho = 0.52$ irrespective of the filler's aspect ratio. This is a reasonable result for fillers with relatively small aspects ratio (< 10). However, nanotubes have much larger aspect ratios. An experimental study of the packing fraction on aspect ratio was conducted by J. V. Millewski [36] that

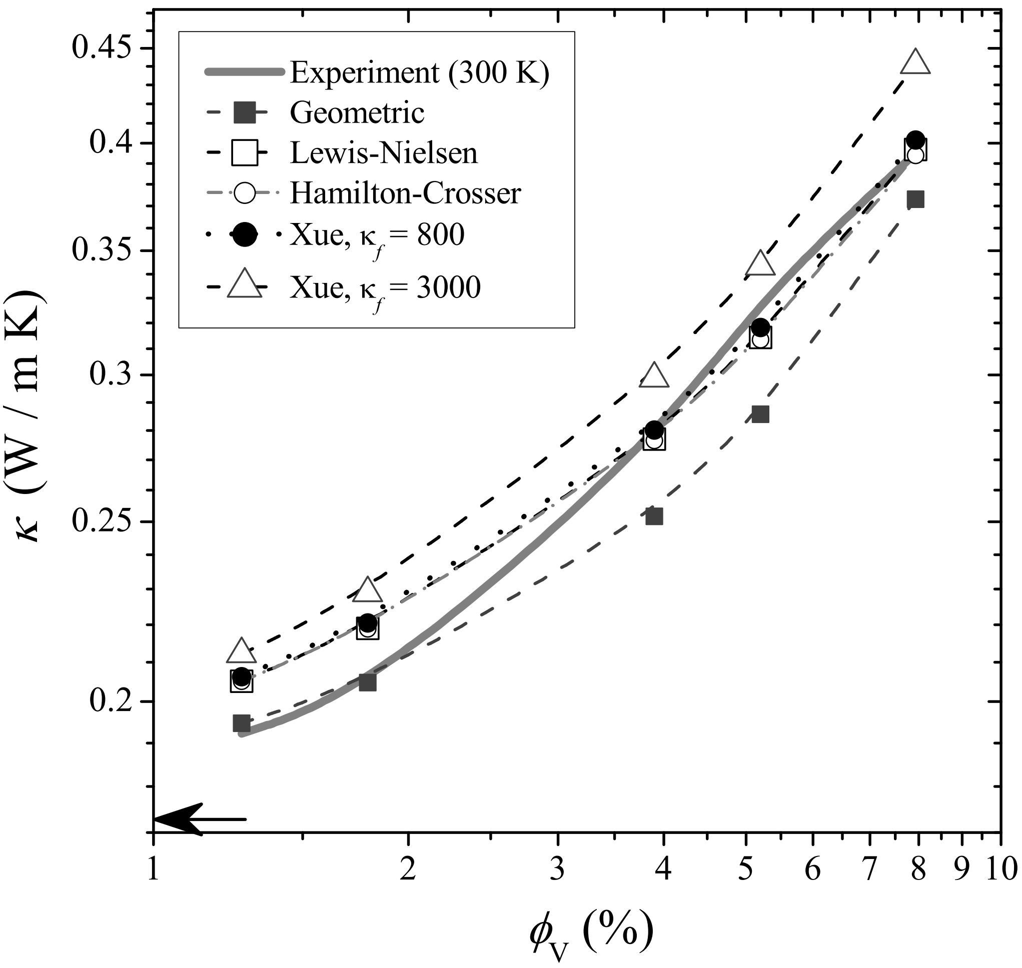

FIGURE 6.4: Log-log plot of the measured effective thermal conductivity of PMMA and PMMA+SWCNT composites for different vol% SWCNTs at 300 K compared to the various theoretical models of Lewis/Nielsen, Hamilton/Crosser, Geometric(series), and Xue as listed in the legend. See text for details. The arrow indicates the thermal conductivity of pure PMMA as measured in this work.

yielded a relationship between the maximum packing fraction and the aspects ratio of the filler, which was used for our estimate of ρ. The Lewis/Nielsen model can then be simplified as

$$\kappa_c(\phi_v) = \kappa_p \left\{ \frac{\kappa_f + A\kappa_p - A\phi_v(\kappa_p - \kappa_f)}{\kappa_f + A\kappa_p + \phi_v\psi(\kappa_p - \kappa_f)} \right\}. \tag{6.5}$$

by substituting for the parameter B explicitly.

The Hamilton/Crosser model [20] accounts for the particle shape in determining the thermal conductivity of composite materials differently. The Hamilton/Crosser model for the effective κ_c of a composite two-component system is given by

$$\kappa_c(\phi_v) = \kappa_p \left\{ \frac{\kappa_f + (n-1)\kappa_p - (n-1)\phi_v(\kappa_p - \kappa_f)}{\kappa_f + (n-1)\kappa_p + \phi_v(\kappa_p - \kappa_f)} \right\} \tag{6.6}$$

where n is the shape factor of the dispersed filler particles. The shape factor is calculated as $n = 3/\chi$ where χ is the sphericity defined as the surface area of a sphere having the same volume as the dispersed filler particle to the surface area of the particle [21, 37]. The models given by Eqs. (6.5) and (6.6) are very similar since the Hamilton/Crosser model follows the same approach as Lewis/Nielson but assumes the maximum packing fraction $\rho = 1$ and $\psi = 1$.

The Geometric model [17] estimates the effective thermal conductivity of these polymer nano-composite systems based on assuming various thermal paths or circuits through the composite medium. Here, κ_c is given by

$$\kappa_c = \kappa_f^{\phi_v} \kappa_p^{(1-\phi_v)} \tag{6.7}$$

but to estimate this value, a specific thermal circuit must be assumed. The two simplest thermal circuits composed of polymer and filler are series and parallel. For a series arrangement of fillers and polymers, κ_c is given by

$$\kappa_c(\phi_v) = (1 - \phi_v)\kappa_p + \phi_v \kappa_f. \tag{6.8}$$

For a parallel arrangement of the heat flow, κ_c is given by

$$\frac{1}{\kappa_c} = \frac{1-\phi_v}{\kappa_p} + \frac{\phi_v}{\kappa_f}. \tag{6.9}$$

Each of these thermal path assumptions are used to compare with the observed κ.

The Xue model [21] takes into account the nature of carbon nanotubes in the composite. The Xue model has shown good agreement with experimental results on oil+CNT composites. The Xue model for the effective κ_c is given by

$$\kappa_c(\phi_v) = \kappa_p \left\{ \frac{1 - \phi_v + 2\phi_v \left(\frac{\kappa_f}{\kappa_f - \kappa_p}\right) ln \left(\frac{\kappa_f + \kappa_p}{2\kappa_p}\right)}{1 - \phi_v + 2\phi_v \left(\frac{\kappa_p}{\kappa_f - \kappa_p}\right) ln \left(\frac{\kappa_f + \kappa_p}{2\kappa_p}\right)} \right\} \tag{6.10}$$

where two different thermal conductivity values of the carbon nanotubes, $\kappa_f = 800$ and 3000 W m^{-1} K^{-1}, are used for comparison in this work.

Figure 6.4 shows the experimental and the best theoretical fit of the Lewis/Nielsen, Hamilton/Crosser, Geometric, and Xue models of κ_c in the glass state (300 K) for the PMMA+SWCNT samples. The aspect ratio of 15 and maximum packing fraction $\rho = 0.6$ was used for the Lewis/Nielsen model. This aspect ratio is small compared to that expected for a single nanotube, and likely due to aggregation of many nanotubes forming bundles. Guthy et.al, [30] reported an aspect ratio as 26 for a bundle of SWCNTs consisting $\sim$ 92 nanotubes of 1.3 nm diameter each. However the aspect ratio depends upon the quality of the dispersion of nanotubes inside polymers matrix. Typically, as the nanotubes aggregate their aspect ratio should decrease. The thermal conductivity of the SWCNT filler was assumed to be $\kappa_f = 3000$ W m^{-1} K^{-1} for the models used here. However, the Xue model gave better agreement to the experimental results using a lower value of $\kappa_f = 800$ W m^{-1} K^{-1}.

The Geometric model using a series thermal path assumption agrees well with the observed κ for low SWCNT volume fraction (pure PMMA to $\phi_m \approx 0.034$). However, this model strongly deviates from the measured values for larger mass fraction while the parallel thermal path assumption underestimates κ over the whole range of ϕ_m. Recall that the Geometric model depends only on the amount of fillers and does not account for the geometry or size of the filler particles, which is apparently a valid assumption for low SWCNT volume fraction. For SWCNTs, $\phi_m > 0.034$, the Lewis/Nielsen and Hamilton/Crosser models are both equally consistent with measurements and indicate the need to take into account details of the particle size and filler packing within the polymer. These results essentially indicate that the onset of significant SWCNT interactions, perhaps resulting in a spanning thermal path across the sample, occurs near $\phi_m \approx 0.034$ for PMMA+SWCNT composites.

6.3.4 MDSC Study of PMMA+SWCNT Composites

Because the nanofiller of SWCNT can influence the structural relaxations for glass forming materials like PMMA, dynamics play an important role. For dynamic thermal measurements, the control parameter is the temperature scan rate. Fig. 6.5 shows the reversible heat capacity, RevΔC_p as measured by MDSC normalized to the value deep in the liquid state (at 405 K) of pure PMMA (left panels) and $\phi_m = 0.070$ PMMA+SWCNT composite sample (right panels) for scan rates of 10, 5, 1, 0.5, and 0.1 K/min.

Here, the heating scan at the indicated rate was immediately followed by the cooling scan. For pure PMMA, a progressively larger hysteresis between heating and cooling

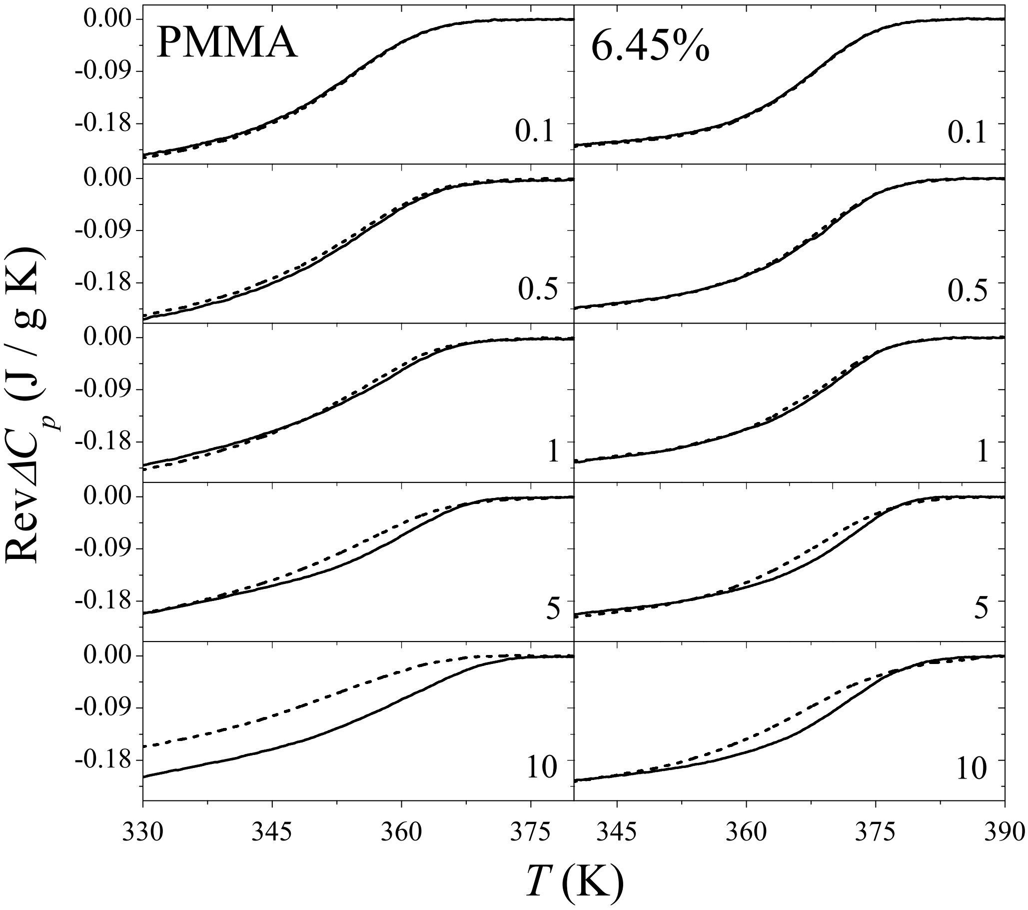

FIGURE 6.5: Difference of the reversible specific heat, RevΔC_p from the high-temperature liquid state dependence for pure PMMA (left panels) and $\phi_m = 0.070$ composite (right panels) for scan rates from 0.1 (top) to 10 K/min (bottom) on heating (solid line) and cooling (dashed line).

is seen as the scan rates increase to 10 K/min. For the $\phi_m = 0.070$ PMMA+SWCNT sample, very little hysteresis, except in the temperature region near and about the glass transition, is seen for even the highest scan rate. Similar results were seen for the other PMMA+SWCNT samples. The suppression of hysteresis in the composites suggests the partial quenching of structural relaxations of PMMA by the nanotubes. The difference in enthalpy between heating and cooling $\Delta H_{hyst} = H_{cool} - H_{heat}$ extracted from Fig. 6.5 is shown in a log-log plot in Fig. 6.6. Although this plot minimizes the difference among the samples, it highlights the significant increase in hysteresis for scan rates higher than about 0.5 K/min.

Because of the scan rate dependent hysteresis, the glass transition temperature is determined from cooling scans shown in Fig. 6.7 and taken as the inflection point of the RevΔC_p step-like temperature dependence. The resulting values of T_g are shown in

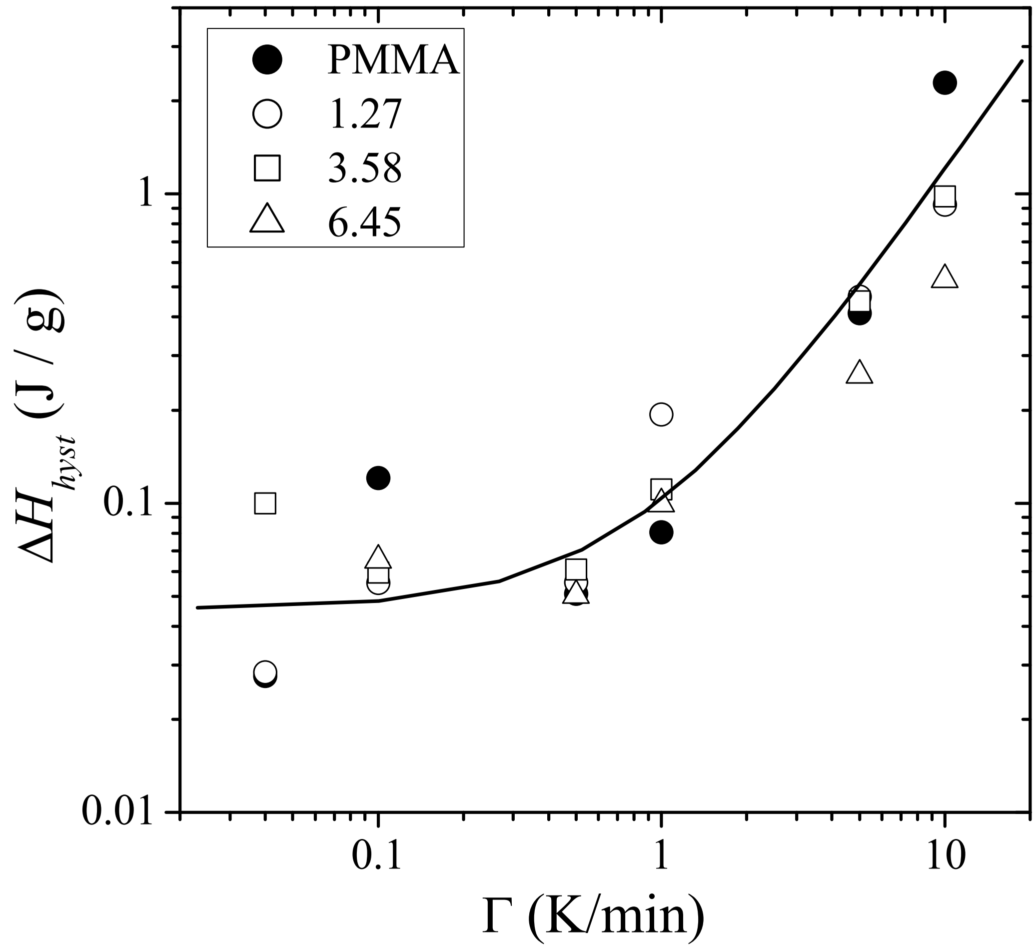

FIGURE 6.6: Log-log plot of the hysteresis between RevΔC_p areas, ΔH_{hyst}, for heating and cooling runs taken by integrating the data in Fig. 6.5 from 300 to 400 K for pure PMMA and PMMA+SWCNT samples. See legend.

Fig. 6.8 as a function of scan rate for pure PMMA and three composite samples. When T_g is extrapolated to zero scan rate, the resulting glass transition temperature T_g^0 is shown in the inset of Fig. 6.8 as a function of ϕ_m revealing a nearly linear increase.

All MDSC measurements employed identical sample treatments and history. However, heat treatment or annealing can significantly alter the behavior of polymer composites. The MDSC experiments utilized a protocol where the samples were heated into the liquid state for 15 min prior loading but the ACC experiments annealed the samples at 400 K for 3 – 4 hr before collecting data.

To explore the effect of heat treatment, MDSC scans were performed on pure PMMA and the $\phi_m = 0.014$ PMMA+SWCNT sample after heating into the liquid state (400 K) for 15, 30, 45, and 60 min prior to a cooling scan at 1 K/min. The resulting RevΔC_p for pure PMMA (top panel) and the $\phi_m = 0.014$ sample (bottom panel) are shown in

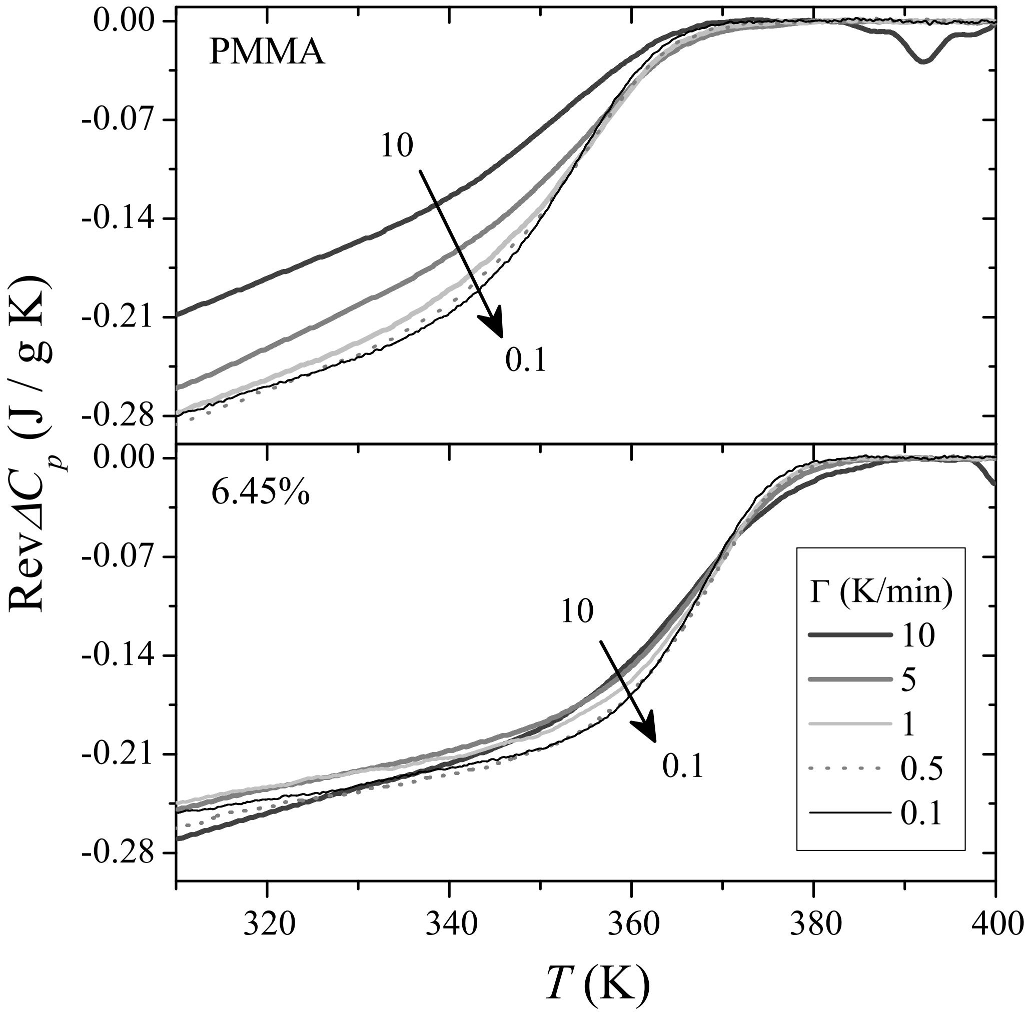

FIGURE 6.7: The RevΔC_p of cooling scans for pure PMMA (top panel) and $\phi_m = 0.070$ composite (bottom panel) for scan rates from 0.1 to 10 K/min. The arrow indicates order of scan rate commensurate with the inset legend.

Fig. 6.9. Heat treatment of pure PMMA shifts T_g towards higher temperature and tends to sharpen the step-like behavior in RevΔC_p. The introduction of SWCNT appears not to affect both trends, consistent with that observed in the thermal hysteresis results.

6.4 Summary

This work presents a detailed calorimetric study of the specific heat and effective thermal conductivity of a macroscopic arrangement of randomly dispersed SWCNTs inside a polymer host. Using ACC and MDSC techniques, the enhancement of the effective thermal conductivity is significant with increased loading of SWCNTs. Higher thermal conductivity of polymer+CNT composites can be achieved by using suitable dispersion

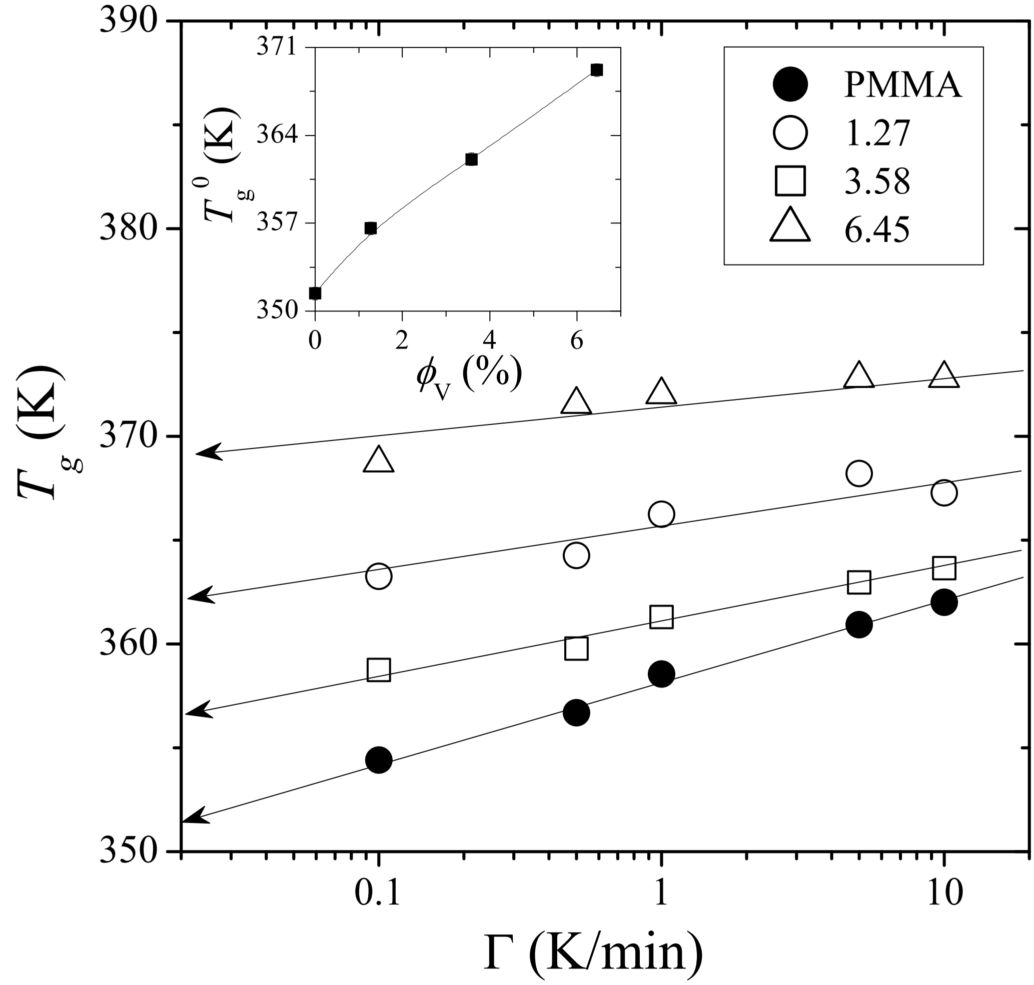

Figure 6.8: Semi-log plot of the glass transition temperature, T_g, as a function of scan rate for pure PMMA and three PMMA+SWCNT samples. See legend. Inset shows the glass transition temperature extrapolated to zero-scan rate, T_g^0, as a function of SWCNT mass fraction ϕ_m.

methods and higher quality nanofiller materials. The glass transition characteristics, thermal conductivity, electrical conductivity, and mechanical properties of polymer composites can be controlled by adjusting the properties of the nanofillers. The increase in κ with increasing ϕ_m of SWCNT is consistent with essentially independent particles for low concentration that is describable by a simple Geometric model. For SWCNT higher than $\phi_m \sim 0.034$, a model that takes into account the packing fraction as well as nanoparticle shape is needed and indicates the onset of interactions among SWCNT, suggesting the presence of a spanning network. The increase in the zero-scan rate glass transition temperature and suppression of the enthalpic hysteresis supports the view that the random inclusions of SWCNT in PMMA quenches structural relaxations and stabilizes the glass state. Continued experimental study, specifically by rheological techniques, is required

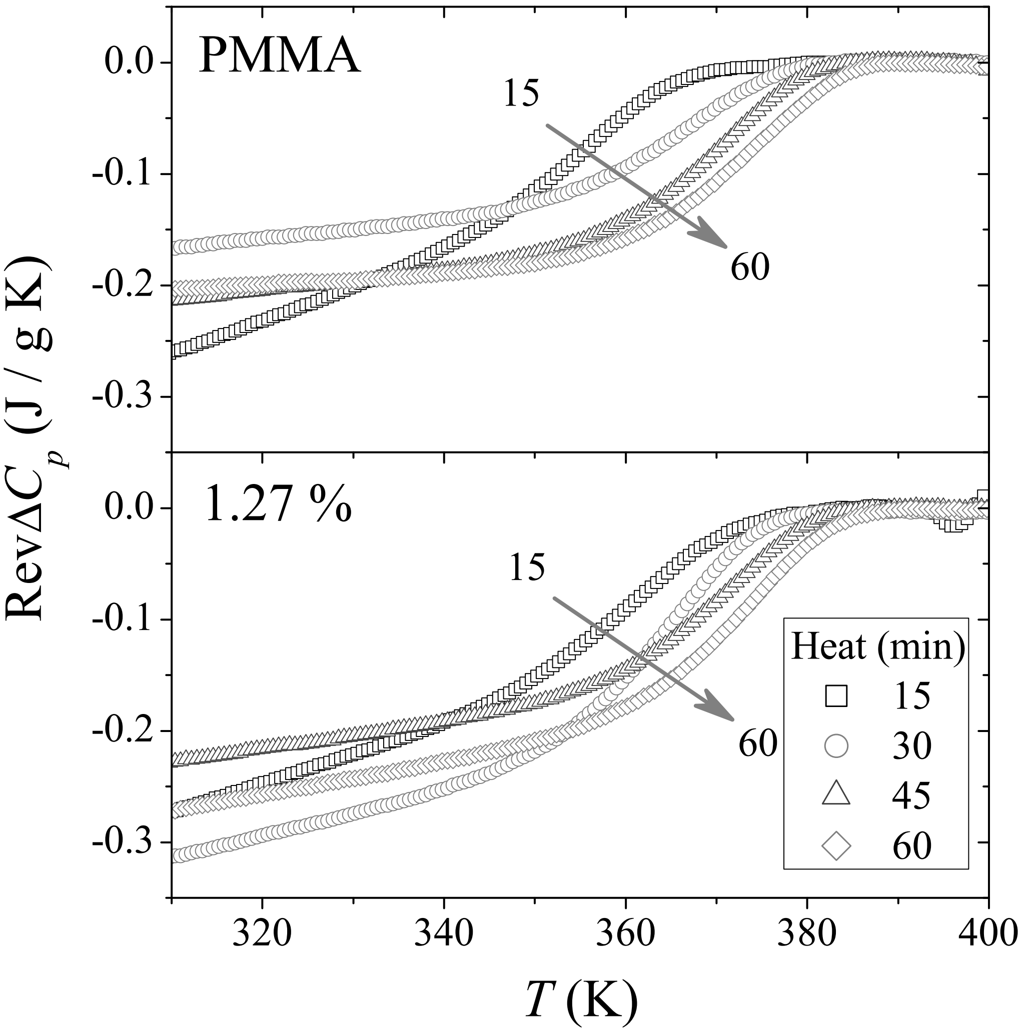

FIGURE 6.9: Aging effect on the RevΔC_p cooling scans (1 K/min) of freshly mounted pure PMMA (top panel) and $\phi_m = 0.014$ composite sample (bottom panel) after annealing for 15, 30, 45, and 60 min at 400 K. See legend for data labels.

for these types of complex composite systems as well as a more comprehensive modeling to properly understand and calibrate/engineer the macroscopic properties.

Bibliography

[1] S. J. Tans, M. H. Devoret, H. Dai, A. Theses and R. E. Smalley, *Nature.*, **386,** 474 (1997).

[2] H. Dai, J. H. Hafner, A. G. Rinzler, D. T. Colbert, and R. E. Smalley, *Nature.*, **384,** 147 (1996).

[3] S. J. Sander, J. Tans, A. R. M. Verschueren, and C. Dekker, *Nature.*, **393,** 49 (1999).

[4] Ijima Sumio, Helical microtubules of graphitic carbon,*Nature.*, **354,** 8, No.56 (1991).

[5] S. Glushanin, V. Y. Topolov, and A. V. Krivoruchko, *Materials Chemistry and Physics.*, **97,** 357 (2006).

[6] P. Hine, V. Broome, and I. Ward, *Polymer.*, **46,** 10935 (2005).

[7] N. Cioffi, L. Torsi, N. Ditaranto, G. Tantillo, L. Ghibelli, L. Sabbatini, T. Bleve-Zacheo, M. D. Alessio, P. G. Zambonin, and E. Traversa, *Chemistry of Materials.*, **317,** 5255 (2005).

[8] A. Pelaiz-Barranco and P. Marin-Franch, *J. Appl. Phys.*, **97,** 034104 (2005).

[9] A. Bar-Cohen, A. Watwe, and K. N. Seetharamu, Fundamentals of Thermal Management in Fundamentals of Microsystems Packaging, Chapter 6, Ed., R.R. Tummala, McGraw Hill, New York (2001).

[10] B. Wunderlich, Thermal Analysis of Polymeric Materials. Springer-Velag: *Berlin, Heidelberg*, (2005).

[11] B. Wunderlich, Thermal analysis. New York: *Academic Press.*, **135,** 205 (1990).

[12] M. Meyyappan, Carbon nanotubes science and applications, CRC Press: Boca Raton, FL (2005).

[13] P. J. F. Harris, Carbon nanotubes and related structures new materials for the twenty-first century;Cambridge University Press: Cambridge (2001).

[14] *www.pageout.net/user/www/l/y/lyee/specificheat.pdf.*

[15] M. J. Assael, S. Botsios, K. Gialou and N. Metaxa,*International Journal of Thermophysics*,**26,** ,1995 (2005).

[16] C. Rauwendal,*Polymer Extrusion*,PUBLISHER - Hanser**Munich, GDR** (1986).

[17] S. Agarwal, M. Mashud, K. Khan, and R. K. Gupta, *Polymer Eng and Science.*, **129,** 1 (2008).

[18] Y. Yang, M. C. Gupta, J. N. Zalameda and W. P. Winfree, *Micro and Nano Letters*, **3,** No.2, 35-40 (2008).

[19] L. E. Nielsen, *Ind. Eng. Chem. Fundam.*, **13,** 17 (1974).

[20] R. L. Hamilton and O. K. Crosser, *Ind. Eng. Chem. Fundamen.*, **1,** 187 (1962).

[21] Q. Z. Xue, 368, 302 (2005).,*Physica B.*, **368,** 302 (2005).

[22] N. R. Pradhan, H. Duan, J. Liang, and G. S. Iannacchione, Vol-I, 159 (2008).,*Proceedings: Materials Processing and Properties TMS.*, **Vol-I,** 159 (2008).

[23] S. Sinha, S. Barjami, G. Iannacchione, A. Schwab, and G. Muench, *J. Nanopart. Res.*, **7,** 651 (2005).

[24] P. S. Clegg, C. Stock, R. J. Birgeneau, C. W. Garland, A. Roshi, and G. S. Iannacchione, *Phys. Rev. E.*, **67,** 021703 (2003).

[25] A. Roshi, G. S. Iannacchione, P. S. Clegg, and R. J. Birgeneau, *Phys. Rev. E.*, **69,** 031703 (2004).

[26] N. R. Pradhan, D. Huanan, J. Liang, and G. S. Iannacchione, *Nanotechnology.*, **19,** 485712 (2008).

[27] N. R. Pradhan, H. Duan, J. Liang, and G. S. Iannacchione, *Nanotechnology.*, **20,** 245705 (2009).

[28] N. J. Coleman and D. Q. M. Craig, *International Journal of Pharaceutics.*, **135,** 13 (1996).

[29] Y. Jin, J. Bonilla, Y-G. Lin, J. Morgan, L. McCracken and J Carnahan, *Journal of Thermal Analysis and Calorimetry*, **46,** No.3-4, 1047-1059 (2005).

[30] C. Guthy, F. Gu, S. Brand, K. I. Winey, and J. E. Fischer, *Transaction of the ASME.*, **129,** 1097 (2007).

[31] C. Guthy, F. Du, S. Brand, K. I. Wieny, and J. E. Fischer,*J. Heat Transfer.*, **129,** 1096 (2007).

[32] H. Zhong and J. R. Lukes, *Phys. Rev. B.*, **74,** 125403 (2006).

[33] S. Shenogin, L. Xue, R. Oziski, P. Keblinski, and D. G. Cahill, *J. Appl. Phys.*, **95,** 8136 (2004).

[34] C. W. Nan and R. Birringer, 81, 6692 (1997)., *J. Appl. Phys.*, **81,** 6692 (1997).

[35] P. H. Hasselman, *J. Composites Materials.*, **21,** 508 (1987).

[36] J. V. Millewski, *Ind. Eng. Chem. Prod. Res. Dev.*, **17,** No.4, 363 (1978).

[37] I. Tavman, A. Turgut, M. Chirtoc, H. P. Schuchmann and S. Tavman, *Archives of Materials Science and Engineering*, **34,** 99-104 (2008).

Chapter 7

RELAXATION DYNAMICS OF THE GLASS TRANSITION IN PMMA+SWCNT COMPOSITES BY TEMPERATURE MODULATED DSC

7.1 Introduction

Recently the modulated differential scanning calorimetry (MDSC) [1–3] study has been widely used to investigate the dynamics of glass transitions of polymer composites and related materials. In MDSC analysis, the sample is decomposed into reversing and non-reversing signals, is widely used and appears to avoid the uncertain meaning of dynamic thermal analyses in analogy to, e.g., dynamic mechanical or dielectric spectroscopies. In recent studies it has been commonly accepted to present the dynamic thermal properties in terms of the complex, real (storage), and imaginary (loss) heat capacities (C_p^*, $C_p^{'}$ and $C_p^{''}$). The concept of frequency-dependent specific heat $C_p^*(\omega,\mathrm{T})$ $(= C_p^*(\omega))$ was introduced and the first measurement performed in the 1980s [4–7] with an alternating current calorimeter technique. After that it has been widely used to study the dynamics of glass transition of different polymer systems. From a statistical point of view, $C_p^*(\omega)$

appears as a consequence of entropy fluctuations [8]. One advantage of the dynamic heat capacity in comparison to other techniques is the fact that $C_p^*(\omega)$ reflects the contribution of all modes, orientational and translational, providing global and direct information of the slow dynamics associated with the glass transition. Thus MDSC is a widely used technique to study the phase transition, glass transition and specific heat measurement of widely available polymeric systems. But the concept of frequency-dependent specific heat is not widely held. It is especially the case in the application fields of polymers, food sciences, pharmaceuticals etc. where it could be of most interest to characterize the molecular mobility.

Carbon nanotubes (CNTs) have outstanding electrical, mechanical, optical and thermal properties. These properties have significant promise in a vast range of applications such as quantum wires [9], tips for scanning probe microscope [10], and molecular diodes [11]. Polymers play a very important role in numerous fields of everyday life due to their advantages in lightness, ease of processing, resistance to corrosion, and low cost production. To improve the performance of polymers, composites of polymers and a filler have been extensively used and studied. The use of various nano-fillers such as metals, semiconductors, organic and inorganic particles and fibers, especially carbon structures [12–15], are of particular interest and the subject of intense investigation. The unique properties of carbon nanotubes; extremely high strength, lightweight, elasticity, high thermal and air stability, high electric and thermal conductivity, and high aspect ratio, offer crucial advantages over other nano-fillers.

The potential of using nanotubes as filler in polymer composite has not been fully realized because of processing difficulties. Structural relaxation is the process by which amorphous materials in the glassy state approach a state of thermodynamic equilibrium. Calorimetry, such as DSC, has revealed enthalpic relaxations occurring near the glass transition T_g in glassy polymers aged after a variety of heating treatments. It is well known that annealing or variation of heating and cooling rates leads to significant hysteresis in T_g because of these structural relaxations [16, 17]. The introduction of nano-fillers is expected to interact strongly with these short-range structural relaxations. However, the effective utilization of CNTs in polymer composite applications strongly depends upon the quality/uniformity of the nanotubes and the ability to disperse them homogeneously throughout the polymer host [18, 19]. Our previous work was to produce and investigate SWCNT-based nano-composite polymer materials as candidates for next generation of high-strength, light weight and enhanced thermal conducting materials [17]. The structural relaxation has been characterized for many polymers by Dielectric spectroscopy method, but this method is versatile and widely used to see the dynamics of the sample in high frequency, where it is found likely that the calorimetric results are on the extension of dielectric results. The calorimetric T_g includes total degree of freedom such as rotation, diffusion and vibration, while the dielectric T_g originates only from the reorientation of molecules.

The main objective of this report is to study the relaxation dynamics of the glass transition in PMMA+SWCNTs composites at very low frequencies using MDSC and presents a detailed frequency dependent MDSC technique. There are many studies that have been done to describe relaxation behavior, glass transition for pure polymer in frequency domain but so far no results reported in Carbon nanotube polymer composites. The PMMA+SWCNT composites were prepared by dispersing SWCNTs and PMMA in a chloroform solution using sonication then slowly evaporating the solvent leaving a homogeneous dispersion. The complex heat capacity was measured as a function of temperature and different frequency of temperature modulation from 0.0138 to 0.0826 s^{-1}. Then the real and imaginary parts of heat capacity were estimated with the phase between input heat flow and heating rate. In all samples, we observed the peak maximum in imaginary part of heat capacity. The effective glass transition temperature, T_g, activation energy and dynamics observed in real and imaginary part are dependent upon the applied modulated frequency of temperature oscillation. The measurement was reported in the region of glass transition of polymers and composites and other regions are not of interest in this study as the dynamics do not change with frequency.

Following this introduction, Section 7.2 describes some of the basic experimental procedures for the MDSC and sample preparation. Section 7.3 presents the experimental results and discussion followed by a general conclusion with future directions presented in Section 8.5.

7.2 Experimental

7.2.1 Modulated Differential-Scanning Calorimetry (MDSC):

Modulated (temperature) differential scanning calorimetry (MTDSC/MDSC) allows for simultaneous measurement of the evolution of both heat flow and heat capacity. MDSC differs from conventional DSC where the sample is subjected to a more complex heating program incorporating a sinusoidal temperature modulation accompanied by an underlying linear heating ramp. Whereas DSC is only capable of measuring the total heat flow, MDSC can simultaneously determine the non-reversible (kinetic component) and the reversible (heat capacity component) heat flows. A detailed description of the MDSC method can be found elsewhere [3, 20–25].

The MDSC experiment was performed using a Model $Q200$ from TA Instruments, USA. Prior to doing the experiment with our sample, temperature calibration was done with a sapphire disk, in the same condition of the measurements we have used for our sample studied. $Q200$ is an extension of heat flux type of a conventional DSC. The method to obtain complex specific heat has been proposed by Schawe based on the linear response theory [3, 21]. In general a temperature oscillation is described as:

$$T = T_0 + q_0 t + A_T sin(\omega t) \tag{7.1}$$

where T_0 is the initial temperature at time t = 0, T is the temperature at time t, q_0 is the underlying scan rate, A_T the temperature amplitude and ω (ω = 2πf) the angular frequency of the temperature modulation. f = 1/τ is the frequency in s^{-1} where τ was taken as period of modulation.

The results are plotted in the scale of frequency f instead of ω. The heating rate is given by:

$$q = \frac{dT}{dt} = q_0 + A_q cos(\omega t) \tag{7.2}$$

where A_q is the amplitude of the heating rate ($A_q = A_T\omega$). Since the applied heating rate in MDSC consists of two components: q_0 underlying heating rate and A_q cos(ωt) periodic heating rate, the measured heat flow also can be separated into two components, i.e, the response to the underlying heating rate and response to the periodic heating rate.

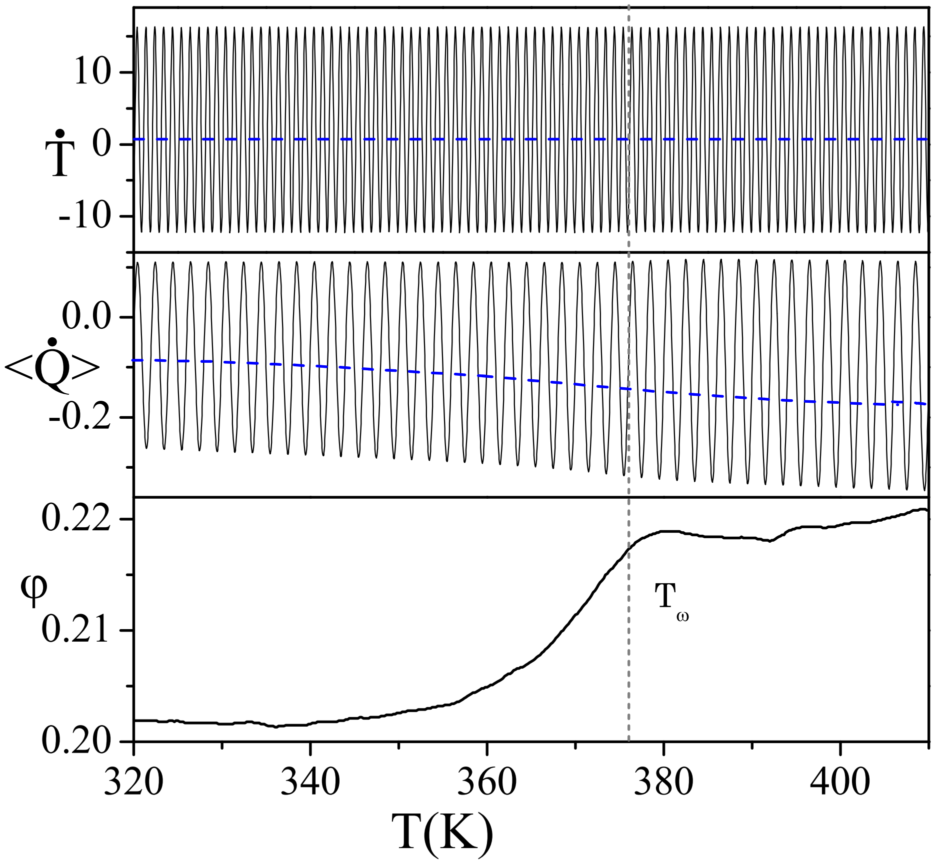

FIGURE 7.1: (Top): Modulated heat flow raw data and (Middle): modulated heat in PMMA+SWCNT composites. (Bottom) and their temporal average (Blue lines): Phase angle raw data, which allow the determination of the complex heat capacity (the phase lag ϕ is not corrected). The phase lag exhibits a peak at a temperature T_ω where the amplitude of the modulated heat flow $\dot{Q}$ strongly decreases.

The latter can be described by

$$HF_{period} = A_{HF} cos(\omega t - \phi) \tag{7.3}$$

where HF$_{period}$ is the heat flow response to the periodic heating rate, A_{HF} is the amplitude of the heat flow and ϕ is the phase angle between heat flow and heating rate. An absolute value of complex specific heat can be obtained by:

$$|C_p^*| = \frac{A_{HF}}{mA_q} \tag{7.4}$$

where m is the mass of a sample.

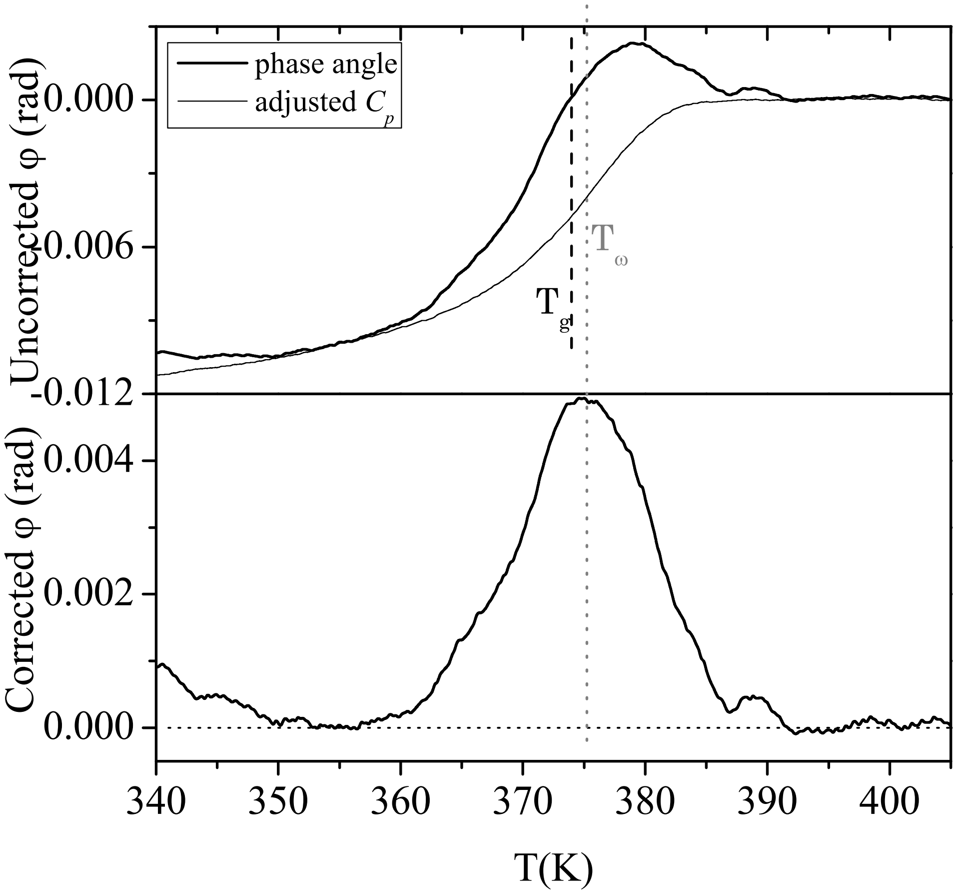

FIGURE 7.2: (Top): Uncorrected phase angle (thick line) with adjusted C_p (thin line) and (Bottom): Corrected phase angle. T_ω is not necessarily equal with the glass transition temperature T_g. his temperature T_ω is not equal with the calorimetric glass transition temperature T_g.

The data was analyzed with correcting the phase shift between heating rate and heat flow rate signal. The imaginary part of the complex heat capacity was calculated by correcting the phase angle. The detail correction procedure can be found elsewhere [26]. By the proper calibration for a raw phase angle, we can obtain real $C_p^{'}$ and imaginary $C_p^{''}$ parts by

$$C_p^{'} = \left|C_p^*\right| cos(\phi), \tag{7.5}$$

$$C_p^{''} = \left|C_p^*\right| sin(\phi) \tag{7.6}$$

Measured phase angle was corrected by using the reported method [26], then the real and imaginary part of the complex heat capacity was estimated.

Examples of the signals obtained on PMMA+SWCNTs in our experiment during the glass transformation range are shown in fig. 7.1. Figure 7.2 shows the how uncorrected phase angle (Top) has corrected (Bottom).

7.2.2 Preparation of PMMA+SWCNT Composites:

The required amount of polymer PMMA ($M_n = 120,000$ g mol^{-1}, obtained from Aldrich) and SWCNTs (Obtained from *Helix materials solution Texas*, purity > 90 %, ash 5 %) was first dissolved in chloroform, in a separate container. Then the SWCNT contained chloroform solution was sonicated for 8 hrs to separate the bundles of nanotubes into individual particles. Then both of the PMMA dissolved with chloroform and SWCNT dispersed with chloroform mixed together and again was kept 6 hrs in an ultrasonic bath. Scanning electron micrographs of the SWCNTs used in this work are given in a previous report [27]. After that the PMMA+SWCNT solution was finally mixed with touch mixer (Fisher Touch-Mixer model 12-810) for 10 mins. Optical micrograph studies have been done to clarify the good dispersion of SWCNTs inside host PMMA. The mass fraction was calculated with the following formula from the mass of the carbon nanotubes and PMMA. The volume fraction was derived by taking the density of PMMA as 1.2 g/cm^3 and assuming the density of carbon nanotubes as 1.4 g/cm^3:

$$\phi_m = \frac{M_f}{M_f + M_p} = \frac{M_f}{M_T} \tag{7.7}$$

$$\phi_v = \frac{\rho_p M_f}{\rho_f M_p + \rho_p M_f} \tag{7.8}$$

where, ϕ_m is the mass fraction, M_f is the mass of filler (SWCNTs), M_p is the mass of polymer (PMMA), ϕ_v is the volume fraction of SWCNTs, ρ_p is the density of PMMA and ρ_f is the density of filler (SWCNTs).

Due to high van der Wall attraction, carbon nanotubes get bundled together in high mass fraction, which prevent the dispersion quality of nanotubes inside polymer matrix. In our case, after casting the required amount of sample on a silver sheet, the remaining solution of PMMA+SWCNT+choloform was stored in a tightly capped bottle and no significant segregation occurred over several days indicating the quality of dispersions. For the MDSC measurements, the samples were sealed inside a standard hermetically sealed pan.

Before sealed in a hermite pan, each sample is heated for 15 min at 127 ^{0}C in vacuum to remove the trapped chloroform. The MDSC experiment was carried out with underlying heating and cooling rates of 2.0, 0.4 and 0.1 K/min with dry ultra pure Nitrogen gas with flow rate 50ml/min that was purged through the DSC cell. For accurate measurement of specific heat or to decrease the uncertainty, the reference and the sample hermite pan were chosen carefully. The mass of the pan used as (0.0504±0.0004)g, here the 0.0004 is the standard deviation of the pan for three different sample pans (three different mass fractions of PMMA+SWCNT) and a reference pan used for this study. The mass of the three samples taken in all the measurements are $\sim$ 10±0.2 mg. The temperature modulation amplitude was chosen to 1.2 K. We have studied three distinct samples, pure PMMA, and 0.014 and 0.080 mass fractions of SWCNTs dispersed with PMMA composites. Each sample was scanned with the above three different scan rates mentioned and with modulation frequency ranges from 1/160 to 1/30 s^{-1}.

7.3 Results and Discussion

Figure 7.3 shows the real (UP) and imaginary (Bottom) part of the complex specific heat capacity of 0.014 mass fraction SWCNTs inside PMMA matrix under heating (Left panel) and cooling (Right panel) rate at 0.4^0 K/min from 1/30 to 1/150 s^{-1} frequency of temperature modulation.

The real part of specific heat ($\Delta C_p^{'}$) was normalized to zero far above the glass transition, at 405 K and the imaginary part was also normalized by subtracting a base line. It is observed that the maximum rate of change of $C_p^{'}$ occurs in the region of glass transition and is dependent upon the applied frequency of temperature modulation. Similar change of $\Delta C_p^{'}$ observed during heating and cooling of real part of heat capacity. The change in magnitude of imaginary part of heat capacity $\Delta C_p^{''}$, shows different during heating and cooling with frequency of temperature modulation. This explains the difference of structural relaxation and the mobility of the sample during heating and cooling. There is no difference in the real part of specific heat observed in SWCNTs+PMMA composite samples during heating and cooling. The magnitude of $\Delta C_p^{'}$ between liquid and glass region i.e., $\Delta C_p^{(L-G)} = \Delta C_{p(405)}^{'}$ - $\Delta C_{p(340)}^{'}$ shows in Fig. 7.4.

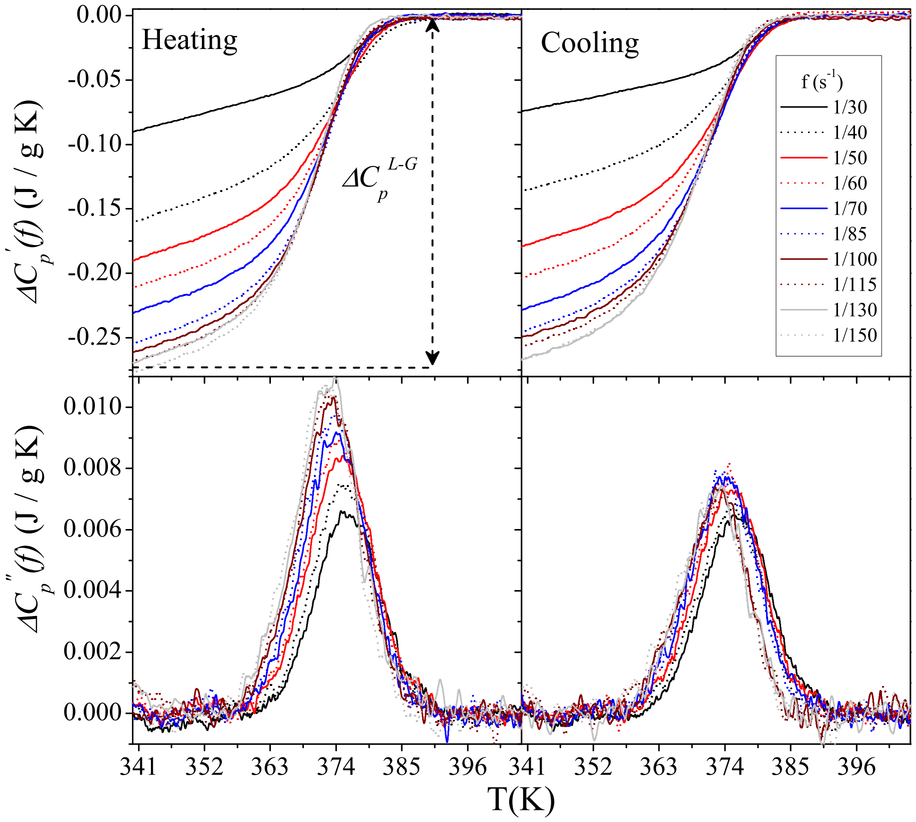

FIGURE 7.3: The normalized real part of the heat capacity $\Delta C_p^{'}$(f) (top panel) and imaginary heat capacity $\Delta C_p^{"}$)(f) (bottom panel) of a PMMA+SWCNT composites ϕ_m = 0.014 sample from 340 to 405 K, for different applied heating frequencies from 1/30 to 1/150 s^{-1}, (see legend). In top panel, the difference between liquid and glass heat capacity ΔC_p^{L-G} is defined.

This shows, $\Delta C_p^{(L-G)}$ increases with decreasing frequency of temperature modulation. Figure 7.4, shows $\Delta C_p^{(L-G)}$ for the pure PMMA (Upper), 0.014 (Middle) and 0.080 (Bottom) mass fraction of SWCNT in PPMA composites with frequency of temperature modulation. For PMMA, $\Delta C_p^{(L-G)}$ increases with decreasing scan rate all over the frequency range studied except at higher frequency 0.035 s^{-1}, which seems to be equal. This change of $\Delta C_p^{(L-G)}$ with respect to scan rate disappears as the mass fraction of SWCNT increases inside the host polymer. The 0.080 mass fraction of SWCNT does not show any difference of $\Delta C_p^{(L-G)}$ with respect to the scan rate all over the frequency range studied. The imaginary part of the complex specific heat capacity, during heating $\Delta C_p^{''}(\omega)$ (Fig. 7.3, Bottom panel), is characterized by an asymmetric peak with a smaller slope at the low temperature side than at the high temperature side,

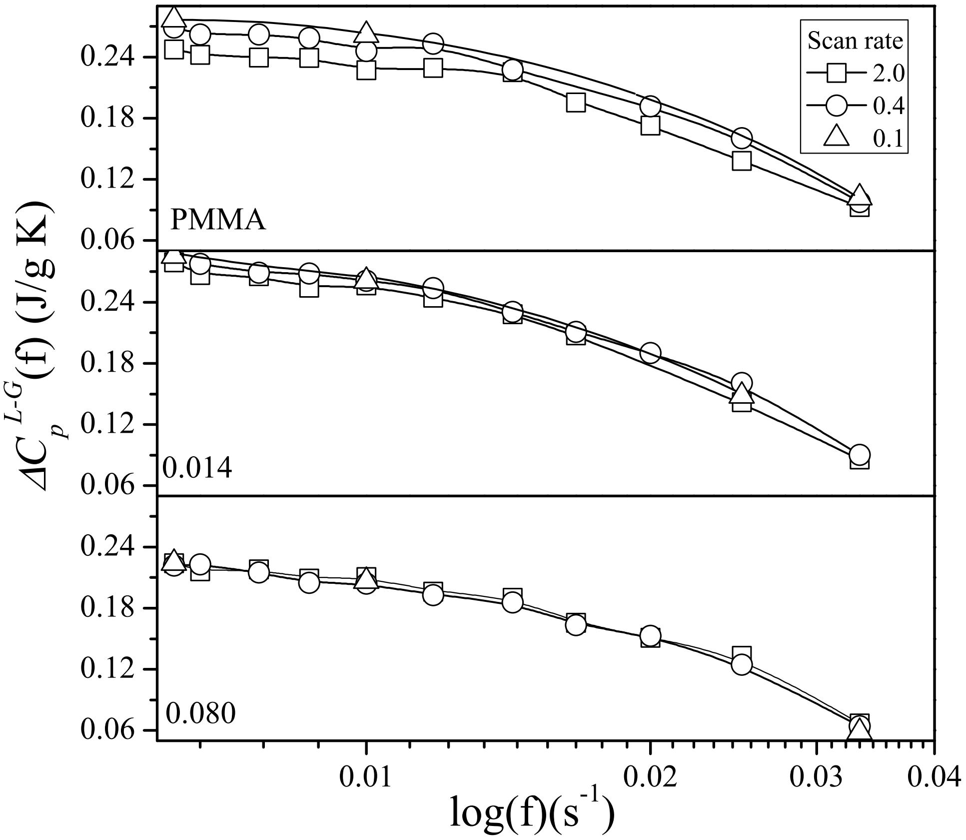

FIGURE 7.4: Semi-logrithmic plot of ΔC_p^{L-G} as a function of temperature modulation frequency *f* for scan rates 2.0, 0.4, and 0.1 K/min, for PMMA (top), 0.014 (middle), and 0.080 (bottom) mass fraction of SWCNTs.

which can be characterized by the molecular distribution of intrinsic structural relaxation and related to the dynamic glass transition. The slope increases with decreasing the frequency of temperature modulation in low temperature without changing the high temperature slope during heating. The temperature where imaginary specific heat shows maximum value (T_{max}) shifted towards lower temperature with decreasing frequency indicating the dynamics of the systems slowing down. The cooling $\Delta C_p''$ shows similar peak maximum shifted to lower temperature from 1/30 to 1/70 s^{-1} and less change in magnitude than heating results. After 1/70 s^{-1}, there is no significant change of peak maximum observed during cooling as compared to heating. The $\Delta C_p''$ peak during cooling shows very symmetric without any change of slope in high and low temperature side.

In our previous study [17], we experimented with the glass transition temperature, which

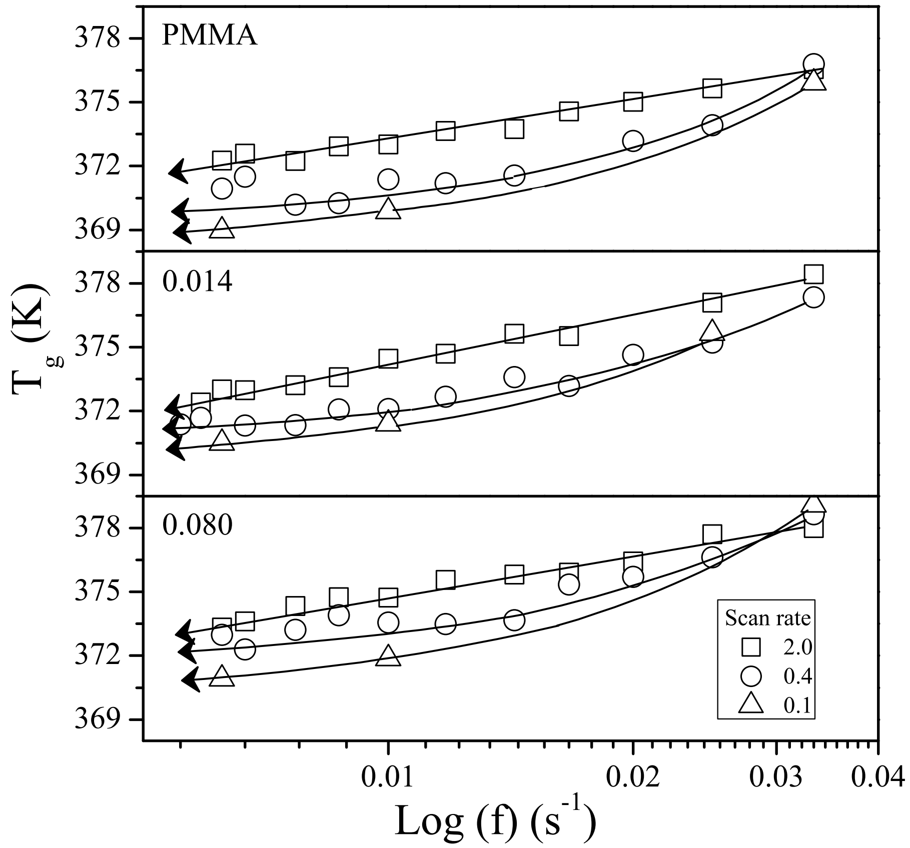

FIGURE 7.5: Semi-log plot of the glass transition temperature (T_g) as a function of temperature modulation frequency for pure PMMA (top), 0.014 (middle) and 0.080 (bottom) mass fraction of SWCNTs at scan rates 2.0, 0.4, and 0.1 K/min. Lines are given to the eye and arrows indicate the zero-frequency extrapolated T_g.

shows T_g increases with scan rate. Figure 7.5 shows the glass transition temperature for PMMA, 0.014 and 0.080 mass fraction of SWCNT+PMMA composites with frequency of temperature modulation.

In all of these three samples, highly dependent T_g increases with the increasing frequency of temperature modulation and scan rate. But this shows that in all PMMA and SWCNT+PMMA composites, T_g of a different scan rate approaches to the same value as the frequency of temperature modulation increases, and after certain frequency of modulation, the lower scan rate becomes higher T_g than higher scan rate. This crossover of T_g between different scan rates with frequency of modulation shifted to a lower frequency as ϕ_m increases. This shows that the dynamics of the glass transition

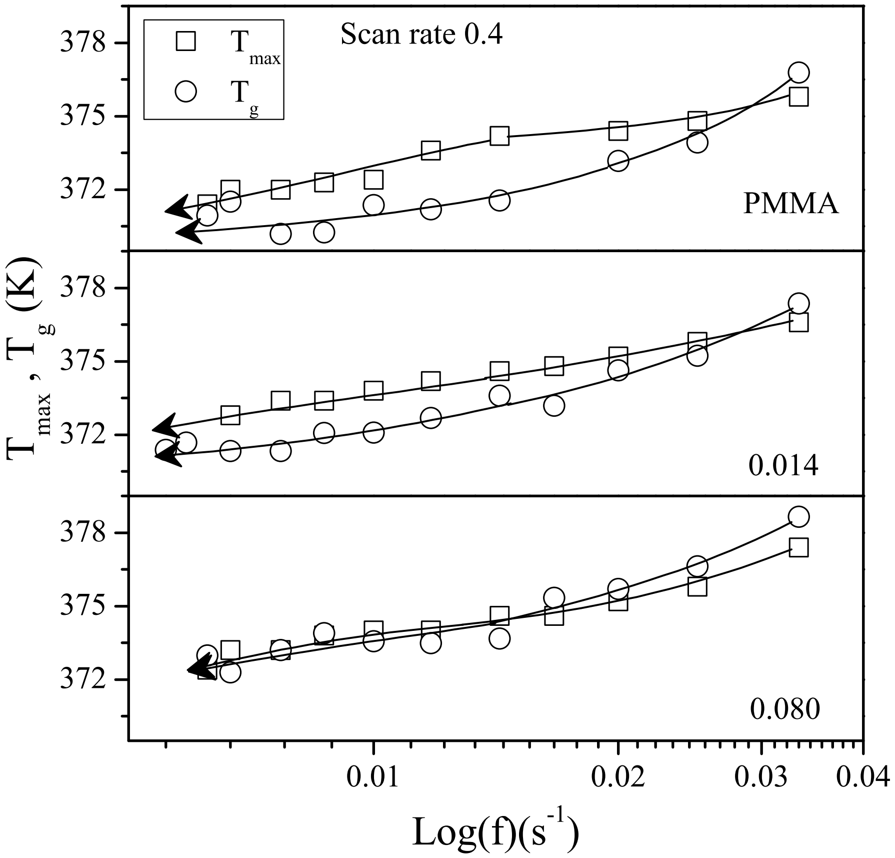

FIGURE 7.6: Semi-log plot shows comparison of maximum temperature in imaginary part of complex heat capacity (T_{max}) and glass transition temperature (T_g) with frequency of temperature modulation of PMMA (Top), 0.014 (Middle) and 0.080 (Bottom) mass fraction of SWCNTs in PMMA.

is highly dependent upon the frequency and the nanotube dispersion can significantly alter these dynamics with modulated frequency.

Figure 7.6 shows the maximum peak temperature of imaginary parts of complex specific heat (T_{max}) and glass transition temperature T_g, with frequency of temperature modulation, for PMMA, 0.014 and 0.080 mass fraction of SWCNTs in host PMMA at 0.4 K/min scan rate. T_{max} is the peak value of the imaginary part of specific heat while heating and T_g obtained by using DSC software from the heating run of reversible heat capacity during step like feature of transition. T_{max} is the temperature where maximum loss appears. The glass transition is where the polymer undergoes a liquid like phase to a glassy region and both T_{max} and T_g may not be same. For pure PMMA and 0.014 mass fraction of SWCNT+PMMA composites, T_{max} is higher than the T_g, in low frequency

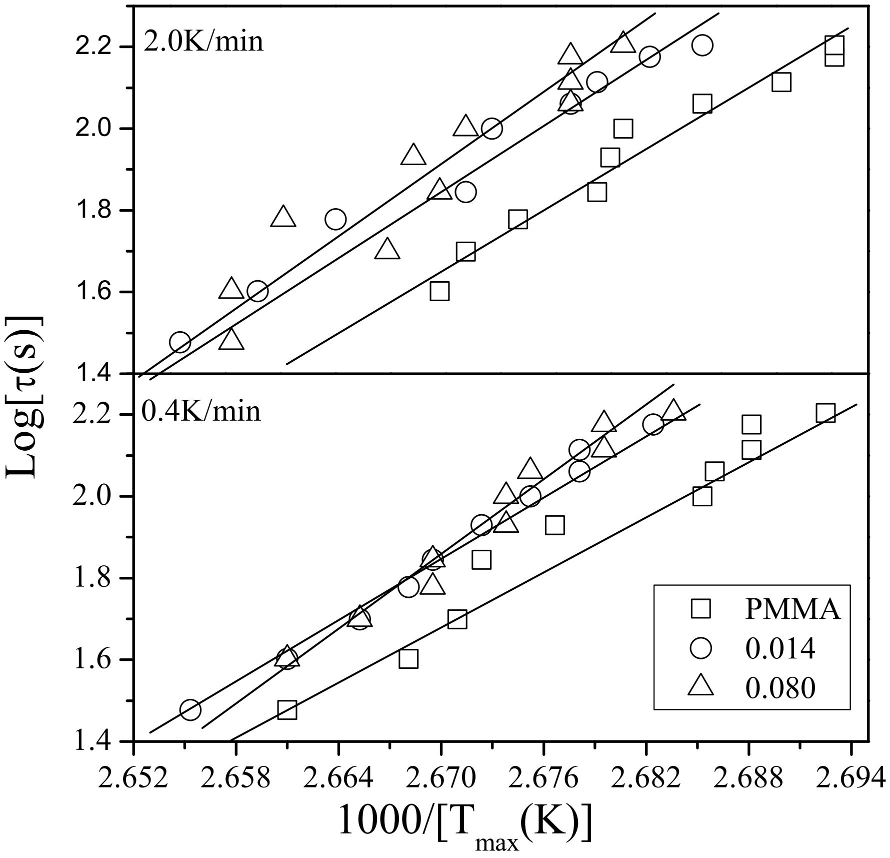

FIGURE 7.7: Arrhenius plot of logarithm of time period of temperature oscillation with inverse of the peak $C_p^{''}$ temperature obtain at rate 2.0, and 0.4 K/min for PMMA, 0.014 and 0.080 mass fraction of PMMA+SWCNTs composites.

region and both the T_{max} and T_g value approach each other as frequency increases and at particular frequency (0.029 s^{-1} for PMMA) they cross each other and become T_g higher than T_{max}. As SWCNTs mass fraction increases, for 0.080 mass fraction, T_{max} and T_g values overlap up to 0.17 s^{-1} and then cross each other to become T_g value higher than the T_{max}. It indicates that the crossover point between T_g and T_{max} shifted towards the lower frequency as ϕ_m increases.

The frequency dependence glass transition can also be interpreted by Arhenius Law. Figure 7.7 shows the relaxation time (τ in s^{-1}: τ is the modulation time period) in log scale, versus inverse peak temperature of the imaginary part of complex heat capacity ($1000/T_{max}$). Figure 7.7 shows from two different scan rates 2.0 K/min (Upper) and 0.4 K/min (Bottom) for PMMA, 0.014 and 0.080 mass fraction of SWCNT+PMMA

Table 7.1: Activation Energy (E) and characteristic time (τ_0) in two different scan rates of PMMA and PMMA+SWCNT composites.

Sample	2D/min		0.4D/min	
ϕ_m	E(K)	τ_0(s)	E(K)	τ_0(s)
PMMA	25,600	1.18×10^{-28}	23,000	8.87×10^{-27}
0.014	26,000	5.54×10^{-30}	27,000	3.98×10^{-31}
0.080	29,000	3.62×10^{-34}	29,200	1.10×10^{-33}

composites. The fitted Arhenius Law is given as:

$$\tau = \frac{1}{\omega} = \tau_0 \times exp\left(\frac{E}{T_{max}}\right) \tag{7.9}$$

where E is the activation energy and τ_0 is the characteristic time. Deviations with regards to the Arhenius behavior are shown in case of 2 K/min scan rate. The pure PMMA data follows better the Arhenius behavior than the nanotube composite sample. It is clear from the fitting that the slope increases with the nanotubes volume fraction in PMMA+SWCNT composites. Fitted values of activation energy and characteristic time are given in Table 7.1. The activation energy in 2.0 and 0.4 K/min scan rates, for pure PMMA, 0.014 and 0.080 mass fraction of SWCNT+PMMA composites were 25600, 26000, 29000 K and 23000, 27000, 29200 K respectively.

This shows that activation energy increases as the volume fraction of nanotubes increases inside the polymer systems. In other words, during the process of formation of a continuous network, polymer chains stack over the carbon nanotubes to form a strong network, thus there is a significant increase in the activation energy, and since this follows arhenius behavior, materials become stronger. On the other hand the characteristic time decreases with increases the mass fraction of SWCNTs for both scan rates, shown in Table 7.1.

Fig. 7.8 shows the enthalpy ($\Delta H^{''}$) of PMMA and 0.080 mass fraction of SWCNT+PMMA composite with frequency of temperature modulation. This Enthalpy was estimated by integrating the imaginary part of complex specific heat $C_p^{''}$. In low frequency range, $\Delta\ H_{heating}^{''}$ and $\Delta\ H_{cooling}^{''}$ shows a large deviation in both PMMA and 0.080 mass fraction of SWCNT+PMMA composite. Both the cooling and heating enthalpy approach each other as the frequency of modulation increases. This deviation of $\Delta H^{''}$ between heating and cooling at low frequency decreases with scan rate. For a very low scan rate at 0.1 K/min, there was no significant deviation observed between heating and cooling

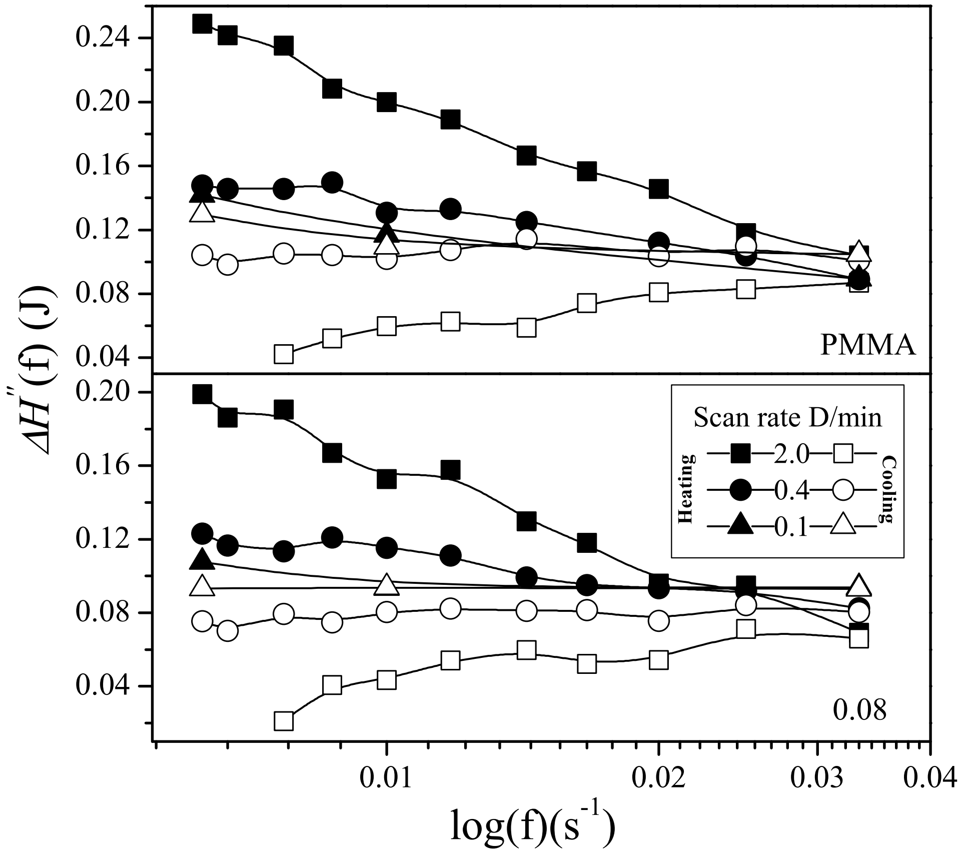

FIGURE 7.8: Semi-log plot of the imaginary enthalpy $\Delta H''$ *(f)*, which was obtained by integrating the imaginary part of the complex heat capacity, as a function of temperature modulation frequency for pure PMMA (top) and $\phi_m = 0.080$ PMMA+SWCNT (bottom) sample. Heating (closed symbol) and cooling (open symbol) data are shown at the temperature scan rates, see legend.

throughout the frequency range studied. Another significant difference can be marked from the figure, that is enthalpy $\Delta H''$ increases at frequency 0.033 s^{-1} as the scan rate decreases in the SWCNT + PMMA composite which does not occur clearly in the case of pure polymer.

7.4 Summary

Frequency dependence dynamic heat capacity of PMMA and SWCNT+PMMA composites have been observed in glass transition region by Modulated DSC. In the vicinity of T_g, the remarkable temperature dependence is clearly observed in the real and imaginary part of complex heat capacity. The interesting relaxation phenomena observed in the imaginary part and dynamics of glass transition obtained from the real part of heat capacity were discussed with frequency of temperature modulation, when the polymers undergo a transition from a solid like region to a liquid like state. The Activation energy calculated from Arhenius behavior increases with mass fraction of nanotubes. The change of Enthalpy between heating and cooling data was discussed with different scan rates to understand the molecular behavior during glass transition. This experimental study must be helpful to understand thermal properties such as glass transition, fragility, relaxation behavior, Enthalpy loss and mechanical properties of polymer-carbon nanotube based composites. These parameters can be controlled by adjusting the properties of the nanofillers, applied frequency and rate of heating and cooling the materials.

Bibliography

[1] M. Reading, D. Elliott and V. L. Hill, *J. Thermal Anal.*, **40 ,** 949 (1993).

[2] B. Wunderlich, Y. Jin and A. Boller, *Thermochim. Acta*, **238,** 277 (1994).

[3] J. E. K. Schawe, *Thermochim. Acta.*, **271,** 127 (1996).

[4] N. O. Birge and S. R. Nagel, *Phys. Rev. Lett.*, **54,** 2674 (1985).

[5] N. O. Birge, *Phys. Rev. B*, **34,** 1631 (1986).

[6] P. K. Dixon, *Phys. Rev. B*, **42,** 8179 (1990).

[7] T. Christensen, *J. Physics (Paris Colloq)*, **46,** C8-635 (1985).

[8] N. O. Birge, P. Dixon and N. Menon,*Thermochim. Acta*, **304**, No.305, 51 (1997).

[9] S. J. Tans, M. F. Devoret, H. D. A. Theses and R. E. Smalley, *Nature*, **386,**, 474 (1997).

[10] H. Dai, J. H. Hafner, A. G. Rinzler, D. T. Colbert and R. E. Smalley, *Nature*, **384,** 147 (1996).

[11] S. J. Sander, J. Tans, A. R. M. Verschueren and C. Dekker, *Nature*, **393,** 49 (1998).

[12] S. Glushanin, V. Y. Topolov and A. V. Krivoruchko, *Materials Chemistry and Physics*, **97,** No.2-3, 357-364 (2006).

[13] P. Hine, V. Broome and I. Ward, *Polymer,* **46,** No.24, 10936-10944 (2005).

[14] N. Cioffi, L. Torsi, N. Ditaranto, G. Tantillo, L. Ghibelli, L. Sabbatini, T. Bleve-Zacheo, M. D. Alessio, P. G. Zambonin and E. Traversa, *Chemistry of Materials*, **17,** No.21 5255-5262 (2005).

[15] A. Pelaiz-Barranco and P. Marin-Franch, *Journal of Applied Physics*, **97,** No.3, 97 (2005).

[16] B. Wunderlich, *Thermal analysis. New York: Academic Press*, **135,** 135, 205 (1990).

[17] N. R. Pradhan and G. S. Iannacchione, *Submitted to ournal of Physical Chem B*, (2009).

[18] M.Meyyappan05, *Carbon nanotubes science and applications, CRC Press: Boca Raton, FL* (2005).

[19] P. J. F. Harris, *Carbon nanotubes and related structures new materials for the twenty-first century;Cambridge University Press: Cambridge* (2001).

[20] Nichola J. Coleman and Duncan Q. M. Craig, *International journal of pharaceutics*, **135,** 13-29 (1996).

[21] J. E. K. Schawe, *Thermochim. Acta*, **261,** 183 (1995).

[22] J. M. Hutchinson and S. Montserrat, *J. Thermal Anal.*, **47,** 103 (1996).

[23] A. Hensel, J. Dobbertin, A. Boller and J. E. K. Schawe, *J. Thermal Anal.*, **46,** 935 (1996).

[24] B. Wunderlich, *J. Thermal Anal.*, **48,** 207 (1997).

[25] S. R. Aubuchon and P. S. Gill, *J. Thermal Anal.*, **49,** 1039 (1997).

[26] S. Weyer, A. Hensel and C. Schick, *Thermochimica Acta*, **304/305,** 267-275 (1997).

[27] N. R. Pradhan, H. Duan, J. Liang and G. S. Iannacchione, *Nanotechnology*, **20,** No.24, 245705 (2009).

Chapter 8

IMAGING AND DYNAMICS OF LIQUID CRYSTALS CONFINED INSIDE CARBON NANOPIPES

8.1 Introduction of Nanofluid Device

The study of liquid crystals (LCs) began in 1888 when an Austrian botanist named Friedrich Reinitzer observed that a material known as cholesteryl benzoate had two distinct melting points. In his experiments, Reinitzer increased the temperature of a solid sample and watched the crystal change into a hazy liquid. As he increased the temperature further, the material changed again into a clear, transparent liquid. Because of this early work, Reinitzer is often credited with discovering a new phase of matter - the liquid crystal phase. A liquid crystal is a thermodynamic stable phase characterized by anisotropy of properties without the existence of a three-dimensional crystal lattice, generally lying in the temperature range between the solid and isotropic liquid phase, hence the term mesophase. Liquid crystal materials are unique in their properties and uses. As research into this field continues and as new applications are developed, liquid crystals will play an important role in modern technology.

There are different phases in existence of liquid crystals, according to their orientation from the direction of director of LC molecules. This orientation of molecules depends upon the temperature, pressure, external applied field, interaction with other molecules in the environment and also the surface interactions on which it is placed, etc. These novel properties of LCs make todays technology much more sophisticated than the last decades. Much research work has been done in the past and much more advanced research work is going on to enhance the technological application of liquid crystal. In recent years, scientists were much more focused on the polymer - carbon nanotubes based research.

Carbon nanotubes (CNTs) are excellent candidates in the application of electronics, opto-electronics, optics, and the hollow cylinders of pure carbon and the nanochannels within them are big enough to accommodate various atoms and even small molecules.

Little work has been done on liquid crystals mixed with carbon nanotubes. Now scientists are very keen to study the liquids and other particles confined inside carbon nanotubes or carbon nanopipes (CNPs). CNPs are long carbon nanotubes with a diameter from 150 - 200 nm, and both ends are open like hollow bamboo shapes. This chapter contains the dynamic behavior of liquids inside CNPs and is pretty broad, comprising the investigation of liquid entering inside the nanotubes, and the subsequent filling of them. The overall flow inside the carbontubes/nanopipes, wetting the nanotubes wall, and molecular arrangement inside the nanotubes were discussed. Another important parameter is represented by the diameter of nanotubes: on one hand the interest has been placed in liquids inside nanotubes having a diameter of a few nanometers with the promise of observing non-continuum fluid dynamics effects due to confinement inside the nano channel. On the other hand, now many of the researchers are focused on larger nanotubes (diameters $>$ 10 nm) for applications where handling of large volume of materials is required, with the liquid not necessarily experiencing non-continuum behavior. Non-continuum behavior is expected to be observed below 10 nm diameter nanotubes [1].

Interest in nanofluidics increased with more widespread availability of carbon nanotubes, which appeared to have the ideal characteristics for these kinds of studies. The natural scale of nanotube channels appeared to yield the possibility of bypassing the complexities of microfabrication and obtaining tubular structures with diameters as small as

1 nm. In reality, numerous obstacles inherent to the structure and synthesis process of carbon nanotubes have been encountered for their use as nanoscale fluid channels: the presence of kinks and bends, internal closures and caps or catalyst particles [2], all represent obstacles to the flow of fluids inside the tubes. Some efforts have been directed towards the development of carbon nanotubes with structure and properties tailored for nanofluidic studies [3].

The use of nanotubes for nanoscale fluidic studies has also raised the interest in the nature of the interactions between the nanotube walls and the fluid molecules and effect on the flow. Understanding the interactions between the fluid and the tube, or the tubes wettability, will prove to be one of the fundamental aspects of nanofluidics, and an important step towards the development of nanofluidic devices.

8.1.1 SWCNTs and MWCNTs for Nanofluidic Applications

Carbon nanotubes have been identified traditionally as single-wall nanotubes (SWNT). In reality, CNTs are a large family of materials with different sizes, structures, and properties, which are largely determined by their synthesis techniques [2, 4] also mentioned in chapter 1. SWCNTs, with typical diameters in the range 0.62 nm and comprised of a single shell, have semiconducting or metallic properties, depending on their chirality (Chapter-1). CNTs can have two (double-wall nanotubes, DWNT) or more coaxial shells (multi-wall nanotubes, MWNT), with diameters ranging from 2 to 100 nm and even more. Noncoaxial CNTs have also been produced, having a so-called herringbone structure [5, 6], with the graphitic shells placed at an angle with respect to the axis. Nanotubes with internal closures, dubbed bamboo-like have also been demonstrated [7]. Tens of synthesis techniques have been developed, from arc discharge [8, 9] to hydrothermal synthesis [10–12] and catalytic chemical vapor deposition (cCVD) [13–18], most of them employing a metal catalyst. For storing large amounts of liquid or other molecules or nanoparticles, the SWCNT or DWCNTs cannot be suitable [19, 20]. A different class of nanotubes is based on the concept of template-assisted synthesis of nanomaterials [21]: chemical vapor deposition (CVD) of carbon has been performed inside the pores of commercial alumina membranes [22–24], previously used as filters. These membranes initially had pores with an average diameter of 100 - 250 nm in the middle of the membrane and pore branching close to the two surfaces. With progress in membrane production, nanotubes with diameters as small as 10 nm have been synthesized [3, 25]. Template-grown nanotubes have many characteristics that make them better suited for nanofluidic studies: straight, long walls, with open ends and small wall thickness compared to the internal diameter of the bore, similar to a macroscopic pipe. In this method we can easily produce forests of well aligned and excellent quality MWCNTs.

8.1.2 Behavior of Liquids Inside CNPs

One of the first proofs that carbon nanotubes (CNTs) were indeed hollow was obtained by filling carbon nanotubes with molten metals, salts [26, 27] and oxides, through metal evaporation [28, 29], melting [30, 31], and capillary filling [32], with subsequent observation under the TEM. After a few years of initial experiments with molten metals and salts, the first high resolution transmission electron microscopy (TEM) micrographs of aqueous fluids trapped inside CNTs suggested that water could indeed wet the internal cavity of CNTs [10]. Water, along with gases, was trapped inside the nanotubes during the synthesis process [11, 33]. Later by using an autoclave system, it has been reported that, water was forced inside 25 nm closed MWNTs through its walls and observed using high resolution TEM [5, 6, 34]. It has been shown that water preferentially condenses inside the CNPs when the appropriate temperature and pressure conditions are reached inside the chamber of an environmental scanning electron microscope (ESEM)[35, 36]. Carbon nanopipes have also been filled with magnetic [37] and fluorescent [38] particles dispersed in liquid media which penetrated the tubes and then dried up by evaporation. Experimentally dynamic studies of liquids inside CNPs have been done much less compared to the static studies. The main reason is the high complexity of experimental setup to perform such experiments, such as miniaturizing a liquid pumping system to fit a TEM stage. Few dynamic studies can be seen in literature by molecular dynamic simulation methods [39, 40].

8.1.3 Nanofludic and Energy Storage Applications

Although no nanofluidic devices have reached the commercial stage, there are promising applications that have already been reported in literature. There is the possibility of using CNPs/CNTs as the nanoscale equivalent to syringe needles for interrogation of cells and sub cellular entities. The first result shows MWCNTs about diameter 100 nm attached to AFM tips could poke the cellular membrane of a cell without destroying it [41], but in this case no liquid transfer was possible. This was achieved by magnetic assembly of carbon nanotubes loaded with magnetic particles inside a glass micropipette with a tip tapered down to 300 - 400 nm [19]. Later it was shown to be possible with 200 nm diameter CNPs by using fluorescent dye [42].

CNT-tipped pipettes for cell interrogation appears, to date, as the most promising nanofluidic application of carbon nanotubes, and the one which is closer to commercialization than other biomedical applications of nanotubes. Other major topics, at different stages of investigation and development, concern DNA translocation and analysis, and nanotube-based membranes.

Carbon nanotube-based membranes are also attracting much interest for their characteristic ultra-fast liquid flow, as mentioned earlier. Water filtration and desalination as well as separation of many other liquids and gases could be the most promising applications of nanotube membranes. Fundamental studies of chemistry at liquid-liquid and liquid-gas interfaces, and nano- and microscale chemical reactors on a chip will both be enabled by the availability of nanotube fluid conduits.

Recently published results show that SWCNTs filled C_{60} exhibit unusual electronic and mechanical properties when compared to empty SWCNTs [43–47]. Selective incorporation of foreign carbons into CNTs could indeed improve the spatial occupancy inside the CNT channels in a controlled manner, thereby providing a potential way to optimize their porosities for various applications such as gas adsorption, heavy metal ion removal, and energy storage.

Liquid crystalline materials offered a promising application in the last few decades for their application in electro-optic, Optic and display technology. Interest in liquid crystalline materials confined to restrictive geometries has expanded in recent years because of their interesting physical phenomena and their potential use in a plethora of electro-optic applications [48]. During the last two decades, there have been numerous basic studies of liquid crystals confined to a restrictive environment. These studies are most conveniently classified according to the confining template: random porous glass [49–51], aerosol and aerogel dispersions [52–59], cylindrical confinement [60–65], and spherical containment [66, 67]. As the size of confinement shrinks to the nanoscale, it becomes extremely difficult to image the molecular ordering within the cavities with experimental techniques. Confinement of discotic liquid crystal has been studied recently [68] by High Resolution TEM. They successfully filled the liquid crystal by a capillary filtration process and visualize the director inside the 5 nm cavity of MWCNT. Another study shows the filling of 5CB liquid crystal confined inside 200 nm diameter CNPs [69].

In this chapter we studied the filling of 8CB and 10CB liquid crystals inside the ∼200 nm diameter MWCNPs. The filling in our study refers to complete filling of LCs inside the MWCNTs and also coating the inside wall of MWCNTs. These two different types of coating and complete filling are achieved by different types of filling techniques. The other aspects of this chapter are to study the dynamics of phase transition of these confined liquid crystals inside CNPs by the Modulated Differential Scanning Calorimeter (MDSC) technique. This technique is already described in detail in previous chapters. Here, experimental section contains the synthesis of MWCNPs and filling of liquid crystals, then the imaging and MDSC results are discussed.

8.2 Experimental

8.2.1 Synthesis of MWCNPs

CNPs are synthesized with a noncatalytic chemical vapor deposition (CVD) method using commercially available Anodic Aluminum Oxide (AAO) membranes, a porous template (Whatman Anodic, average pore diameter: 200 nm±10%, thickness: 60 μm) described in chapters 4 and 5. These grown MWCNPs inside an AAO template were taken and the excess amount of carbon layer on the top and/or back surface was removed by a thermal treatment process. By thermally treating we obtained the well aligned MWCNPs with both ends opened.

Figure 8.1 shows the cartoon of synthesis procedure how it looks after growing MWCNPs inside the AAO channel and after dissolving the AAO template.

8.2.2 Filling of LCs inside Carbon Nanopipes

The opened ended MWCNPs grown inside the AAO template were taken for the filling of liquid crystals. A small quantity of LCs materials were mixed with the acetone solvent

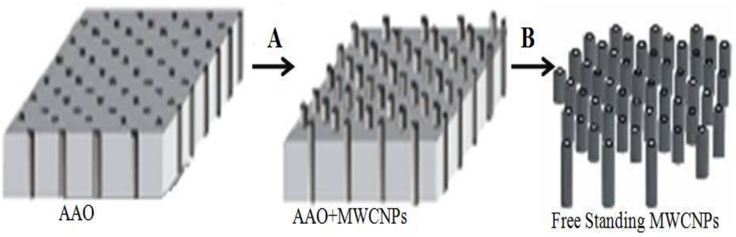

FIGURE 8.1: Synthesis procedure of MWCNPs by CVD method. A: is the CVD grown of MWCNP inside AAO nano-pores, B: Free standing MWCNPs obtained by dissolving the AAO template with NaOH solution.

to make a solution of LCs and directly dropped on the top of AAO+MWCNP template, then placed on the hot plate [temperature slightly greater than the Nematic to Isotropic transition temperature (T_{NI})] in vacuum environment immediately after pouring, for 1 - 2 minutes. Then we observed that the top surface of the sample covered with a thin layer of liquid crystals sucked inside the nanopipes. There was also an excess amount of LCs layer lying on the top surface of the AAO+MWCNPs sample. This liquid crystal layer was cleaned with filter paper or bird feather very smoothly without breaking the sample. The SEM micrograph observed that the top surface of the sample was clean of the liquid crystal. The liquid crystal was confined inside the MWCNPs, where the MWCNPs were arranged parally inside the AAO template and named later as an aligned sample. Then the confined liquid crystal inside the aligned MWCNPs was taken and dissolved with NaOH solution to remove the AAO part. Then we had the randomly oriented MWCNPs contained liquid crystals. These randomly oriented MWCNPs were imaged by HRTEM to confirm the presence of liquid crystal inside the MWCNPs. These two types of LCs confined inside the MWCNPs were taken to be experimented in MDSC studies for their phase transition.

The other types of filling went through a similar procedure with bulk liquid crystal (no solvent added) dropped on the top of the MWCNP grown AAO sample then placed on the hot plate and kept in vacuum, then heated for 3 - 4 mins just above T_{NI}. The liquid crystal then melted and entered inside the MWCNPs in vacuum. Then the above similar procedure followed to clean the surface of sample to remove excess LCs and again

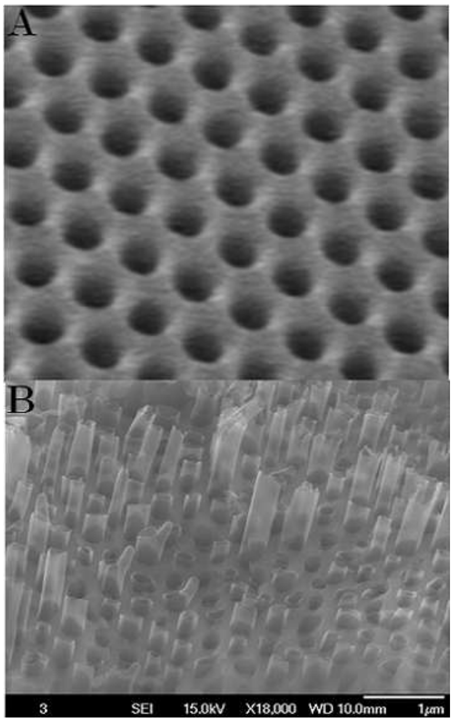

Figure 8.2: Top: Commercially purchased AAO template of average diameter 200 nm and thickness 60 μm. Bottom: SEM image of grown MWCNPs inside AAO template of average diameter 190 nm and length 60 μm.

dissolved the AAO template to extract only MWCNP contained LCs.

8.3 Imaging of LCs Confined inside MWCNPs

Figure 8.2 (TOP) shows the SEM images of the commercially purchased AAO template (200 nm diameter pore sizes and 60 μm thickness of template or length of the pores) and (Bottom) MWCNPs, average diameter 190 nm and 60 μm long grown inside the AAO template. MWCNPs tips very clearly show that the quality of the nanotubes were good and straight inside the nanochannel. Almost all the nanopores are filled with nanotubes and all the tips are opened on both ends by a thermal cleaning process. This configuration of the sample was taken for the filling of liquid crystal.

Figure 8.3 shows the filling of solution cast LCs. In this way we have achieved the coating of the inner surface of the MWCNP's wall. Both the left and right side of

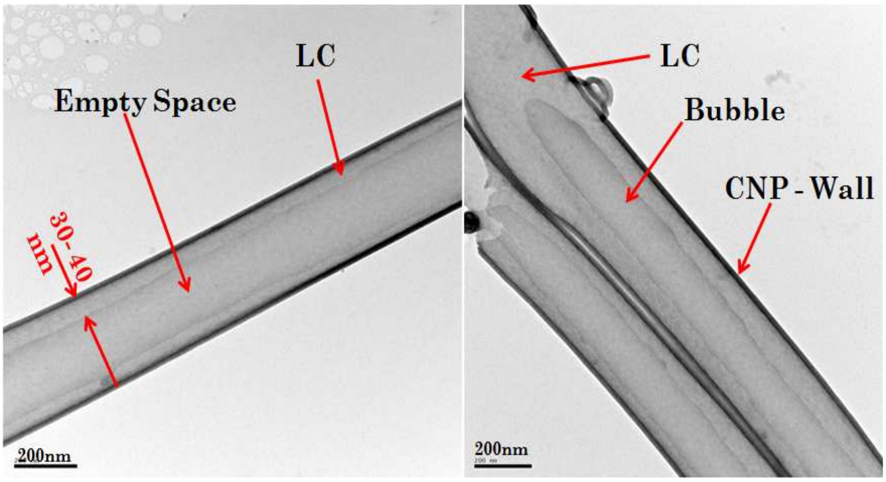

Figure 8.3: HRTEM images of 10CB Liquid Crystals filled inside MWCNPs by solvent+LC mixture. 30-40nm thick layer of LCs was seen to be coated in inner surface of the nanopipes.

Fig. 8.3 shows the 10CB LCs are coated on the inner wall surface of CNPs making the middle/axial part of the nanopipes empty. The coating thickness ranges from 30-40 nm inside the tube. We can also see the bubble formed on one of the nanopipes by blocking the LCs in one end Figure 8.3 (right, TOP). The filling of bulk LCs shows complete filling of LCs inside the nanopipes shown in Fig. 8.4. In this case no inner-wall coating was observed and the LCs easily filled completely inside the nanotubes. The reason of coating observed in case of solution cast LC filling was due to the evaporation of solvent (acetone) in vacuum after completely filling the LC solution inside nanopipes.

8.4 Study of Phase Transition of 8CB and 10CB Liquid crystals inside MWCNPs by Modulated DSC:

Modulated Differential Calorimetric study has been carried out to confirm the existence of LCs inside carbon nanopipes and also to learn some of the dynamics of molecules

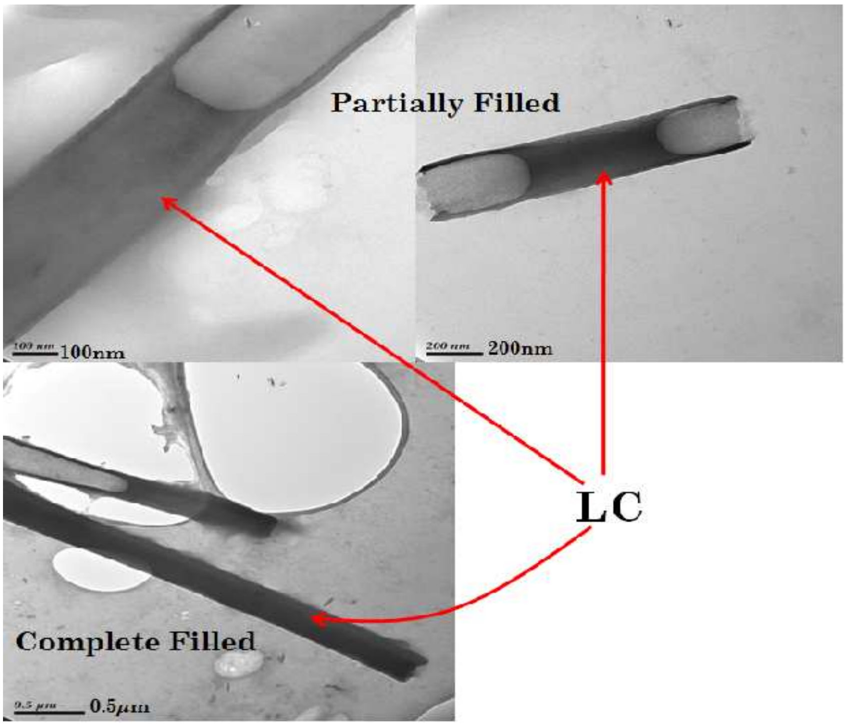

FIGURE 8.4: HRTEM images of filled 10CB liquid crystal inside MWCNPs by directly using bulk 10CB. Complete/partially filling of nanopipes shows in this case.

inside confined space.

The experimental details of MDSC are described in previous chapters. Figure 8.5 shows the normalized reversible heat capacity of pure 8CB (red color) and 8CB liquid crystal confined inside MWCNPs. The data was normalized at T_{NI} transition temperature. MDSC has done with different modulated frequency of temperature oscillation and 0.3 D/min scan rate.

Bulk 8CB shows the strong Smectic-A to Nematic at 305.3 K and Nematic to Isotropic transition at 312.6 K as expected and also has been checked with high resolution AC Calorimeter technique. 8CB, confined inside MWCNPs does not show suppression of Nematic to Isotropic transition completely, but the transition temperature shifted towards the higher temperature to 312.8 K. The Isotropic to Nematic transition shows drastic suppression or no transition observed.

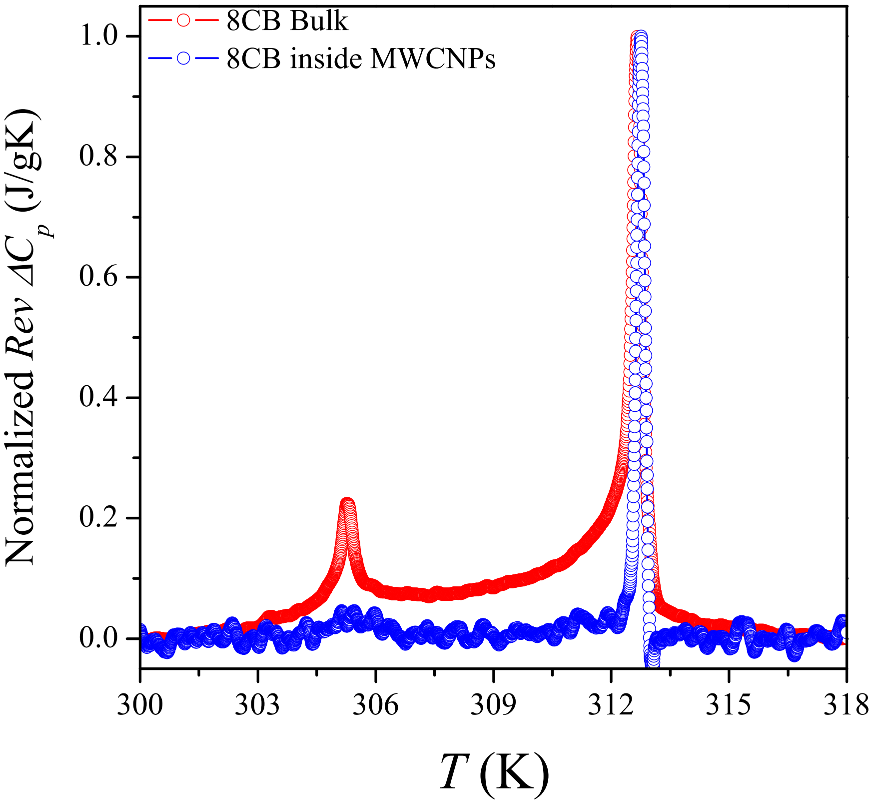

FIGURE 8.5: Normalized Reversible specific heat capacity of Pure 8CB (red color) and 8CB confined inside a MWCNPs (Blue color).

Figure 8.6 shows the zoomed data of Fig. 8.5, Normalized Reversible specific heat capacity of Pure and confined in MWCNPs, which distinctly shows the suppression of $T_{SmecA-N}$ transition and shifted T_{NI} transition. This also gives enough ideas about the molecular arrangement of 8CB liquid crystal inside MWCNPs.

Due to the strong π-π interaction between the liquid crystal carbon molecule and the carbon atom of nanotubes, LCs molecules aligned along the axis and stack along the wall of the carbon nanotube surface. This allows LCs in the nematic state rather than smectic state in room temperature. This clearly shows in the specific heat data in Fig. 8.6 (Left), $T_{SmecA-N}$ transition has been suppressed or was not even seen while going from room temperature to Nematic state for confined 8CB LC. There is a temperature shift (≈0.10 K) of Nematic to Isotropic transition observed in 8CB confined in MWCNPs shown in Fig. 8.6 (Right). This is due to the confinement effect of LCs inside such nanopipes. It also shows the area of T_{NI} peak is decreased, indicating less energy

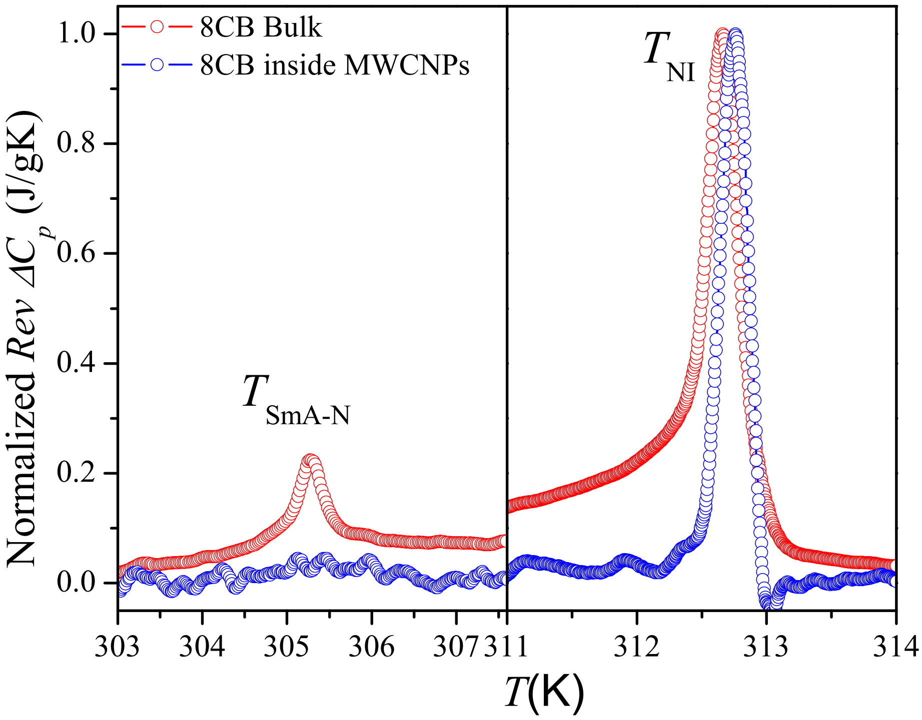

FIGURE 8.6: Reversible specific heat capacity of Pure 8CB (red color) and 8CB confined inside a MWCNPs (Blue color).

required to align the LC molecules to go from Isotropic to Nematic state, when confined inside carbon nanopipes.

The 10 CB liquid crystal was also studied in a similar way in the MDSC setup. The 8CB study has been done in bulk and LCs are confined inside aligned MWCNPs which are grown inside a highly isotropic AAO nanochannel. But the 10CB study has been done in both isotropic oriented MWCNPs holding 10CB LCs and again by liberating LCs filled MWCNPs from the AAO template and making the randomly oriented MWCNPs filled with LCs.

Figure 8.7 shows the normalized data of reversible specific heat of bulk 10CB (diamond symbol, right most), 10CB confined inside aligned MWCNPs (square symbol, middle) and randomly oriented MWCNPs contained 10CB liquid crystals (circle symbol, left). 10CB liquid crystal has only one Smectic - Isotropic (T_{Smec-I}) transition that occurs at 324.5 K. The 10CB confined inside aligned MWCNPs shows the T_{Smec-I} transition at 324.3 K. This is about 0.2 K lower in temperature than the pure 10CB. This shifting is due to the confinement effect of LC molecules inside MW Carbon nanochannels.

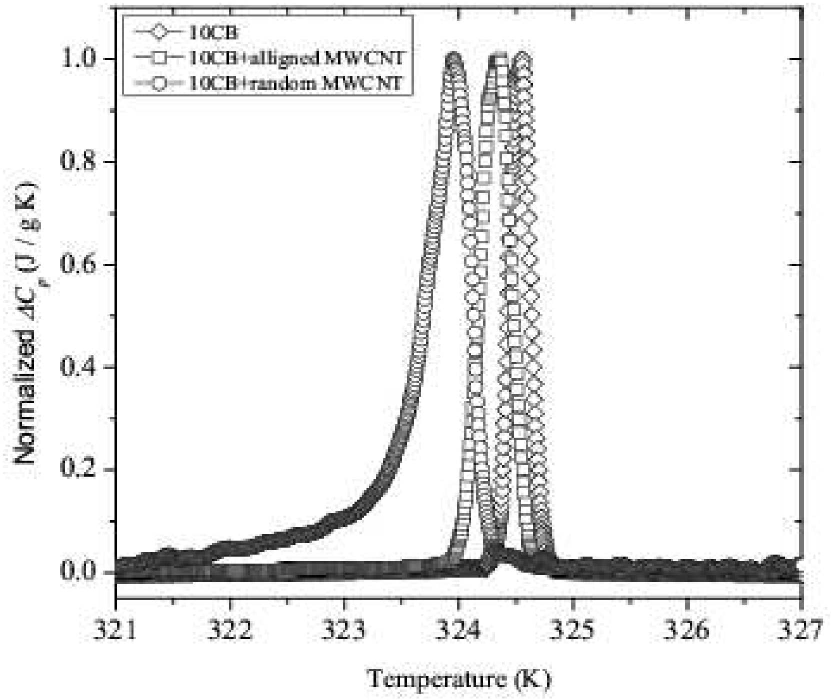

FIGURE 8.7: Reversible specific heat capacity of Pure 10CB (Diamond symbol), 10CB inside aligned MWCNPs (Square symbol) and 10CB confined inside liberated MWCNPs (Circular symbol).

The randomly oriented MWCNPs containing 10CB liquid crystal shows the T_{Smec-N} transition at 323.9 K which is 0.6 K lower in temperature than the pure 10CB. Since the same liquid crystal confined inside the MWCNPs in same dimensions of nanopipes, the transition would not be expected to change as it is observed in random oriented CNPs. This change in the transition temperature in randomly oriented samples could be due to the effect of processing the materials while the AAO template dissolved in NaOH solution and then separated the MWCNPs containing 10CB to make a randomly oriented sample.

8.4.1 Frequency dependent Study:

Frequency dependent specific heat capacity has been done by the Modulated Differential Scanning Calorimeter for 8CB liquid crystal confined inside MWCNPs. All the frequency

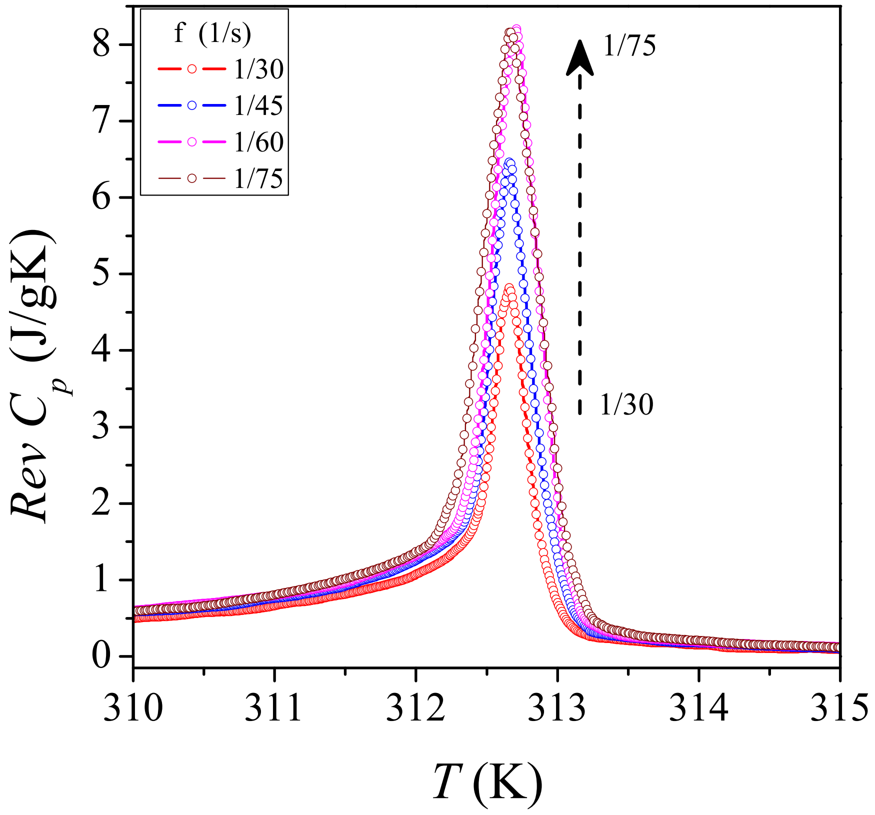

FIGURE 8.8: Frequency dependent Reversible specific heat capacity of Pure 8CB from 1/30 to 1/75 s^{-1}.

scans plotted here are at a scan rate at 0.3D/min, from 1/30 to 1/120 s^{-1} frequency of temperature modulation.

Figure 8.8 shows the normalized specific heat capacity with temperature in different frequency of temperature oscillation for pure 8CB during T_{NI} transition. It was observed that the magnitude of specific heat increases as the frequency of temperature modulation decreases while going from frequency 1/30 to 1/60 s^{-1}, and specific heat does not increase as the frequency further decreases. The transition temperature (T_{NI}) remains unchanged with the frequency of temperature modulation. This behavior of increasing specific heat does not show up during $T_{SmecA-N}$ transition.

The opposite behavior of change in magnitude of specific heat during T_{NI} transition with frequency of temperature modulation was observed in 8CB liquid crystal confined inside aligned MWCNPs and shown in Fig. 8.9. The magnitude of specific heat increases

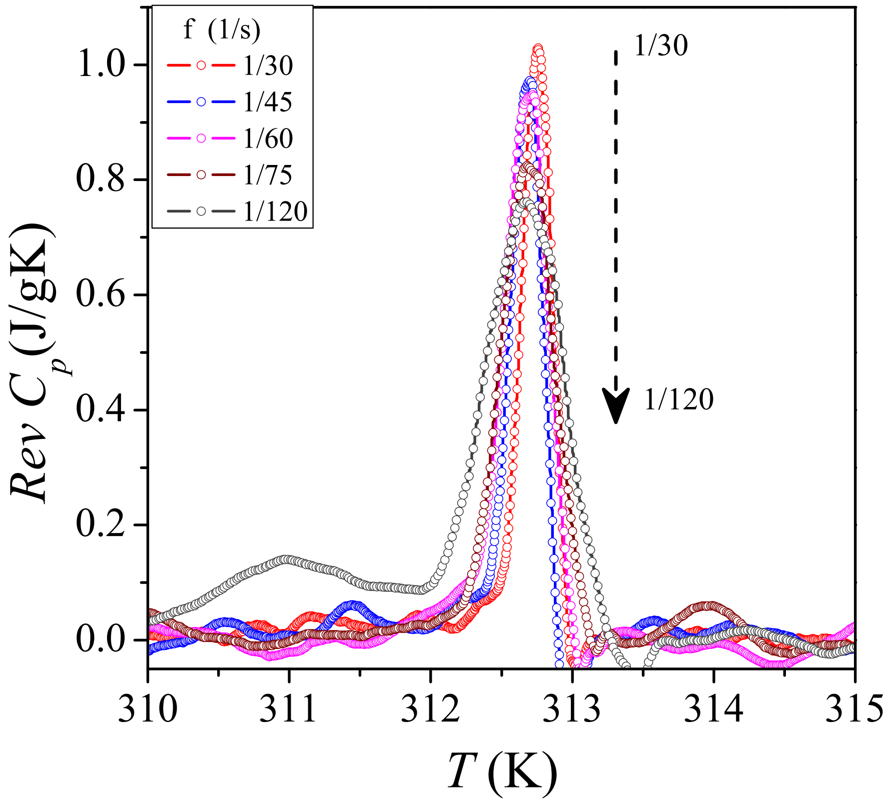

FIGURE 8.9: Frequency dependent Reversible specific heat capacity of 8CB confined inside aligned MWCNPs from 1/30 to 1/120 s^{-1}.

as the frequency of temperature modulation increases, where the opposite behavior was observed during pure 8CB liquid crystal.

This opposite behavior of frequency dependent shows quite an interesting molecular interaction of LC molecules with the surface of carbon nanotubes. The simulation study might makes us better understanding of the interaction between LCs and the nanotubes wall when LCs molecules confined inside CNPs with frequency of temperature modulation.

8.5 Summary

The filling, imaging and dynamics of the phase transition of liquid crystal inside the carbon nanopipes/carbon nanotubes have been studied for 8CB and 10CB molecular structures. We were successfully able to fill the liquid crystal inside MWCNPs in two different approaches and both approaches showed quite a different filling of LCs inside the MWCNPs. The solution mixed LCs filling shows the filling of innerwall coating and the filling pure bulk liquid crystal shows complete or partial filling of MWCNPs. These filling were confirmed by TEM images and also with the calorimetric techniques of phase transition. The dynamics of these confined liquid crystal molecules studied by this MDSC technique shows more dramatic changes than pure liquid crystals. The frequency dependent studied showed one of the exciting phenomena of molecules of LCs and their interaction with the surface of carbon nanotubes due to confinement. This study tells us some of the rich physics of liquids confined inside carbon nanopipes. This also provides some understanding of the flow of liquids inside nanopipes for application of nanofluidic devices.

Bibliography

[1] M. Whitby and N. Quirke, *Nat Nanotechnology*, **2,** 87-94 (2007).

[2] P. J.F. Harris, *Cambridge University Press, Cambridge*, (1999).

[3] D. Mattia, Templated growth and characterization of carbon nanotubes for nanofluidic applications. PhD Thesis, *Drexel University*, **http://dspace.library.drexel.edu/bitstream/1860/1772/1/**$Mattia_{-}$**Davide.pdf.** (2007).

[4] Y. Gogotsi, Nanotubes and nanofibers, *CRC Press, Boca Raton*, (2006).

[5] H. Ye, N. Naguib, Y. Gogotsi, TEM study of water in carbon nanotubes. *JEOL News*, **39,** 38-43 (2004).

[6] H. Ye, N. Naguib, Y. Gogotsi,Y, A. G. Yazicioglu and C. M. Megaridis, *Nanotechnology*, **15,** 232-236 (2004).

[7] D. H. Jung,Y. K. Ko, H. T. Jung, *Mater Sci Eng C*, **,** 117-121 (2004).

[8] J. L. Hutchison, N. A. Kiselev, E. P. Krinichnay, A. V. Krestinin, R. O. Loutfy, A. P. Morawsky, V. E. Muradyan, E. D. Obraztsova, J. Sloan, S. V. Terekhov and D. N. Zakharov, *Carbon*, **39**, 761-770 (2001).

[9] J. C. Bae, Y. J. Yoon, S. J. Lee, K. M. Song, H. K. Baik, *Carbon*, **40,**, 2905-2911 (2002).

[10] Y. Gogotsi, J. A. Libera and M. Yoshimura, *J Mater Res*, **15,** 2591-2594 (2000).

[11] J. A. Libera and Y. Gogotsi, *Carbon*, **39,** 1307-1308 (2001).

[12] J. M. Calderon Moreno, S. S. Swamy, T. Fujino and M. Yoshimura, *Chem Phys Lett*, **329,** 317-322 (2000).

[13] M. Su, B. Zheng and J. Liu,*Chem Phys Lett,* **322,** 321326 (2000).

[14] L. Ci, Z. Rao, Z. Zhou, D. S. Tang, X. Yan, Y. Liang, D. Liu, H. Yuan, W. Zhou and Gea Wang, *Chem Phys Lett*, **359,** 6367 (2002).

[15] Z. Kang, E. Wang, L. Gao, S. Lian, M. Jiang, C. Hu and L. Xu, *J Am Chem Soc.*, **125,** 13652-13653 (2003).

[16] V. L. Kuznetsov, A. N. Usoltseva, A. L. Chuvilin, E. D. Obraztsova and J-M. Bonard, *Phys Rev B*, **64,** 235401235407 (2001).

[17] J. H. Hafner, M. J. Bronikowski, B. R. Azamian, P. Nikolaev, A. G. Rinzler, D. T. Colbert, K. A. Smith and R. E. Smalley, *Chem Phys Lett*, **296,** 195-202 1998).

[18] A. M. Cassell, J. A. Raymakers, J. Kong and H. Dai, *J Phys Chem B.*, **103,** 6484-6492 (1999).

[19] J. R. Freedman, D. Mattia, G. Korneva, Y. Gogotsi, G. Friedman and A. K. Fontecchio, *Appl Phys Lett,* **90,** 103108 (2007).

[20] B. M. Kim, S. Sinha S and and H. H. Bau, *Nano Lett*, **4,** 2203-2208 (2004).

[21] C. R. Martin, *Science*, **266,** 1961-1966 (1994).

[22] T. Kyotani, L. F. Tsai and A. Tomita, *Chem Mater*, **7,** 1427-1428 (1995).

[23] T. Kyotani, L. F. Tsai and A. Tomita, *Chem Mater*, **8,** 2109-2113 (1996).

[24] T. Kyotani, J. Chmiola and Y. Gogotsi, Carbons and composites for electrochemical energy storage systems, *Press Taylor and Francis*, **London** (2008).

[25] D. Mattia, H. H. Bau and Y. Gogotsi, *Langmuir*, **22,** 1789-1794 (2006).

[26] D. Ugarte, T. Stockli, J. M. Bonard, A. Chatelain, W. Ad. Heer, *Appl Phys A*, **67,** 101-105 (1998).

[27] C. Xu, J. Sloan, G. Brown, S. R. Bailey, V. C Williams, S. Friedrichs, K. S. Coleman, E. Flahaut, J. L. Hutchison, R. E. Dunin-Borkowski and M. L. H. Green, *Nat Nanotechnology*, *Chem Commun*, **,** 2427-2428 (2000).

[28] P. M. Ajayan and S. Iijima, *Nature*, **361,** 333 (1993).

[29] S. Iijima, *Nature*, **354,** 56-58 (1991).

[30] T. Ebbesen, *J Phys Chem Solids*, **57,** 951955 (1996).

[31] E. Dujardin, T. Ebbesen, H. Hiura and K. Tanigaki, *Science*, **265,** 1850 (1994).

[32] J. Mittal, M. Monthioux, H. Allouche and O. Stephan,*Chem Phys Lett*, **339,** 311318 (2001).

[33] Y. Gogotsi, J. A. Libera, A. G. Yazicioglu and C. M. Megaridis, *Appl Phys Lett*, **79,** 1021-1023 (2001).

[34] N. Naguib, H. Ye, Y. Gogotsi, A. G. Yazicioglu, C. M. Megaridis and M. Yoshimura, *Nano Lett*, **4,** 22372243 (2004).

[35] M. P. Rossi, H. Ye and Y. Gogotsi, *In ASME Heat Transfer/Fluid Engineering Summer Conference Charlotte, USA*, (2004).

[36] M. P. Rossi, H. Ye, Y. Gogotsi, S. Babu, P. Ndungu and J. C. Bradley, *Nano Lett.*, **4,** 989-993 (2004).

[37] G. Korneva, H. Ye, Y. Gogotsi, D. Halverson, G. Friedman, J. C. Bradley and K. G. Kornev, *Nano Lett.*, **5,** 879884 (2005).

[38] B. M. Kim, S. Qian and H. H. Bau, *Nano Lett.*, **5,** 87378 (2005).

[39] A. G. Yazicioglu, C. M. Megaridis and Y. Gogotsi, *J Heat Transfer*, **126,** 506-606 (2004).

[40] A. G. Yazicioglu, C. M. Megaridis, A. Nicholls and Y. Gogotsi, *J Vis*, **8,** 137144 (2005).

[41] N. A. Kouklin, W. E. Kim, A. D. Lazareck and J. M. Xu, *Appl Phys Lett*, **87,** 173901 (2005).

[42] M. G. Schrlau, E. M. Falls, B. L. Ziober and H. H. Bau, *Nanotechnology*, **,** 015101 (2008).

[43] J. Zhang, Y. S. Hu, J. P. Tessonnier, G. Weinberg, J. Maier,R. Schlogl and D. S. Su, *Advanced Materials*, **20,** 1450-1455 (2008).

[44] B. W. Smith, M. Monthioux and D. E. Luzzi, *Nature*, **396,** 323 (1998).

[45] J. Sloan, A. I. Kirkland, J. L. Hutchison and M. L. H. Green, *Chem. Comm.*, **,** 1319 (2002).

[46] I. V. Krive, R. I. Shekhter and, M. Jonson, *Low Temp. Phys.*, **32,** 887 (2006).

[47] J. W. Kang and H. J. Hwang, *Nanotechnology*, **15,** 1825 (2004).

[48] G. P. Crawford and S. Zumer, Liquid Crystals in Complex Geometries Formed By Polymer and Porous Networks, *Taylor and Francis*, **London** (1996).

[49] J. Leys, G. Sinha, C. Glorieux, and J. Thoen, *Phys. Rev. E*, **71,** 051709 (2005).

[50] G. S. Iannacchione, G. P. Crawford, S. Qian, J. W. Doane, and D. Finotello, *Phys. Rev. E*, **53,** 2402 (2004).

[51] D. E. Feldman and R. A. Pelcovits, *Phys. Rev. E*, **70,** 040702 (2004).

[52] M. K. Ramazanoglu, P. S. Clegg, R. J. Birgeneau, C. W. Garland, M. E. Neubert, and J. M. Kim, *Phys. Rev. E*, **69,** 061706 (2004).

[53] L. O. Dolgov and O. V. Yaroshchuk, *Colloid Polym. Sci.*, **282,** 1403 (2004).

[54] R. Bandyopadhyay, D. Liang, R. H. Colby, J. L. Harden, and R. L. Leheny, *Phys. Rev. Lett.*, **94,** 10781 (2005).

[55] F. Mercuri, S. Paoloni, U. Zammit, and M. Marinelli, *Phys. Rev. Lett.*, **94,** 247801 (2005).

[56] A. V. Zakharov and J. Thoen, *Eur. Phys. J. E*, **17,** 447 (2005).

[57] R. L. Leheny, S. Park, R. J. Birgeneau, J. L. Gallani, C. W. Garland, and G. S. Iannacchione, *Phys. Rev. E*, **67,** 011708 (2003).

[58] A. Zidansek, G. Lahajnar, and S. Kralj, *Appl. Magn. Reson.*, **27,** 311 (2004).

[59] L. M. Chen and J. Toner, *Phys. Rev. Lett.*, **94,** 137803 (2005).

[60] R. J. Ondris-Crawford, G. P. Crawford, S. Zummer, and J. W. Doane, *Phys. Rev. Lett.*, **70,** 194 (1993).

[61] G. P. Crawford, D. W. Allender, and J. W. Doane, *Phys. Rev. A*, **45,** 8693 (1992).

[62] G. P. Crawford, R. J. Ondris-Crawford, S. Zummer, and J. W. Doane, *Phys. Rev. Lett.*, **70,** 1838 (1993).

[63] T. Jin, G. P. Crawford, R. J. Crawford, S. Zumer, and D. Finotello, *Phys. Rev. Lett.*, **90,** 015504 (2003).

[64] B. Zalar, R. Blinc, S. Zummer, T. Jin, and D. Finotello, *Phys. Rev. E*, **65,** 041703 (2002).

[65] T. Jin, B. Zalar, A. Lebar, S. Zumer, and D. Finotello, *Eur. Phys. J. E*, **16,** 159 (2005).

[66] M. Vilfan, N. vrbancic-Kpoac, B. Zalar, S. Zumer, and G. P. Crawford, *Phys. Rev. E*, **59,** R4754 (1999).

[67] A. Golemme, S. Zumer, J. W. Doane, and M. E. Neubert, *Phys. Rev. A*, **37,** 559 (1988).

[68] K. Jian, R. H. Hurt, B. W. Sheldon and G. P. Crawford, *Appl. Phys. Lett.*, **88,** 163110 (2006).

[69] Hemang J. Sahah and Adam K. Fontecchio, *Appl. Phys. Lett.*, **89,** 043123 (2006).

Chapter 9

CONCLUSIONS

9.1 Conclusions

This dissertation presents an experimental study of the thermal transport of metal nanowires, carbon nanotubes and polymer-carbon nanotubes composites. The filling mechanism of Liquid crystals inside small nanopipes is also included in last chapter which provides physics of dynamics of liquids inside small carbon nanopipes.

The major part of this thesis work was to understand the fundamental phonon transport phenomena in the one dimensional system of nanowires/nanotubes in different orientations. These experimental measurements and results resemble the promising applications of these materials in electronic, optoelectronic, sensors, photonics, thermoelectrics, thermal management, high thermal stability and display technology. This thesis work definitely replaces some of the existing materials for higher efficient device production. This chapter will summarize the experimental measurement work done in this thesis and some of the future directions to expand this study.

CoNWs and MWCNTs were grown by electro chemical deposition and CVD techniques inside an AAO template. The diameter of fabricated CoNWs and MWCNTs were 80 nm and length 20 μm. The well aligned CoNWs and MWCNTs inside the AAO template were used to study the anisotropic measurement of thermal properties. The same batch of CoNWs and MWCNTs were taken and dissolved in the AAO by NaOH to obtain pure CoNWs and MWCNTs in powder form, where the nanowires and nanotubes are randomly oriented. These randomly oriented nanowires and nanotubes are taken to make a thin film of respective sample. This sample was used for the same thermal properties measurement called thermal conductivity in randomly oriented direction, where heat transfer is across the randomly oriented nanowires/nanotubes. The measured specific heat and extracted thermal conductivities in anisotropic and randomly oriented directions were compared with their respective bulk sample of Cobalt and graphite powder (particle sizes ∼micro meter order). The SWCNTs were also purchased from the Helix materials solution company and used for the same thermal study in randomly oriented mat sample and compared with MWCNTs.

The high resolution AC Calorimeter technique has been successfully used to measure the heat capacity of the sample. The sample was sandwiched between two silver sheets in such a way that, both the top and bottom silver sheet did not electrically connect with each other. Heater (120Ω) was attached on the top of one silver sheet and a thermister of 1MΩ was attached on the top of the other silver sheet. In this configuration of sample arrangement, we can achieve the thermal wave propagation only through the sample, and the result gives the intrinsic thermal properties of materials.

The particle nature of the bulk powder and randomly orientated CoNWs found deviations of both κ and C_p from that of pure solid cobalt. The κ and C_p exhibit a much stronger temperature dependence and show peak-like maximums and explain the dominance of phonon-boundary scattering in the temperature range 300-400 K. Thermal conductivity of CoNWs was 83 times less than the bulk cobalt, which suggests the dominance of phonon-phonon or phonon-defect scattering. The phonon mean free path in nanowires also describes the anisotropic and scattering propagation of phonon waves. Further study is needed with diameter dependent thermal conductivity to understand much of the basics and insight of phonon transport inside these nanostructures. Different diameter and length dependent thermal studies will give more insight into the science which will help to make promising nanowire based devices.

In the case of MW and SW carbon annotubes measurement, specific heat of all the samples shows very similar behavior from 300-400 K. But thermal conductivity of anisotropic MWCNTs was much higher than the random mat sample of MWCNTs, SWCNTs and graphite powder. This suggested that the phonon propagation along the long axis of carbon nanotubes is one dimensional in nature. There is less or no phonon-boundary scattering. The random composite sample shows a peak-like feature, indicating the phonon-phonon scattering inside the nanotubes, which decreases thermal conductivity as temperature increases. Thermal conductivity also depends upon the diameter of the nanotubes, the smaller the diameter the larger the thermal conductivity as the contact resistance between nanotubes decreases in the mat sample. This was clearly shown in our result. The SWCNTs diameter was less than the MWCNTs, and thus observed higher thermal conductivity. The calculated thermal conductivity along the long axis of MWCNTs was about 700 W m^{-1} K^{-1}, much higher than the random mat sample. The theoretical prediction of thermal conductivity of single nanotubes (10,10 nanotubes) along the long-axis was found to be 6600 W m^{-1} K^{-1}, and the experimental results seems to be very less. So there is more research needed in experimental and simulation to understand the parameters involved in thermal transport in the different configuration of nanotubes heat flow.

The thermal conductivity of PMMA and SWCNTs composites has been measured from 300 - 400 K with different vol% of nanotubes inside polymer matrix. We used a very simple method of dispersion of nanotubes inside the polymer matrix which showed very good dispersion quality. The result shows 130% increase of thermal conductivity with 7.9 vol% dispersion of carbon nanotubes inside polymer matrix. The observed enhanced thermal conductivity has been studied by some theoretical models such as Lewis-Nielsen, Hamilton-Crosse, Xue and the Geometric model. Some of the models closely predict our experimental results, which suggested the good dispersion of carbon nanotubes inside the polymer matrix. The main focus of this polymer composite thermal study was to create high thermal stability materials with dispersing an ultra-low quantity of high thermal, and mechanical stability carbon nanotubes. Not only did the thermal properties of the polymer-nanotube composites change, but also the strength of the materials increased and the electrical conductivity showed percolation behavior, which was studied by many groups and excluded in this thesis. The glass transition (T_g) study done with the MDSC experiment suggested that, T_g value increases with increasing vol% of carbon nanotubes, temperature scan rate and time of heat treatment of the sample prior to do the measurement. These results firmly suggest the higher thermal stability of these nanotube composite systems than the pure polymer. One of the general problems to achieve good dispersion of nanotubes inside the polymers is, when the nanotubes vol% increases, the nanotubes get agglomerate. This makes the composites properties limited in their quality of uses. So a novel method needs to be discovered to overcome such difficulty in dispersion when vol% of carbon nanotubes increases. There is also a more thorough theoretical/simulation study needed to understand the nanotubes thermal wave propagation inside the polymers when vol% of nanotubes increases.

The relaxation dynamic of glass transitions of these polymer-nanocomposites (PMMA + SWCNTs) has been studied with frequency of temperature oscillation by Modulated DSC. The effective glass transition temperature T_g depends upon the frequency of temperature oscillation applied to the sample and also depends on nanotube concentration and rate of heating or cooling the materials. In the vicinity of Tg, a remarkable temperature dependence is clearly observed in the real and imaginary parts of complex heat capacity. The interesting relaxation phenomena observed in the imaginary part and the dynamics of glass transition obtained from the real part of heat capacity are discussed with frequency of temperature modulation, when the polymers undergo a transition from the solid-like region to the liquid-like state. The T_g and T_{max} value are not necessarily equal during heating or cooling but these two values show very differently/similar with the applied frequency of temperature modulation. This experimental study must be helpful in understanding the thermal properties such as glass transition, fragility, relaxation behavior, enthalpy loss and mechanical properties of polymer-CNT based composites. These parameters can be controlled by adjusting the properties and quantity of the nanofillers, applied frequency and rate of heating and cooling the materials.

There has been so much interesting phenomena observed in carbon nanotubes in many different fields of application. In the last chapter we have successfully shown the filling of carbon nanotubes (∼190 nm diameter and 60 μm length) with liquid crystals. Two different ways of filling result in the different structures/molecular arrangement of LCs inside carbon nanopipes. The solvent mixture LCs filling results coating the entire inside wall of the nanotubes and the bulk pure LCs filling, filled the nanopipes completely without any gaps. We also studied the dynamics of phase transition of these liquid crystals confined inside nanopipes. These results predict quite interesting phase transition phenomena of liquid crystals. This study also helps us to understand the liquid flow inside small nanopipes for future nano devices such as nanopippets for drug delivery systems inside the cells. There is further simulation study required to understand the interaction of LC molecules within the confined carbon nanopipes, which can improve the design of future nanofluidic devices.

It is shown that nanowires and carbon nanotubes as components of various nanocomposites have a significant effect on the mechanical, electrical, and thermal properties of these hybrid materials. This study indicates the potential of utilizing nanowires/CNT-based nanocomposites towards electronic, optoelectronic, sensors, and display technology. This study also helps to understand the many basic physics in molecular level of the phonon transport mechanism in nanostructures, dynamics of molecules in polymer nanocomposite systems and in confined nanochannels.

Chapter 10

APPENDIX

10.1 PUBLICATIONS

1. N.R. Pradhan, H. Duan, J. Liang and G.S. Iannacchione, Specific heat and thermal conductivity measurements for anisotropic and random macroscopic composites of cobalt nanowires. *Nanotechnology*, 19, 485712-485712 (2008).

Abstract: We report simultaneous specific heat (C_p) and thermal conductivity (κ) measurements for anisotropic and random macroscopic composites of cobalt nanowires (Co NWs), from 300 to 400 K. Anisotropic composites of Co NW consist of nanowires grown within the highly ordered, densely packed array of parallel nanochannels in anodized aluminum oxide. Random composites are formed by drop-casting a thin film of randomly oriented Co NWs, removed from the anodized aluminum oxide host, within a calorimetric cell. The specific heat measured with the heat flow parallel to the Co NW alignment ($C_p^{\|}$) and that for the random sample (C_p^R) deviate strongly in temperature dependence from that measured for bulk, amorphous, powder cobalt under identical experimental conditions. The thermal conductivity for random composites (κ_R) follows a bulk-like behavior though it is greatly reduced in magnitude, exhibiting a broad maximum near 365 K indicating the onset of boundaryphonon scattering. The thermal conductivity in the anisotropic sample ($\kappa_{\|}$) is equally reduced in magnitude but increases smoothly with increasing temperature and appears to be dominated by phononphonon scattering.

2. N.R. Pradhan, H. Duan, J. Liang and G.S. Iannacchione, The specific heat and effective thermal conductivity of composites containing single-wall and multi-wall carbon nanotubes, *Nanotechnology* 20, 245705-245705 (2009).

Abstract: We present a study of the specific heat and effective thermal conductivity in anisotropic and randomly oriented multi-wall carbon nanotube (MWCNT) and randomly oriented single-wall carbon nanotube (SWCNT) composites from 300 to 400 K. Measurements on randomly oriented MWCNTs and SWCNTs were made by depositing a thin film of CNTs within a calorimetric cell. Anisotropic measurements were made on MWCNTs grown inside the highly ordered, densely packed nanochannels of anodic aluminum oxide. The specific heat of randomly oriented MWCNTs and SWCNTs showed similar behavior to the specific heat of bulk graphite powder. However, the specific heat of aligned MWCNTs is smaller and has weaker temperature dependence than that of the bulk above room temperature. The effective thermal conductivity of randomly oriented MWCNTs and SWCNTs is similar to that of powder graphite, exhibiting a maximum value near 364 K indicating the onset of phononphonon scattering. The effective thermal conductivity of the anisotropic MWCNTs increased smoothly with increasing temperature and is indicative of the one-dimensional nature of the heat flow.

3. N.R. Pradhan, H. Duan, J. Liang and G.S. Iannacchione, Relaxation dynamics of glass transition in PMMA + SWCNT composites by temperature-modulated DSC. *J. Phys. D: Appl. Phys.* 43, 105401 (2010).

Abstract:

The experimental technique offered by temperature-modulated differential scanning calorimeter (TMDSC) used to investigate the thermal relaxation dynamics through the glass transition as a function of frequency was studied for pure PMMA and PMMA-single wall carbon nanotubes (SWCNTs) composites. A strong dependence of the temperature dependence peak in the imaginary part of complex heat capacity (T_{max}) is found during the transition from the glass-like to the liquid-like region. The frequency dependence of Tmax of the imaginary part of heat capacity (C_p) is described by Arrhenius law. The activation energy obtained from the fitting shows increases while the characteristic relaxation time decreases with increasing mass fraction (ϕ_m) of SWCNTs. The dynamics of the composites during glass transition, at slow and high scan rates, are also the main focus of this experimental study. The change in enthalpy during heating and cooling is also reported as a function of scan rate and frequency of temperature modulation. The glass transition temperature (T_g) shows increases with increasing frequency of temperature modulation and m of SWCNTs inside the polymer host. Experimental results show that Tg is higher at higher scan rates but as the frequency of temperature modulation increases, the Tg values of different scan rates coincide with each other and alter the scan rate dependence. From the imaginary part of heat capacity, it is obvious that T_{max} is not the actual glass transition temperature of pure polymer but T_{max} and T_g values can be superimposed when m increases in the polymer host or when the sample undergoes a transition with a certain frequency of temperature modulation.

4. N.R. Pradhan, H. Duan, J. Liang and G.S. Iannacchione, Specific heat and thermal conductivity measurements parallel and perpendicular to the long-axis of Cobalt Nanowires. Supplemental Proceedings: Volume I: Materials Processing and Properties TMS (The Minerals, Metals and Materials Society), Page 159-164 (2008).

Abstract: This paper reports the synthesis and sample construction as well as measurements of the specific heat and thermal conductivity of cobalt nanowires (CoNWs). Specific heat (C_p) and thermal conductivity (κ) is measured by an AC calorimetric technique from 300 to 400 K parallel and perpendicular to the CoNW long-axis. The specific heat both parallel ($C_p^{||}$) and perpendicular ($C_p^{\perp}$) to the long-axis deviates strongly from the bulk amorphous powder behavior above room temperature. The perpendicular thermal conductivity ($\kappa_{\perp}$) of CoNWs follows a bulk-like behavior revealing a maximum value near 365 K, indicating the onset of boundary-phonon scattering. The parallel thermal conductivity ($\kappa_{||}$) increases smoothly with the increase of temperature from 300 to 380 K and appears to be dominated by phonon-phonon scattering.

10.2 PUBLICATIONS PENDING

1. N.R. Pradhan and G.S. Iannacchione, Thermal Properties and Glass Transition in PMMA+SWCNT Composites.

2. N.R. Pradhan, Q. Yang, J. Liang and G.S. Iannacchione, Imaging and Dynamics study of Liquid Crystals Confined Inside Carbon Nanopipes.

Specific heat and thermal conductivity measurements for anisotropic and random macroscopic composites of cobalt nanowires

2008 Nanotechnology 19 485712

(http://iopscience.iop.org/0957-4484/19/48/485712)

IOP Publishing Nanotechnology
Nanotechnology **19** (2008) 485712 (8pp) doi:10.1088/0957-4484/19/48/485712

Specific heat and thermal conductivity measurements for anisotropic and random macroscopic composites of cobalt nanowires

N R Pradhan[1], **H Duan**[2], **J Liang**[2] **and G S Iannacchione**[1]

[1] Department of Physics, Worcester Polytechnic Institute, Worcester, MA 01609, USA
[2] Department of Mechanical Engineering, Worcester Polytechnic Institute, Worcester, MA 01609, USA

Received 12 September 2008, in final form 16 October 2008
Published 12 November 2008

Abstract
We report simultaneous specific heat (c_p) and thermal conductivity (κ) measurements for anisotropic and random macroscopic composites of cobalt nanowires (Co NWs), from 300 to 400 K. Anisotropic composites of Co NW consist of nanowires grown within the highly ordered, densely packed array of parallel nanochannels in anodized aluminum oxide. Random composites are formed by drop-casting a thin film of randomly oriented Co NWs, removed from the anodized aluminum oxide host, within a calorimetric cell. The specific heat measured with the heat flow parallel to the Co NW alignment ($c_p^{\parallel}$) and that for the random sample (c_p^{R}) deviate strongly in temperature dependence from that measured for bulk, amorphous, powder cobalt under identical experimental conditions. The thermal conductivity for random composites (κ_{R}) follows a bulk-like behavior though it is greatly reduced in magnitude, exhibiting a broad maximum near 365 K indicating the onset of boundary–phonon scattering. The thermal conductivity in the anisotropic sample ($\kappa_{\parallel}$) is equally reduced in magnitude but increases smoothly with increasing temperature and appears to be dominated by phonon–phonon scattering.

1. Introduction

Rapid progress in the synthesis, characterization, and processing of materials on the nanometer scale has created promising applications for industry and science. Commensurate in the reduction of size is the reduction of dimensionality. One-dimensional (1D) materials, such as nanowires and nanotubes, attract substantial interest due to the constraints that dimensionality places on physical properties, which is an area of great scientific research. Also, such systems are important for their potential in optoelectronics, sensing, energy conversion, as well as electronic and computing devices [1–7]. While most of the current research effort has been focused on electronic and optical properties, thermal transport properties are starting to attract great interest for basic science and intriguing technical applications [8].

When crystalline solids are confined to the nanometer scale, phonon transport can be significantly altered due to various effects such as increased boundary scattering, change in phonon dispersion, and quantization of phonon transport [5, 6]. Many materials with high thermal conductivity, such as diamond, graphite, natural graphite/epoxy, copper, carbon, as well as SiC and carbon nanotubes, have been investigated and demonstrated promising potential for electronic and optoelectronic devices. Many of these materials can be used in commercial and aerospace applications, including power systems, servers, notebook computers, aircraft, spacecraft and defense electronics [9]. Predicting the thermal conductivity of nanowires plays a crucial role in two important fields: (i) heat dissipation, which is essential for designing future microprocessors, where nanowires may be used as heat drains [6] and (ii) new thermoelectric materials, in which a small thermal conductivity combined with high electronic conductivity typically yields high thermo-power. Because of the unique properties of nanowires, better performance of thermoelectric refrigeration could be realized [8–11].

Knowledge of nanowire thermal and thermoelectric properties is critical for the thermal management of nanowire devices and essential for the design of nanowire thermoelectric devices.

Several theoretical studies on the thermal conductivity (κ) of nanowires [5, 12–18] have shed light on the physics of their basic properties. It is generally understood that nanoscale porosity decreases the permittivity of amorphous dielectrics. But porosity also strongly decreases thermal conductivity [12, 19]. For nanowires with diameters smaller than the bulk phonon mean-free-path (λ_p^B), theory suggests that the thermal conductivity of nanowires will be reduced when compared to the bulk [5, 12, 14, 16–18]. However, there are no predictions regarding the influence of confinement on the behavior of the specific heat (c_p). Knowledge of both c_p and κ is important in determining the thermal relaxation time of materials. It is notable that there have been comparatively few experimental investigations at room temperature and above. The lack of experimental data is due to the difficulty in preparing single nanowire samples with the required specifications. Moreover, measurements made parallel or perpendicular to the long axis of a single nanowire or nanotube are difficult. The use of these materials are more likely in large macroscopic composites where their distribution can be controlled.

Cobalt is a magnetic material and Co nanowires (Co NWs) have distinctive magnetic properties, displaying promising use in applications such as recording media, nanosensors and nanodevices. There are a few experimental investigation of Co NWs magnetic properties [20, 21]. So far to our knowledge there is no experimental work done in measuring thermal conductivity of Co NWs.

This work employs an AC (modulation)-calorimetric technique to measure simultaneously the specific heat and thermal conductivity as a function of temperature on composite samples containing Co NWs from 300 to 400 K. By utilizing both a thin film of randomly oriented Co NWs between thin silver sheets and a composite material containing highly ordered Co NWs array embedded in an aluminum oxide matrix (also sandwiched between thin silver sheets), measurements were made over randomly oriented Co NWs and parallel to the long axis of Co NWs. For comparison a thin film of bulk cobalt in the form of an amorphous powder was also studied under identical experimental conditions.

Following this introduction, section 2 describes the synthesis of the samples and the experimental technique. The results and discussions for the bulk cobalt and Co NWs samples are presented in section 3. Section 4 draws conclusions and presents possible future directions.

2. Experimental procedure

2.1. Synthesis of cobalt nanowires

Co NWs were synthesized by electrodeposition assisted by a homemade anodic aluminum oxide (AAO) template. Figure 1 provides a schematic of the synthesis steps. The AAO templates were obtained by a well-established two-step anodization process [22–25]. Briefly, the first anodic oxidation of aluminum (99.999% pure, Electronic Space Products International) was carried out in a 0.3 M oxalic acid solution at 40 V and 10 °C for 16–20 h. The porous alumina layer formed during this first anodization step was completely dissolved by chromic acid at 70 °C. The treated sample was then subjected to a second anodization with the same conditions as the first. The thickness of the anodic film was adjusted by varying the time of the second anodization step. The resulted AAO templates can be further treated by acid etching to widen the nanopores. Pore diameters were controlled to within 45–80 nm by varying the anodizing voltage and etching time.

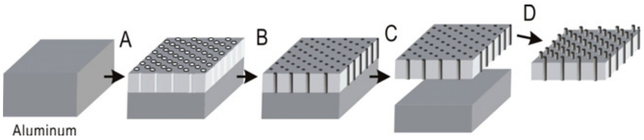

Figure 1. Synthesis process of Co NWs by electrodeposition. The anodized aluminum oxide (AAO) template is obtained by electro-chemical anodization of a pure aluminum sheet (A), the cobalt metal nanowires are electro-deposited inside the pores (B), the separation of Co NWs from Al substrate (C), and finally, the Co NW sample with exposed tips from AAO template (D) after wet etching.

Cobalt nanowires were then electrochemically deposited by AC electrolysis in this nanoporous template using 14 V at 100 Hz for 150 min in an electrolyte solution consisting of 240 g l^{-1} of $CoSO_4{\cdot}7H_2O$, 40 g l^{-1} of HBO_3, and 1 g l^{-1} of ascorbic acid [23, 25]. After Co deposition, AAO can be partially or fully removed by etching with a 2 M NaOH solution to either expose the tips of the Co NWs or to obtain Co NW powders.

The CO NWs were examined by x-ray diffraction (XRD) using a Rigaku CN2182D5 diffractometer and scanning electron microscopy (SEM) using a JEOL JSM-982 microscope equipped with energy-dispersion x-ray spectroscopy (EDS).

For comparison, bulk cobalt powder from Aldrich Inc. (−100 mesh, 99.9 + % pure) with particle size in the range of 2–10 μm was chosen. This bulk powder was used after degassing and drying in vacuum at ~100 °C.

2.2. AC-calorimetry

A modulated (AC) heating technique is used to measure the heat capacity of the Co NWs and bulk powder cobalt samples. In this technique, the sample and cell, loosely coupled to a constant thermal bath, are subjected to a small, oscillatory, heat input. The specific heat and the thermal conductivity can be determined by measuring the frequency dependence of the amplitude and phase of the resulting temperature oscillation. The heat input $P_0 e^{-\omega t}$ with $P_0 \approx$ 0.5 mW is supplied to the sample + cell typically results in a modulated temperature having an amplitude $T_{ac} \approx 5$ mK. The experimental details of our application of AC-calorimetry can be found elsewhere [26–28].

The amplitude T_{ac} is inversely proportional to the heat capacity of the sample. The measured T_{ac} is related to the applied power, heating frequency, total heat capacity, and the various thermal relaxation times by

$$T_{\mathrm{ac}} = \frac{P_0}{2\omega C}\left(1 + (\omega\tau_{\mathrm{e}})^{-2} + \omega^2\tau_{\mathrm{ii}}^2 + \frac{2R_{\mathrm{s}}}{3R_{\mathrm{e}}}\right)^{-1/2} \qquad (1)$$

where P_0 is the power amplitude, ω is the angular frequency of the applied heating power, and $C = C_{\mathrm{s}} + C_{\mathrm{c}}$ is the total heat capacity of the sample + cell. Here, $C_{\mathrm{c}} = C_{\mathrm{H}} + C_{\mathrm{GE}} + C_{\mathrm{AAO}} + C_{\mathrm{Ag}}$ accounts for the contributions to the cell heat capacity by the heater (H), general electric #7031 varnish (GE), silver cell container (Ag), and the AAO template (for the parallel measurement). By subtracting the cell contributions, the heat capacity of the Co NWs may be isolated $C_{\mathrm{CoNW}} = C - C_{\mathrm{c}}$ and by dividing by the mass of Co NWs yields the desired specific heat. Note that the contribution of the carbon-flake thermistor (θ) is much smaller than all these elements and is typically ignored.

There are two important thermal relaxation time constants contained in equation (1), the external $\tau_{\mathrm{e}} = R_{\mathrm{e}}C$ and the internal $\tau_{\mathrm{ii}}^2 = \tau_{\mathrm{s}}^2 + \tau_{\mathrm{c}}^2$ that is the sum of the squared thermal relaxation times for the sample (τ_{s}) and cell (τ_{c}). Here, R_{s} is the sample's thermal resistance and R_{e} is the external thermal resistance to the bath. There is also a phase shift Φ between the applied heat and resulting temperature oscillations but it is more convenient to define a reduced phase shift $\phi = \Phi + \pi/2$ since for heating frequencies between $1/\tau_{\mathrm{e}}$ and $1/\tau_{\mathrm{ii}}$, $\Phi \approx -\pi/2$. The reduced phase shift, to the same accuracy as equation (1), is given by

$$\tan(\phi) = (\omega\tau_{\mathrm{e}})^{-1} - \omega\tau_{\mathrm{i}} \qquad (2)$$

where here $\tau_{\mathrm{i}} = \tau_{\mathrm{s}} + \tau_{\mathrm{c}}$. Since τ_{c} is typically small compared to τ_{s} such that $\tau_{\mathrm{i}} \cong \tau_{\mathrm{ii}}$, equation (2) can be rewritten to give $\tau_{\mathrm{s}} \equiv R_{\mathrm{s}}C_{\mathrm{s}} \cong 1/(\omega^2\tau_{\mathrm{e}}) - (\tan\phi)/\omega$. The measured reduced phase shift ϕ also contains a linear ω dependence due to the fixed digitization rate of the thermal oscillation as the heating frequency increases. The observed ϕ is then given by

$$\phi_{\mathrm{exp}} = \arctan((\omega\tau_{\mathrm{e}})^{-1} - \omega\tau_{\mathrm{i}}) + a\omega + \phi_0 \qquad (3)$$

where a is determined by the digitization rate (in our case, $a \approx 1$) and ϕ_0 is the resulting phase shift due to the digitizing dead-time (delay), which for our apparatus is negligible. Figure 2 shows a typical frequency scan of an AAO only sample at 340 K and illustrates the two relaxation time constants. The solid lines are fits using equations (1) and (3) and indicate the quality of this thermal model. Several such scans were performed at various temperatures to ensure the applicability of thermal analysis. The temperature dependent data shown below were done at a fixed frequency of $\omega = 0.1885\ \mathrm{s}^{-1}$, which is above but close to $1/\tau_{\mathrm{e}}$. In figure 2 at frequencies near twice $1/\tau_{\mathrm{i}}$, a pronounced dip in the temperature amplitude occurs at $3.13\ \mathrm{s}^{-1}$ as well at multiples of this frequency. These features are likely due to the formation of standing waves within the cell and occur when the thermal diffusion length are multiple fractions of the physical thickness of the cell.

The *effective* thermal conductance, the inverse of the thermal resistance, of the sample can then be evaluated from the AC-calorimetric parameters as

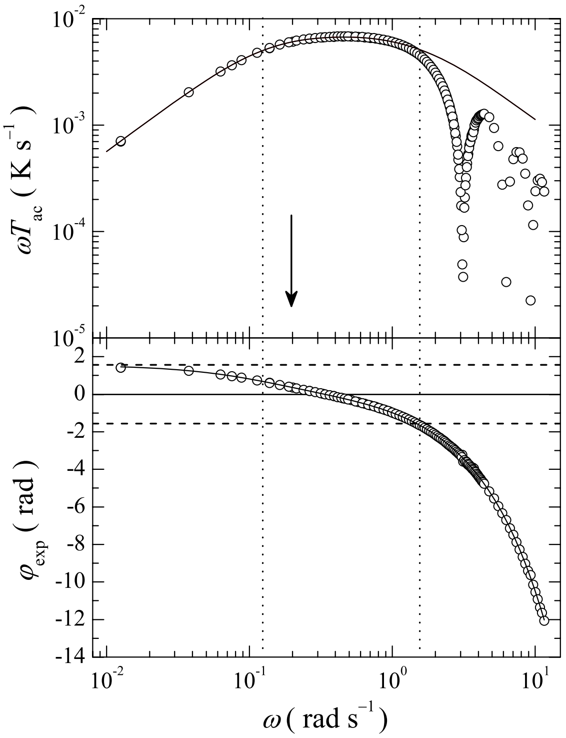

Figure 2. Typical frequency scan of an AAO sample at 340 K representative of all scans performed for all samples. Top: traditional view of the amplitude frequency dependence using a log–log plot of ωT_{ac} versus ω. Bottom: semi-log plot of the observed ϕ versus ω where the horizontal dashed lines indicate $\pm\pi/2$. The solid lines are fits to these data using equations (1) and (3), respectively, yielding consistent time constants. The resulting internal and external time constants are denoted in the plots as the vertical dotted lines. Note that the operating frequency for temperature scans is indicated by the arrow. See text for details.

$$K_{\mathrm{s}} \cong \frac{\omega^2\tau_{\mathrm{e}}C_{\mathrm{s}}}{1 - \omega\tau_{\mathrm{e}}\tan\phi} \qquad (4)$$

where K_{s} is in units of $\mathrm{W\,K^{-1}}$. With the geometric dimensions of sample + cell configuration, the effective thermal conductivity κ_{s} in units of $\mathrm{W\,m^{-1}\,K^{-1}}$ can be calculated directly as $\kappa_{\mathrm{s}} = K_{\mathrm{s}}L/A$, where L is the thickness and A is the area of the Co NWs.

2.3. Sample configurations

The cell and Co NWs samples were prepared in two different ways for measurements with the heat flow parallel to the long axis (anisotropic, denoted with superscript $\|$) and through a randomly oriented (denoted with superscript R) film of nanowires. The sample + cell configuration for the anisotropic measurement is shown in figure 3(a). The general sample + cell configuration consists of a sandwich arrangement of heater, thin silver sheet (0.1 mm thick and 5 mm square), sample, thin silver sheet, and thermistor, all held together by thin applications of GE varnish.

For the anisotropic configuration, the Co NWs embedded in an AAO template were first separated from the Al substrate

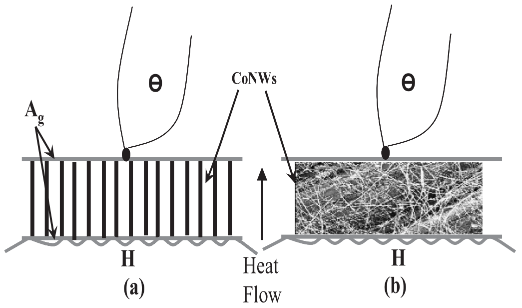

Figure 3. Sample + cell configuration for thermal study. (a) Anisotropic Co NWs configuration. (b) Randomly oriented Co NWs configuration. Labels are H—heater, θ—thermistor, Ag—silver sheet.

by wet etching in a 0.1% $HgCl_2$ solution, and the barrier layer was removed by wet etching in 0.5% H_3PO_4 for 30 min. To ensure a good thermal contact between the Co NWs and the silver sheets, the AAO template was etched by 0.1 M NaOH solution to expose about 2 μm Co NWs on both ends. The typical thickness of Co NWs-AAO sample is about 20 μm. It was carefully sandwiched between the two silver sheets and secured by a thin layer of GE varnish. A 120 Ω strain-gauge heater is attached to one side of the stack and a 1 MΩ carbon-flake thermistor to the other side by GE varnish.

Measurements with the heat flow through a randomly oriented film of nanowires were conducted in a similar arrangement, as shown in figure 3(b). Co NWs were released from the AAO template by completely dissolving the AAO in 0.1 M NaOH. The powder formed of Co NWs were then dispersed in ethanol and drop cast onto one of the cell's silver sheets. This deposition resulted in a film of random oriented Co NWs approximately 0.1 mm thick. The remaining components of the cell were attached again by a thin application of GE varnish. In this randomly oriented sample Co NWs, the heat flow was averaged over all orientations of the nanowires.

For comparison, bulk powder measurements were done under nearly identical experimental conditions. The many point contacts between particles of pure powder Co mimic the random arrangement of the thin film configuration of Co NWs. All sample + cell arrangements had essentially identical areas, contact resistances between sample and cell, and similar thicknesses. In the random oriented and bulk powder sample + cells, the silver sheets might not be perfectly parallel to each other in the sandwich arrangement, but did not touch each other.

Estimation of specific heat and effective thermal conductivity of the cobalt bulk and nanowire samples is straightforward. Each component of the above described sample + cell arrangement was measured separately to determine the contribution of the thin silver sheets, heater, thermistor, GE varnish, and an empty AAO template (identically prepared but without the embedded Co NWs) as measured by the calorimeter under identical experimental conditions. The specific heat (c_p) of the cobalt is then calculated by subtracting these contributions from the total heat capacity and dividing by the cobalt mass. For the anisotropic sample, the mass of the Co NWs embedded in the AAO template was estimated by weight of released Co NWs per unit area. When calculating the effective thermal conductance, we assumed that the entire sample was covered by the cobalt for the bulk powder and random Co NW samples, and Co NWs are parallel to each other for anisotropic samples in AAO nanochannels.

For these measurements, contact resistance plays an important role. All samples and the components of the sample + cell, were measured under identical configurations (thickness, area, mass, and external thermal link). All have the sample, Co powder or NWs, attached to the silver cell with GE varnish as the thermal contact. Thus, the contact resistance contribution should be essentially the same for all measurements. This crucial similarity as well as the choice of bulk Co powder for comparison, allows the behavior of Co NW in the macroscopic samples to be isolated.

3. Results and discussion

3.1. Morphology and microstructure study of Co NWs

Figure 4 shows SEM images of Co NWs embedded in the AAO templates. In figure 4(a), an oblique view of the sample before etching by NaOH solution shows the highly ordered hexagonal pattern of the nanopores. The pore diameter and interpore separation are about 80 and 40 nm, respectively. Figure 4(b) is an SEM image of the Co NWs with the tips exposed by about 2 μm and figure 4(c) is a high-magnification image of the cobalt nanowires. With careful control of the etching process, etching in NaOH solution for 10 min is sufficient to expose all of the NWs tips. The majority of the Co NWs stood straight upward without severe agglomeration. If etching for prolonged time, the exposed Co NWs tended to bend and bundle together, forming islands.

A microstructure study of the as-prepared Co NWs was performed by x-ray diffraction (XRD) and shown in figure 5. The results demonstrates that the Co NWs consists of a mixture of fcc and hcp structures. This is consistent with a nuclear magnetic resonance (NMR) study by Strijkers *et al* [29] on Co NWS synthesized by direct current method. The XRD peaks near 41.685° and 47.57° correspond to the $(10\bar{1}0)$ and $(10\bar{1}1)$ planes of the hcp structure. The peak near 51.522° is attributed to the (200) plane of the fcc structure. The peak near 44° could be a combination of the diffraction from the (0002) plane of the hcp structure and the (111) plane of the fcc structure; that near 75° could be a combination of the diffraction from the (1120) plane of the hcp structure and the (220) plane of the fcc structure. It is also shown that the fabricated Co nanowires have a preferential orientation of direction (0002). The preferred orientation of the nanowires is attributed to the growth of the nanowires within the pores of the alumina film. No diffraction peaks from cobalt-oxide or from the alumina are seen in figure 5.

3.2. Specific heat of Co NWs

The Specific heats of bulk powder cobalt as well as anisotropic Co NWs and randomly oriented Co NWs mat configuration

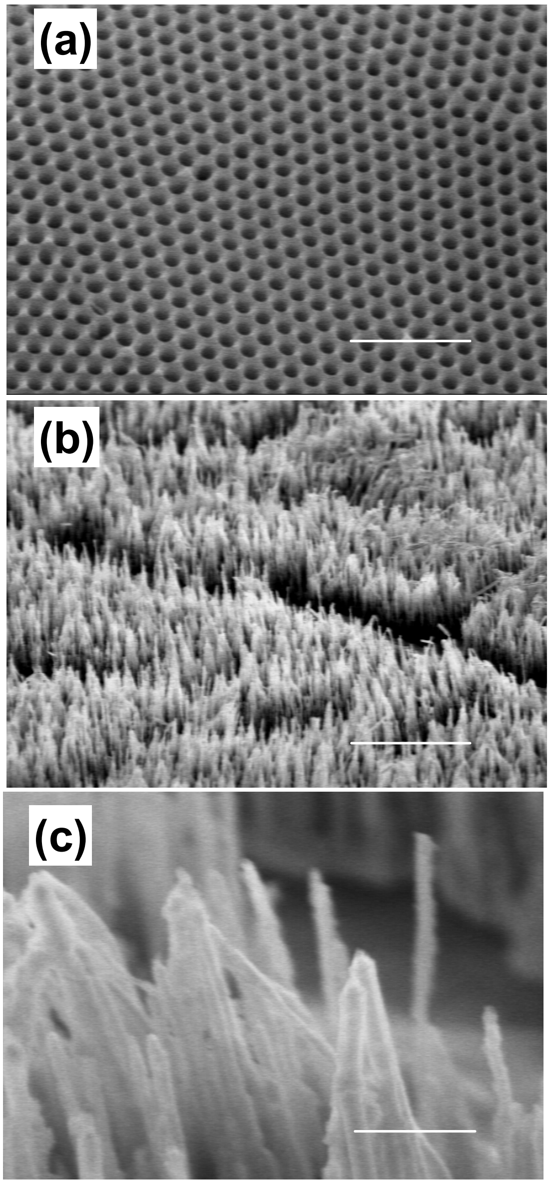

Figure 4. SEM images of (a) the as-prepared Co NWs sample before etching, (b) 'forest' of Co NWs after partially etching of the AAO membrane, and (c) Co NWs with higher magnification. The scale bar is 500 nm (a), 5 μm (b), and 500 nm (c).

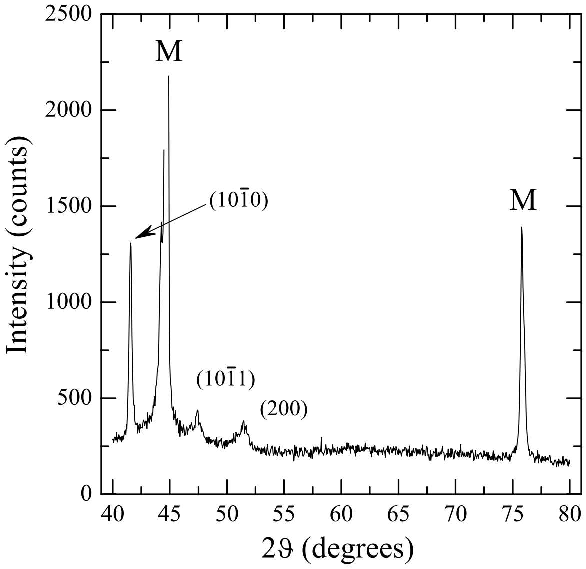

Figure 5. XRD pattern of Co NWs showing different planes.

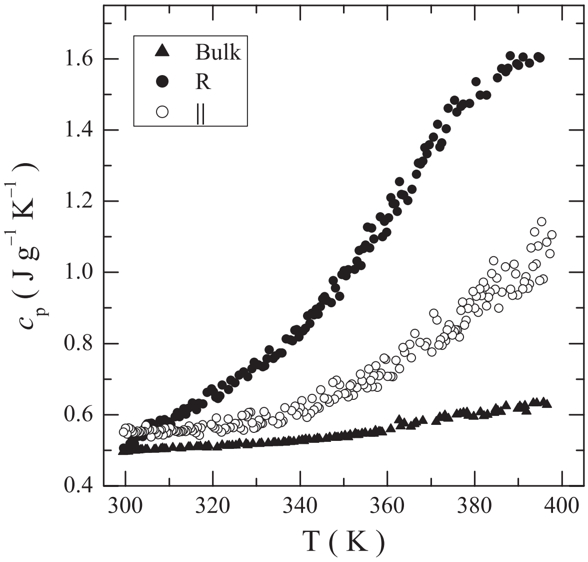

Figure 6. Specific heat of bulk powder cobalt (solid triangles) and randomly oriented Co NWs samples (dots) and anisotropic Co NWs samples (open circles) from 300 to 400 K.

are shown in figure 6. The specific heats of all samples were determined as a function of temperature from 300 to 400 K. The cobalt bulk powder sample measurement yields a $c_p^B = 0.49$ J g^{-1} K^{-1} at 300 K increasing smoothly to 0.61 J g^{-1} K^{-1} at 400 K. This result is about 13% higher in magnitude at 325 K but similar in temperature dependence with the literature [30, 31] and indicates the absolute uncertainty in magnitude. However, as is typical for an AC-calorimetric technique, the relative uncertainty (i.e. temperature dependence) is very higher (better than 0.5%). The magnitude of the specific heat for the two Co NW samples are $c_p^{\parallel} = 0.53$ J g^{-1} K^{-1} and $c_p^R = 0.50$ J g^{-1} K^{-1} at 300 K. For the anisotropic Co NW configuration, $c_p^{\parallel}$ increases linearly from room temperature to ~320 K in a fashion similar to bulk sample. Above 320 K, $c_p^{\parallel}$ increases much more rapidly with temperature than the bulk. In the case of randomly oriented mat sample, c_p^R increases more rapidly than that of either the anisotropic or the bulk sample from 318 to 387 K, above which it begins to decrease.

In principle, since the specific heat is a scalar quantity related to the thermal fluctuations of internal energy, one would expect that c_p should be independent of heat-flow geometry for a given structure of the cobalt. The differences observed here are likely due to the composite nature of the sample + cell configuration. The similarity, at least just above room temperature, between $c_p^{\parallel}$ and c_p^B is understandable as in this heat-flow configuration, the length of the Co NWs is comparable to the size of the bulk powder sample. The deviation beginning at ~320 K may be a consequence of the 1D nature of the nanowires since one might expect 'bunching' of the phonons (phonon–phonon scattering) to dominate at some elevated temperature. For the random Co NW film sample, there is likely a very large number of contacts, on the nanometer scale, between individual Co NWs. Thus, the c_p^R measured is almost certainly an effective value for the sample + cell composite. However, the observed strong temperature dependence and maximum at ~370 K for c_p^R is an intriguing indication of engineering materials with specific thermal properties.

3.3. Thermal conductivity of Co NWs

Figure 7(a) shows the effective thermal conductivity of bulk powder cobalt at 300 K to be $\kappa_B \approx 67$ W m^{-1} K^{-1} with a strong temperature dependence reaching a maximum at ~360 K. The literature value for pure cobalt at 300 K is 90 W m^{-1} K^{-1} and displays only a weak temperature dependence [32]. The extracted thermal conductivity κ_B is lower by 20 % is most likely due to incomplete filling of the cell. The maximum observed is also likely due to the powder nature of micron sized amorphous particles sandwiched in the cell where boundary–phonon scattering begins to dominate at ~360 K. Again, as with the specific heat, the uncertainty in these measurements are typical for the absolute value but retains the high relative precision. The choice of samples and the carefully matched sample + cell configuration allow for direct comparison between these bulk measurements with those for the Co NW samples.

The derived thermal conductivity of the Co NWs for the two heat-flow configurations are shown in figure 7(b). Both $\kappa_\parallel$ and κ_R have values 83 times less than the bulk at 300 K. However, for increasing temperatures, $\kappa_\parallel(T)$ behaves quite differently from the observed bulk trend, increasing in a smooth manner up to ~380 K at which a small 'kink' is seen to a nearly constant value of $\kappa_\parallel \approx 4$ W m^{-1} K^{-1}. Although the uncertainty in absolute values is higher for the measured κ compared to c_p, the marked reduction of magnitude of κ in both configurations with respect to the bulk is consistent with the 1D nature of the materials, in which phonon–boundary scattering dominates the phonon–phonon scattering. Very similar results are reported in bismuth telluride nanowires by Zhou *et al* [33]. However, for $\kappa_\parallel$, the kink to a constant value at ~380 K may be an indication of a cross-over from phonon–phonon to defect–phonon scattering within the NWs. For the random Co NW sample, κ_R exhibits a similar temperature dependence as the bulk, although of greatly reduced magnitude. As with κ_B, the observed maximum for κ_R seen at ~360 K is again likely due to the composite nature of the sample + cell arrangement and the onset of boundary–phonon scattering. The junctions between the nanowires dominant the heat transfer for κ_R just as the contacts between bulk powder particles were for κ_B. The slight difference in temperature for the observed maximum is consistent with the bulk powder particles being of much larger size (microns) compared to the diameter of the nanowires.

To better compare the temperature dependence of the effective thermal conductivity, normalized values (to that observed at 300 K, i.e. $\kappa/\kappa_{300\,K}$) are shown in figure 8 for the bulk powder and the Co NWs in the two heat-flow configurations. The fractional change of κ is much larger in the randomly oriented Co NWs samples and, as mentioned previously, is likely due to the enormous number of wire–wire junctions. The fractional change of the anisotropic configuration matches closely up to 360 K with the bulk cobalt powder. Above 360 K the bulk begins to decrease. Although study on Co NW with different diameters is still in-going in our lab, it has been recently found that the thermal conductivity of silicon nanowires increases with increasing diameter [34], consistent with a cross-over to bulk-like behavior seen in our investigation between the random film of Co NW and bulk powder Co.

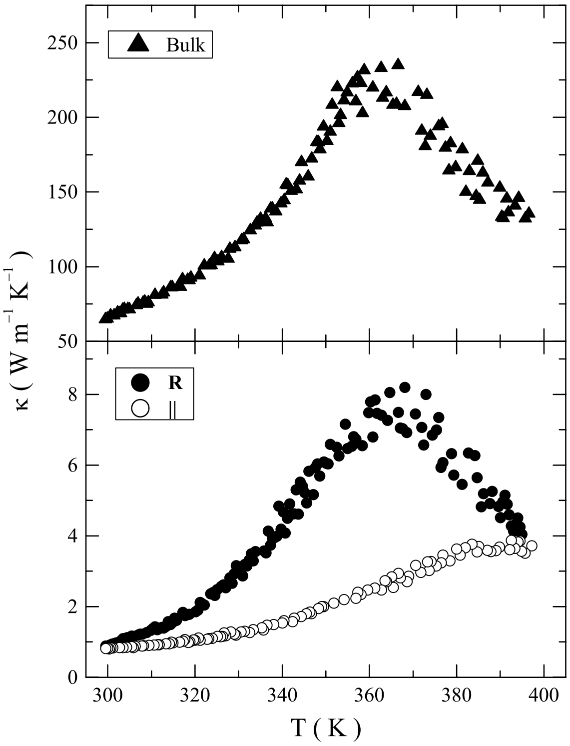

Figure 7. Top panel—effective thermal conductivity of bulk Co as a function of temperature from 300 to 400 K. Bottom panel—effective thermal conductivity of anisotropic Co NWs (open circles) and randomly oriented powder Co NWs (dots) as a function of temperature from 300 to 400 K.

3.4. Phonon mean-free-path

Although the results obtained here are for macroscopic composite samples, some insight can be obtained by considering the contribution of phonons with respect to the heat-flow configurations. The lattice specific heat provides important information of the modified phonon spectrum in low-dimensional system such as nanotubes and nanowires [35, 36]. The temperature dependent phonon mean-free-path (λ_p), obtained from thermal conductivity measurements, is the result of scattering of phonons from domain boundaries, by defects, and/or phonon–phonon scattering [37]. Therefore, it is interesting to estimate λ_p in

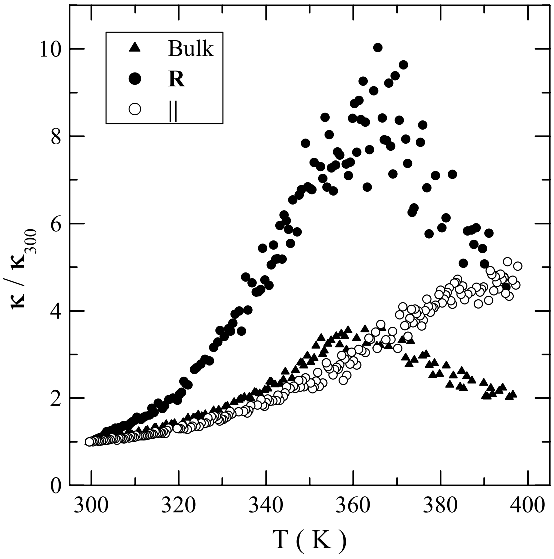

Figure 8. Normalized effective thermal conductivity of bulk cobalt (solid triangles), anisotropic (open circles), and randomly oriented Co NWs sample (dots) as a function of temperature from 300 to 400 K.

a nanowires and compare the relative magnitudes among the samples studied.

The phonon mean-free-path may be calculated from the experimentally measured thermal conductivity and specific heat using

$$\lambda_p = \frac{3\kappa}{v_p c_p \rho}, \tag{5}$$

where ρ is the mass density of the cobalt sample and v_p is the velocity of phonons in cobalt (here taken as that for pure cobalt 4700 m s^{-1} and a constant). The values estimated for anisotropic Co NW is $\lambda_p^{\parallel} \approx 485$ nm and in the random configuration is $\lambda_p^R \approx 203$ nm at 300 K. For the bulk powder cobalt sample, $\lambda_p^B \approx 40$ μm at 300 K. Since the cobalt nanowires are 20 μm long, 80 nm in diameter, and that bulk particles are 2–10 μm in size, one would expect that boundary scattering would dominate for the randomly oriented Co NWs samples ($\lambda_p^R > 80$ nm) and bulk powder ($\lambda_p^B > 10$ μm) beginning at the lowest temperatures. Conversely, one would not expect boundary–phonon scattering to play a significant role for the anisotropic configuration since $\lambda_p^{\parallel} \ll 20$ μm instead one can consider phonon–phonon or defect–phonon scattering mechanisms. The maximums observed in κ for the bulk and randomly oriented Co NW configuration could be the result of the onset of additional scattering mechanisms.

It is interesting to note that the maximums in κ and c_p seen for the randomly oriented mat sample of Co NWs do not occur at the same temperatures, being ~365 K and ~382 K, respectively. Also, the maximum in κ observed in the bulk are not reflected by a similar feature in c_p just as the plateau in κ seen for the anisotropic Co NW configuration has no companion feature in its c_p. These observations indicates that the fluctuations in internal energy reflected in c_p are independent to the scattering mechanisms responsible for the κ results in these macroscopic composite sample + cell arrangements.

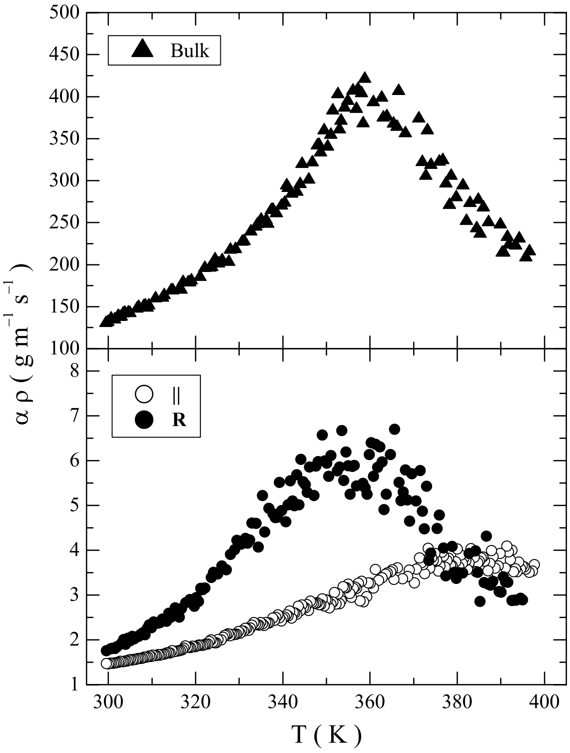

Figure 9. Plot of the product of mass density (ρ) and thermal diffusivity (α) over the temperature range 300–400 K. Top panel—bulk cobalt. Bottom panel—anisotropic (open circles) and randomly oriented Co NWs sample (dots). Note that $\alpha\rho \propto \lambda_p v_p$; see text for details.

The assumption of using the pure cobalt phonon velocity as a constant in temperature and the same for all samples is a weak one. From the definition of the thermal diffusivity, $\alpha = \kappa/c_p\rho$, one can estimate the temperature dependence of the product of the phonon mean-free-path and the phonon velocity as

$$\alpha\rho = \lambda_p v_p \rho/3 = \frac{\kappa}{c_p} \tag{6}$$

where α is the thermal diffusivity. Here, we assume that the mass density ρ is taken as constant and so, from equation (6) gives $\lambda_p v_p \propto \kappa/c_p$. Figure 9 shows the result for the bulk powder and the Co NW configurations studied as a function of temperature. A broad maximum centered at ~350 K is seen for the Co NW(random mat) sample and a much sharper 'peak' is seen at a slightly higher temperature of 360 K for the bulk cobalt. For Co NW (||), only a plateau is revealed beginning at 380 K. These results suggest that the phonon mean-free-path and velocity are not trivially related and have complex temperature dependence for these macroscopic composite samples.

4. Conclusion

We report the experimental results of the specific heat and effective thermal conductivity of two types of arrangement of

Co NWs, i.e. randomly oriented and anisotropic, and compare them with bulk cobalt powders. The particle nature of the bulk powder and randomly orientated Co NWs leads to strong deviations of both κ and c_p from that of pure solid cobalt. The κ and C_p exhibit a much stronger temperature dependence and show peak-like maximums versus temperature. The results suggest the dominance of phonon–boundary scattering in the temperature range 300–400 K. Whereas the thermal properties of the more uniform and confined anisotropic Co NWs samples demonstrate smooth temperature dependence, which suggests the dominance of phonon–phonon or phonon-defect scattering. These results suggest that the composite materials containing nanowires can be engineered for a wide range of applications.

Acknowledgments

H Duan and J Liang would like to thank the National Nanotechnology Infrastructure Network/Center for Nanostructured Systems at Harvard University for use of their nanofabrication and microscopy facilities.

References

[1] Collins P G, Bando H and Zettl A 1998 *Nanotechnology* **9** 153
[2] Cui Y and Lieber M 2001 *Science* **291** 851
[3] Dresselhaus M S, Lin Y-M, Cronin S B, Rabin O, Black M R, Dresselhaus G and Koga T 2001 *Semicond. Semimet.* **71** 1
[4] Wu Y, Fan R and Yang P 2002 *Int. J. Nanosci.* **1** 1
[5] Yang R, Chen G and Dresselhaus M S 2005 *Phys. Rev.* B **72** 125418
[6] Mingo N, Yang L, Li D and Majumdar A 2003 *Nano Lett.* **3** 1713
[7] McConnel A D and Goodson K E 2005 *Ann. Rev. Heat Transfer* **14** 129
[8] Cahill D G, Ford W K, Goodson K E, Mahan G D, Majumdar A, Maris H J, Merlin R and Phillpot S R 2002 *J. Appl. Phys.* **93** 793
[9] Zou J and Balandin A 2001 *Proc. Electrochem. Soc.* **2001** 70
[10] Mahan G, Sales B and Sharp J 1997 *Phys. Today* **50** 42
[11] Hicks L D and Dresselhaus M S 1993 *Phys. Rev.* B **47** 12727
[12] Li D, Wu Y, Kim P, Shi L, Yang P and Majumdar A 2003 *Appl. Phys. Lett.* **14** 2934
[13] Barman S and Srivastava G P 2006 *Phys. Rev.* B **73** 205308
[14] Chena Y, Lib D, Yangc J, Wuc Y and Majumdare J R L A 2004 *Physica* B **349** 270
[15] Chen Y, Li D, Lukes J R and Majumdar A 2005 *J. Heat Transfer* **127** 1129
[16] Volz S and Chen G 1999 *Appl. Phys. Lett.* **75** 2056
[17] Prasher R 2006 *Phys. Rev.* B **74** 165413
[18] Chen K-Q, Li W-X, Duan W, Shuai Z and Gu B-L 2005 *Phys. Rev.* B **72** 045422
[19] Trit T M 1999 *Science* **283** 804
[20] Xu J, Huang X, Xie G, Fang Y and Liu D 2005 *Mater. Lett.* **59** 981
[21] Vila L, George J M, Faini G, Popa A, Ibels U, Ounadjea K and Paux L 2002 *IEEE Trans. Mag.* **38** 185
[22] Zhou Z F, Zhou Y C, Pan Y and Wang X G 2008 *Mater. Lett.* **62** 3419
[23] Liang J, Chik H, Yin A and Xu J M 2002 *J. Appl. Phys.* **91** 2544
[24] Liang J, Chik H and Xu J M 2002 *IEEE J. Sel. Top. Quantum Electron.* **8** 998
[25] Li J, Papadopoulos C, Xu J M and Moskovits M 1999 *Appl. Phys. Lett.* **75** 367
[26] Sinha S, Barjami S, Iannacchione G, Schwab A and Muench G 2005 *J. Nanopart. Res.* **7** 651
[27] Clegg P S, Stock C, Birgeneau R J, Garland C W, Roshi A and Iannacchione G S 2003 *Phys. Rev.* E **67** 021703
[28] Roshi A, Iannacchione G S, Clegg P S and Birgeneau R J 2004 *Phys. Rev.* E **69** 031703
[29] Strijkers G J, Dalderop J H J, Broeksteeg M A A, Swagten H J M and de Jonge W J M 1999 *J. Appl. Phys.* **86** 5141
[30] Ramji Rao R and Ramanand A 1979 *Phys. Rev.* B **19** 1972
[31] Bendick W and Pepperhoff W J 1979 *J. Phys. F: Met. Phys.* **11** 2185
[32] Tritt T M 2004 *Thermal Conductivity: Theory Properties and Application* vol 4 (Dordrecht/New York: Kluwer Academic/Plenum)
[33] Zhou J, Jin C, Seol J, Li X and Shi L 2005 *Appl. Phys. Lett.* **87** 133109
[34] Hochbaum A, Chen R, Delgado R D, Liang W, Garnett E C, Najarian M, Majumdar A and Yang P 2008 *Nature* **451** 163
[35] Dames C, Powdel B, Wang W Z, Huang J Y, Ren Z F, Sun Y, Oh J I and Chen G 2005 *Appl. Phys. Lett.* **87** 031901
[36] Hone J, Batlogg B, Benes Z, Johnson A T and Fischer J E 2000 *Science* **289** 1730
[37] Hone J, Whitney M, Piskoti C and Zettl A 1999 *Phys. Rev.* B **59** R2514

The specific heat and effective thermal conductivity of composites containing single-wall and multi-wall carbon nanotubes

2009 Nanotechnology 20 245705

(http://iopscience.iop.org/0957-4484/20/24/245705)

IOP PUBLISHING NANOTECHNOLOGY
Nanotechnology **20** (2009) 245705 (7pp) doi:10.1088/0957-4484/20/24/245705

The specific heat and effective thermal conductivity of composites containing single-wall and multi-wall carbon nanotubes

N R Pradhan[1], **H Duan**[2], **J Liang**[2] **and G S Iannacchione**[1]

[1] Department of Physics, Worcester Polytechnic Institute, Worcester, MA 01609, USA
[2] Department of Mechanical Engineering, Worcester Polytechnic Institute, Worcester, MA 01609, USA

Received 31 January 2009, in final form 24 April 2009
Published 27 May 2009
Online at stacks.iop.org/Nano/20/245705

Abstract
We present a study of the specific heat and effective thermal conductivity in anisotropic and randomly oriented multi-wall carbon nanotube (MWCNT) and randomly oriented single-wall carbon nanotube (SWCNT) composites from 300 to 400 K. Measurements on randomly oriented MWCNTs and SWCNTs were made by depositing a thin film of CNTs within a calorimetric cell. Anisotropic measurements were made on MWCNTs grown inside the highly ordered, densely packed nanochannels of anodic aluminum oxide. The specific heat of randomly oriented MWCNTs and SWCNTs showed similar behavior to the specific heat of bulk graphite powder. However, the specific heat of aligned MWCNTs is smaller and has weaker temperature dependence than that of the bulk above room temperature. The effective thermal conductivity of randomly oriented MWCNTs and SWCNTs is similar to that of powder graphite, exhibiting a maximum value near 364 K indicating the onset of phonon–phonon scattering. The effective thermal conductivity of the anisotropic MWCNTs increased smoothly with increasing temperature and is indicative of the one-dimensional nature of the heat flow.

1. Introduction

Since their discovery in 1991 by Sumio [1], carbon nanotubes (CNTs) have been the focus of intense research and have many potential application in electronic, optical, thermal management and energy conversion devices because of their unique properties. The electrical and mechanical properties of CNTs have been extensively investigated [2, 3], while the thermal properties of CNTs are of interest in basic science as nanotubes are model systems for low-dimensional materials. However, for large scale technical applications, the manipulation of single nanotubes becomes impractical. Several groups have measured the thermal properties of millimeter sized thin CNT films and packed carbon fibers [4–10]. Current efforts to exploit the attractive properties of carbon nanotubes have focused on macroscopic composites containing engineered or self-assembled arrays of CNTs. One route has been to order the CNTs through the interaction of an anisotropic liquid crystalline host [11] while another route has been to grow the CNT within the ordered porous structures of a host matrix [12].

Numerous studies, mostly theoretical, have been recently conducted to understand the thermal properties of CNTs and assess their potential for applications [13–18]. These theoretical investigations have indicated that single-wall CNTs (SWCNT) have the highest thermal conductivity along the long axis of the nanotube, predicted to be as high as 6600 W m^{-1} K^{-1} at room temperature [19]; three times that of diamond. The experimentally measured thermal conductivity of an individual multi-wall CNT (MWCNT) is reasonably consistent and was found to be 3000 W m^{-1} K^{-1} [20]. However, the thermal conductivity of a random film sample of SWCNT was reported to be only 35 W m^{-1} K^{-1} [7]. For SWCNT bundles, the reported value of thermal conductivity was 150 W m^{-1} K^{-1} by Shi *et al* [21]. The thermal conductivity of aligned MWCNTs samples was reported to range between 12 and 17 W m^{-1} K^{-1} [10] and even as low as 3 W m^{-1} K^{-1} [22]. Other results found it a somewhat higher near 27 W m^{-1} K^{-1} [4, 23, 24]. An attempt to understand this wide variation of the measured thermal conductivity (and to a lesser extent the specific heat) of MWCNTs evoked the existence of thermal boundary resistance as a possible mechanism for the dramatically lower thermal conductivity of MWCNT bundles and films compared to that of a single MWCNT [25]. However, the situation remains unresolved.

In this paper, we report measurements of the specific heat and effective thermal conductivity by an AC-calorimetric technique on composites containing random and aligned dense packing of carbon nanotubes. For the random film of CNTs, the heat flow is predominately perpendicular to the long nanotube axis while in the composites of aligned CNTs in dense packed nanochannels of anodic aluminum oxide (AAO) the heat flow is primarily along the long axis. The bulk powder graphite was also studied as a reference having a similar packing of nano-particles within an identical sample + cell arrangement. The temperature scans ranged from 300 to 400 K for aligned MWCNTs in AAO, and randomly oriented films of MWCNTs, SWCNTs, and graphite powder. In general, the temperature dependence of the specific heat of randomly oriented films of MWCNTs and SWCNTs is similar with that of bulk graphite powder. In contrast, the specific heat of aligned MWCNTs in AAO has a weaker temperature dependence than bulk behavior above room temperature. The effective thermal conductivity of randomly oriented MWCNTs and SWCNTs is similar to that of powder graphite, exhibiting a maximum value near 364 K indicating the onset of boundary-phonon scattering. The effective thermal conductivity of the anisotropic MWCNTs increases smoothly with increasing temperature and is indicative of the one-dimensional nature of the heat flow.

Following this introduction, the experimental details including material synthesis, composite sample fabrication, and calorimetric details are shown in section 2. The resulting data are presented and discussed in section 3. Conclusions are drawn and future work outlined in section 4.

2. Experimental details

2.1. Synthesis of carbon nanotubes and samples

Multi-wall carbon nanotubes were synthesized by a chemical vapor deposition (CVD) technique in an AAO template as shown in figure 1. The AAO template was obtained by a two-step anodization process; details of which have been previously published [26, 27, 12]. Briefly, the first-step anodization of aluminum (99.999% pure, Electronic Space Products International) was carried out in a 0.3 M oxalic acid solution under 40 V at 10 °C for 16–20 h. The porous alumina layer formed during this first anodization step was completely dissolved by chromic acid at 70 °C. The sample was then subjected to a second anodization step under the same conditions as the first. The thickness of the porous anodic film was adjusted by varying the time of the second anodization step. The resulted AAO templates can be further treated by acid etching to widen the nanopores. For the samples used in this work, the pore diameter was controlled to within 45–80 nm by varying the anodizing voltage and etching time.

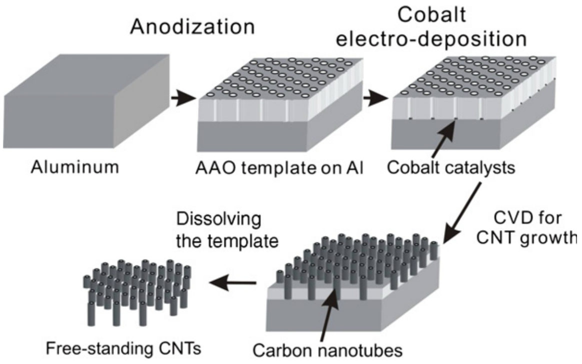

Figure 1. Diagram of the synthesis steps of CNTs by chemical vapor deposition. The anodized-aluminum-oxide (AAO) template is obtained by electrochemical anodization of a pure aluminum sheet, the cobalt catalyst are electro-deposited inside the pores and the CNT is grown by CVD method. The CNTs are separated from Al substrate by dissolving AAO template with NaOH solution.

Cobalt particles, used as catalysts for the carbon nanotube growth, were electrochemically deposited at the bottom of the pores using AC electrolysis (14 V at 100 Hz) for 30 s in an electrolyte consisting of $CoSO_4 \cdot 7H_2O$ (240 g l^{-1}), HBO_3 (40 g l^{-1}), and ascorbic acid (1 g l^{-1}). The ordered array of nanotubes were grown by first reducing the catalyst by heating the cobalt-loaded templates in a tube furnace at 550 °C for 4 h under a CO flow (60 cm^3 min^{-1}). The CO flow was then replaced by a mixture of 10% acetylene in nitrogen at the same flow rate. In a typical synthesis, the acetylene flow was maintained for 1 h at 600 °C. The as-prepared MWCNTs embedded in the AAO template were used as the aligned MWCNT sample. The MWCNTs can be released from the template by removing the aluminum oxide in a 0.1 M NaOH solution at 60–80 °C for 3 h. The released MWCNTs were used to make randomly oriented MWCNT film sample. From a 3 cm^2 MWCNT + AAO sample, 1.82 mg of MWCNTs were released corresponding to an embedded mass of MWCNT of 0.61 mg cm^{-2}. From the dimensional information of the MWCNT and assuming an AAO pore density of about 10^{10} cm^{-2}, a theoretical value of the MWCNT mass per area of MWCNT + AAO is 0.86 mg cm^{-2}, reasonably close to the measured value. The mass of the MWCNTs embedded inside the AAO template sample was thus estimated by using the measured mass of released CNTs per unit area of composite.

Single-wall carbon nanotubes (SWCNT) were obtained from Helix Material Solutions, Inc. [28] and used without further processing. The reference graphite powder was obtained from AGS and has the following composition; 95.2% carbon, 4.7% ash, and 0.1% moisture and other volatiles. The graphite powder was used after degassing at 100 °C under vacuum for 2 h. Morphology of the MWCNTs, SWCNTs and graphite particles were examined by a JEOL JSM-7000F scanning electron microscope (SEM) and a Philips CM12 transmission electron microscope (TEM) before the calorimetric measurements. Aspects of the sample morphology, particularly the diameters of the CNTs, were analyzed using the *Image J* processing software. The dimensions were measured 10 times from multiple TEM images for all samples and the average and standard deviations were reported.

For the calorimetric measurements, contact resistance plays an important role. All samples and the components of the sample + cell, were measured under identical experimental conditions (e.g. thickness, area, mass, and external thermal link), and were similarly configured in a sandwiched pattern between two silver or silver and aluminum oxide (for aligned MWCNTs) samples. Although the similarity of construction should result in similar contact resistance, due to local variation of surface roughness, sample-to-sample variations, and uncertainties in particle geometries, the contact resistance should be considered averaged over the ∼cm in-plane length-scale of the composite sample and thus lead to large uncertainties in the absolute magnitude of the derived thermal conductivity. However, the relative precision of the temperature dependence of the thermal conductivity should be comparable.

2.2. *Sample + cell configurations*

Details of the experimental sample + cell configuration have been reported elsewhere [12] and also shown in figure 2. Briefly, the aligned MWCNT + AAO sample were in excellent thermal contact on one end by their anchoring to the Al base of the AAO and contact on the other end was made to a thin silver sheet by a thin layer of GE varnish (General Electric #7031 varnish). The typical thickness of MWCNT + AAO sample was about 20 μm. This aligned sample was arranged as a silver sheet/GE varnish/MWCNT + AAO/Al sandwich. One side of the 'stack' has attached a 120 Ω strain-gauge heater and the other a 1 MΩ carbon-flake thermistor. For the randomly oriented thin film samples, the powder-form MWCNTs, separately obtained SWCNTs, and graphite powders were drop cast on a thin silver sheet then sandwiched by another identical silver sheet on top by a thin layer of GE varnish forming a nearly identical 'stack' (in dimension and total mass) as the aligned sample. All components of all sample + cells were carefully massed in order to perform background subtractions.

2.3. *AC-calorimetric technique*

An AC (modulated) heating technique is used for the measurements presented in this paper. A sinusoidal heat input $P_0 e^{-\omega t}$ with $P_0 \approx 0.5$ mW was supplied to one side and the resulting modulated temperature oscillation T_{ac} was measured at opposite side of the sample + cell. The experimental technique details can also found elsewhere [12]. The amplitude T_{ac} can be expressed as:

$$T_{ac} = \frac{P_0}{2\omega C}\left(1 + (\omega\tau_e)^{-2} + \omega^2\tau_{ii}^2 + \frac{2R_s}{3R_e}\right)^{-1/2}, \qquad (1)$$

where ω is the applied heating frequency, $C = C_s + C_c$ is the total heat capacity (C_s is the heat capacity of sample and C_c is the heat capacity of cell). Here, $C_c = C_H + C_{GE} + C_{AAO} + C_{Ag} + C_{Al}$ for the aligned MWCNT + AAO sample and $C_c = C_H + C_{GE} + C_{Ag}$ for randomly oriented MWCNT, SWCNT, and bulk powder graphite samples. By subtracting the cell contribution, the heat capacity of the carbon nanotubes may be isolated as $C_{CNT} = C_s = C - C_c$ and $C_p = C_s/m$, where m is the mass of the nanotubes or graphite powder. The contribution of the carbon-flake thermistor is negligible, having a very weak temperature dependence, and so, is ignored.

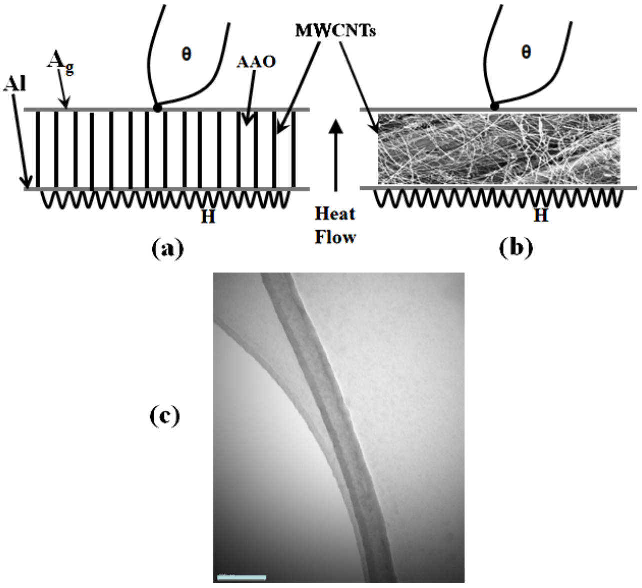

Figure 2. In (a) and (b), a cartoon depicting the sample cell configuration for the aligned MWCNT + AAO sample (a) and for the random film of MWCNT, SWCNT, or graphite powder samples (b). In (c) a typical TEM of a MWCNT is shown with the bar in the lower left of the micrograph representing 100 nm. Image analysis of such micrographs yield the geometric properties of the CNTs.

There are two important thermal relaxation time constants in equation (1), $\tau_e = R_e C$ and $\tau_{ii}^2 = \tau_s^2 + \tau_c^2$, the external and internal respectively, where τ_s refers to sample relaxation and τ_c refers to cell relaxation time constants. Here, R_s is the sample internal thermal resistance and R_e is the external thermal resistance linking the sample + cell to the bath. The reduced phase shift (ϕ) between the input heat and resulting temperature oscillation as a function of heating frequency scan can directly measure τ_e and τ_i using:

$$\tan(\phi) = (\omega\tau_e)^{-1} - \omega\tau_i, \qquad (2)$$

where $\tau_i = \tau_s + \tau_c$ and typically $\tau_c \ll \tau_s$, hence $\tau_i \simeq \tau_{ii}$. Equation (2) can be rewritten to give $\tau_s \equiv R_s C_s \cong 1/(\omega^2\tau_e) - (\tan\phi)/\omega$. The effective thermal conductance, the inverse of the effective thermal resistance, of the sample can then be evaluated from the experimental parameters as:

$$K_s \cong \frac{\omega^2\tau_e C_s}{1 - \omega\tau_e \tan\phi} \qquad (3)$$

where K_s is given in watts per kelvin. With the known geometric dimensions of the sample, the effective thermal conductivity κ_s can be estimated as $\kappa_s = \frac{K_s L}{A}$, with L the thickness and A the area of the sample.

In order to extract the effective thermal conductivity, certain geometric estimates were needed. The outer and inner diameter of MWCNT was taken as 54 and 22 nm, respectively.

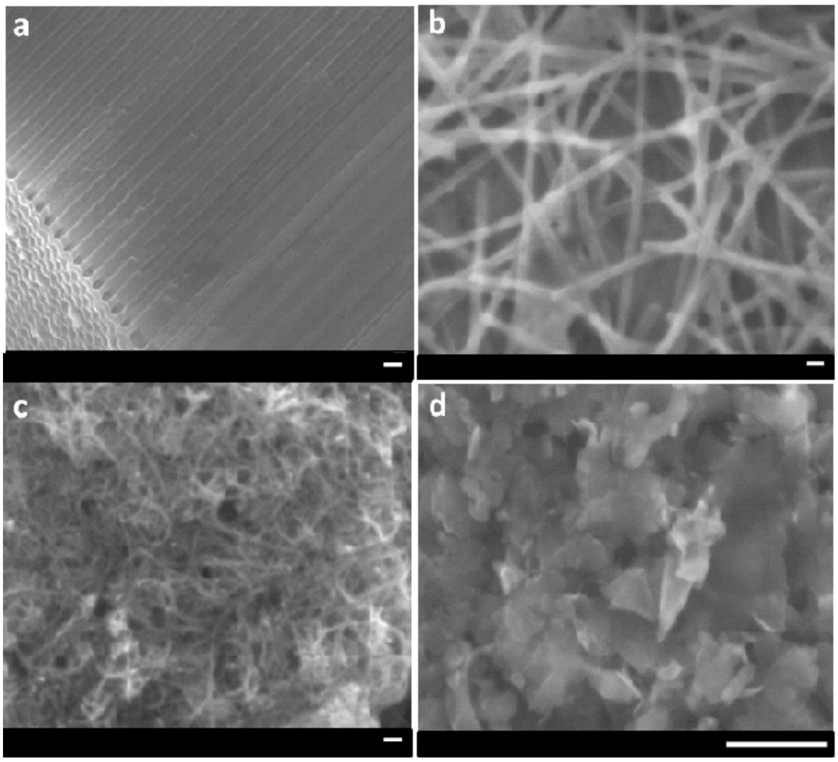

Figure 3. SEM micrographs of arrays of MWCNTs inside AAO template (a), released MWNTs from AAO template (b), SWCNTs (c), and graphite powder (d). MWCNTs are 20 μm long with 60 nm outside and 25 nm outer diameter. The scale bar in (a)–(c) are 100 nm and in (d) is 1 μm.

See section 3.1 for details. By assuming the density of nanotubes to be 1.3 g $\mathrm{cm^{-3}}$ and the interlayer separation of graphene sheets as 0.34 nm [29], the estimated mass is found to be ~30% higher than that determined by sample area and gives a conservative estimate of absolute uncertainty. To extract the thermal conductivity, the whole area of the AAO pores is assumed to be filled by MWCNTs to determine the effective thermal conductivity. By subtracting the inside hollow area of each nanotubes, the estimated value of thermal conductivity for anisotropic MWCNT could be two orders of magnitude larger. Thus, the absolute value of the conductivity is not well known but its temperature dependence should be well defined.

3. Results and discussion

3.1. Morphology study

Scanning electron microscope images were taken of the samples studied and are shown in figure 3. For the aligned MWCNT embedded in the AAO channels, the cross-section SEM in figure 3(a) shows that each channel contains a well-confined MWCNT suggesting a very high filing fraction (essentially 1), with all the channels and MWCNTs parallel to each other throughout the thickness of the MWCNT + AAO composite. As confirmed by previous studies [27, 26], the outer diameter of the MWCNTs were determined by the 60 nm pore size of the AAO template. The analyzed tunneling electron micrographs, an example shown in figure 2(c), indicate that the inner diameter of the synthesized MWCNT was 22 ± 8 nm and the outer diameter 54 ± 5 nm. As shown in figure 3(b), the liberated MWCNTs thin films are randomly oriented, laying flat with one on top of the another. In figure 3(c), the randomly oriented SWCNT thin films appear to be highly entangled. Here, SWCNTs are approximately 1.3 nm in diameter, 0.5–40 μm long, and $\gtrsim$90% pure [28]. The reference sample of graphite powder shown in figure 3(d) have a large particle size of ~1 μm and a wide particle size distribution.

3.2. Specific heat of CNT composites

The anisotropic measurement of specific heat ($c_p^{||}$) and randomly oriented specific heat (c_p^{M}) for MWCNT, randomly oriented specific heat (c_p^{S}) for SWCNT, and that of bulk graphite powder (c_p^{B}) are shown in figure 4. The specific heat of all samples were determined as a function of temperature from 300 to 400 K on heating. The bulk graphite powder sample yields a $c_p^{\mathrm{B}} = 0.73$ J $\mathrm{g^{-1}\ K^{-1}}$ at 300 K and a weak, nearly-linear, temperature dependence up to 360 K reaching 0.80 J $\mathrm{g^{-1}\ K^{-1}}$. These values obtained from our experimental arrangements are 2.1% higher and 5.5% lower, respectively, from literature values [30] and indicate in absolute value uncertainty of about 5% (conservatively) and an uncertainty in slope of about 7%.

For the aligned MWCNT composite sample $c_p^{||} = 0.74$ J $\mathrm{g^{-1}\ K^{-1}}$ while for the randomly oriented thin film sample $c_p^{\mathrm{M}} = 0.75$ J $\mathrm{g^{-1}\ K^{-1}}$ at 300 K, very similar to bulk graphite with similar temperature dependence. For randomly

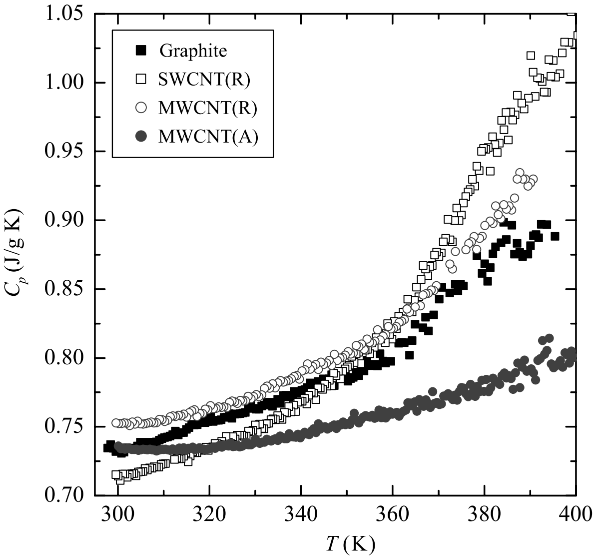

Figure 4. The measured specific heat of bulk graphite powder (solid squares), SWCNT (open squares) and MWCNT (open circles) random thin film samples (labeled R), and aligned MWCNTs measured parallel to the long axis (solid circles—labeled A) from 300 to 400 K.

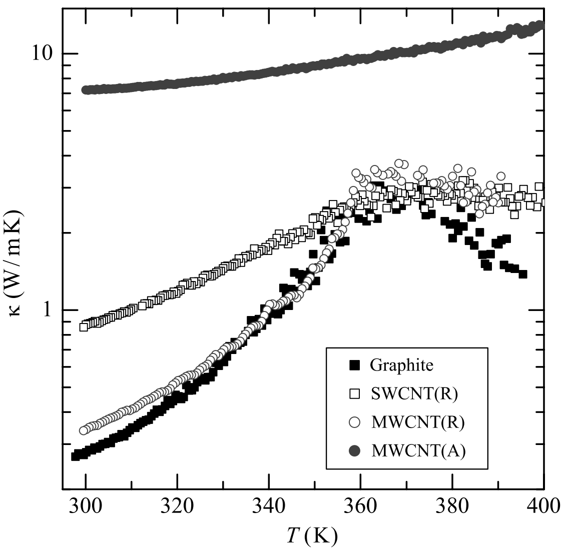

Figure 5. A semi-log plot of the derived effective thermal conductivity of bulk graphite powder (solid squares), random thin films of SWCNT (open squares) and MWCNT (open circles), as well as aligned MWCNT (solid circles) as function of temperature from 300 to 400 K.

oriented SWCNT thin film sample, $c_p^S = 0.72\ \mathrm{J\,g^{-1}\,K^{-1}}$ at 300 K and increases linearly up to 362 K similar to bulk graphite, but then exhibits a much stronger temperature dependence up to 385 K, reaching $c_p^S = 1.02\ \mathrm{J\,g^{-1}\,K^{-1}}$. There are few experimental or theoretical investigations of the specific heat or thermal conductivity reported in the literature at these high temperatures. One of the few, Yi *et al* [4], reported the specific heat of a single aligned MWCNT at 300 K to be ≈0.5 $\mathrm{J\,g^{-1}\,K^{-1}}$ while similar temperature dependence up to 400 K have been observed [31]. Several studies at lower temperatures have shown that nanowires and nanotubes can have very different phonon dispersion than in the bulk due to phonon confinement, waveguiding effects, and increased elastic modulus, that effectively determine phonon velocity [32–35].

It is expected that the magnitude of the specific heat of graphite and carbon nanotube samples would be the same at high temperatures, as seen from low temperatures up to 200 K [36]. This is generally true for our results, to within 7% for the reference graphite powder and the random films of SWCNT and MWCNT samples. Variations among these samples of the magnitude of c_p is likely due to the composite nature of the sample arrangement. However, the temperature dependence of the aligned MWCNT in the AAO channels is much weaker than can be explained by experimental uncertainties.

3.3. Thermal conductivity of CNTs

Figure 5 shows the effective thermal conductivity of bulk graphite powder, randomly oriented thin films of SWCNTs and MWCNTs (labeled with an R extension), as well as aligned arrays of MWCNT in AAO (labeled with an A extension) from 300 to 400 K. The bulk graphite and MWCNT(R) samples are nearly identical up to about 360 K after which, near 365 K, a broad peak is observed (slightly sharper for the graphite). The SWCNT(R) sample has a higher magnitude and weaker temperature dependence as bulk graphite and MWCNT(R) but reaches the same magnitude at a broad peak or plateau near 365 K. These results are similar to a broad peak-like behavior in the thermal conductivity simulated by Osman [37] with the heat flow perpendicular to the nanotube long axis. These results are also consistent with measurements for bulk powder cobalt and random thin films of cobalt nanowires [12]. It is likely that the thermal conductivity of these structures over this temperature range is dominated by phonon-boundary scattering. Basically, the randomly oriented thin films of CNTs behave similar to the graphite powder due to the large number particle boundary contacts/junctions. The broad peak near 365 K can be understood as due to the phonon–phonon bunching at these boundaries, which can cause a dramatic reduction of the thermal conductivity. For SWCNT(R) thin films, the effective thermal conductivity is 0.8 $\mathrm{W\,m^{-1}\,K^{-1}}$ at 300 K and increases linearly up to 360 K, then its decreases slowly with further increasing temperature. This is consistent with that observed by Hone's group [5–8] on a similar sample arrangement finding $\kappa = 0.7\ \mathrm{W\,m^{-1}\,K^{-1}}$ at 300 K. The uncertainty of the absolute magnitude depends strongly on the density of CNTs per unit area of film and the results presented here likely underestimate the true value. However, the larger magnitude of κ for the SWCNT(R) sample would be expected from the smaller diameter of the SWCNTs compared to the studied MWCNTs or the size of the graphite powder particles.

The observed temperature dependence of the effective thermal conductivity of aligned MWCNT inside the AAO nanochannel, MWCNT(A) is quite different than the random thin film samples as seen in figure 5. The derived MWCNT(A) κ is about 23 times that of bulk graphite powder

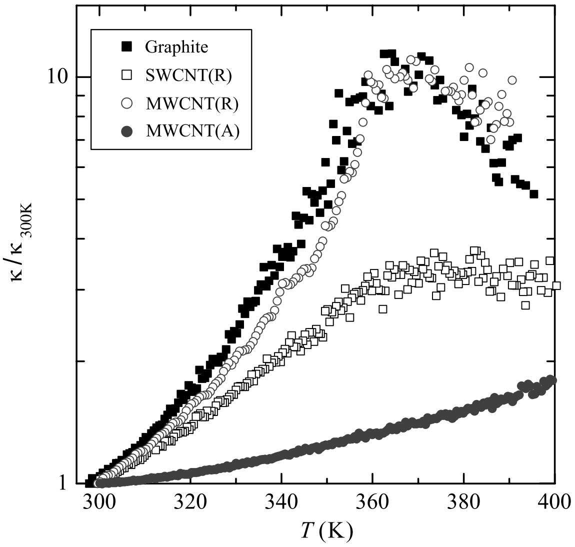

Figure 6. A semi-log plot of the effective thermal conductivity normalized to that determined for each sample at 300 K to reveal the fractional change as a function of temperature. Shown are the bulk graphite powder (solid squares), random thin films of SWCNT (open squares) and MWCNT (open circles), along with aligned MWCNT (solid circles) from 300 to 400 K.

or MWCNT(R) thin films and 8 times that of SWCNT(R) thin film at 300 K. Unlike the random thin film samples, κ of MWCNT(A) increases smoothly from 300 to 400 K without any indications of a plateau or broad peak. Similar observations of a smoothly increasing thermal conductivity have been reported for CNTs aligned by a magnetic field [38] and supports the one-dimensional nature of the heat flow in our sample. From purely geometric considerations, the estimated value of thermal conductivity for a single MWCNT along the long axis at 300 K is approximately 700 W $\mathrm{m^{-1}\ K^{-1}}$. While the uncertainty of the absolute magnitude of these measured effective κ are large, perhaps as large as an order of magnitude, it cannot explain the difference with that expected for a 'scaled-up' geometric estimate of κ along the long axis. Similarly for random thin film samples, an estimate assuming the whole sample area is filled completely by sample (a filling fraction of 1) yields a value at least two orders of magnitude or larger than that derived here. Thus, the composite nature of these macroscopic samples must be intrinsically different than simply scaling up the behavior of a single nanotube to these dimensions.

To better compare the temperature dependence of the effective thermal conductivity, normalized values (to that observed for each sample at 300 K, i.e. $\kappa/\kappa_{300\ \mathrm{K}}$) of the bulk graphite powder, the random thin films of SWCNT(R) and MWCNT(R), as well as aligned MWCNT(A) in AAO a shown in figure 6. This construction illustrates the fractional change of the observed κ and indicate that the random thin film samples are all dominated by its granular nature while the aligned MWCNT sample, though higher in magnitude, has a much small fractional change up to 400 K.

The effective thermal conductivity is greatly affected by the interface contact resistance between surfaces and sample as well as among the sample particles (nanotubes or graphite powder) [39, 40]. The results presented in this work reveal that the heat transfer in aligned nanotubes is dominated by the nanotube–nanotube interfacial resistance, nanotube length, diameter, and spacing. Paradoxically, the nanotube thermal resistance decreases with increasing nanotube length [39, 41]. For aligned MWCNT + AAO, the heat flow is essentially one-dimensional across each single nanotube, but their coupling to the AAO matrix and the cell surfaces leads to increased thermal resistance. However, in the case of a randomly oriented thin film sample, the nanotube–nanotube resistance decreases due to the proliferation of contacts among nanotubes improving the heat exchange. In all samples, the interfacial resistance also depends upon the geometry of the contacting surfaces through surface roughness [42]. Because anharmonic phonons can be created, destroyed or scattered from each other leading to a finite mean-free-path and so, limiting the thermal conductivity [43].

The heat transfer across interfaces can be represented by a single parameter known as the thermal interfacial resistance R [39] and is given by

$$R = A\Delta T/Q = t/(\kappa A); \tag{4}$$

where A is the area of the interface contact, ΔT is the steady-state temperature jump between two surfaces of contact, Q is the rate of heat flow across the interface, t is the thickness of sample, and κ is the thermal conductivity. Equation (4) applies to one-dimensional heat flow through the area A across the thickness t.

Since the heat flow in these measurements across the randomly oriented and aligned samples are same, the thermal contact resistance between nanotubes or powders (in randomly oriented sample), nanotubes–matrix (in aligned sample), as well as between contact areas plays an important role and induces temperature gradients. Recently reported calculations describe the effect of thermal contact resistance on a random film sample of carbon nanotubes and obtained a very low thermal conductivity as compared that along the long axis of a single nanotube [44]. The energy transfer between carbon nanotubes in van der Waals contact is limited by a large contact resistance [39] arising from weak inter-particle bonding. The contact resistance for larger diameter CNT is smaller than the smaller diameter CNT due to larger contact area, whereas the number of contacts per unit volume will be larger for smaller nanotubes due to large aspect ratio.

4. Conclusions

In this work, experimental results of the specific heat and effective thermal conductivity of a macroscopic composite containing randomly oriented single-wall and multi-wall carbon nanotubes, graphite powder, and aligned multi-wall carbon nanotube embedded in a porous aluminum matrix are reported from 300 to 400 K. The specific heat are generally consistent among all carbon samples with the graphite powder and random thin film of MWCNT being most similar. The random thin film of SWCNT has a stronger while the aligned MWCNT in AAO has a weaker temperature dependence than the bulk behavior measured here. Though small, these differences are due to the intrinsic properties of SWCNT for the former and the macroscopic arrangement in the composite for the latter sample. The effective thermal conductivity reveals the most striking effect of composite construction. In all the random thin film samples of SWCNT, MWCNT, and graphite powder, a broad peak-like feature is seen in κ near 365 K, similar to that seen in a similar cobalt-based composites [12]. The absolute value of effective thermal conductivity measured here of the single-wall and multi-wall CNTs are expected to be different because of their differences in length, diameter, and overall purity. Given that all three random thin film sample + cell configuration of SWCNT(R), MWCNT(R), and graphite powder are nearly identical, the phonon-boundary scattering mechanism is the most likely and the difference in absolute value is likely due to uncertainties in mass approximation and sample purity.

These results on how the thermal properties of carbon nanotube composites vary with construction can be combined with the recent work of Hone's group [7, 8] on the thermal conductivity for an unaligned SWCNT sample in presence of a magnetic field finding $\approx$25 W m^{-1} K^{-1} at 300 K and increases with increasing temperature until saturating at $\approx$35 W m^{-1} K^{-1} near 400 K. Thus, detailed engineering of thermal properties is a strong possibility. Future work on more complex composite arrangements would further detail the possible variations and should hopefully inspire complimentary theoretical or computational work to better understand such systems.

Acknowledgment

G Iannacchione would like to thank the Department of Physics at Worcester Polytechnic Institute for their support.

References

[1] Sumio I 1991 *Nature* **354** 8
[2] Olk C H and Heremans J P 1994 *J. Mater. Res.* **9** 259
[3] Dekker C 1999 *Phys. Today* **52** 22
[4] Yi W, Lu L, Dian-Lin Z, Pan Z W and Xie S S 1999 *Phys. Rev.* B **59** R9015
[5] Hone J, Whitney M, Piskoti C and Zettl A 1999 *Phys. Rev.* B **59** R2514
[6] Hone J, Whitney M and Zettl A 1999 *Synth. Met.* **103** 2498
[7] Hone J, Batlogg B, Benes Z, Johnson A T and Fischer J E 2000 *Science* **289** 1730
[8] Hone J, Llaguno M C, Nemes N M, Johnson A T, Fisher J E, Walters D A, Casavant M J, Schmidt J and Smalley R E 2000 *Appl. Phys. Lett.* **77** 666
[9] Hone J, Llaguno M C, Biercuk M J, Johnson A T, Batlogg B, Benes Z and Fisher J E 2002 *Appl. Phys.* A **74** 339
[10] Yang D J, Zhang Q, Chen G, Yoon S F, Ahn J, Wang S G, Zhou Q, Wang Q and Li J Q 2002 *Phys. Rev.* B **66** 165440
[11] Basu R and Iannacchione G S 2008 *Appl. Phys. Lett.* **93** 183105
[12] Pradhan N R, Huanan D, Liang J and Iannacchione G S 2008 *Nanotechnology* **19** 485712
[13] Tong T, Majumdar A, Zhao Y, Akashi A, Delzeit L and Meyapan M 2006 *IEEE* pp 1406–11
[14] Zhang K, Chai Y, Yuan M M F, Xio D G W and Chan P C H 2008 *Nanotechnology* **19** 215706
[15] Xu Y, Leong C and Chung D D L 2007 *J. Electron. Mater.* **36** 1181
[16] Park J-J and Taya M 2006 *J. Electron. Packag.* **128** 46
[17] Amama P B, Cola B A, Sands T D, Xu X and Fisher T S 2007 *Nanotechnology* **18** 385303
[18] Xu J and Fisher T S 2006 *Int. J. Heat Mass Transfer* **49** 1658
[19] Berber S, Kwon Y K and Tomanek D 2000 *Phys. Rev. Lett.* **84** 4613–6
[20] Kim P, Shi L, Majumdar A and McEuen P L 2001 *Phys. Rev. Lett.* **87** 215502
[21] Shi L, Li D, Yu C, Jang W, Kim D, Yao Z, Kim P and Majumdar A 2003 *J. Heat Transfer* **125** 881
[22] Zhang H-L, Li J-F, Zhang B-P, Yao K-F, Liu W-S and Wang H 2007 *Phys. Rev.* B **75** 205407
[23] Xie S, Li W, Pan Z, Chang B and Sun L 2000 *J. Phys. Chem. Solids* **61** 1153
[24] Lu L, Yi W and Zhang D L 2001 *Rev. Sci. Instrum.* **72** 2996
[25] Prasher R 2008 *Phys. Rev.* B **77** 075424
[26] Li J, Papadopoulos C, Xu J M and Moskovits M 1999 *Appl. Phys. Lett.* **75** 367
[27] Liang J, Chik H, Yin A and Xu J M 2002 *J. Appl. Phys.* **91** 2544
[28] 2009 http://www.helixmaterial.com
[29] Lavin J G, Subramoney S, Rouff R S, Berber S and Tomanek D 2002 *Carbon* **40** 1123
[30] Nihira T and Iwata T 2003 *Phys. Rev.* B **68** 134305
[31] Xie H 2007 *J. Mater. Sci.* **42** 3695
[32] Dresselhaus M S, Lin Y-M, Cronin S B, Rabin O, Black M R, Dresselhaus G and Koga T 2001 *Semicond. Semimet.* **71** 1
[33] Gu M X, Yeung T C, Tan C M and Nosik V 2006 *J. Appl. Phys.* **100** 094304
[34] Rego L G C and Kirczenow G 1998 *Phys. Rev. Lett.* **81** 232
[35] Mahan G 2002 *Phys. Rev.* B **65** 235402
[36] Mizel A, Benedict L X, Cohen M L, Louie S G, Zettl A, Budraa N K and Beyermann W P 1999 *Phys. Rev.* B **60** 3264
[37] Osman M A and Srivastava D 2001 *Nanotechnology* **12** 21
[38] Fischer J E, Zhou W, Vavro J, Liaguno M C, Guthey C, Haggenmuller R, Cassavant M J, Walters D E and Smalley R E 2003 *J. Appl. Phys.* **93** 2157
[39] Zhong H and Lukes J R 2006 *Phys. Rev.* B **74** 125403
[40] Shenogin S, Xue L, Oziski R, Keblinski P and Cahill D G 2004 *J. Appl. Phys.* **95** 8136–44
[41] Huxtable S T *et al* 2003 *Nat. Mater.* **2** 731
[42] Pollack G L 1969 *Rev. Mod. Phys.* **41** 48
[43] Meng F Y, Ogata S, Xu D S, Shibutani Y and Shi S Q 2007 *Phys. Rev.* B **75** 205403
[44] Prasher R S, Hu X J, Chalopin Y, Mingo N, Lofgreen K, Volz S, Cleri F and Keblinski P 2009 *Phys. Rev. Lett.* **102** 105902

IOP Publishing Journal of Physics D: Applied Physics

J. Phys. D: Appl. Phys. **43** (2010) 105401 (7pp) doi:10.1088/0022-3727/43/10/105401

Relaxation dynamics of glass transition in PMMA + SWCNT composites by temperature-modulated DSC

N R Pradhan and G S Iannacchione

Department of Physics, Worcester Polytechnic Institute, Worcester, MA 01609, USA

Received 30 October 2009, in final form 25 December 2009
Published 25 February 2010
Online at stacks.iop.org/JPhysD/43/105401

Abstract

The experimental technique offered by temperature-modulated differential scanning calorimeter (TMDSC) used to investigate the thermal relaxation dynamics through the glass transition as a function of frequency was studied for pure PMMA and PMMA-single wall carbon nanotubes (SWCNTs) composites. A strong dependence of the temperature dependence peak in the imaginary part of complex heat capacity ($T_{\max}$) is found during the transition from the glass-like to the liquid-like region. The frequency dependence of $T_{\max}$ of the imaginary part of heat capacity (C_p) is described by Arrhenius law. The activation energy obtained from the fitting shows increases while the characteristic relaxation time decreases with increasing mass fraction (ϕ_m) of SWCNTs. The dynamics of the composites during glass transition, at slow and high scan rates, are also the main focus of this experimental study. The change in enthalpy during heating and cooling is also reported as a function of scan rate and frequency of temperature modulation. The glass transition temperature (T_g) shows increases with increasing frequency of temperature modulation and ϕ_m of SWCNTs inside the polymer host. Experimental results show that T_g is higher at higher scan rates but as the frequency of temperature modulation increases, the T_g values of different scan rates coincide with each other and alter the scan rate dependence. From the imaginary part of heat capacity, it is obvious that $T_{\max}$ is not the actual glass transition temperature of pure polymer but $T_{\max}$ and T_g values can be superimposed when ϕ_m increases in the polymer host or when the sample undergoes a transition with a certain frequency of temperature modulation.

1. Introduction

Recently, the modulated differential scanning calorimetry (MDSC) [1–3] study has been widely used to investigate the dynamics of glass transitions of polymer composites and related materials. In MDSC analysis, the sample is decomposed into reversing and non-reversing signals, is widely used and appears to avoid the uncertain meaning of dynamic thermal analyses in analogy to, e.g., dynamic mechanical or dielectric spectroscopies. In recent studies it has been commonly accepted to present the dynamic thermal properties in terms of the complex, real (storage) and imaginary (loss) heat capacities (C_p^*, C_p' and C_p''). The concept of frequency-dependent specific heat $C_p^*(\omega, T)$ ($=C_p^*(\omega)$) was introduced and the first measurement was performed in the 1980s [4–7] with an alternating current calorimeter technique. After that it has been widely used to study the dynamics of glass transition of different polymer systems. From a statistical point of view, $C_p^*(\omega)$ appears as a consequence of entropy fluctuations [8]. One advantage of dynamic heat capacity in comparison with other techniques is the fact that $C_p^*(\omega)$ reflects the contribution of all modes, orientational and translational, providing global and direct information of the slow dynamics associated with the glass transition. Thus MDSC is a widely used technique to study the phase transition, glass transition and specific heat measurement of widely available polymeric systems. But the concept of frequency-dependent specific heat is not widely used. It is specially the case in the application fields of polymers, food sciences, pharmaceuticals, etc. where it could be of great interest to characterize the molecular mobility.

Carbon nanotubes (CNTs) have outstanding electrical, mechanical, optical and thermal properties. These properties have significant potential in a vast range of applications such as quantum wires [9], tips for scanning probe microscope [10] and molecular diodes [11]. Polymers play a very important role in numerous fields of everyday life due to their advantages in lightness, ease of processing, resistance to corrosion and low cost of production. To improve the performance of polymers, composites of polymers and a filler have been extensively used and studied. The use of various nanofillers such as metals, semiconductors, organic and inorganic particles and fibres, especially carbon structures [12–15], is of particular interest and a subject of intense investigation. The unique properties of CNTs such as extremely high strength, lightweight, elasticity, high thermal and air stability, high electric and thermal conductivity and high aspect ratio, offer crucial advantages over other nanofillers.

The potential of using nanotubes as a filler in polymer composites has not been fully realized because of processing difficulties. Structural relaxation is the process by which amorphous materials in the glassy state approach a state of thermodynamic equilibrium. Calorimetry, such as DSC, has revealed enthalpic relaxations occurring near the glass transition T_g in glassy polymers aged after a variety of heating treatments. It is well known that annealing or variation of heating and cooling rates leads to significant hysteresis in T_g because of these structural relaxations [16, 17]. The introduction of nanofillers is expected to interact strongly with these short-range structural relaxations. However, the effective utilization of CNTs in polymer composite applications strongly depends on the quality/uniformity of the nanotubes and the ability to disperse them homogeneously throughout the polymer host [18, 19]. Our previous work was to produce and investigate SWCNT-based nano-composite polymer materials as candidates for the next generation of high-strength, lightweight and enhanced thermal conducting materials [17]. Structural relaxation has been characterized for many polymers by the dielectric spectroscopy method, but this method is versatile, and widely used to study the dynamics of a sample at high frequencies, where it is found that the calorimetric results are the extension of dielectric results. The calorimetric T_g includes total degree of freedom such as rotation, diffusion and vibration, while the dielectric T_g originates only from the reorientation of molecules.

The main objective of this paper is to study the relaxation dynamics of the glass transition of PMMA + SWCNTs composites at very low frequencies using MDSC and to present the details of frequency-dependent MDSC techniques. Many studies have been done to describe the relaxation behaviour and glass transition for pure polymers in the frequency domain but so far no results have been reported on CNT polymer composites. The PMMA + SWCNT composites were prepared by dispersing SWCNTs and PMMA in a chloroform solution using sonication, and then slowly evaporating the solvent leaving a homogeneous dispersion. The complex heat capacity was measured as a function of temperature and different frequencies of temperature modulation from 0.0138 to 0.0826 s^{-1}. Then the real and imaginary parts of heat capacity was estimated with the phase between input heat flow and heating rate. In all the samples, we observed the peak maximum in the imaginary part of heat capacity. The effective glass transition temperature, T_g, activation energy and dynamics observed in the real and imaginary parts are dependent on the applied modulated frequency of temperature oscillation. The measurement was reported in the region of glass transition of polymers and composites and other regions are not of interest in this study as the dynamics do not change with frequency.

Following this introduction, section 2 describes some of the basics of the experimental procedures for the MDSC and sample preparation. Section 3 presents the experimental results and discussion followed by a general conclusion with future directions presented in section 4.

2. Experimental

2.1. Modulated differential scanning calorimetry

Modulated (temperature) differential scanning calorimetry (MTDSC/MDSC) allows for the simultaneous measurement of the evolution of both heat flow and heat capacity. MDSC differs from conventional DSC where the sample is subjected to a more complex heating program incorporating a sinusoidal temperature modulation accompanied by an underlying linear heating ramp. Whereas DSC is only capable of measuring the total heat flow, MDSC can simultaneously determine the non-reversible (kinetic component) and the reversible (heat capacity component) heat flows. A detailed description of the MDSC method can be found elsewhere [3, 20–25].

MDSC experiments were performed using a Model Q200 from TA Instruments, USA. Prior to the experiment with our sample, temperature calibration was done with a sapphire disc, under the same conditions of measurements we used for our studied sample. Q200 is an extension of the heat flux type of a conventional DSC. The method to obtain complex specific heat has been proposed by Schawe based on the linear response theory [3, 21]. In general a temperature oscillation is described as

$$T = T_0 + q_0 t + A_T \sin(\omega t), \tag{1}$$

where T_0 is the initial temperature at time $t = 0$, T is the temperature at time t, q_0 is the underlying scan rate, A_T is the temperature amplitude and ω ($\omega = 2\pi f$) is the angular frequency of the temperature modulation. $f = 1/\tau$ is the frequency in s^{-1} where τ was taken as the period of modulation. The results are plotted in the scale of frequency f instead of ω. The heating rate is given by

$$q = \frac{\mathrm{d}T}{\mathrm{d}t} = q_0 + A_q \cos(\omega t), \tag{2}$$

where A_q is the amplitude of heating rate ($A_q = A_T\omega$). Since the applied heating rate in MDSC consists of two components, q_0 the underlying heating rate and $A_q \cos(\omega t)$ the periodic heating rate, the measured heat flow can also be separated into two components, i.e. the response to the underlying heating rate and response to the periodic heating rate. The latter can be described by

$$\mathrm{HF}_{\mathrm{period}} = A_{\mathrm{HF}} \cos(\omega t - \phi), \tag{3}$$

where $\mathrm{HF_{period}}$ is the heat flow response to the periodic heating rate, A_{HF} is the amplitude of heat flow and ϕ is the phase angle between heat flow and heating rate. An absolute value of complex specific heat can be obtained by

$$\left|C_p^*\right| = \frac{A_{\mathrm{HF}}}{mA_q}, \tag{4}$$

where m is the mass of a sample.

The data were analysed correcting the phase shift between heating rate and heat flow rate signal. The imaginary part of the complex heat capacity was calculated by correcting the phase angle. The detailed correction procedure can be found elsewhere [26]. By proper calibration for a raw phase angle, we can obtain real C_p' and imaginary C_p'' parts by

$$C_p' = \left|C_p^*\right| \cos(\phi), \tag{5}$$

$$C_p'' = \left|C_p^*\right| \sin(\phi). \tag{6}$$

The measured phase angle was corrected using the reported method [26]; then the real and imaginary parts of the complex heat capacity were estimated.

2.2. Preparation of PMMA + SWCNT composites

The required amounts of polymer PMMA ($M_{\mathrm{n}} = 120\,000\,\mathrm{g\,mol^{-1}}$, obtained from Aldrich) and SWCNTs (obtained from Helix Materials Solution, Texas, purity > 90%, ash 5%) were first dissolved in chloroform, in separate containers. Then the chloroform solution containing SWCNT was sonicated for 8 h to separate the bundles of nanotubes into individual particles. Then both PMMA dissolved in chloroform and SWCNT dispersed in chloroform were mixed together and again kept for 6 h in an ultrasonic bath. Scanning electron micrographs of the SWCNTs used in this work were given in a previous paper [27]. After that the PMMA+SWCNT solution was finally mixed in a touch mixer (Fisher Touch-Mixer model 12-810) for 10 min. Optical micrograph studies have been done to clarify the good dispersion of SWCNTs inside host PMMA. The mass fraction was calculated using the following formula from the mass of the CNTs and PMMA. The volume fraction was derived by taking the density of PMMA as $1.2\,\mathrm{g\,cm^{-3}}$ and assuming the density of CNTs as $1.4\,\mathrm{g\,cm^{-3}}$:

$$\phi_m = \frac{M_{\mathrm{f}}}{M_{\mathrm{f}} + M_{\mathrm{p}}} = \frac{M_{\mathrm{f}}}{M_T}, \tag{7}$$

$$\phi_v = \frac{\rho_{\mathrm{p}} M_{\mathrm{f}}}{\rho_{\mathrm{f}} M_{\mathrm{p}} + \rho_{\mathrm{p}} M_{\mathrm{f}}}, \tag{8}$$

where ϕ_m is the mass fraction, M_{f} is the mass of the filler (SWCNTs), M_{p} is the mass of the polymer (PMMA), ϕ_v is the volume fraction of SWCNTs, ρ_{p} is the density of PMMA and ρ_{f} is the density of filler (SWCNTs).

Due to strong van der Waal attraction, CNTs bundle together in high mass fraction, which reduces the dispersion quality of nanotubes inside a polymer matrix. In our case, after casting the required amount of sample on a silver sheet, the remaining solution of PMMA + SWCNT + choloform was stored in a tightly capped bottle and no significant segregation occurred over several days indicating the quality of dispersions. For the MDSC measurements, the samples were sealed inside a standard hermetically sealed pan.

Before sealing in the hermite pan, each sample was heated for 15 min at 127 °C in vacuum to remove the trapped chloroform. The MDSC experiment was carried out with heating and cooling rates of 2.0, 0.4 and $0.1\,\mathrm{K\,min^{-1}}$ and dry ultra pure nitrogen gas with a flow rate of $50\,\mathrm{ml\,min^{-1}}$ was purged through the DSC cell. For accurate measurement of specific heat or to decrease the uncertainty, the reference and the sample hermite pans were chosen carefully. The mass of the pan used was (0.0504 ± 0.0004) g; here 0.0004 is the standard deviation of the pan for three different sample pans (three different mass fractions of PMMA + SWCNT) and a reference pan used for this study. The mass of the three samples taken in all the measurements is $\sim 10 \pm 0.2$ mg. The temperature modulation amplitude was chosen to be 1.2 K. We have studied three distinct samples, pure PMMA, and 0.014 and 0.080 mass fractions of SWCNTs dispersed in PMMA composites. Each sample was scanned with the above-mentioned three different scan rates and with modulation frequencies ranging from 1/160 to $1/30\,\mathrm{s^{-1}}$.

3. Results and discussion

Figure 1 shows the real (up) and imaginary (bottom) parts of the complex specific heat capacity of 0.014 mass fraction SWCNTs inside PMMA matrix under heating (left panel) and cooling (right panel) rates of $0.4\,\mathrm{K\,min^{-1}}$ with frequency of temperature modulation from 1/30 to $1/150\,\mathrm{s^{-1}}$. The real part of specific heat ($\Delta C_p'$) was normalized to zero far above the glass transition at 405 K and the imaginary part was also normalized by subtracting a base line. It is observed that the maximum rate of change of C_p' occurs in the region of glass transition and it depends on the applied frequency of temperature modulation. Similar change in $\Delta C_p'$ was observed during heating and cooling of the real part of heat capacity. The change in magnitude of the imaginary part of heat capacity, $\Delta C_p''$, shows a difference during heating and cooling with frequency of temperature modulation. This explains the difference in structural relaxation and mobility of the sample during heating and cooling. There is no difference in the real part of specific heat observed in the SWCNTs + PMMA composite samples during heating and cooling. The magnitude of $\Delta C_p'$ between the liquid and the glass regions, i.e. $\Delta C_p^{(\mathrm{L-G})} = \Delta C'_{p(405)} - \Delta C'_{p(340)}$ is shown in figure 2. This shows that $\Delta C_p^{(\mathrm{L-G})}$ increases with decreasing frequency of temperature modulation. Figure 2 shows $\Delta C_p^{(\mathrm{L-G})}$ for pure PMMA (upper), 0.014 (middle) and 0.080 (bottom) mass fractions of SWCNT in PPMA composites with frequency of temperature modulation. For PMMA, $\Delta C_p^{(\mathrm{L-G})}$ increases with decreasing scan rate in the entire frequency range studied except at a higher frequency of $0.035\,\mathrm{s^{-1}}$, where they seem to be equal. This change in $\Delta C_p^{(\mathrm{L-G})}$ with respect to scan rate disappears as the mass fraction of SWCNT increases inside the host polymer. The 0.080 mass fraction of SWCNT does not show any difference in $\Delta C_p^{(\mathrm{L-G})}$ with respect to scan rate in the entire frequency

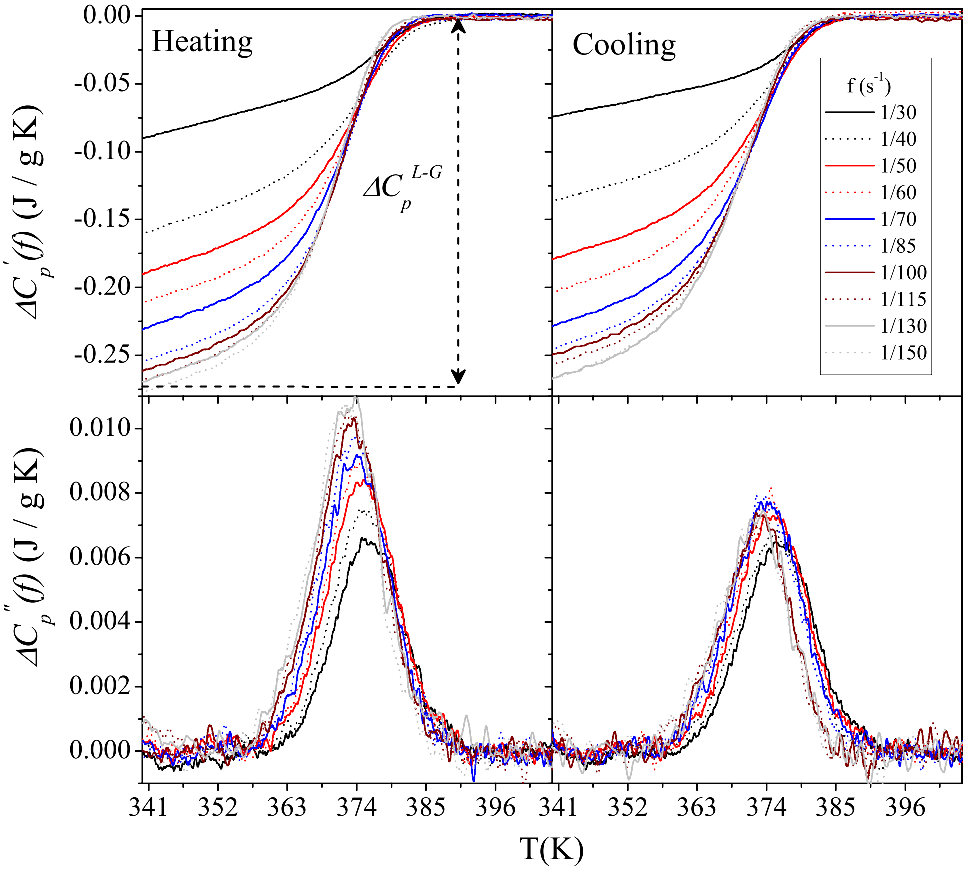

Figure 1. The normalized real part of heat capacity $\Delta C_p'(f)$ (top panel) and imaginary heat capacity $\Delta C_p''(f)$ (bottom panel) of a PMMA + SWCNT composite ($\phi_m = 0.014$ sample) from 340 to 405 K, for different applied heating frequencies from 1/30 to 1/150 s^{-1} (see legend). In the top panel, the difference between liquid and glass heat capacities $\Delta C_p^{\mathrm{L-G}}$ is defined.

(This figure is in colour only in the electronic version)

range studied. The imaginary part of complex specific heat capacity, during heating, $\Delta C_p''(f)$ (figure 1, bottom panel), is characterized by an asymmetric peak with a smaller slope at the low temperature side than at the high temperature side, which can be characterized by the molecular distribution of intrinsic structural relaxation and related to the dynamic glass transition. The slope increases with decreasing frequency of temperature modulation at low temperatures without changing the high temperature slope during heating. The temperature where the imaginary specific heat shows the maximum value ($T_{\max}$) shifted towards a lower temperature with decreasing frequency indicating the slowing down of the dynamics of the systems. The cooling $\Delta C_p''$ shows a similar peak maximum shifted to a lower temperature from 1/30 to 1/70 s^{-1} and less change in magnitude than the heating results. After 1/70 s^{-1}, there is no significant change in peak maximum observed during cooling as compared with heating. The $\Delta C_p''$ peak during cooling is very symmetric without any change in slope in the high and low temperature sides.

In our previous work [17], we studied the glass transition temperature, which showed that T_g increases with scan rate. Figure 3 shows the glass transition temperature for PMMA, 0.014 and 0.080 mass fractions of SWCNT + PMMA composites with frequency of temperature modulation. In all these three samples, highly dependent T_g increases with

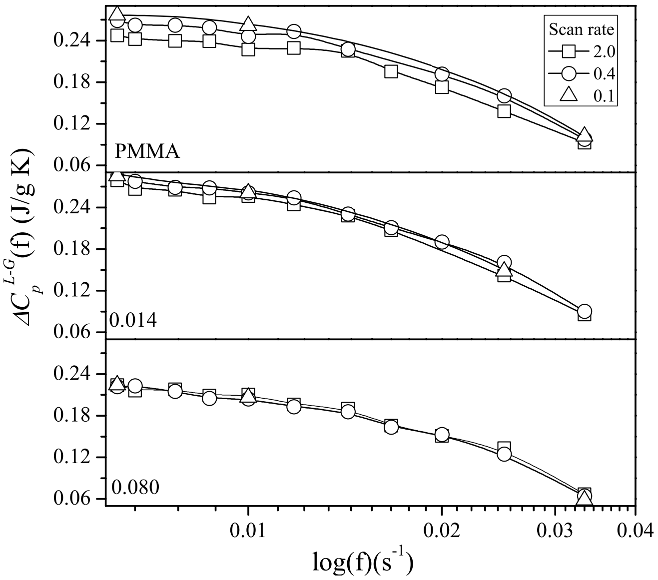

Figure 2. Semi-logarithmic plot of $\Delta C_p^{\mathrm{L-G}}$ as a function of temperature modulation frequency f for scan rates 2.0, 0.4 and 0.1 K min^{-1}, for PMMA (top), 0.014 (middle) and 0.080 (bottom) mass fractions of SWCNTs.

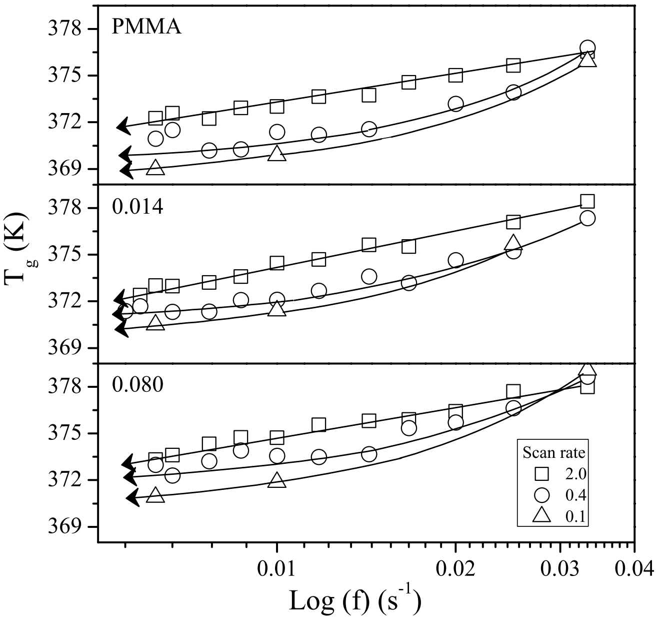

Figure 3. Semi-log plot of glass transition temperature (T_g) as a function of temperature modulation frequency for pure PMMA (top), 0.014 (middle) and 0.080 (bottom) mass fractions of SWCNTs at scan rates 2.0, 0.4 and 0.1 K min^{-1}. Lines are guide to the eye and arrows indicate the zero-frequency extrapolated T_g.

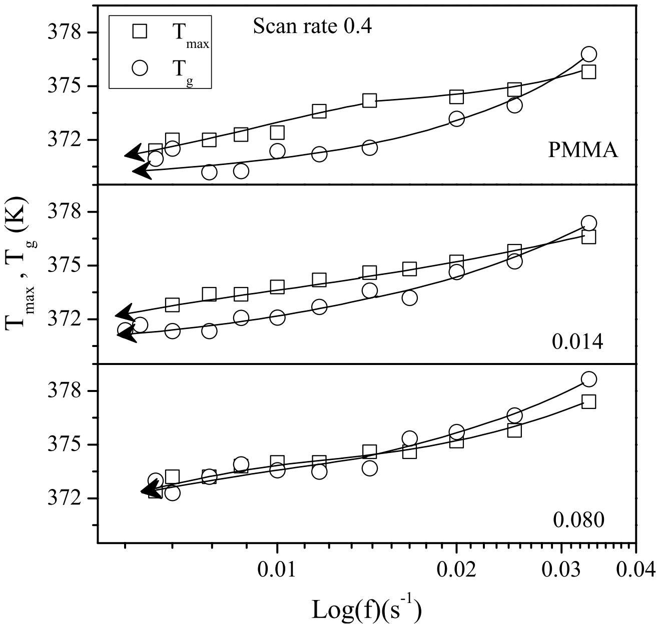

Figure 4. Semi-log plot shows comparison of maximum temperature in the imaginary part of complex heat capacity (T_{max}) and glass transition temperature (T_g) with frequency of temperature modulation of PMMA (top), 0.014 (middle) and 0.080 (bottom) mass fractions of SWCNTs in PMMA.

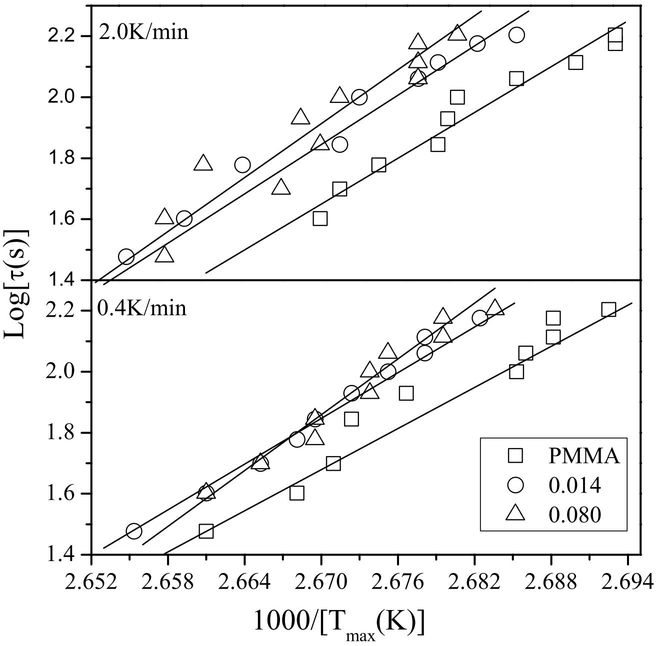

Figure 5. Arrhenius plot of logarithm of time period of temperature oscillation with inverse of the peak C_p'' temperature obtained at rates 2.0 and 0.4 K min^{-1} for PMMA, 0.014 and 0.080 mass fractions of PMMA + SWCNTs composites.

increasing frequency of temperature modulation and scan rate. But this shows that in all PMMA and SWCNT + PMMA composites, T_g of different scan rates approach the same value as the frequency of temperature modulation increases, and after a certain frequency of modulation, the T_g value of low scan rate (0.1 K min^{-1}) becomes greater than for the high scan rate (2 K min^{-1}) (figure 3, bottom). This cross over of T_g between different scan rates with frequency of modulation shifts to a lower frequency as ϕ_m increases. This shows that the dynamics of the glass transition are highly dependent on the frequency and the nanotube dispersion can significantly alter these dynamics with modulated frequency.

Figure 4 shows the maximum peak temperature of the imaginary parts of complex specific heat (T_{max}) and glass transition temperature T_g, with frequency of temperature modulation, for PMMA, 0.014 and 0.080 mass fractions of SWCNTs in host PMMA at 0.4 K min^{-1} scan rate. T_{max} is the temperature of peak value of the imaginary part of specific heat while heating and T_g obtained using DSC software from the heating run of reversible heat capacity during step like feature of transition. T_{max} is the temperature where maximum loss appears. The glass transition where the polymer undergoes change from the liquid-like phase to the glassy region and both T_{max} and T_g may not be the same. For pure PMMA and 0.014 mass fraction of SWCNT + PMMA composites, T_{max} is higher than T_g, in the low frequency region and both T_{max} and T_g values approach each other as the frequency increases and at a particular frequency (0.029 s^{-1} for PMMA) they cross each other and T_g becomes higher than T_{max}. As the mass fraction of SWCNTs increases, for 0.080 mass fraction, T_{max} and T_g values overlap up to 0.17 s^{-1} and then cross each other to give a T_g value higher than the T_{max} value. This indicates that the cross over point between T_g and T_{max} shifted towards the lower frequency as ϕ_m increases.

The frequency dependence of glass transition can also be interpreted by Arrhenius law. Figure 5 shows the relaxation time (τ in s^{-1}: τ is the modulation time period) in log scale, versus inverse peak temperature of the imaginary part of complex heat capacity (1000/T_{max}). Figure 5 shows two

Table 1. Activation energy (E) and characteristic time (τ_0) at two different scan rates of PMMA and PMMA + SWCNT composites.

Sample	2 K min^{-1}		0.4 K min^{-1}	
ϕ_m	E (K)	τ_0 (s)	E (K)	τ_0 (s)
PMMA	25 600	1.18×10^{-28}	23 000	8.87×10^{-27}
0.014	26 000	5.54×10^{-30}	27 000	3.98×10^{-31}
0.080	29 000	3.62×10^{-34}	29 200	1.10×10^{-33}

different scan rates, 2.0 K min^{-1} (upper) and 0.4 K min^{-1} (bottom), for PMMA, 0.014 and 0.080 mass fractions of SWCNT + PMMA composites. The fitted Arrhenius law is given as

$$\tau = \frac{1}{\omega} = \tau_0 \times \exp\left(\frac{E}{T_{\max}}\right), \quad (9)$$

where E is the activation energy and τ_0 is the characteristic time. Deviations with regard to the Arrhenius behaviour are shown in the case of 2 K min^{-1} scan rate. The pure PMMA data follow better Arrhenius behaviour than the nanotube composite sample. It is clear from the fitting that the slope increases with the volume fraction of the nanotubes in PMMA + SWCNT composites. The fitted values of activation energy and the characteristic time are given in table 1. The activation energies at 2.0 and 0.4 K min^{-1} scan rates, for pure PMMA, 0.014 and 0.080 mass fractions of SWCNT + PMMA composites were 25 600 K, 26 000 K, 29 000 K and 23 000 K, 27 000 K, 29 200 K, respectively. This shows that activation energy increases as the volume fraction of nanotubes increases inside the polymer systems. In other words, during the process of formation of a continuous network, the polymer chains stack over the CNTs to form a strong network, thus the significant increase in the activation energy and since this follows Arrhenius behaviour, materials become stronger. On the other hand the characteristic time decreases with increasing mass fraction of SWCNTs for both the scan rates, as shown in table 1.

Figure 6 shows the enthalpy ($\Delta H''$) of PMMA and 0.080 mass fraction of SWCNT + PMMA composite with frequency of temperature modulation. This enthalpy was estimated by integrating the imaginary part of complex specific heat C_p''. In the low frequency range, $\Delta H''_{\text{heating}}$ and $\Delta H''_{\text{cooling}}$ show a large deviation in both PMMA and 0.080 mass fraction of SWCNT + PMMA composite. Both the cooling and heating enthalpies approach each other as the frequency of modulation increases. This deviation of $\Delta H''$ between heating and cooling at a low frequency decreases with scan rate. For a very low scan rate of 0.1 K min^{-1}, there was no significant deviation observed between heating and cooling throughout the frequency range studied. Another significant difference can be noticed from the figure, that is enthalpy $\Delta H''$ increases at frequency 0.033 s^{-1} as the scan rate decreases in the SWCNT + PMMA composite which does not occur clearly in the case of pure polymer.

4. Conclusion

Frequency dependent dynamic heat capacities of PMMA and SWCNT + PMMA composites have been observed in the glass transition region by modulated DSC. In the vicinity of T_g, a remarkable temperature dependence is clearly observed in the real and imaginary parts of complex heat capacity. The interesting relaxation phenomena observed in the imaginary part and the dynamics of glass transition obtained from the real part of heat capacity are discussed with frequency of temperature modulation, when the polymers undergo a transition from the solid-like region to the liquid-like state. The activation energy calculated from Arrhenius behaviour increases with mass fraction of nanotubes. The change in enthalpy between heating and cooling data is discussed with different scan rates to understand the molecular behaviour during glass transition. This experimental study must be helpful in understanding the thermal properties such as glass transition, fragility, relaxation behaviour, enthalpy loss and mechanical properties of polymer–CNT based composites. These parameters can be controlled by adjusting the properties of the nanofillers, applied frequency and rate of heating and cooling the materials.

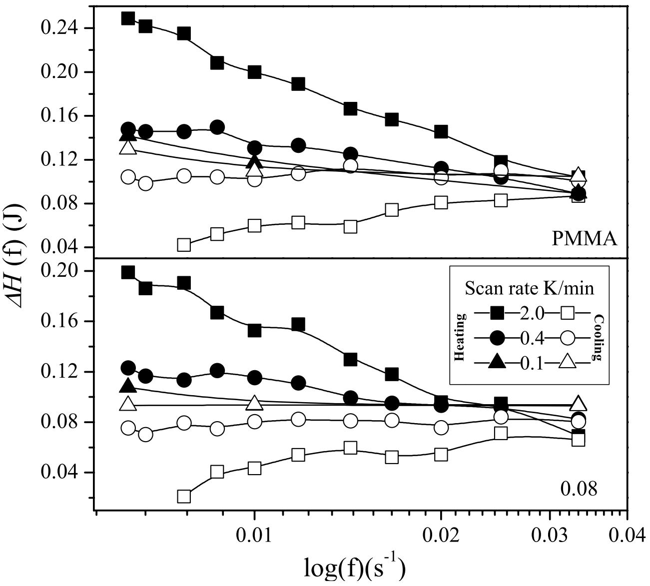

Figure 6. Semi-log plot of the imaginary enthalpy $\Delta H''(f)$, which was obtained by integrating the imaginary part of complex heat capacity, as a function of temperature modulation frequency for pure PMMA (top) and $\phi_m = 0.080$ PMMA + SWCNT (bottom) sample. Heating (closed symbols) and cooling (open symbols) data are shown at the temperature scan rates, see the legend.

Acknowledgments

The authors thank Professor Jianyu Liang, Department of Mechanical Engineering at WPI, for providing the SWCNTs and PMMA materials. This work was supported by the NSF award DMR-0821292 (MRI) and the Department of Physics at WPI.

References

[1] Reading M, Elliott D and Hill V L 1993 *J. Therm. Anal.* **40** 949
[2] Wunderlich B, Jin Y and Boller A 1994 *Thermochim. Acta* **238** 277

[3] Schawe J E K 1996 *Thermochim. Acta* **271** 127

[4] Birge N O and Nagel S R 1985 *Phys. Rev. Lett.* **54** 2674

[5] Birge N O 1986 *Phys. Rev.* B **34** 1631

[6] Dixon P K 1990 *Phys. Rev.* B **42** 8179

[7] Christensen T 1985 *J. Phys. (Paris) Colloq.* **46** C8 635–7

[8] Birge N O, Dixon P and Menon N 1997 *Thermochim. Acta* **304/305** 51–66

[9] Tans S J, Devoret M F, Theses H D A and Smalley R E 1997 *Nature* **386** 474

[10] Dai H, Hafner J H, Rinzler A G, Colbert D T and Smalley R E 1996 *Nature* **384** 147

[11] Sander S J, Tans J, Verschueren A R M and Dekker C 1998 *Nature* **393** 49

[12] Glushanin S, Topolov V Y and Krivoruchko A V 2006 *Mater. Chem. Phys.* **97** 357

[13] Hine P, Broome V and Ward I 2005 *Polymer* **46** 10936

[14] Cioffi N, Torsi L, Ditaranto N, Tantillo G, Ghibelli L, Sabbatini L, Bleve-Zacheo T, Alessio M D, Zambonin P G and Traversa E 2005 *Chem. Mater.* **17** 5255

[15] Pelaiz-Barranco A, Marin-Franch P 2005 *J. Appl. Phys.* **97** 034104

[16] Wunderlich B 1990 *Thermal Analysis* vol 135 (New York: Academic) p 205

[17] Pradhan N R and Iannacchione G S 2009 *J. Appl. Phys.* submitted

[18] Meyyappan M 2005 *Carbon Nanotubes Science and Applications* (Boca Raton, FL: CRC Press)

[19] Harris P J F 2001 *Carbon Nanotubes and Related Structures New Materials for the Twenty-first Century* (Cambridge: Cambridge University Press)

[20] Coleman N J and Craig D Q M 1996 *Int. J. Pharmaceut.* **135** 13

[21] Schawe J E K 1995 *Thermochim. Acta* **261** 183

[22] Hutchinson J M and Montserrat S 1996 *J. Therm. Anal.* **47** 103

[23] Hensel A, Dobbertin J, Boller A and Schawe J E K 1996 *J. Therm. Anal.* **46** 935

[24] Wunderlich B 1997 *J. Therm. Anal.* **48** 207

[25] Aubuchon S R and Gill P S 1997 *J. Therm. Anal.* **49** 1039

[26] Weyer S, Hensel A and Schick C 1997 *Thermochim. Acta* **304/305** 267

[27] Pradhan N R, Duan H, Liang J and Iannacchione G S 2009 *Nanotechnology* **20** 245705

Supplemental Proceedings: Volume I: Materials Processing and Properties
TMS (The Minerals, Metals & Materials Society), 2008

SPECIFIC HEAT AND THERMAL CONDUCTIVITY MEASUREMENTS PARALLEL AND PERPENDICULAR TO THE LONG-AXIS OF COBALT NANOWIRES

N. R. Pradhan[1], H. Duan[2], J. Liang[2], G. S. Iannacchione[1]

[1] Department of Physics and [2]Department of Mechanical Engineering,
Worcester Polytechnic Institute, Worcester, MA, 01605, USA

Keywords: specific heat, thermal conductivity, nanowires, Phonon scattering.

Abstract

This paper reports the synthesis and sample construction as well as measurements of the specific heat and thermal conductivity of cobalt nanowires (CoNWs). Specific heat (c_p) and thermal conductivity (κ) is measured by an AC calorimetric technique from 300 to 400 K parallel and perpendicular to the CoNW long-axis. The specific heat both parallel ($c_p^{||}$) and perpendicular ($c_p^{\perp}$) to the long-axis deviates strongly from the bulk amorphous powder behavior above room temperature. The perpendicular thermal conductivity ($\kappa_{\perp}$) of CoNWs follows a bulk-like behavior revealing a maximum value near 365 K, indicating the onset of boundary-phonon scattering. The parallel thermal conductivity ($\kappa_{||}$) increases smoothly with the increase of temperature from 300 to 380 K and appears to be dominated by phonon-phonon scattering.

Introduction

Recent advances in synthesis, processing, and microanalysis are enabling the promising materials with structures that varies on the scale of several nanometers. Examples such as super-lattices, nanotubes, nanowires, quantum dots, polymer nanocomposites, have advantages in optoelectronics, microelectronics, and micro-mechanical sensors. Many of these nanostructures already have important useful commercial applications. Nanowires are especially attractive for nanoscience studies as well as for nanotechnology applications. Because of their unique density of states, narrow cross-section, and large surface area, nanowires are expected to have significantly different optical, electrical, and thermal properties compared to the bulk. These characteristics may enhanced the exciton binding energy, induce diameter dependent band-gaps, and cause surface scattering of electrons and phonons to dominate the transport properties. In most recent technological applications of nanostructures, thermal management is an important issue in managing undesired heating. Such applications would require highly directional and tunable thermal conductivity and specific heats.

There have been several theoretical studies on the thermal conductivity (κ) of nanowires [1, 2, 3, 4, 5, 6, 7, 8], which has shed light on the physics of their properties. It was found that nanoscale porosity decreases the permittivity of amorphous dielectrics. But porosity also results in a strongly decreased thermal conductivity [5, 9]. Theory suggests that for nanowires with diameters smaller than the bulk phonon mean-free-path (λ_p^B) the thermal conductivity of nanowires will be greatly reduced compared to the bulk [2, 4, 5, 6, 7, 8]. However, there are no predictions regarding the influence of nano-confinement on the behavior of the specific

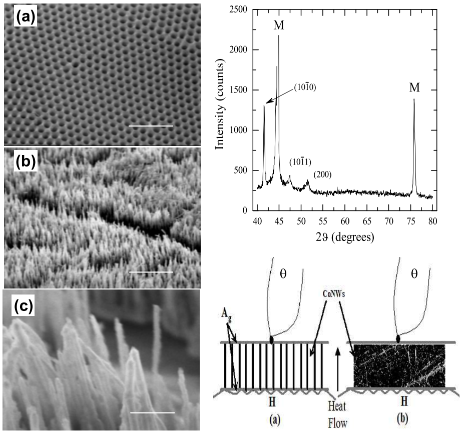

Figure 1: LEFT: SEM micrographs of (a) anodic aluminium oxide with 20 μm long and 80 nm diameter parallel non-interconnected cylindrical cavities, (b) "forest" of CoNWs after removal, and (c) expanded view of CoNWs. The scale bars are 500 nm (a), 5 μm (b), and 500 nm (c). RIGHT TOP: XRD pattern of CoNWs. RIGHT BOTTOM: Sample + Cell configuration for thermal study. (a) parallel alignment of CoNWs to heat flow. (b) Perpendicular alignment of CoNWs to heat flow.

heat (c_p). Knowledge of both c_p and κ is important in determining the thermal relaxation time of materials. It is notable that there have been comparatively few experimental investigations, especially at room temperature and above. The lack of experimental data is due to the difficulty in preparing nanowire samples with the required specification as well as the challenge of precise measurements on such delicate samples.

Synthesis of Cobalt Nanowires

CoNWs were synthesized by electrodeposition assisted by a homemade anodic aluminum oxide (AAO) template. The AAO templates were obtained by a well-established two-step anodization process [10, 11]. Briefly, the first anodic oxidation of aluminum (99.999% pure, Electronic Space Products International) was carried out in a 0.3 M oxalic acid solution at an anodizing voltage of 40 V at 10 °C for $16-20$ hr. The porous alumina layer formed during first anodization process is dissolved by chromic acid at 70 °C. The treated samples are subjected to the second anodization with the same conditions as the first. The thickness of the anodic film was adjusted by appropriately setting the anodization time. The resulting AAO templates were then immersed in a 0.1 M phosphoric acid etching solution at room temperature for 30 min to widen the pores and thin the oxide barrier layer at the pore bottom. Pore diameters were controlled to lie in the range of $80-120$ nm by varying the anodizing voltage and etching times.

Cobalt nanowires were then electrochemically deposited by AC electrolysis from the bottom of the pores up using 14 V at 100 Hz for 150 mins in an electrolyte solution consisting of 240 g/L of $CoSO_4$+$7H_2O$, 40 g/L of HBO_3, and 1 g/L of ascorbic acid [10, 11].

Structural characterization was performed by means of x-ray diffraction using a Rigaku goniometer with Cu Kα radiation ($\lambda = 0.15406$ nm), operated routinely at 37.5 kV and 25 mA with 0.5° divergent and anti-scattering slits coupled with 0.3 mm receiving slits. Diffraction patterns were acquired at 2θ steps of 0.05° and 5 s/step exposures. The filling of the pores as well as the morphology of the nanowire array before and after removing the alumina template was monitored with a JEOL 982 field-emission scanning electron microscopy (SEM).

For comparison, bulk cobalt was obtained from Aldrich Inc. in a fine powder form (99.9% pure) with particle size in the range of 2 to 10 μm. This bulk powder was used after degassing and drying in vacuum at $\sim$ 100 °C for about 2 hr.

Sample Configuration

The CoNW samples were prepared for directional measurements of heat flow parallel and perpendicular to the long-axis of the nanowires. The sample+cell configuration for the parallel measurement is shown in Fig. 1-RIGHT BOTTOM(a). The general sample+cell configuration consists of a sandwich (or stack) arrangement of heater, thin silver sheet (0.1 mm thick and 5 mm square), sample, thin silver sheet, and thermistor, all held together by a thin application of GE varnish.

For the parallel configuration, the CoNWs embedded in an AAO template were first separated from the Al substrate by a 0.1% $HgCl_2$ solution, and the barrier layer was removed by wet etching in 0.5% H_3PO_4 for 30 mins. To ensure a good thermal contact between the CoNWs and the silver sheets, the AAO template is etched by 0.1 M NaOH solution to expose the tips of the CoNWs from both ends. This 20 μm thick CoNW+AAO sample is then carefully sandwiched between the two silver sheets and secured by a thin layer of GE varnish. A 120 Ω strain-gauge heater is attached on one side of the stack and a 1 MΩ carbon-flake thermistor on the other side by GE varnish. In this arrangement, the applied heat should transfer along the nanowires.

Measurements with the heat flow perpendicular to the long-axis of the nanowires were conducted in a similar arrangement. The CoNW embedded AAO template was immersed in a 0.1 M NaOH solution to completely dissolve the AAO and release the nanowires. The powder form of CoNWs was then dispersed in a solvent and drop cast onto one of the cell's silver sheets. This deposition results in a mat-like arrangement of the CoNWs approximately 0.1 mm thick and essentially perpendicular to the stack. The remaining components of the cell are attached again by a thin application of GE varnish. It is important to note that although the geometry has the heat transfer perpendicular to the nanowire long-axis, there are a large number of contacts between the sides of the nanowires in the layer of CoNWs. The bulk powder measurements were done in the same way with a similar film thickness. All sample+cell arrangements had essentially identical areas.

The AC calorimetric technique used to measure heat capacity and thermal conductivity is described elsewhere [12, 13]. Each component of the above described sample+cell arrangement was measured separately to determine the contribution of the thin silver sheets (Ag), heater (H), thermistor (θ), and GE varnish. In addition, an empty AAO template was also measured. The specific heat (c_p) is then calculated by subtracting these contributions from the total heat capacity and dividing by the cobalt mass. The thermal conductivity estimation for these macroscopic samples requires the assumption that the entire sample volume of thickness L and area A is filled by the cobalt for the bulk powder and perpendicular configuration samples since the filling fraction is not known. For the parallel configuration, $\kappa_{\|}$ of the nanowires is estimated by assuming that the AAO and CoNWs are in a parallel circuit arrangement. Thus, it is expected that the thermal conductivity measured here is

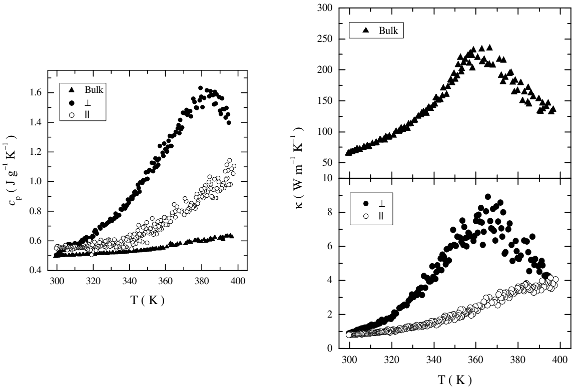

Figure 2: LEFT: Specific heat of bulk powder cobalt (triangles) and cobalt nanowires measured perpendicular (solid circles) and parallel (open circles) to the long-axis. RIGHT: (a) Effective thermal conductivity of bulk powder cobalt as a function of temperature. (b) Effective thermal conductivity of CoNWs as a function of temperature measured parallel (open circles) and perpendicular (solid circles) to the long-axis.

an effective κ and would have a higher uncertainty in its absolute value than that for the specific heat.

Morphology CoNWs

Fig. 1-LEFT shows SEM images of CoNWs embedded in the AAO templates. In Fig. 1-LEFT(a), an oblique view of the sample before etching by NaOH solution showing the highly ordered hexagonal pattern of the AAO pores. The pore diameter and interpore separation are about 80 and 40 nm, respectively. Fig. 1-LEFT(b) is an SEM image of the CoNWs with the tips exposed by about 3 μm and Fig. 1-LEFT(c) is a high-magnification image of the cobalt nanowires.

A microstructure study of the resulting CoNWs was performed by x-ray diffraction (XRD) and shown in Fig. 1-RIGHT TOP. From the scattering angle 2θ dependence of the x-ray intensity it is shown that the CoNWs consists of a mixture of *fcc* and *hcp* structures. This is consistent with an nuclear magnetic resonance (NMR) study by Strijkers. et al. [14] although direct current was applied there to synthesize CoNWs. The XRD peaks at 2θ near 41.685° and 47.57° can be assigned to the $(10\bar{1}0)$ and $(10\bar{1}1)$ planes of an *hcp* structure. The peak at 2θ near 51.522° is attributed to the (200) plane of a *fcc* structure. The remaining peaks indexed as M in Fig. 1-RIGHT TOP could be a combination of diffraction from the (0002) and (1120) planes of the *hcp* structure. Alternatively, the peaks near 44° and 75° could be a combination of the (111) and (220) planes of the *fcc* structure. It is also shown that the fabricated Co nanowires have a preferential orientation (0002). The preferentially oriented growth of the nanowires is attributed to the growth of the nanowires within the pores of the alumina film. No diffraction peaks from cobalt oxide or from the alumina are seen, indicating that the cobalt nanowires are of high purity.

Specific Heat of CoNWs

The specific heats of bulk powder cobalt as well as CoNWs in parallel and perpendicular to the long-axis configuration are shown in Fig. 2-LEFT. The specific heats of all samples were determined as a function of temperature from 300 to 400 K. The cobalt bulk powder sample yields a $c_p^B = 0.49$ J g^{-1} K^{-1} at 300 K and a weak, nearly-linear, temperature dependence consistent with the literature [15, 16]. The magnitude of the specific heat for the two CoNW samples are $c_p^{||} = 0.53$ J g^{-1} K^{-1} and $c_p^{\perp} = 0.50$ J g^{-1} K^{-1} at 300 K. For the parallel CoNW configuration, $c_p^{||}$ increases linearly from room temperature to $\sim$ 320 K in a bulk-like fashion. Above 320 K, $c_p^{||}$ increases much more rapidly with temperature than the bulk. In the case of perpendicular measurement, $c_p^{\perp}$ increases more rapidly than either the parallel or the bulk behavior from 318 to 370 K, above which it begins decreasing.

The differences in c_p observed here are likely due to the composite nature of the sample+cell configuration. The similarity, at least just above room temperature, between $c_p^{||}$ and c_p^B is understandable as in this heat-flow configuration, the length of the CoNW is comparable to the size of the bulk powder sample. The deviation beginning at $\sim$ 320 K may be a consequence of the 1-D nature of the nanowires. As a result, one might expect "bunching" of the phonons (or phonon-phonon scattering) to dominate at some elevated temperature. For the perpendicular arrangement and although laying flat to the silver sheets, the random deposition of CoNWs within the cell likely results in a very large number of contacts, on the nanometer scale, between individual CoNWs. Thus, the $c_p^{\perp}$ measured is almost certainly an effective result for the sample+cell composite.

Thermal Conductivity of CoNWs

Fig. 2-RIGHT(top panel) shows the effective thermal conductivity of bulk powder cobalt at 300 K of $\kappa_B \approx 67$ W m^{-1} K^{-1} with a strong temperature dependence reaching a maximum at $\sim$ 360 K. The the literature value for pure cobalt at 300 K is 90 W m^{-1} K^{-1} and displays a weak temperature dependence [17]. As with $c_p^{\perp}$, the effective thermal conductivity of bulk powder cobalt measured here is a consequence of the composite nature of micron sized amorphous particles sandwiched in the cell "stack". As such, it seems likely that the observed maximum is due to boundary-phonon scattering.

The derived thermal conductivity of the CoNWs for the two heat-flow configurations are shown in Fig. 2-RIGHT(bottom panel). Both $\kappa_{||}$ and $\kappa_{\perp}$ have values 83 times less than the bulk at 300 K. However, for increasing temperatures, $\kappa_{||}(T)$ behaves quite differently from the observed bulk trend, increasing in a smooth manner up to $\sim$ 380 K at which a small "kink" is seen to a nearly constant value of $\kappa_{||} \approx 4$ W m^{-1} K^{-1}. Although the uncertainty in absolute values is higher for the measured κ compared to c_p, the marked reduction of magnitude of κ in both configurations with respect to the bulk is consistent with the 1-D nature and boundary scattering. However, for $\kappa_{||}$, the kink to a constant value at $\sim$ 380 K may be an indication of phonon-phonon and defect-phonon scattering. For the perpendicular heat-flow measurement of CoNWs, $\kappa_{\perp}$ exhibits a similar temperature dependence as the bulk, although of greatly reduced magnitude. As with κ_B, the observed maximum for $\kappa_{\perp}$ seen at $\sim$ 360 K is again likely due to the composite nature of the sample+cell arrangement. The junctions between the nanowires dominant the heat transfer for $\kappa_{\perp}$ as the contacts between bulk powder particles were for κ_B. The difference in temperature for the observed maximum is consistent with the bulk powder particles being much larger in size.

Conclusions

This paper reports measurements of the specific heat and effective thermal conductivity of a macroscopic arrangement of cobalt nanowires, CoNWs, with the orientation of the nanowire parallel and perpendicular to direction of the heat-flow and compared with results for bulk-powder cobalt. The particle nature of the bulk-powder and random deposition of the CoNW($\perp$) configuration, lead to strong deviations of both κ and c_p from that expected for pure *solid* cobalt. Perpendicular heat-flow arrangement appears to be dominated by phonon-boundary scattering. Parallel heat-flow measurements appear dominated by phonon-phonon or phonon-defect scattering. These results suggest the interesting possibility of engineering both the specific heat and thermal conductivity of nano-composite materials.

References

[1] S. Barman and G. P. Srivastava. *Phys. Rev. B*, 73:205308, 2006.

[2] K-Q. Chen, W-X. Li, W. Duan, Z. Shuai, and B-L. Gu. *Phys. Rev. B*, 72:045422, 2005.

[3] Y. Chen, D. Li, J. R. Lukes, and A. Majumdar. *J. Heat Trans.*, 127:1129, October 2005.

[4] Y. Chena, D. Lib, J. Yangc, Y. Wuc, J. R. Lukes, and A. Majumdare. *Physica B*, 349:270, 2004.

[5] D. Li, Y. Wu, P. Kim, L. Shi, P. Yang, and A. Majumdar. *Appl. Phys. Lett.*, 14:2934, 2003.

[6] R. Prasher. *Phys. Rev. B*, 74:165413, 2006.

[7] S. Volz and G. Chen. *Appl. Phys. Lett.*, 75:2056, 1999.

[8] R. Yang, G. Chen, and M. S. Dresselhaus. *Phys. Rev. B*, 72:125418, 2005.

[9] T. M. Trit. *Sci.*, 283:804, 1999.

[10] J. Li, C. Papadopoulos, J. M. Xu, and M. Moskovits. *Appl. Phys. Lett.*, 75:367, 1999.

[11] J. Liang, H. Chik, A. Yin, and J. M. Xu. *J. Appl. Physics*, 91:2544, 2002.

[12] A. Roshi, G. S. Iannacchione, P. S. Clegg, and R. J. Birgeneau. *Phys. Rev. E*, 69:031703, 2004.

[13] S. Sinha, S. Barjami, G. S. Iannacchione, A. Schwab, and G. Muench. *J. Nanopart. Res.*, 7(6):651, December 2005.

[14] G. J. Strijkers, J. H. J. Dalderop, M. A. A. Broeksteeg, H. J. M. Swagten, and W. J. M. de Jonge. *J. Appl. Phys.*, 86(9):5141–5145, 1999.

[15] W. Bendick and W. J. Pepperhoff. *J. Phys. F: Metal Phys.*, 11(11):2185, 1979.

[16] R. R. Rao and A. Ramanand. *Phys. Rev. B*, 19(4):1972, 1979.

[17] T. M. Tritt. *Thermal conductivity: Theory Properties and Application.* Number 4. Kluwer Academyc/Plenum Publishers, 2004.

Index